Computational and Spectroscopic Investigations of Intermolecular Interactions in Clusters

By

Patrick James Joseph Carr

A thesis

presented to the University of Waterloo

in fulfilment of the

thesis requirement for the degree of

Doctor of Philosophy

in

Chemistry

Waterloo, Ontario, Canada, 2019

Examining Committee Membership

The following served on the Examining Committee for this thesis. The decision of the Examining Committee is by majority vote.

External Examiner	Dr. Paul Hockett Associate Research Officer National Research Council, Ottawa, ON, Canada
Supervisor	Dr. W. Scott Hopkins Associate Professor University of Waterloo, Waterloo, ON, Canada
Internal Member	Dr. Pierre-Nicholas Roy Professor; Canada Research Chair in Quantum Molecular Dynamics University of Waterloo, Waterloo, ON, Canada
Internal-external Member	Dr. David Hawthorn Professor; Associate Chair, Graduate Studies University of Waterloo, Waterloo, ON, Canada
Other Member(s)	Dr. Germán Sciaini Associate Professor; Canada Research Chair in Atomically Resolved Dynamics and Ultrafast High-Resolution Imaging University of Waterloo, Waterloo, ON, Canada

Author’s Declaration

This thesis consists of material all of which I authored or co-authored: see Statement of Contributions included in the thesis. This is a true copy of the thesis, including any required final revisions, as accepted by my examiners.

I understand that my thesis may be made electronically available to the public.

Statement of Contributions

This thesis contains works which have been published in peer reviewed journals. These works have been acknowledged in the references section of this thesis. My contributions, relating to this thesis are summarized below:

Chapter 4: Mode-Selective Laser-Control of Palladium Catalyst Decomposition is reproduced from the following publication:

Carr, P. J. J.; Lecours, M. J.; Burt, M. J.; Marta, R. A.; Steinmetz, V.; Fillion, E.; Hopkins, W. S. Mode-Selective Laser Control of Palladium Catalyst Decomposition. *The Journal of Physical Chemistry Letters* **2018**, *9* (1), 157–162.

My contributions to this work include traveling to the CLIO facility in 2014 to conduct the IRMPD studies and submission and analysis of the theoretical computations. The basin hopping studies were conducted by Chuantian Zhan, a former undergraduate thesis student.

Sections of Chapter 5: Clusters of $B_{12}X_{12}^{2-}$ (X = H, F, Cl) are reproduced from the following publications:

Hopkins, W. S.; Carr, P. J. J.; Huang, D.; Bishop, K. P.; Burt, M.; McMahon, T. B.; Steinmetz, V.; Fillion, E. Infrared-Driven Charge Transfer in Transition Metal $B_{12}F_{12}$ Clusters. *The Journal of Physical Chemistry A* **2015**, *119* (31), 8469–8475.

My contributions to this work include traveling to the CLIO facility in 2014 to conduct the IRMPD studies and analysis of the experimental and computational data. Theoretical calculations were conducted by Denzel Huang, a former undergraduate co-operative education student.

Carr, P. J. J.; Warneke, J.; Featherstone, J.; Jenne, C.; Loire, E.; Hopkins, W. S. The Structure of Proton-Bound Triethylammonia $B_{12}X_{12}^{2-}$ (X = F, Cl) Clusters. *Molecular Physics* **2019**, 1–8.

My contributions to this work include conducting theoretical calculations and analysis of the experimental and theoretical data. The experimental data was collected at the CLIO facility in 2017 by a team of Hopkins and McMahon group members.

Abstract

In this thesis, the study of intermolecular interactions within cluster systems is presented. Covalently and non-covalently bound clusters possess oftentimes unique and unexpected properties which can be tuned by adjustment of size, composition, and geometry to target desired properties for use in nanotechnologies. Additionally, clusters present a computationally tractable model of bulk systems such as reactive sites on bulk heterogeneous catalysts. Infrared spectra have been collected of various clusters and theoretical computations have been conducted to interpret spectra and provide predictions for other properties to guide future works. Investigations of the forces binding cluster species together are conducted to provide insight into the fundamental underpinning of molecular properties with applications in the field of nanomaterial design.

A variety of clusters have been studied here. Computational studies of size-dependency in nitrous oxide reactions with rhodium sulphide clusters have been conducted. Barriers to competing N_2O desorption and decomposition have been ascertained and compared with and without thermal corrections. Inclusion of the sulphur atom is found to alter which reaction pathway is preferred, as seen by comparison with analogous studies on pure rhodium clusters. Infrared multiple photon dissociation (IRMPD) spectroscopy is utilized to probe the additional clusters; a series of palladium coordination complexes and a series of clusters containing icosahedral $B_{12}X_{12}^{2-}$ (X = H, halogen) cages complexed with a cationic transition metal atom, a cationic amine, or a neutral polar cyclohexane-based compound. This IRMPD technique successfully produced infrared spectra for these species in the gas phase and unique properties were observed for each cluster upon IR induced dissociation. Density functional theory calculations determined geometries, dissociation thresholds, and interpreted IR spectra. Additional theoretical tools quantified molecular orbital interactions and topographical parameters of the electron density.

Acknowledgements

Completion of this Ph. D. would not have been possible without the unfailing optimism, guidance, and belief in my abilities from Dr. W. Scott Hopkins, my supervisor. His genuine concern and tireless dedication toward his students will be a persistent source of inspiration for many years to come. I would like to thank Dr. Terry McMahon for his advice over the years, for the many "borrowed" tools, and his involvement in the many CLIO trips which provided the vast majority of experimental data presented in this thesis. I would also like to thank my supervisory and examining committees.

The many current and former members of the Hopkins lab and McMahon lab have been invaluable to the completion of this thesis. Drs. Steve Walker, Neville Coughlan, and Jeff Crouse have each put many hours into assisting me with the VMI project, helping me understand various scientific concepts, and proof reading much of my writing. Mr. Mike Lecours has been a good friend and developed many time saving job submission and data analysis scripts, including the most recent version of the basin hopping algorithm. I would like to mention Mr. Josh Featherstone for his "McMahon Suite" of automation scripts and for his spectrum analysis script. Ms. Su Ji Lim is another member who has worked with me on the VMI and laser systems; her support and friendship has also helped me achieve this goal.

Finally, I would like to thank my family. My mother and stepfather who supported me during my undergraduate degree. My mother- and father-in-law who always provided a Sunday dinner to look forward to. My brother, Chris Carr, who has been an inspiring role model. Last but not least, my wife, Ms. Alisha Carr; she has put her life on hold for this pursuit and without her believing in me and sacrificing her time and energy, this thesis would have never been completed.

Table of Contents

List of Figures

List of Tables

List of Abbreviations

AO	Atomic Orbital
BCP	Bond Critical Point
BH	Basin Hopping
CCP	Cage Critical Point
CHELPG	Charge from an electrostatic potential with grid sampling
CLIO	Centre Laser Infrarouge d'Orsay
DFT	Density Functional Theory
ESI	Electrospray Ionization
FEL	Free Electron Laser
FMO	Frontier Molecular Orbital
FT-ICR	Fourier Transform Ion Cyclotron Resonance
GHG	Greenhouse Gas
HOMO	Highest Occupied Molecular Orbital
IR	Infrared
IRMPD	Infrared Multiple Photon Dissociation
IVR	Intramolecular Vibrational Energy Redistribution
LCAO	Linear Combination of Atomic Orbitals
LUMO	Lowest Occupied Molecular Orbital
MM	Molecular Mechanics
MO	Molecular Orbital
NAO	Natural Atomic Orbital
NBO	Natural Bonding Orbital
NPA	Natural Population Analysis
PE	Photoelectron
PES	Potential Energy Surface
PNNL	Pacific Northwest National Laboratories
QIT	Quadrupole Ion Trap
QTAIM	Quantum Theory of Atoms in Molecules
RCP	Ring Critical Point
STQN	Synchronous Transit Quasi-Newton
TEA	Triethylammonium
TM	Transition Metal
TS	Transition State
UFF	Universal Force Field

1 Introduction

Clusters present a fascinating and challenging area of study. They represent a bridging size regime between atomic/molecular systems, with discrete quantum structure, and bulk phase with classical properties arising from the convergence of many quantum states into continua or band structures. As such, size dependent studies are often employed to understand the evolution of quantum properties into those of the bulk phase.[1] An exciting realization of such size-dependent studies is that clusters have been found to display drastically different properties than their bulk or quantum counterparts.[2] This presents an opportunity to uncover and exploit the unique and unpredictable properties of clusters by tuning size, composition, and structure. It is the forces, covalent and non-covalent, which bind clusters together that dictate the observed properties, and a better understanding of these forces could lead to improved control of cluster properties for specific applications.

The study of clusters provides an opportunity to push the boundaries of theoretical and computational models. Pursuing the theoretical treatment of cluster species that represent the boundary of computational tractability is not only challenging, but also presents the potential for the advancement of current theoretical models. The computational work described herein helps establish limits for some model chemistries, highlighting strengths and uncovering deficiencies, and thereby assisting theoreticians in their efforts to improvement upon current models.

Studies of clusters usually exploit a combination of theoretical and experimental approaches.[2] Here, we primarily use density functional theory (DFT) for calculations and infrared multiple photon dissociation (IRMPD) spectroscopy for experimental validation. The general

approach has been to theoretically identify the lowest energy geometric isomers of a cluster species and compare calculated spectra to those acquired at the Centre Laser Infrarouge d'Orsay (CLIO) free electron laser (FEL) facility of Université de Paris XI in Orsay, France. Having experimentally validated a computational method, other cluster properties can be predicted with confidence. Properties key to this thesis include: charge distribution, stabilization energies of orbital interactions, reaction barrier heights, binding energies, and electron density at critical points. A brief introduction to each model cluster system follows. Detailed motivations and literature review can be found in the introduction sections of each corresponding chapter.

In Chapter 3, we use a purely computational approach to study reactions of nitrous oxide on cationic rhodium sulphide clusters. Previous studies on analogous pure rhodium clusters spectroscopically validate the computational methods that are applied here.[3] Confidence in our global minimum geometries comes from the exhaustive searches of the potential energy surfaces conducted using our custom-written basin hopping (BH) algorithm. The motivation for this study comes from the use of bulk rhodium in catalytic converters for decomposition of nitrous oxide, a potent greenhouse gas.[3,4] Small gas phase rhodium clusters are used to model the reactive sites in heterogeneous catalysis.[1,2] Here, we model the competing decomposition and desorption of nitrous oxide on rhodium sulphide clusters, $Rh_nS^+ \bullet N_2O$ (n = 2 – 9). We include sulphur because it is a well-known bulk phase catalyst poison; it is an open question as to if these poisoning properties persist in the small cluster size regime.[5] In this study, three key stationary points and a transition state along the proposed N_2O decomposition reaction pathway are investigated using basin hopping and DFT. The global minimum geometries of $Rh_nS^+ \bullet N_2O$, $Rh_nS^+ \bullet O$, and $Rh_nSO^+ \bullet N_2$ (n = 2–9) are identified and their vibrational spectra are predicted. Optimizations are performed on $Rh_nS^+ \bullet N_2O^{\ddagger}$ transition state structures along the N-O fission coordinate of a bent N_2O moiety

that brings the oxygen atom in contact with a rhodium atom of the cluster core. The relative height of these reaction barriers is compared to the N_2O desorption threshold to establish whether N_2O decomposition is likely to occur as was done previously for the analogous pure rhodium clusters.[3]

In Chapter 4 we study catalytic organopalladium complexes. Five different complexes of the form $RPdL_2$, which vary in the organic residue or the ligand, are interrogated using IRMPD and the results are interpreted with the aid of DFT calculations. A key finding is that IR excitation can be used to mode-selectively induce ligand scrambling reactions. IR induced dissociation products are analyzed and the energetic thresholds to produce those products are calculated. We find the wavenumber dependence on the formation of ligand scrambling products and the associated energetic thresholds have major implications regarding the redistribution of vibrational energy, a key tenant of the IRMPD process.

Chapter 5 addresses molecular clusters of $B_{12}X_{12}^{2-}$ (X = H, F, Cl) and three different types of coordinating moieties, which emphasize different intermolecular interactions. $B_{12}X_{12}^{2-}$ molecules all adopted an icosahedral geometry with B-X units at each vertex; the boron atoms form an icosahedral cage and the X atoms are directed outward from the cage center, essentially forming an isolating halogen layer around the boron atoms. We separate this work into three related studies. The first study investigates the complexation of a single transition metal (TM) atom with $B_{12}F_{12}^{2-}$. Twelve different transition metals from the last four groups of the d-block are considered. IRMPD spectra were recorded for the isolable species and DFT calculations are employed to model the systems of interest. The second study investigates the interactions between $B_{12}X_{12}^{2-}$ (X = F, Cl) and triethylammonium, $[(CH_3CH_2)_3NH]^+$ (TEA). TEA is found to orient such that the charge-carrying proton points towards the center of a triangular face formed by three X atoms, leading to the formation of B-X•••H-N hydrogen bonds. Detailed investigations of the molecular

orbital (MO) interactions and electron topology are conducted. IRMPD spectra are collected for the fluorinated and chlorinated clusters, and fragments associated with TEA loss and cage fission to form $B_nX_m^-$ are observed. DFT energies of the various dissociation pathways reveal that both proton transfer and charge transfer thresholds are accessed during IRMPD, and that both thresholds give rise to their own fragmentation patterns. The third study investigates the interaction between all-*cis* 1,2,3,4,5,6-hexafluorocyclohexane, $C_6H_6F_6$ (referred to as **1**), and $B_{12}X_{12}^{2-}$ (X = H,F). **1** is a neutral molecule with an unusually large dipole moment (~7.3 D) owing to the placement of all fluorine atoms on the same face of the cyclohexane ring.[6–8] Complexes of **1** with $B_{12}H_{12}^{2-}$ present an excellent opportunity to study the exotic dihydrogen bond, six of which are expected to form at each $B_{12}H_{12}^{2-}$/**1** interface. Clusters of up to four **1** molecules around $B_{12}H_{12}^{2-}$ are isolated and probed using IRMPD. Additionally, photoelectron (PE) spectra of $[\mathbf{1}_n{\bullet}B_{12}H_{12}]^{2-}$ (n = 1 – 5), have been collected. DFT is used to calculate global minimum geometries, IR spectra, and (considerably large) cluster binding energies. Natural bond orbital (NBO) analysis is used to investigate atomic partial charges and stabilization energies of intermolecular MO interactions. Further to this, the quantum theory of atoms in molecules (QTAIM) is used to analyze the electron topology at the $B_{12}H_{12}^{2-}$/**1** interfaces. The effects of sequential addition of **1** around the $B_{12}H_{12}^{2-}$ cage are considered. Comparisons are made to the analogous fluorinated cage clusters, $[\mathbf{1}_n{\bullet}B_{12}F_{12}]^{2-}$ n = 1 – 4.[7]

Taken as a whole, this thesis provides a detailed investigation of intermolecular interactions between moieties that exhibit complex electronic and/or geometric structures. The interactions studied range from essentially covalent through to essentially ionic in nature, and we very clearly see how the interplay between electronic and geometric structure gives rise to interesting, and oftentimes unexpected, behavior such as mode-selectivity, catalyst poisoning, and dihydrogen

bonding. While non-covalent interactions have for many years been implicated in determining the physicochemical properties of systems such as biological macromolecules and catalysts,[2,9–12] a deep understanding of the physics underpinning these phenomena is still being developed. With the research described herein, we hope to have provided a little more clarity and direction for this fascinating subject.

2 Methods

2.1 Computational

2.1.1 Basin Hopping

In general, the quantum chemist's goal is to determine the lowest energy spatial arrangement of nuclei within a molecule. It is well known to be the dominant contributor to that molecule's room temperature physicochemical properties since it is geometry that defines the quantum structure. Accurate determination of a molecule's thermally accessible (*i.e.* lowest vibronic energy) geometries is therefore of paramount concern to the field of computational chemistry. Often DFT is utilized to optimize molecular structure such that it minimizes the electronic energy on the potential energy surface (PES). This is an effective strategy when dealing with geometrically simple molecules where the global minimum geometry is already known or can be intuited. However, when the global minimum geometry of a molecule is less obvious, the molecular structure can optimize to a stable, but high energy local minimum rather than the global minimum of that PES. The strategy we have adopted to assist with determining the global minimum geometry of geometrically complex systems is to generate as many unique and chemically relevant input geometries for DFT optimization as possible with a custom-written molecular simulation code based on the basin hopping (BH) algorithm.[13–15]

The BH algorithm searches for minima on a PES by using a modified Monte-Carlo based energy minimization technique.[13–15] To initiate the algorithm a single input geometry is optimized to a local minimum using molecular mechanics (MM), see Section 2.1.2 Page 8 for details, as implemented by the Gaussian 09 program.[16] The MM optimized input geometry is then randomly distorted to produce a new candidate structure. The distortion is applied to specific degrees of

freedom selected by the user. For example, the user can choose to vary the orientation of a surface moiety through translation and/or rotation or change bond angles and/or dihedral angles. The user must also specify several other input parameters including: the range over which the random distortion may be applied, a containment volume for the system, minimum internuclear distances, and a simulation temperature, T. These parameters control the degree to which the PES is sampled and ensures the generated structures are chemically relevant.

The newly distorted geometry, *n*, is optimized at the MM level of theory to produce the most stable isomer in that region of the PES. The energy of *n* (E_n) is then compared to the energy of the current MM global minimum (E_{GM}). Acceptance of n can occur if $E_n < E_{GM}$, which establishes *n* as the new MM global minimum, or if $E_n > E_{GM}$ and the Boltzmann population ratio, P_n/P_{GM}, at temperature T (Eq. 2.1) is less than a randomly selected value between zero and one.

$$\frac{P_n}{P_{GM}} = e^{\frac{(E_{GM}-E_n)}{k_B T}} \qquad \text{Eq. 2.1}$$

If geometry *n* fails both energy comparisons it is rejected and the geometry that was distorted to produce *n* (*i.e.*, *n*-1 in the BH sequence) is re-distorted. The first energy comparison, where $E_n < E_{GM}$ is evaluated, directs the search towards the MM global minimum geometry. The second energy comparison prevents the algorithm from getting trapped in a deep basin where the $E_n < E_{GM}$ condition would be impossible to satisfy without the application of a substantial distortion. Preventing energetic trapping ensures a full sampling of the PES. Commonly, the acceptance-to-rejection ratio, ε, is monitored to assess the search efficiency. Usually, we seek to employ a value of $\varepsilon \approx 0.5$, meaning that if 15,000 structures pass the BH routine, 30,000 geometries were sampled.

2.1.2 Molecular Mechanics

Molecular mechanics employs a classical approach to calculate the total energy for a nuclear arrangement. The energy calculated by MM is relative to idealized geometric parameters from the hybridization of atomic orbitals in valence bond theory.[17] This energy is therefore referred to as a strain energy since it is a sum of terms related to the deviation from the idealized values. The strain energies of bonds and angles are calculated using the harmonic oscillator model. The summation of these strain energies is equal to the energy of the bonding interactions, see Eq. 2.3.[17] Non-bonding interactions are defined by van der Waals parameters and Coulomb's law to treat electrostatic interactions between partial charges (see Eq. 2.4).[17] The sum of the bonding and non-bonding energies yields the total MM energy of the molecule, as per Eq. 2.2. The specific functional form and input parameters for Eq. 2.3 and Eq. 2.4 are provided by the chosen force field. The force fields for this work were the universal force field (UFF) and the AMBER force field. Discussion of the chosen force fields can be found in the relevant sections of this thesis, Sections 3.2 and 4.3.

$$E_{total} = E_{bonding} + E_{non-bonding} \qquad \text{Eq. 2.2}$$

$$E_{bonding} = \sum_{bonds} K_r(r - r_{eq})^2 + \sum_{angles} K_\theta(\theta - \theta_{eq})^2 + \sum_{torsions} K_P[1 - Pcos(\omega - \omega_{eq})] \qquad \text{Eq. 2.3}$$

$$E_{non-bonding} = \sum_{i<j} \left[\frac{A_{ij}}{r_{ij}^{12}} - \frac{B_{ij}}{r_{ij}^{6}} + \frac{q_i q_j}{4\pi\epsilon_0 r_{ij}}\right] \qquad \text{Eq. 2.4}$$

In Eq. 2.3, K_r and K_θ are the harmonic force constants for the bond stretching and bond angle bending respectively, r and θ are the values for input bond length and bond angle, and r_{eq} and θ_{eq} are the equilibrium values for the specific bond type (*e.g.*, C-C or C=C). P is the periodicity of the

dihedral angle, K_P is a proportionality constant for that periodicity, ω is the dihedral angle, and ω_{eq} is the equilibrium value for the specific bond type. In Eq. 2.4, A and B are the van der Waals parameters describing short- and long-range interactions, i and j are nuclear indices, q is the atomic charge, and ϵ_0 is the vacuum permittivity. Typically, atomic charges are calculated for a DFT pre-optimized guess structure using the charge from an electrostatic potential with grid sampling (CHELPG) partition scheme.[18,19] CHELPG determines the atomic partial charges by a least-squares fitting the DFT electrostatic potential outside the van der Waals surface of the molecule.[15,18]

The MM model is used exclusively in the BH routine. The simplicity of MM results in the calculations being very computationally inexpensive, typically completing in less than five seconds for the species studied here. A computationally inexpensive model is of primary importance for a BH simulation because the number of candidate structures is typically in the range of 10^3 - 10^4. The disadvantage of using MM on small molecules such as those studied here is the relative inaccuracy of a method which relies on valence bond theory idealized geometries, van der Waals radii, and Coulombic attractions. To mitigate this issue, the output MM structures identified by BH are used as starting geometries for optimization at the (much more accurate) density functional level of theory.

2.1.3 Density Functional Theory

Density functional theory has become an indispensable tool for interpreting and predicting experimental results. In contrast to wavefunction based methods such as Hartree-Fock theory, DFT models the properties of many-electron systems by treating the spatially dependent electron density, which is more computationally efficient than treating each electron independently. The electron density function can be used to define the components of the electronic Hamiltonian:

kinetic energy, electron-nuclear interaction energy, Coulomb energy, and the exchange/correlation energy.[17] Given that the electron density is itself a function, the terms of the electronic Hamiltonian are therefore functionals (*i.e.*, functions of functions).

For implementation, a trial electron density, in combination with the linear combination of atomic orbitals (LCAO) approximation, are used to define a trial wavefunction. Determination of a trial wavefunction and a Hamiltonian naturally leads to a trial energy. The trial electron density is iteratively adjusted by the standard self-consistent field approach until a minimum energy is reached.[15] A challenge in the DFT approach is that the exact form of the exchange/correlation functional is not known and must therefore be approximated.[15,17] The type of exchange/correlation functionals used here are hybrid generalized gradient approximation functionals, which depend on the value of the electron density at a point and the density gradient around that point, as well as a percentage of exact Hartree-Fock exchange.[15] Theoretically, exchange/correlation functionals are independent of the system being studied. However, certain functionals have been found to produce results which better match the experimental data of certain systems. For example, some functionals are better suited for treating organic molecules than inorganic molecules. The specific functionals used and the justification for their choice is given in the methods sections of each results chapter.

To create molecular orbitals (MOs) *via* the LCAO method, a basis set consisting of atomic orbitals (AO) is employed. Basis sets are defined by the number of AOs used, the type of AO (*i.e.*, s, p, d, *etc.*), how the valence electrons are split into different orbitals and if a pseudo-potential is used to treat *e.g.*, core electrons. A split-valence basis set takes the chemically interesting valence orbitals and splits them into multiple valence orbitals. This is done to account for the dependence of the valence orbitals on the chemical bond in which they are participating. A common notation used to represent this type of basis set (*i.e.*, a Pople-type basis set) is K-LMG where K is the

number of s-type primitive Gaussian functions used for the core electrons, L and M are the number of sp-type primitive Gaussians used for the inner and outer valence orbitals and G indicates that Gaussian primitives are being used.[15] A primitive Gaussian refers to an AO-like function in the form of a Gaussian function.[15] Additional AOs can be added to better treat inter- and intramolecular interactions. The polarization basis set, indicated in basis set notation as "(d,p)," addresses the issue that AO functions are centered only on atoms by adding d-orbital functions to non-hydrogen atoms and p-orbital functions to hydrogen atoms. Finally, diffuse s- and p-functions (indicated by "++") can also be added to deal with unpaired electrons and anionic species where it may not be clear with which atom the extra electron is associated.[15]

2.1.4 Natural Bond Orbital Analysis

NBO analysis interprets wavefunctions produced by modern quantum chemistry models into the language of Lewis structure and digestible valence and bonding concepts.[20,21] The NBOs are defined in terms of natural atomic orbitals (NAO) which describes a molecular environment in terms of atom-like components. Lewis type NBOs include highly occupied orbitals which are one-centered, (core) or two-centered (bonding orbitals), whereas non-Lewis type NBOs are low occupancy antibonding and Rydberg orbitals.[22] Orbital interactions occur between donor (Lewis) and acceptor (non-Lewis) orbitals. Their energy of interaction (*i.e.* stabilization energy) is determined using second order perturbation theory as per:

$$\Delta E_{i\rightarrow j} = q_i \frac{F_{ij}^2}{\varepsilon_j - \varepsilon_i} \qquad \text{Eq. 2.5}$$

In Eq. 2.5, q_i is the occupancy of the donor orbital, F_{ij} is the off-diagonal NBO Fock matrix element (*i.e.* orbital overlap), ε_i and ε_j are the diagonal NBO Fock matrix elements (*i.e.* orbital energies) of

the donor and acceptor orbitals, respectively. The stabilization energy is represented diagrammatically in Figure 2.1.

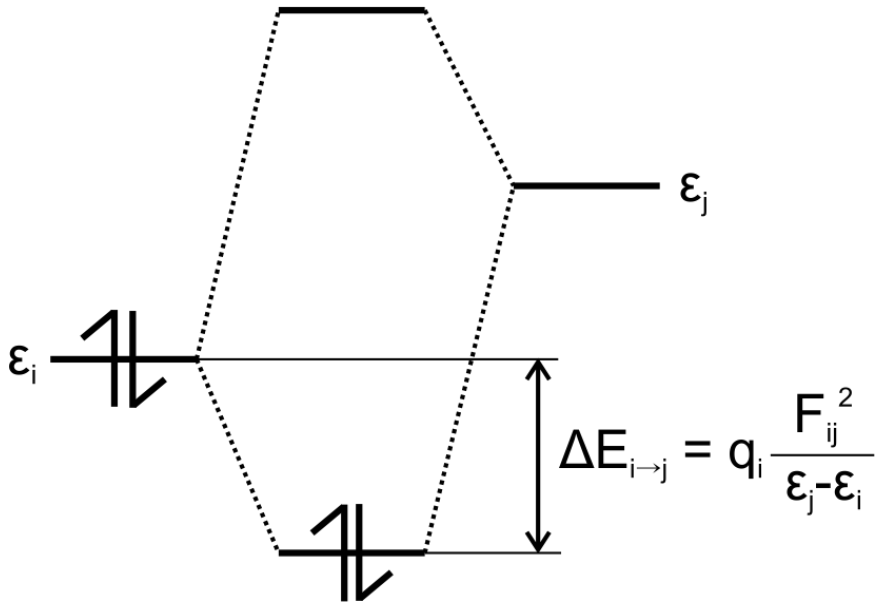

Figure 2.1 Molecular orbital diagram illustrating the stabilization energy ($\Delta E_{i\rightarrow j}$) of donor($\varepsilon_i$)-accepter($\varepsilon_j$) orbital interactions within NBO.

One can also calculate atomic partial charges *via* the NBO approach. Calculation of the atomic partial charges is performed by natural population analysis (NPA) of the NAOs. The expectation value of the first-order reduced density operator on a NAO produces the electron population of that orbital. By repeating the calculation for all NAOs centered on a particular atom and summing orbital contributions the population of the atom is calculated. The atomic partial charge is simply equal to the atom's nuclear charge minus the sum of the orbital populations. NPA adheres to the physical constraints of the Pauli principle; an orbital's population is never less than zero or greater than two, and charge additivity (the sum of the orbital populations for the molecule) equals the total number of electrons in the molecule.[21]

2.1.5 The Quantum Theory of Atoms in Molecules

The quantum theory of atoms in molecules (QTAIM) exploits the electron density to gain information about the nature of the bonding within a molecular system.[23] The gradient and the Laplacian of the electron density are evaluated and from the results one obtains the spatial coordinates of bonding interactions, the electron density at those coordinates, the degree of covalency or non-covalency, and the classification of the interaction.[24] The spatial coordinates of the bonding interactions can be determined by identifying where the gradient is found to be zero, these positions are labelled critical points (CPs). The value of the electron density at the CPs provides a measure of the bond strength.[25–30] CPs are classified as nuclear CPs, bond critical points (BCPs), ring critical points (RCPs), and cage critical points (CCPs) based on the curvature of the electron density around a specific point. The degree of covalency is indicated by the Laplacian; a negative value reflects a concentration of electron density at a CP indicating a covalent interaction, a positive value indicates a depletion of electron density and therefore a non-covalent interaction.[24] Two software packages were used to conduct the AIM analyses, AIMALL and Multiwfn.[31,32]

2.2 Experimental

2.2.1 Infrared Multiple Photon Dissociation

Infrared multiple photon dissociation was used to record vibrational spectra of gas-phase molecules in the region of 800 – 1600 cm^{-1}. This technique has been described extensively in the literature and is the subject of numerous review articles.[2,7,33–47] There is no direct measurement of the emission or absorption of light during the IRMPD process but instead one monitors molecular fragments, IRMPD is referred to as an action or consequence spectroscopy. Fragmentation occurs as a result of the repeated absorption of IR photons until the internal energy of the molecule

increases beyond the lowest dissociation threshold. The number of IR photons required to overcome a typical dissociation threshold is often in the range of 10 – 100.[46] A distinction must be highlighted here between multiphoton processes and multiple photon processes. In multiphoton processes related to vibrational spectroscopy, absorptions of photons promote the subjected normal mode to successively higher vibrational quantum states (i.e. $\nu = 0 \rightarrow 1$, then $\nu = 1 \rightarrow 2$, etc.) either by overcoming anharmonic bottlenecks or *via* non-linear processes. Since every molecule has some degree of anharmonicity, transition frequencies decrease with every subsequent increase in the vibrational quantum number. For example, the $\nu = 0 \rightarrow 1$ transition frequency is $2\omega e\chi e$ higher than that of the $\nu = 1 \rightarrow 2$ transition in a diatomic molecule (assuming Morse potential where $\omega e\chi e$ is the anharmonic constant). A multiple photon process allows for many photons of the same frequency to be absorbed *via* efficient energy transfer out of the excited state once populated. Here, upon excitation of a $\nu = 1$ state , photon energy is transferred to a 'quasi-continuum' of coupled vibrational energy levels known as the bath states[46] *via* a process known as intramolecular vibrational energy redistribution (IVR). Following IVR, the originally excited normal mode is depopulated (returns to the $\nu = 0$ state) and is now capable of absorbing another photon of the same frequency. This cyclical process is illustrated in Figure 2.2.

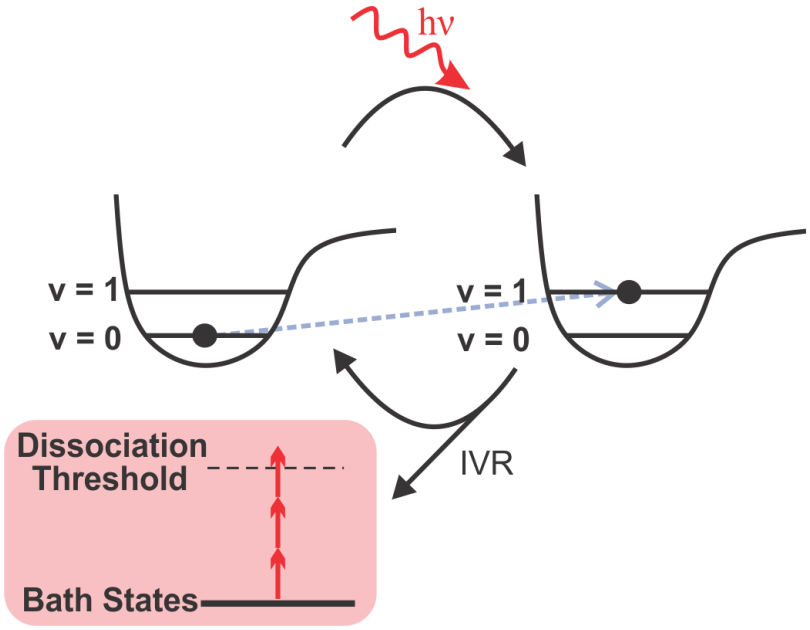

Figure 2.2 Cyclic representation of the IRMPD process. A normal mode is vibrationally excited by an IR photon. The energy is deposited into the bath states via IVR, returning the original normal mode to the ground state (v = 0), but leaving the molecule with increased internal energy. This cycle repeats until molecular dissociation occurs.

The repeated resonant absorption of photons leads to fragmentation of the species of interest and is marked by a decrease in the intensity of a parent ion and the concomitant increase in intensity of a fragment ion in the associated mass spectrum. A logarithmic ratio of fragment (I_{frag}) and parent (I_{par}) ion intensities, known as the fragmentation efficiency (see Eq. 2.6), is recorded as a function of IR wavenumber to generate the spectrum of the parent ion.[35]

$$F_{eff} = -ln\left(\frac{\sum I_{par}}{\sum I_{par} + \sum I_{frag}}\right) \qquad \text{Eq. 2.6}$$

A FEL is typically utilized for generating the high intensity beam of IR photons required for IRMPD. The FEL at CLIO was used to produce all IRMPD spectra presented in this thesis.[48,49] Briefly, a FEL produces IR photons by synchrotron radiation emitted from electrons travelling at relativistic speeds (accelerated by 10 – 50 MeV) through an undulator (see Figure 2.3). The

undulator consists of a series of magnets which alternate in the direction of their poles. Emitted photons are tunable *via* adjustment of the spacing between the magnets which produces a large range of wavelengths in the IR region of 3 – 90 μm and possess a bandwidth of ~ 0.3 %. The tunability of the frequency dependent on the adjustable separation between the magnets. The light emitted is trapped in an optical cavity by mirrors on either end of the undulator and stimulated emission occurs *via* interference with subsequent packets of electrons.[46] The IR beam is then directed into the Paul-type quadrupole ion trap (QIT) of a Bruker Esquire 3000+ mass spectrometer where it is used to fragment the parent ion of interest which have been introduced into the gas phase by electrospray ionization (ESI). A voltage of 5 kV is applied to the ESI needle and a N_2 carrier gas at 180°C assists the delivery of the ions into the ion trap. Typically, IRMPD spectra match best with global minimum geometries identified by DFT and often higher energy isomers (+ 10 kJ/mol) are found to not contribute to the observed spectra indicating an ion trap temperature of no more than 25°C. Trap pressures were on the order of 10^{-7} Torr therefore collisions should be negligible. Figure 2.3 provides a schematic overview of the electron source, the undulator, and the QIT.

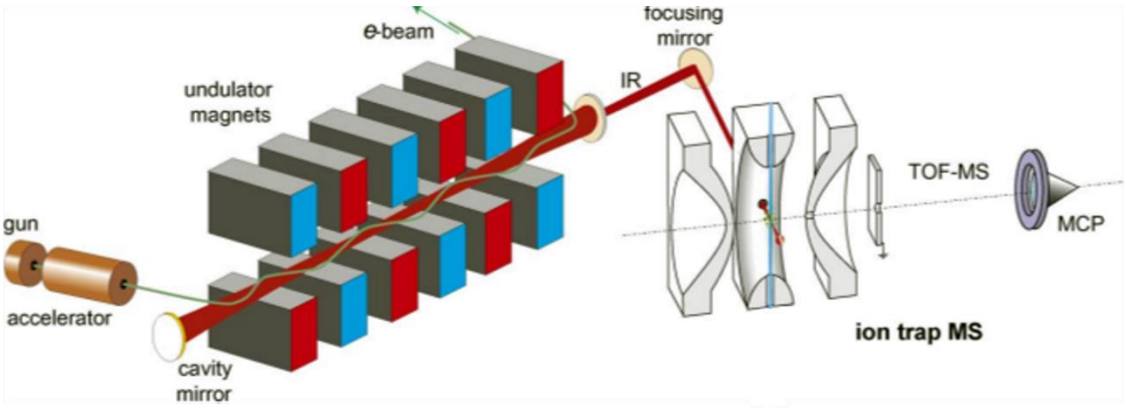

Figure 2.3 Cartoon diagram of the IRMPD experiment. Relativistic electron packets pass through an undulator which generates a high intensity field of IR photons by synchrotron radiation. The IR beam interrogates the selected ions in a QIT. This figure has been adapted from a review article by J. Oomens *et. al.*[46]

The CLIO FEL has a 40 ms duty cycle, wherein a 1 ps burst of light is emitted once every 16 ns for 10 μs. In other words, the sample experiences 625 1 ps bursts of IR radiation over the timespan of 10 μs and is then given 39.99 ms to respond.[48] The mass spectrometric data is averaged over 10 duty cycles for every wavelength and a typical FEL step size was 2.5 – 3 cm^{-1}. The CLIO IR-FEL pulse train is represented on a logarithmic scale in Figure 2.4.

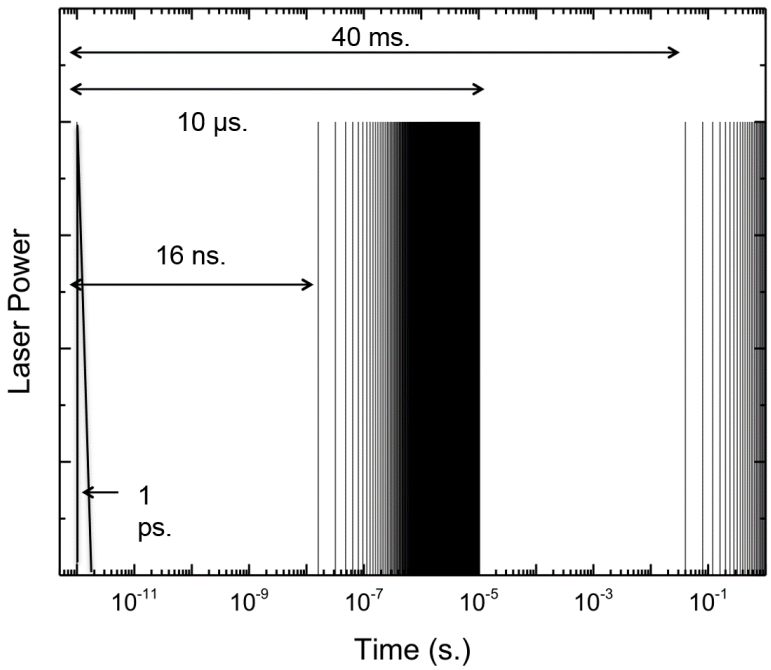

Figure 2.4 Output IR pulse train by the free electron laser at CLIO.

3 Reactions of Nitrous Oxide with Rh_nS^+ (n = 2 – 9)

3.1 Introduction

Rhodium has become an element of great importance due to the transition metal's catalytic abilities. There are many papers in the literature that discuss the use of rhodium as a homogeneous or heterogeneous synthetic catalyst.[4,50–64] With respect to the environment, rhodium is the catalyst of choice for the decomposition of greenhouse gases (GHGs) produced by combustion engines.[61] Transportation accounts for 27 % of GHGs produced by the economic sector in the United States with nitrous oxide comprising 5 % of U.S. GHGs in 2013. Additionally, nitrous oxide remains in the atmosphere for an average of 114 years, and is 300 times more effective at trapping heat than carbon dioxide.[65] Catalytic converters are equipped on all transportation vehicles to decompose GHGs. A wash coat possessing suspended particles of catalytic metals: platinum, palladium, and rhodium, is used to deposit the metals on a ceramic monolith with a honeycomb structure. Deposition of small particulates increases the catalytic surface area and reduces the required amount of the precious metal with comparison to catalysis on a bulk surface. The vehicle's exhaust passes through the honeycomb structure and the combustion gases: hydrocarbons, carbon monoxide, and NO_x (including nitrous oxide) are decomposed.[61]

Prior investigations show that the molecular interactions often occur at defect sites of a heterogeneous catalyst, which can be modelled effectively using gas phase clusters.[66] This approximation has been utilized by many researchers who have demonstrated the significance of cluster size and co-adsorbed species.[3,38,40,60,67–77] For example, Hamilton *et al.* used DFT and IRMPD to study the following nitrous oxide reactions on cationic rhodium clusters Rh_n^+ (n = 4 – 8).[3]

Decomposition: $Rh_n^+ + N_2O \rightarrow Rh_nO^+ + N_2$ (Rxn. 1)

Desorption: $Rh_n^+ \bullet N_2O \rightarrow Rh_n^+ + N_2O$ (Rxn. 2)

Hamilton's study observed mass spectrometric evidence of the IR induced decomposition reaction (Rxn. 1) competing with the desorption reaction (Rxn. 2) on all cluster sizes (n = 4 – 8).[38] An exception occurred for n = 5 which demonstrated only desorption of N_2O. Additionally, blue shifted stretching modes of N_2O was interpreted as proof of terminal nitrogen binding N_2O. A paper by Hermes *et al.* subsequently investigated the anomalously low reactivity of the $Rh_5 \bullet N_2O^+$ cluster using similar techniques.[40] Again, they also observed a preference for the desorption reaction (Rxn. 2) of N_2O when irradiating in the region of the N_2O bend (500 cm^{-1} to 700 cm^{-1}). However, Hermes observed clusters of $Rh_5O \bullet N_2O^+$, which showed a clear preference for N_2O decomposition; producing $Rh_5O_2^+$ and N_2. DFT calculations of the reaction pathways supported the IRMPD results. The barrier to N_2O desorption from Rh_5O^+ was found to be 28 kJ/mol higher than decomposition on Rh_5O^+. The barrier to N_2O desorption on Rh_5^+ was only 1.9 kJ/mol higher than decomposition: the desorption pathway is favoured entropically. These studies have shown that co-adsorbed species and cluster size can significantly alter reaction barrier energetics, changing the outcome of a reaction. The investigation in this chapter will focus on how the presence of a co-adsorbed sulphur atom, a known catalytic poison and fuel impurity, will affect the N_2O surface reaction on cationic rhodium nanoclusters.[5,51,78–84]

In addition to the effect of co-adsorbed species and cluster size on IR induced reactions, the importance of cluster size and geometry on rates of cluster surface reactions have been demonstrated.[60,67,69,73,75–77,85–91] Parry *et al.* observed rates of nitrous oxide decomposition and desorption on Rh_n^+ (n = 5, 6) occurring *via* blackbody infrared dissociation in a Fourier transform ion cyclotron resonance (FT-ICR) mass spectrometer.[90] Extended ion retention times (on the order

of seconds) allow for absorption of IR photons emitted by the ambient blackbody radiation field.[92] This study also highlighted the effects of cluster size and found evidence for the presence of multiple isomers. Observing relative ion signal at a particular mass to charge ratio (m/z) as a function of retention time shows decay of a peak with a *m/z* ratio corresponding to $Rh_5^+ \bullet N_2O$ ($k_{obs} = 0.075\ s^{-1}$) and growth of peaks for Rh_5^+ (the desorption product) and Rh_5O^+ (the decomposition product). Once again competition between reactions (Rxn. 1) and (Rxn. 2) is observed on Rh_5^+. The same experiment was conducted for $Rh_6^+ \bullet N_2O$ however no signal intensity was seen to grow for Rh_6^+, only growth of Rh_6O^+; indicating a clear preference for nitrous oxide decomposition on Rh_6^+. The supporting DFT calculations determined the barrier to reaction (Rxn. 1) and (Rxn. 2) on Rh_5^+ to both be *ca*. 60 kJ/mol. On Rh_6^+ the desorption reaction (Rxn. 2) barrier was *ca*. 80 kJ/mol and the decomposition reaction (Rxn. 1) barrier was *ca*. 60 kJ/mol, favouring decomposition. The addition of a single rhodium atom raises the barrier to desorption sufficiently higher than the barrier to decomposition and only the production of Rh_6O^+ is observed. Also reported are first-order kinetic fits to the decay of parent ion intensity, $Rh_n \bullet N_2O^+$ (n = 5, 6). A sum of exponentials was found to provide a better fit indicating the presence of multiple isomers. Adlhart *et al.* made similar observations of the rates of alkane dehydrogenation reactions catalyzed by Rh_n^+ (n = 1 – 30) under single-collision conditions in an FT-ICR.[60] A bi-exponential rate consisting of a fast and a very slow rate were taken as evidence for the presence of multiple isomeric forms of Rh_{12}^+. Clearly, the rhodium cluster size and geometry must be carefully considered when modelling reactions of this nature.

Small clusters of rhodium atoms have garnered interest on their own due to their unique magnetic properties. A DFT study on Rh_n (n = 2 – 15) clusters by Da Silva *et al.* reported finding large magnetic moments that increase with cluster size.[71] This magnetic moment trend is in

agreement with Harding *et al.* and Lecours *et al.* who reported a 15-tet ground state multiplicity for Rh_9^+ and Rh_9S^+, respectively.[39,76] Experimentally, Ma *et al.* used simultaneous magnetic and electric deflection studies to find evidence of superparamagnetism in select cluster sizes of Rh_n (n = 6 - 40).[93] The smaller cluster sizes possess the largest magnetic moment per atom while the larger clusters showed the magnetic moment per atom trending toward the bulk limit of zero. This evidence points to the need to also carefully consider the multiplicity of clusters in these reactions.

The foundations for the study presented in this chapter were laid in a publication by Lecours *et al.*, a DFT study of $Rh_nS^{\pm,0}$ (n = 1 - 9) and $Rh_n^{\pm,0}$ (n = 2 - 10).[76] Using a potential energy surface searching technique, basin hopping, in combination with DFT, clusters were found to prefer closed polytetrahedral geometries and high spin state electronic configurations which is consistent with results from pure rhodium cluster research.[3,38,39,74,89,94] Additionally, Lecours found sulphur prefers binding sites with larger coordination numbers than the oxygen atom in analogous $Rh_nO^{\pm}$ clusters investigated by Harding *et al.*[40,75,88] Using NBO analysis calculations Lecours *et al.* determined that the tighter binding of sulphur in $Rh_nS^{0,\pm}$ is partially due to favourable overlap of atomic sulphur p-orbitals with atomic rhodium d-orbitals, and back donation from the Rh cluster framework into atomic sulphur d-orbitals. This orbital behaviour is reminiscent of metallic bonding and suggests that sulphur valence electrons are partially delocalizing across the cluster.

An exhaustive computational approach was utilized to study nitrous oxide decomposition (Rxn. 3) and desorption (Rxn. 4) on cationic rhodium sulphur clusters containing 2 – 9 rhodium atoms, Rh_nS^+ (n = 2 - 9).

Decomposition: $Rh_nS^+ + N_2O \rightarrow Rh_nSO^+ + N_2$ (Rxn. 3)

Desorption: $Rh_nS^+ \bullet N_2O \rightarrow Rh_nS^+ + N_2O$ (Rxn. 4)

Figure 3.1 illustrates the main goal of this study, determining the energies of the desorption products, Rh_2S^+ and N_2O, and the stationary points on route to N_2O decomposition. These studies will provide atomistic insights and a map of the decomposition mechanism (or poisoning thereof) on heterogeneous rhodium catalysts.

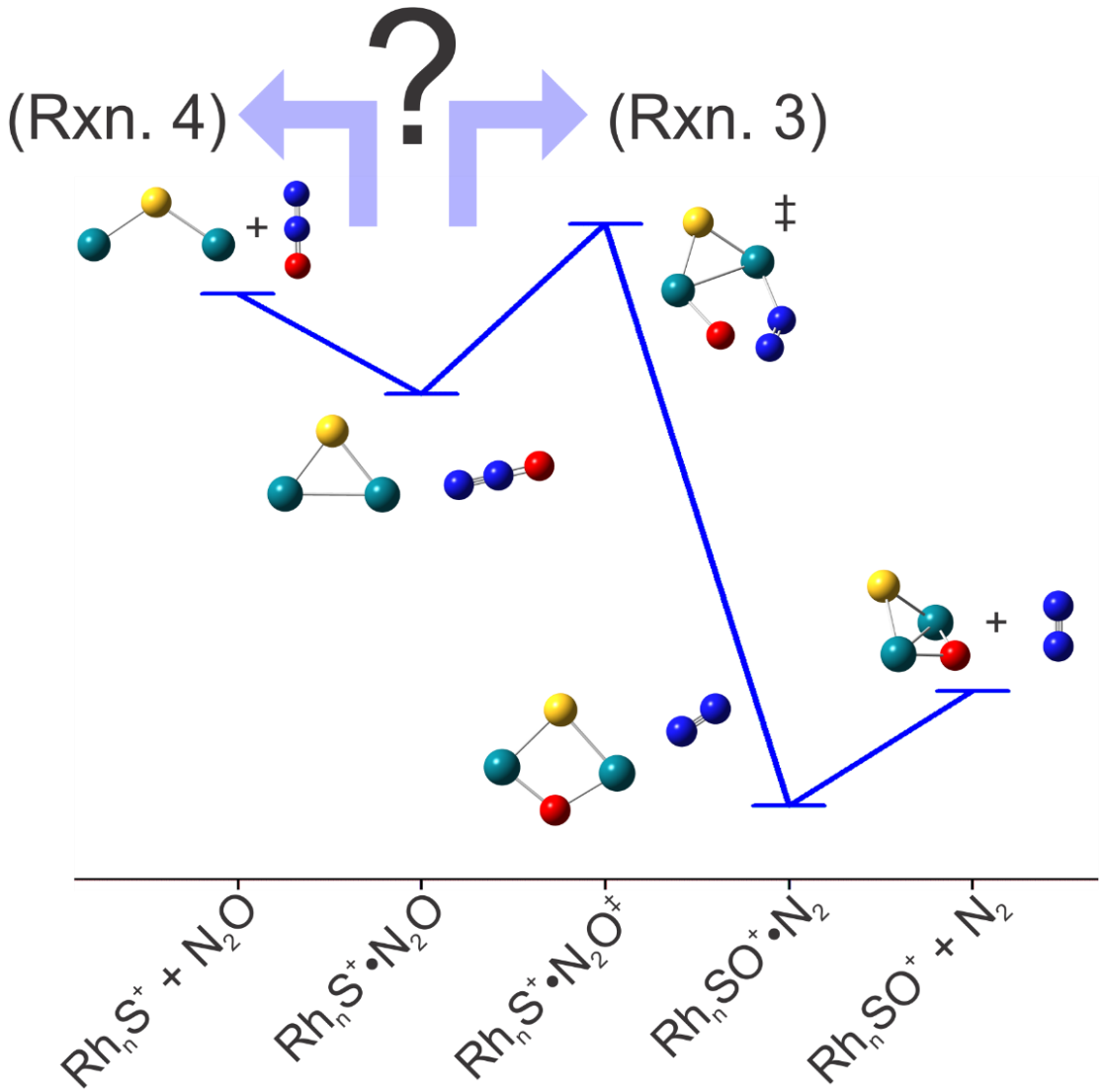

Figure 3.1 A hypothetical reaction coordinate diagram of competing reactions (Rxn. 3) and (Rxn. 4) of N_2O with Rh_2S^+.

3.2 Computational Methods

In pursuit of the main goal of this study the most accurate relative barrier heights possible must be obtained of reactions (Rxn. 3) and (Rxn. 4) where n = 2 - 9. Established above is the need to

thoroughly consider geometric and electronic structure. To that end a PES searching algorithm, basin hopping, was used to locate stationary points (*i.e.* local minima) of the $Rh_nS^+ + N_2O$ PES. The stationary points of interest were $Rh_nS^+•N_2O$, $Rh_nS^+•O$, and $Rh_nSO^+•N_2$ (see Figure 3.1). Basin hopping provided geometric isomers of the position of the moieties (N_2O, O, and N_2) relative to the cluster cores (Rh_nS^+ and Rh_nSO^+) which remained unchanged by the algorithm. The Rh_nS^+ cluster cores are acquired from the study by Lecours *et al.* and the Rh_nSO^+ cluster cores were generated during the course of this study.[76] The cluster core structures used from these studies consisted of the identified global minimum geometry and the higher energy isomers up to 25 kJ mol^{-1} above the global minimum at each cluster size. The isomers acquired from basin hopping served as candidates for the global minimum geometry of each stationary point. DFT is used to energetically order the global minimum candidates of each stationary point with the successful candidate possessing the lowest energy geometry and multiplicity. With the geometries and multiplicities of the stationary points have been identified, optimizations of the first order saddle point (*i.e.*, transition state) which connects the $Rh_nS^+•N_2O$ and $Rh_nSO^+•N_2$ were performed. Frequency calculations were conducted on every structure computed so that normal mode analysis can classify the structures as stationary points (0 imaginary frequencies), first order saddle points (1 imaginary frequency), or higher order saddle points (>1 imaginary frequencies).[95] Frequency calculations are useful in two aspects; for prediction of vibrational spectra which can be compared to future experimental work and for the calculation of the molecular partition function and subsequently the thermochemical corrections to the electronic energies. A better understanding of electronic structure in $Rh_nS^+•N_2O$ can be achieved by conducting NBO analysis. NBO analysis provides many measures including: stabilization energies of various orbital interactions, atomic partial charges by natural population analysis, and cluster stabilities by HOMO-LUMO gaps.

The basin hopping studies were set to generate 5,000 to 10,000 molecular mechanics (MM) optimized candidate structures based on cluster core size (n) and the number of low-lying geometric isomers (<25 kJ/mol of the Rh_nS^+ or Rh_nSO^+ global minimum isomers). MM was chosen for its short optimization times (<5 seconds), a necessity when performing such large numbers of calculations. The chosen force field for use with MM was the AMBER force field as implemented in Gaussian 09.[16,96] The AMBER force field has been designed for use with organic and biologically relevant molecules.[96] It has been used here for proper treatment of the N_2O moiety. Given AMBER's intended use for biological systems, parameters for rhodium are not included and are therefore borrowed from the UFF.[97] In addition to the Cartesian coordinates for each atom, MM input files also require the partial charge for each atom and any force field parameters which are not already contained in the AMBER force field. The partial charges were found using the CHELPG partition scheme.[19] The force field parameters include van der Waals radii, force constants, and all equilibrium bond lengths, angles, and dihedrals. Determination of these parameters is dependent on the previous Rh_nS^+ study which provided DFT calculated frequencies for each cluster size and their isomers.[76] A MM optimization and frequency calculation was run on the particular cluster being prepared for basin hopping using default AMBER parameters for S, N, and O and UFF values for Rh. The results of this MM calculation were compared to the previous DFT results. Alterations were made to the AMBER parameters until the MM results resembled the DFT results (geometries and vibrational frequencies). A MM input file for a Rh_nS^+ or Rh_nSO^+ cluster core with a randomly oriented N_2O, O, or N_2 moiety was submitted to the BH algorithm which is discussed in detail in Section 2.1.1 of this thesis. The following BH input parameters describe how the PES is sampled. The Cartesian coordinates of the moiety's center of mass are altered by a random value of η where $-0.7\ \text{Å} \leq \eta \leq 0.7\ \text{Å}$ and a rotation of the

molecular moieties (N_2O and N_2) by a random θ about the center of mass of the moiety, where $-45^0 \leq \theta \leq 45^0$. The maximum values selected for the translations correspond to the shortest bond length, 74 pm found in H_2.[95] The Boltzmann temperature for the secondary acceptance criterion was selected to be 400K which lead to an acceptance ratio of *ca*. 0.5. Lower temperatures resulted in insufficient sampling of the PES while higher temperatures lead to the acceptance of energetically inaccessible structures. Additionally, bonds are restricted from compressing to values shorter than 0.7 Å and all atoms are constrained to be within a cubic volume of 10 Å x 10 Å x 10 Å. For small distortions the optimization process will typically yield identical geometries and energies. Therefore, the candidates are sorted based on simultaneous uniqueness of geometry and energy and the unique candidates are subjected to further optimization using DFT, chosen for its relatively low computational cost and good experimental agreement.[3,38–40,88,90,91,94]

The chosen computational methods have been guided by previous studies. [3,76] The PBE0 functional with 25% Hartree-Fock exact exchange energy with the TZVP basis set for sulphur, oxygen, and nitrogen and Lanl2DZ for rhodium has been shown to accurately reproduce experimental frequencies and magnetic moments of rhodium clusters.[39,76,98] Low energy geometries have been identified by DFT, however, global minimum identification still requires determination of the lowest energy multiplicities. All geometric isomers within 25 kJ/mol of the lowest energy geometry are re-optimized at various multiplicities to complete global minimum identification of each stationary point of the reaction coordinate. Global minimum structures are re-optimized using the TPSSh functional which includes 10% Hartree-Fock exact exchange and the Def2-TZVP basis set on all atoms.[99–101] This method has been shown to yield reaction barriers which better reflect experimental results than the previous methods.[102–104] In short, the PBE0/Lanl2DZ(Rh), TVZP(S,N,O) method will be used to identify global minimum geometries,

mulitplicities, and frequencies while the TPSSh/Def2-TZVP method will be used to identify reaction energies.

Determination of the barrier to nitrous oxide decomposition, reaction (3), was done utilizing the synchronous transit quasi-newton (STQN) eigenvector following method for optimization of transition state structures, called using the QST3 keyword.[105–107] This method for transition state searching requires three structures for the input: reactant, product, and a guess structure for the transition state. As an example, Figure 3.2 shows structures for input to a QST3 calculation of $Rh_4S^+ \bullet N_2O$. The reactant and product structures are global minimum structures for $Rh_nS^+ \bullet N_2O$ and $Rh_nSO^+ \bullet N_2$, respectively. The reaction pathway studied by Hamilton *et al.* for N_2O decomposition on Rh_n^+ was used as a guide for modelling the $Rh_nS^+ \bullet N_2O$ transition state structures.[3] This pathway involves the nitrous oxide molecule bending at the middle nitrogen to bring the oxygen atom close to a rhodium atom. The pathway continues with forming a rhodium-oxygen bond, breaking the nitrogen-oxygen bond, breaking the nitrogen-rhodium bond, and finally a structural rearrangement to form a cationic rhodium sulphide oxide (Rh_nSO^+) and molecular nitrogen (N_2). Guess structures for the transition states were drawn keeping this in mind and to best connect the reactant and product structures.

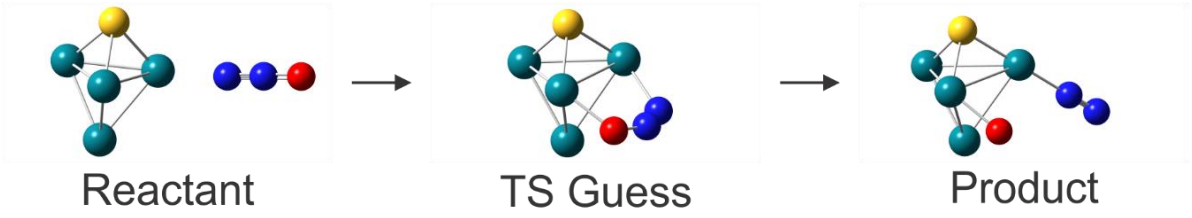

Figure 3.2 Three input geometries used for the determination of the transition state in the nitrous oxide decomposition reaction, $Rh_4S^+ + N_2O \rightarrow Rh_4SO^+ + N_2$.

3.3 Results and Discussion

3.3.1 Geometric Structure

$Rh_nS^+•N_2O$ *n* = 2 – 9. Figure 3.3 shows the global minimum geometries of $Rh_nS^+•N_2O$ (*n* = 2 – 9). All rhodium sulphur cluster cores possessed a distorted polytetrahedral motif. The distortions were a result of the 17% Rh-S bonds compared to Rh-Rh bonds.[3,38,39,69,71,73,74,86,87,89,94,104,108–110] The average Rh-Rh bond was found to be 2.73 Å which is in good agreement with the nearest neighbor distances of 2.69 Å in the fcc lattice of bulk rhodium.[111] The binding of N_2O did not induce a significant change in the geometry of the cluster cores as they were observed to maintained the same geometric shape as the bare Rh_nS^+ species identified by Lecours *et al.*[76] For example, the Rh_6S^+ cluster core possessed a distorted pentagonal bipyramidal geometry. The nitrous oxide molecule is bound by the terminal nitrogen atom to a sulphur adjacent rhodium atom. This $Rh_6S^+•N_2O$ cluster is representative of the N_2O orientation and cluster core geometry for the entire series.

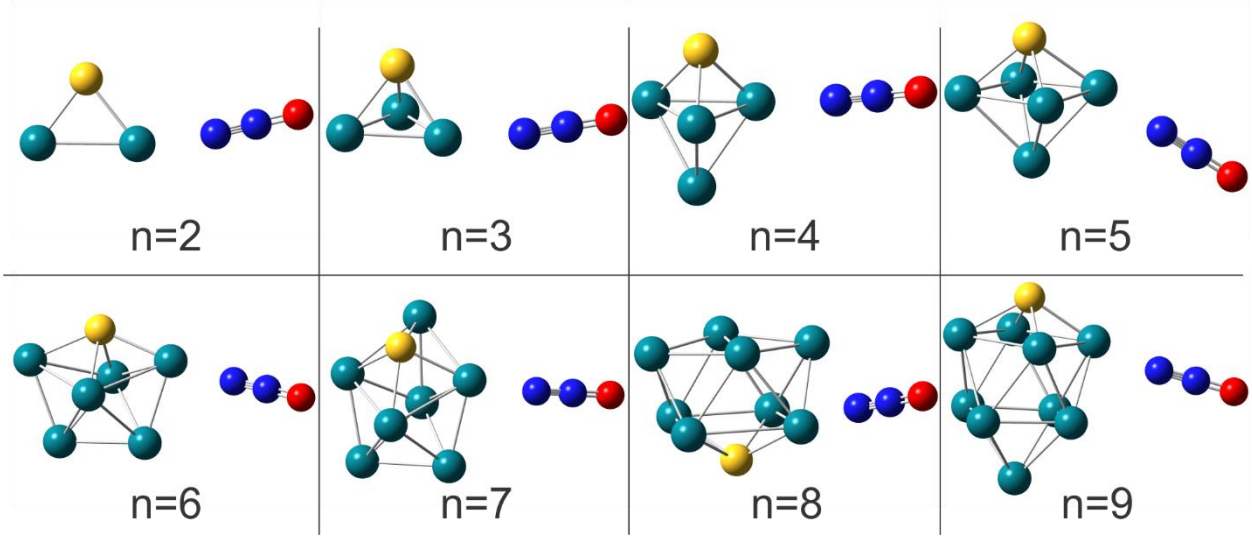

Figure 3.3 DFT optimized global minimum geometries of $Rh_nS^+•N_2O$ (*n* = 2 – 9) at PBE0/Lanl2DZ (Rh), TZVP (S,N,O).

$Rh_8S^+ \bullet N_2O$ was the only cluster to show a change in the preferred geometric shape of the cluster core, Rh_8S^+ when bound to N_2O. Interestingly, reconstruction of the underlying metal frame work, caused by surface moieties, has been seen previously in DFT studies of Rh_6O^+.[75,88] The global minimum geometry of Rh_8S^+ was determined to be bicapped octahedron with the sulphur atom occupying a 3-coordinate face of rhodium atoms (using DFT at PBE0/Lanl2DZ).[76] The global minimum identified here for $Rh_8S^+ \cdot N_2O$ has the cluster core in a bicapped trigonal prism geometry with the sulphur atom occupying a 4-coordinate position (see Figure 3.3). The Lecours study identified the relative energies of bicapped octahedron (BO) Rh_8S^+ (0 kJ mol^{-1}) and the bicapped trigonal prism (BTP) Rh_8S^+ (+5.98 kJ mol^{-1}); these same two geometries were found to be the lowest energy isomers here BTP-$Rh_8S^+ \bullet N_2O$ (0 kJ/mol) and BO-$Rh_8S^+ \bullet N_2O$ (+5.31 kJ mol^{-1}). These small differences in energy suggests both isomers are likely to be present in a gas phase ensemble as + 6 kJ mol^{-1} corresponds to a Boltzmann population of *ca.* 0.09. Average percent differences of the Rh-Rh and Rh-S bonds in Rh_nS^+ compared to $Rh_nS^+ \bullet N_2O$ were 2.8% and an average contraction of the N_2O bound Rh-S bond by 3.6% were the observed changes upon N_2O complexation.

The binding of the N_2O moiety *via* the terminal nitrogen atom is supported by observations of a blue shift in the N_2 stretching mode by various spectroscopic methods on Pt(111), Ir (111), Pd(110), and Ru(001), argon tagged Rh_n^+ ($n = 4 – 8$) gas phase clusters, and on monoatomic complexes with the coinage metals.[3,112–116] Additionally, this binding has been observed in ruthenium coordination complexes such as $Ru^{II}Cl_2(\eta^1\text{-}N_2O)(P\text{-}N)(PPh_3)$ {P-N = [*o*-(dimethylamino)-phenyl]diphenylphosphane} by use of $^{31}P(^1H)$ NMR spectroscopy, for example.[117–120] In a DFT study of these ruthenium coordination complexes a MO diagram was generated based on electronic energies and separated orbital symmetry to illustrate the potential

for favourable overlap between d-orbitals of the Ru(II) center and a nitrogen lone pair donating orbital with σ-symmetry. The analogous oxygen lone pair orbital was determined to be 338 kJ mol^{-1} below the nitrogen lone pair orbital and therefore too energetically different than the metal d-orbitals to overlap with them.[120] In this study, oxygen bound structures were found *ca*. 30 kJ mol^{-1} above the N bound structures. Many competing covalent and non-covalent interactions are likely responsible for the dominance of this motif. NBO calculations were conducted to understand the nature of this binding, the results of which are discussed below.

N_2O bond lengths, free and Rh_nS^+ bound, are presented in Table 3.1. The calculated N-N and N-O bonds in $Rh_nS^+ \bullet N_2O$ are both shorter than their respective bond lengths in experimentally observed free N_2O.[121] This difference in bond lengths will include, in addition to the physicochemical differences between free and bound N_2O, any error from the theoretical treatment of these systems. To focus on the physicochemical properties responsible for the differing bond lengths, comparisons are made to the calculated structure of free N_2O at the PBE0/TZVP level rather than the experimental values. Comparison to the calculated bond lengths of free N_2O, the N-N bond length shows elongation and the N-O bond shows contraction when bound to Rh_nS^+ clusters. The increased N-N bond length suggests reduced electron density between the nitrogen nuclei. This could be possible through donation of electron density out of a N-N bonding molecular orbital or into an anti-bonding orbital. The opposite applies to the N-O bond, the observed contraction could be due to either donation into a bonding or out of an anti-bonding orbital localized on the N-O bond. Bond strength, molecular orbitals, and electron donation can was examined by analysis of the vibrational frequencies and the natural bonding orbital calculations discussed below. In the size regime of two to nine rhodium atoms, N-N bond lengths are empirically fit to linear a function of rhodium atoms (see Figure 3.4 left). Extrapolation of the

linear function for the dependence of r_{N-N} on the number of Rh atoms predicts an unbound (n = 0) r_{N-N} of 1.1203 Å, only 0.1% larger than the free N_2O calculation suggests (See Figure 3.4 and Table 3.2). The N-O bond lengths, as a function of Rh atoms, is empirically fit to a logarithmic function, the limit as n goes to infinity would represent the N-O bond length when found on bulk rhodium with sulphur impurities. This function predicts a N-O bond length of 1.175 Å for $Rh_{100}S^+$. A computational study on N_2O adsorption on Rh(111) predicts $r_{(N-N)}$ and $r_{(N-O)}$ of 1.153 Å and 1.209 Å, respectively.[122] Clearly, this logarithmic function does not extrapolate well to the bulk phase. A recent DFT/ZORA study on the interactions of Pt_8 with nitrous oxide reported a negligible change in the N-N bond with a blue shift in the corresponding stretching mode, also observed here, and a slight increase in the N-O bond, relative to free N_2O. They concluded that charge transfer from the platinum cluster to the moiety was responsible for weakening the N-O bond and promoting N_2O decomposition.[123]

Table 3.1 Bond lengths of N_2O when bound to Rh_nS^+ (n = 2 – 9) and free N_2O.[121] The third and fifth columns were calculated by taking the ratio of the difference of the free N_2O. The PBE0/Lanl2DZ (Rh), TZVP (S,O, N) functional and basis sets were used.

n	r_{N-N} (Å)	Free - Bound Percent Difference	r_{N-O} (Å)	Free - Bound Percent Difference
2	1.1209	-0.16	1.1566	1.64
3	1.1210	-0.17	1.1595	1.40
4	1.1211	-0.17	1.1615	1.23
5	1.1214	-0.20	1.1633	1.08
6	1.1219	-0.25	1.1635	1.06
7	1.1218	-0.24	1.1651	0.93
8	1.1221	-0.27	1.1663	0.82
9	1.1225	-0.30	1.1642	1.00
Free (calc.)	1.1191	-	1.1760	-
*Free (expt.)	1.127292	-	1.185089	-

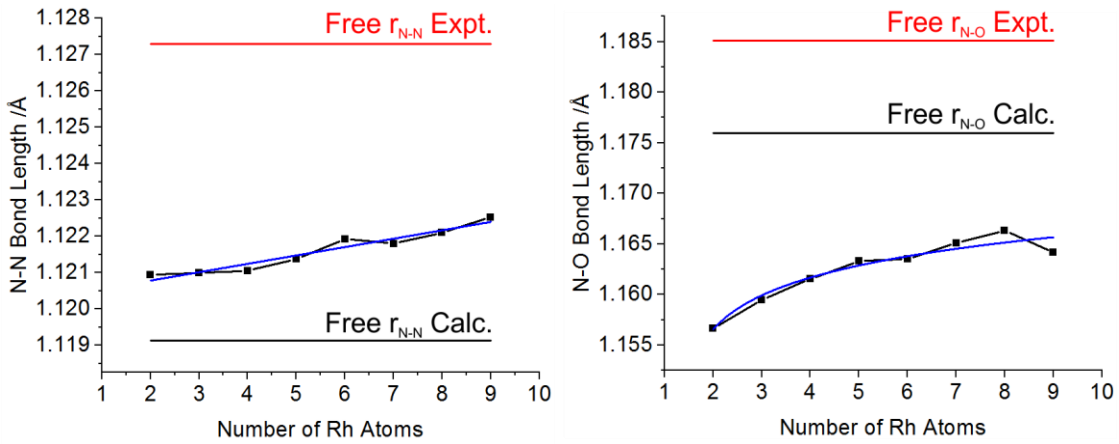

Figure 3.4 **(Left)** Dependence of the N-N bond length in N_2O on the number of rhodium atoms in the Rh_nS^+ cluster core. In both graphs, red is the experimentally reported value of the same bond length in free N_2O[123] and black is the calculated value. The blue line represents a linear fit. **(Right)** Dependence of the N-O bond on the number of rhodium atoms in the cluster. The blue line represents a logarithmic fit.

Table 3.2 Analysis of blue trend lines shown in Figure 3.4

y	N-N Bond Length	N-O Bond Length
x	Number of Rh Atoms	Number of Rh Atoms
Equation	y = a + b*x	y = a - b*ln(x+c)
a	$1.12032 \pm 1.50981 \times 10^{-4}$	1.15787 ± 0.00269
b	$2.3075 \times 10^{-4} \pm 2.534 \times 10^{-5}$	-0.00382 ± 0.00136
c	-	-1.29427 ± 0.66274
R^2	0.93253	0.93846

Rh_nS^+•O n=2—9. Mapping the reaction pathway for N_2O decomposition on Rh_nS^+ requires the investigation of a rhodium sulphur oxide clusters which are the products of decomposition, the other product being molecular nitrogen. The same methods used for determining the global minimum structures for Rh_nS^+•N_2O (n = 2 – 9) are employed for determining the global minimum structures for Rh_nS^+•O (n = 2 – 9) with the resulting geometries presented in Figure 3.5. The DFT studies of $Rh_6O_n^+$ (n = 1 – 4) by Harding *et al.* showed oxygen's preferred binding motif as bridging two Rh atoms (η^2). η^1 (atop one Rh atom) is ~8.7 kJ mol^{-1} above the bridge isomer, and the least preferred binding motif is coordination of three Rh atoms, referred to as hollow site binding (η^3), ~ 60 kJ mol^{-1} above the bridge isomer.[75] The Rh_nS^+•O (n = 2 – 9) structures in Figure

3.5 mostly show preference for a hollow site motif, with three cluster sizes showing bridging. Energetic analysis of the $Rh_6S{\bullet}O^+$ isomers at the optimal spin state contrasts the Rh_6^+ results by showing hollow site (0 kJ mol^{-1}), bridging (19 kJ mol^{-1}), and atop (37 kJ mol^{-1}) as the ordering of preferred binding motifs (*i.e.*, η^3 preferred over η^2). Sulphur prefers larger coordination numbers, usually η^3 or η^4, once the rhodium clusters are large enough to accommodate this. The high coordination number of the sulphur atom is a result of donation into and out of d-orbitals on the sulphur atom. This back donation allows sulphur to behave as if it is a pseudo-metal atom and incorporate itself into the polytetrahedral motif.[76] The oxygen atomic d-orbitals are much higher in energy relative to the valence atomic orbitals. Consequently, oxygen behaves as a surface atom rather than incorporating into the geometric structure of the Rh cluster core.

The polytetrahedral motif of the cluster cores (Rh_nS^+) remained consistent between Rh_nS^+, $Rh_nS^+{\bullet}N_2O$, and $Rh_nS^+{\bullet}O$, however, the addition of the oxygen atom had a larger effect on the Rh-Rh and Rh-S internuclear distances as compared with nitrous oxide. The most significant changes occur at the coordination site of the oxygen atom, as one would expect. In most cases the distances between the rhodium atoms that coordinate the oxygen increase. The degree of perturbation decreases with increasing n. This is seen by taking the average of the Rh-Rh bond lengths and the average of the Rh-S bond lengths in $Rh_nS^+{\bullet}N_2O$ and comparing them to the same values of the $Rh_nS^+{\bullet}O$ structures. There is a difference of 8 % at n = 2 which reduces to 1 % at n = 9. A notable exception was $Rh_6S^+{\bullet}O$ which changes the metal framework from pentagonal bipyramid in $Rh_6S^+{\bullet}N_2O$ (see Figure 3.3) to trigonal prism with a Rh atom cap on a rectangular face (η^4) in $Rh_6S^+{\bullet}O$, an effect of surface adsorbates seen when N_2O binds to Rh_8S^+ and elsewhere.[75,88] The Rh_6S^+ cluster has pentagonal bipyramidal shape with one of the pentagonal corner positions occupied by a sulphur atom. Addition of the oxygen atom results in the Rh_6S^+

cluster core taking on a trigonal prism geometry with a rhodium atom capping a rectangular face and the oxygen atom in Rh_6S^+•O caps a η^3 trigonal face opposite the sulphur atom (see Figure 3.5). This severe distortion of the Rh_6S^+ core amounted to the average internuclear distances changing by 8.7 % upon addition of the oxygen atom.

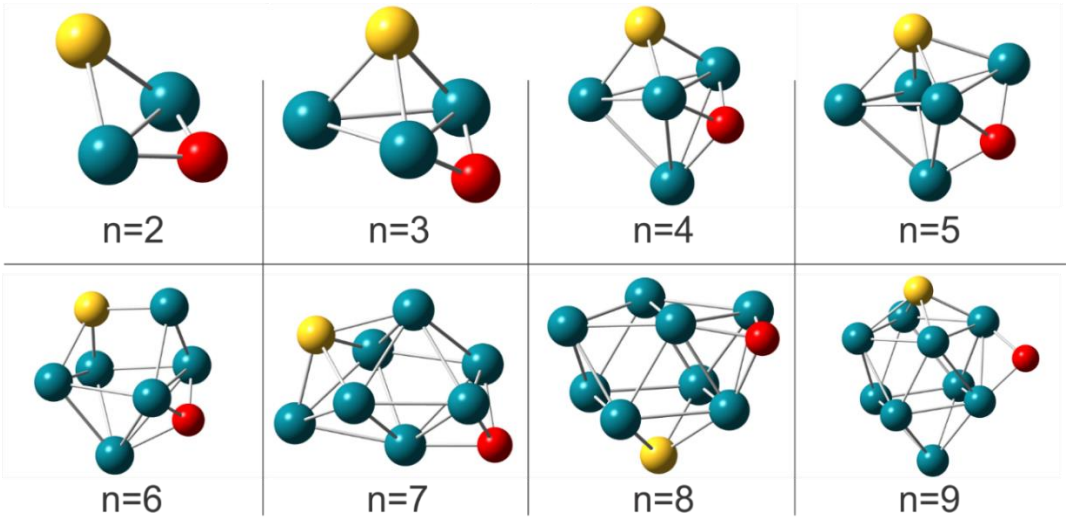

Figure 3.5 Global minimum DFT optimized geometries of Rh_nSO^+ ($n = 2 - 9$) at PBE0/Lanl2DZ (Rh), TZVP (S,O).

Rh_nSO^+•N_2 n=2—9. The final reaction minimum that requires attention to complete the model of N_2O decomposition is a rhodium sulphide oxide cluster core with a molecular nitrogen tag, Rh_nSO^+•N_2 (*i.e.*, charge-induced dipole complex). Global minimum structures provide insight as to the location of the N_2 moiety relative to oxygen following breaking of the nitrogen oxygen bond. This information is pertinent to determining the structures of the Rh_nS^+•$N_2O^{‡}$ transition states. Utilizing the global minimum and low-lying local minima from the Rh_nS^+•O study, Rh_nSO^+•N_2 is studied by varying the position and orientation of N_2 relative to the Rh_nSO^+ cluster core for $n = 2 - 9$ through BH. The resulting geometries are presented in Figure 3.6. Nitrogen was found to bind to a single rhodium atom *via* a single nitrogen atom (η^1). This binding motif is similar to a recent study by Klein *et al*. which investigated N_2 adsorbates on pure rhodium clusters, $[Rh_n(N_2)_m]^+$ $n = 6$ - 15, m = 1-16.[110] The geometry of Rh_nSO^+ remained consistent between the

Rh_nS^+•O and Rh_nSO^+•N_2 studies. For most cases, the positioning of the oxygen atom did as well, the exception being Rh_9SO^+•N_2. The global minimum structure for Rh_9S^+•O involved the oxygen atom bridging (η^2) two rhodium atoms (see Figure 3.5), one of the Rh atoms is also sulphur bound. The resulting global minimum structure for Rh_9SO^+•N_2 has the oxygen atom capping one of the four equivalent trigonal faces furthest from the sulphur atom. The apparent relocation of the oxygen atom may have resulted from the influence of molecular nitrogen, a previously seen effect of binding N_2O to Rh_8S^+ and when comparing the cluster core geometries of Rh_6S^+•N_2O and Rh_6S^+•O.[75,88] The average N-Rh-O bond angle was 178° ± 1.2°. The directionality indicates that the binding of N_2 moiety may possess some covalent nature. This rearrangement of the global minimum core structure for n = 9 displays the preference for the approximately linear N-Rh-O bond angle requirement.

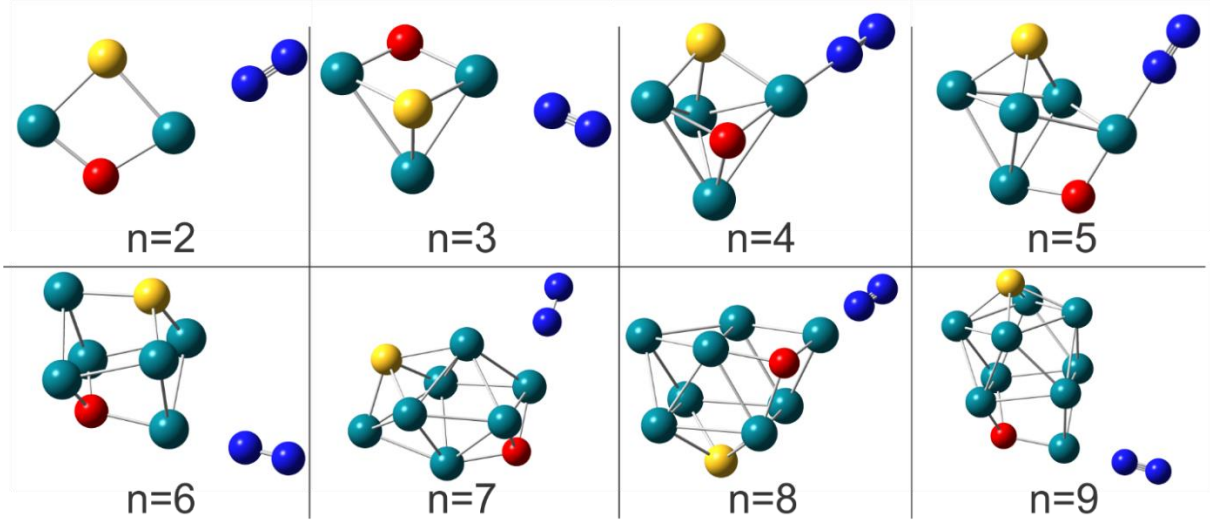

Figure 3.6 Global minimum DFT optimized geometries of Rh_nSO^+•N_2 (n = 2 – 9) at PBE0/Lanl2DZ (Rh), TZVP (S,O, N).

Plotted in Figure 3.7 are the N-N bond lengths for the global minima of the N_2 moiety bound to clusters of Rh_nSO^+; the calculated free N_2 bond length is represented by a dashed line. The N-N bond is elongated by the presence of the metal cluster and continues to increase with the

cluster size over the range studied here. This indicates a donation of electron density from the cluster into the N_2 π^* LUMO and/or donation out of the N_2 σ HOMO.[110]

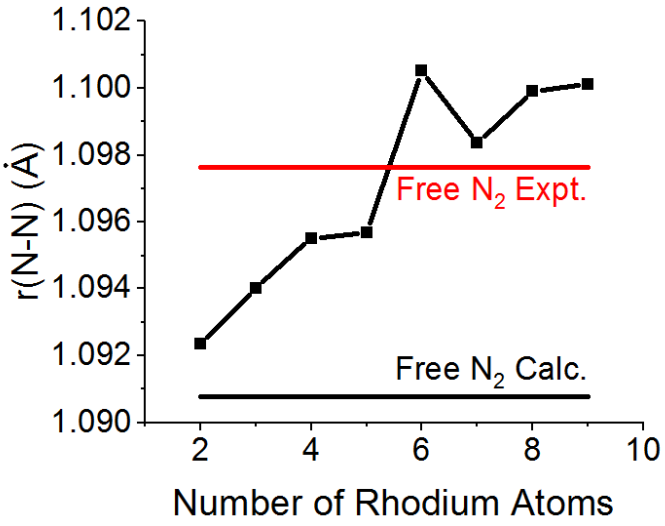

Figure 3.7 N-N bond lengths in $Rh_nSO^+ \bullet N_2$ calculated at PBE0/Lanl2DZ(Rh), TZVP(S,N,O). **(Black)** Free N_2 bond length calculated at PBE0/TZVP and **(Red)** experimental.[124]

Plotted in Figure 3.8 are the Rh-N bond lengths for $Rh_nS^+ \bullet N_2O$, $Rh_n^+ \bullet N_2O$, and $Rh_nSO^+ \bullet N_2$. Published structures for $Rh_n^+ \bullet N_2O$ were reoptimized at PBE0/Lanl2DZ(Rh),TZVP(N,O).[3,39] In all cases there is a decrease in the cluster-moiety separation indicating tighter binding to larger metal clusters of $Rh_nS^+ \bullet N_2O$, $Rh_n^+ \bullet N_2O$, and $Rh_nSO^+ \bullet N_2$. At all cluster sizes molecular nitrogen is bound more closely to the metal containing core (*i.e.*, Rh_nSO^+) than nitrous oxide (Rh_nS^+ core). Given the catalyst poisoning reputation of sulphur one might expect a preference of nitrous oxide desorption for the sulphur clusters, and therefore elongated Rh-N bond lengths. Surprisingly, nitrous oxide is binding more tightly to the sulphur clusters than the pure rhodium clusters.

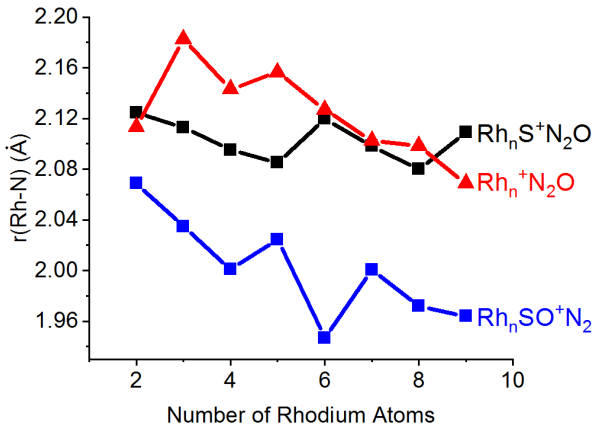

Figure 3.8 Rhodium-nitrogen bond lengths in $Rh_n^+ \bullet N_2O$ (**red**), $Rh_nS^+ \bullet N_2O$ (**black**), and $Rh_nSO^+ \bullet N_2$ (**blue**).

Multiplicity Studies. All basin hopping studies and DFT optimizations conducted to this point were at the multiplicities that Lecours *et al.* determined to be the lowest in energy for Rh_nS^+ ($n = 1 – 9$).[76] Global minima and higher energy isomers, up to 25 kJ mol^{-1} greater than the minimum, were re-optimized at four additional multiplicities: (2S+1)-4, (2S+1)-2, (2S+1)+2, and (2S+1)+4 where (2S+1) represents the originally optimized multiplicity. This was done to achieve the most accurate reaction barriers possible. Additionally, there is precedent for reactions involving open-shell transition metal complexes to undergo electronic state crossings, changing the multiplicity, during the course of a reaction.[125] Four out of the eight n-values studies here retained the same multiplicity when bound to N_2O. The cluster sizes with different global minimum multiplicities between Rh_nS^+ and $Rh_nS^+ \bullet N_2O$ are highlighted in Table 3.3 along with the change in electronic energy when comparing the N_2O bound and unbound multiplicities. In all four cases, the binding of N_2O reduced the multiplicity. The energetic differences here are so small that DFT is unable to definitively state which multiplicity is preferred. Regardless, at room temperature electronic states up to 10 kJ mol^{-1} above the global minimum make a significant contribution (> 1 % populated, assuming Boltzmann population distribution at 298.15 K) to the electronic partition function so all states within 10 kJ mol^{-1} will likely contribute.

Table 3.3 Multiplicities (2S+1) of the global minimum Rh_nS^+ structures with and without N_2O bound to the surface. Differences in electronic energy of $Rh_nS^+ \bullet N_2O$ at the minimum energy spin state of Rh_nS^+ and $Rh_nS^+ \bullet N_2O$ at the minimum energy spin state.

n	Without N_2O	With N_2O	ΔE (kJ/mol)
2	6	2	5
4	8	6	2
7	13	11	17
8	14	12	6

Shown in Figure 3.9, is a plot of the relative electronic energies for isomers of $Rh_9S^+ \cdot N_2O$ which vary in Rh_9S^+ geometry, N_2O orientation, and multiplicity. This plot demonstrates the need for careful consideration of the spin state as the energetic ordering between structural isomers is multiplicity dependent. The large value of the multiplicities for rhodium nanoclusters have been experimentally verified spectroscopically and in magnetic moment measurements.[93] Multiplicity is likely to have a large influence on reaction energetics of rhodium clusters with surface moieties given that the relative energy of spin-state isomers are on the order of *ca.* 25 kJ mol^{-1}.

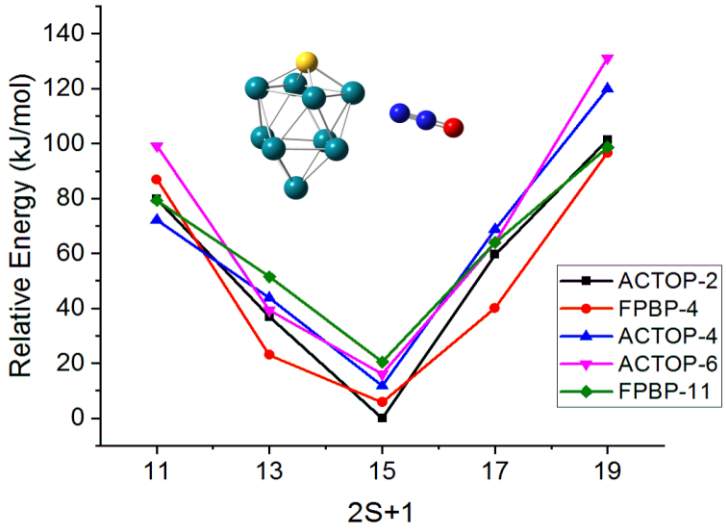

Figure 3.9 Isomers of $Rh_9S^+ \bullet N_2O$ (global minimum inset) calculated at PBE0/Lanl2DZ (Rh), TZVP (S,N,O). Different traces represent different isomers of the Rh_9S^+ core, anti-cubic prism with a rhodium cap on top (ACTOP) and a fused pentagonal bipyramid (FPBP), with varied positioning of nitrous oxide.

$Rh_nS^+ \bullet N_2O^‡$ n=2-9. Having now ascertained the key minima on the reaction pathway we are able to conduct transition state calculations to map the decomposition of nitrous oxide on the rhodium sulphur clusters. Hamilton *et al.*, among others, have previously described nitrous oxide decomposition on Rh clusters to produce molecular nitrogen and oxidized rhodium.[3] This information, along with experimental IRMPD evidence for terminal nitrogen binding guides our exploration of the reaction mechanism on Rh_nS^+.[3,112–116] Our calculations show that erect N_2O molecule bends toward the cluster and brings the oxygen atom in contact with a rhodium atom, forming a Rh-O bond. Next, the N-O bond fractures and finally the Rh-N bond fractures and releases N_2. Transition state (TS) structures were sought along this reaction path with optimized structures consisting of a bent N_2O moiety bridging adjacent rhodium atoms via the terminal nitrogen and oxygen atoms (Figure 3.10). Normal mode analysis was conducted to validate these structures as transition states (*i.e.*, transition state geometries have only one imaginary frequency). The imaginary frequency for each TS is assigned to a N-O stretching mode. The only TS structure that differed was $Rh_7S^+ \bullet N_2O^‡$. This TS still involved the bent N_2O but without changes to the N-O bond length or formation of a Rh-O bond. Additionally, its imaginary frequency was assigned to a N-N-O bending mode. This may imply the existence of at least two transition states in this pathway; one for the bending of N_2O and another for the N-O bond fission, with the possibility of a shallow local minimum between them. This minimum may be similar to that identified by Hamilton *et al.* which consisted of the bent N_2O molecule bridging two rhodium atoms.[3] However, the study detailed here was unable to identify a shallow-lying minimum for any cluster size or the bending TS for any cluster size aside from $n = 7$.

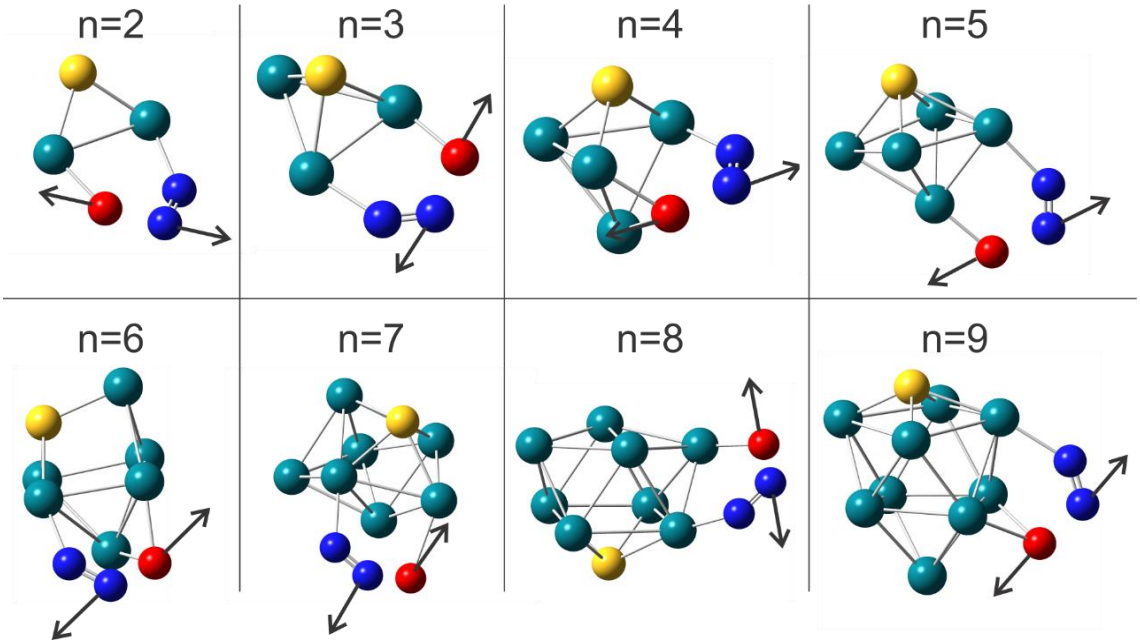

Figure 3.10 DFT optimized transition state geometries of $Rh_nS^+•N_2O^‡$ (n = 2 – 9) on route to N_2O decomposition at PBE0/Lanl2DZ (Rh), TZVP (S,N,O). Transition states found using the QST3 method and normal mode analysis revealed 1 imaginary frequency.

Electronic energies of the TPSSh/Def2-TZVP optimized structures have been used to estimate barrier heights for the following reactions. Note the change in functional and basis set as this method has been shown to better predict experimental reaction outcomes.

N_2O Binding:	$Rh_nS^+•N_2O \rightarrow Rh_nS^+ + N_2O$	(Rxn. 5)
N_2O Activation:	$Rh_nS^+•N_2O \rightarrow Rh_nS^+•N_2O^‡$	(Rxn. 6)
N_2 Binding:	$Rh_nSO^+•N_2 \rightarrow Rh_nSO^+ + N_2$	(Rxn. 7)
O Binding:	$Rh_nS^+•O \rightarrow Rh_nS^+ + O$	(Rxn. 8)
N_2O Decomposition:	$Rh_nS^+•N_2O \rightarrow Rh_nSO^+ + N_2$	(Rxn. 9)

These barrier heights have been tabulated below in Table 3.4 and have been used to illustrate the reaction coordinate diagram in Figure 3.13 (shown only for n = 5 and 9 for clarity). The N_2O binding energy decreases as the number of rhodium atoms in the cluster core increases.

The larger binding energies of molecular nitrogen to Rh_nSO^+ as compared with nitrous oxide to Rh_nS^+ agrees with the shorter Rh-N bond lengths found in the $Rh_nSO^+ \bullet N_2$ structures. No trend is observed for decomposition energies, but all are negative values which indicates energy is released and the decomposition products are more electronically stable than the N_2O bound state. Comparing activation energies for N_2O decomposition vs. desorption energy allows for a prediction to be made with respect to which competing reaction will prevail at each cluster size. Given the reputation of sulphur as a catalytic poison in solid phase bulk Rh metal catalysis, one would expect the decomposition activation energy to be larger than the N_2O binding energy. This is true for five of the eight cluster sizes studied here as can be seen in Table 3.4 and Figure 3.11. Thermal corrections to these relative reaction energies are discussed at the end of the vibrational structure section, 3.3.3 Vibrational Structure.

Table 3.4 Reaction energies for the desorption of N_2O from Rh_nS^+, N_2 from Rh_nSO^+, and O from Rh_nS^+. Also given are the activation energies and the overall change in energy for the N_2O decomposition on Rh_nS^+. All values are changes in the non-zero point corrected electronic energy calculated at TPSSh/Def2-TZVP. All values are in units of kJ mol^{-1}.

n	N_2O Binding Energy	Decomposition Activation Energy	N_2 Binding Energy	O Binding Energy	Decomposition Reaction ΔE
2	93	89	105	403	-106
3	88	91	100	353	-61
4	84	98	126	360	-73
5	77	31	104	381	-101
6	67	63	114	356	-86
7	62	88	77	390	-124
8	60	64	94	389	-126
9	61	104	100	407	-143

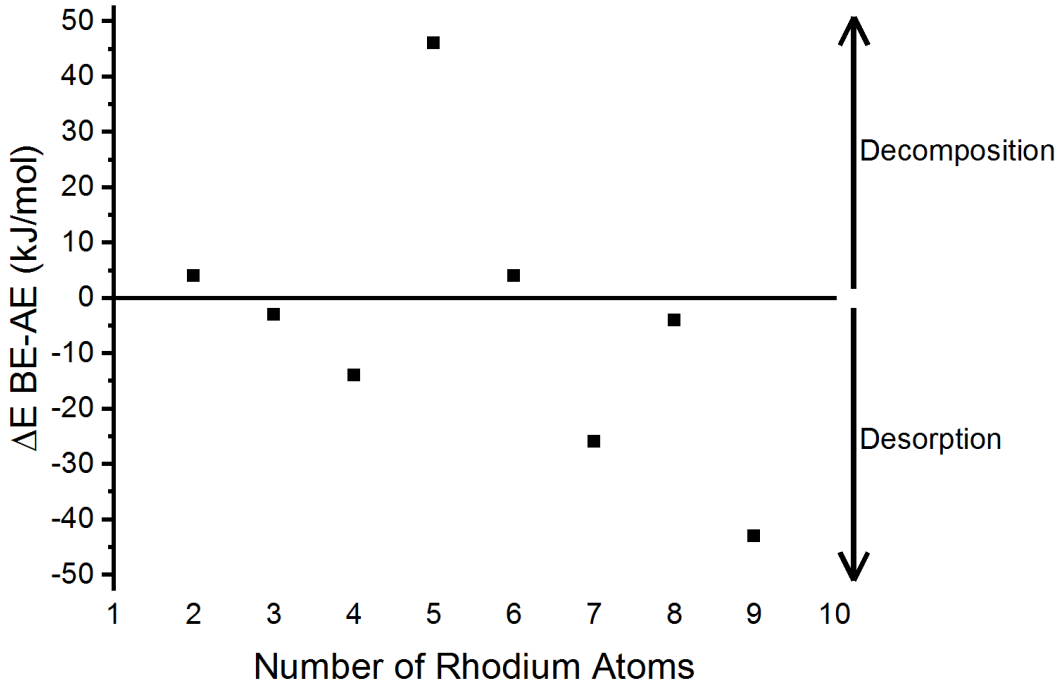

Figure 3.11 The difference in energy between the N_2O binding energy and the decomposition activation energy on Rh_nS^+ at each cluster size. Positive values indicate that N_2O will desorption and negative values indicate that N_2O will decompose.

Figure 3.12 shows the lowest energy multiplicity of each cluster size for each of the structures investigated along the reaction profile. The multiplicities of the transition state structures were chosen to be the same as the reactant multiplicity. However, when the transition state structure for a cluster failed to converge after several attempts, the multiplicity was changed to be closer to or match the multiplicity of the $Rh_nSO^+ \cdot N_2$ structures. This facilitated successful convergence. Only two cluster sizes showed a change in global minimum multiplicity when moving from the N_2 bound Rh_nSO^+ to the unbound structure. All cluster sizes show a change in global minimum multiplicity at some point during the reaction; this requires a crossing of electronic states.

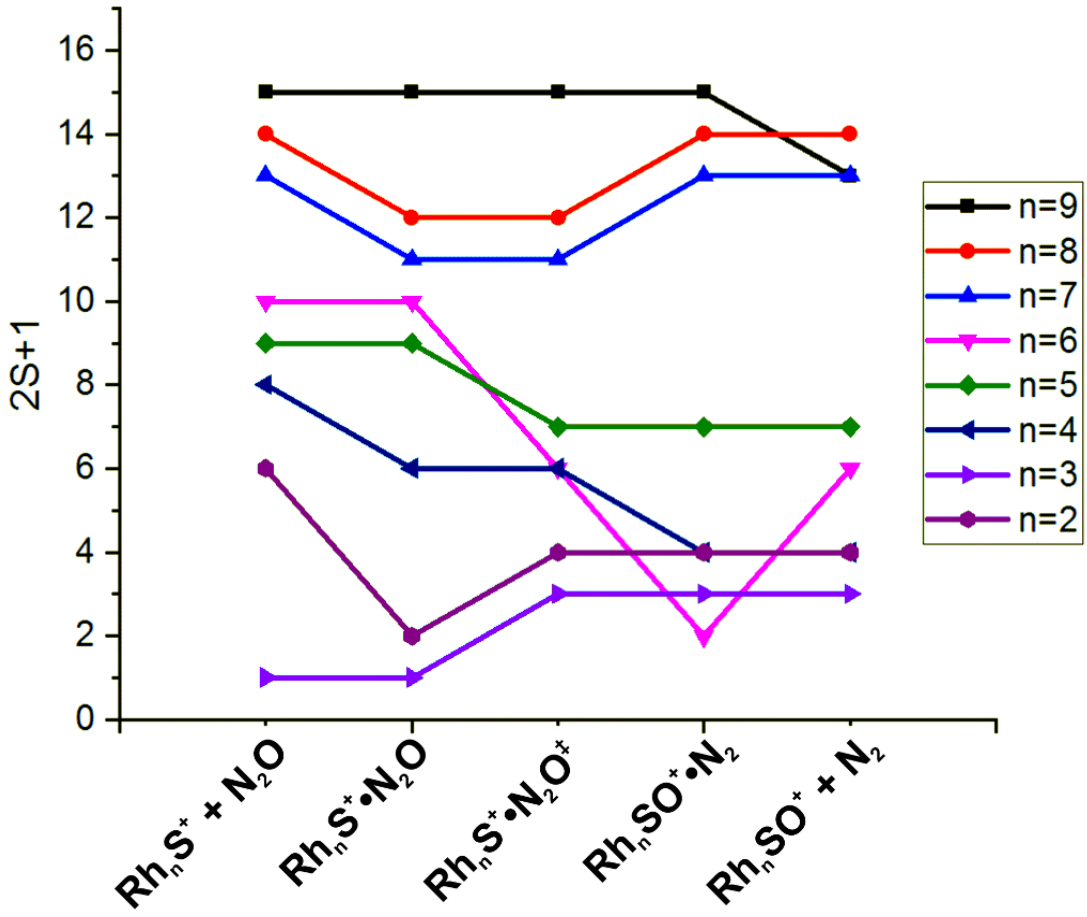

Figure 3.12 Multiplicities of the global minimum structure for each reaction stationary point and the transition state at each cluster size. Calculated with PBE0 and Lanl2DZ(Rh)/TZVP(S,N,O).

To further our understanding of the effects of the sulphur atom on reaction barriers, TPSSh/Def2-TZVP $Rh_n^+•N_2O$ structures have been obtained and transition states have been searched using QST3 and normal mode analysis, as was done for Rh_nS^+. Unfortunately, successful completion of the transition state optimization of $Rh_7^+•N2O^‡$ could not be achieved. N_2O binding energies and the activation energy for the decomposition reaction have been computed and supplied in Table 3.5.

N_2O Binding	$Rh_n^+•N_2O \rightarrow Rh_n^+ + N_2O$	(Rxn. 10)
N_2O Activation	$Rh_n^+•N_2O \rightarrow Rh_n^+•N_2O^‡$	(Rxn. 11)

Decomposition appears to be the preferred reaction, showing a lower barrier than desorption for five of the seven cluster sizes computed. Nitrous oxide binds more strongly to pure rhodium clusters as compared with sulphur doped clusters with the same number of rhodium atoms. To provide insight into the observations made of the electronic energies, analyses of the electronic structure have been conducted and are discussed below.

Table 3.5 Reaction energies for the desorption of N_2O from Rh_n^+. Also given are the activation energies for N_2O on Rh_n^+. All values are changes in the non-zero point corrected electronic energy calculated at TPSSh/Def2-TZVP. All values are given in units of kJ mol^{-1}.

n	N_2O Binding Energy	Decomposition Activation Energy
2	100	51
3	75	12
4	86	113
5	69	106
6	70	39
7	68	-
8	81	35
9	91	69

Nitrous oxide binding energies on Rh_n^+ clusters reported here agree well with similar calculations reported by Hermes *et al*.[40] For example, they reported binding energies for $Rh_5^+ \bullet N_2O$ of 69.8 kJ mol^{-1} and $Rh_6^+ \bullet N_2O$ of 74.3 kJ mol^{-1}. However, their reported decomposition activation energies of 73.3 kJ mol^{-1} for $Rh_5^+ \bullet N_2O$ and 67.5 kJ mol^{-1} for $Rh_6^+ \bullet N_2O$ do not agree with those that we calculate. These inconsistencies in the energy of the optimized transition states relative to global minimum geometries of the nitrous oxide bound stationary points illustrate the need for experimental validation of theoretical studies such as this.

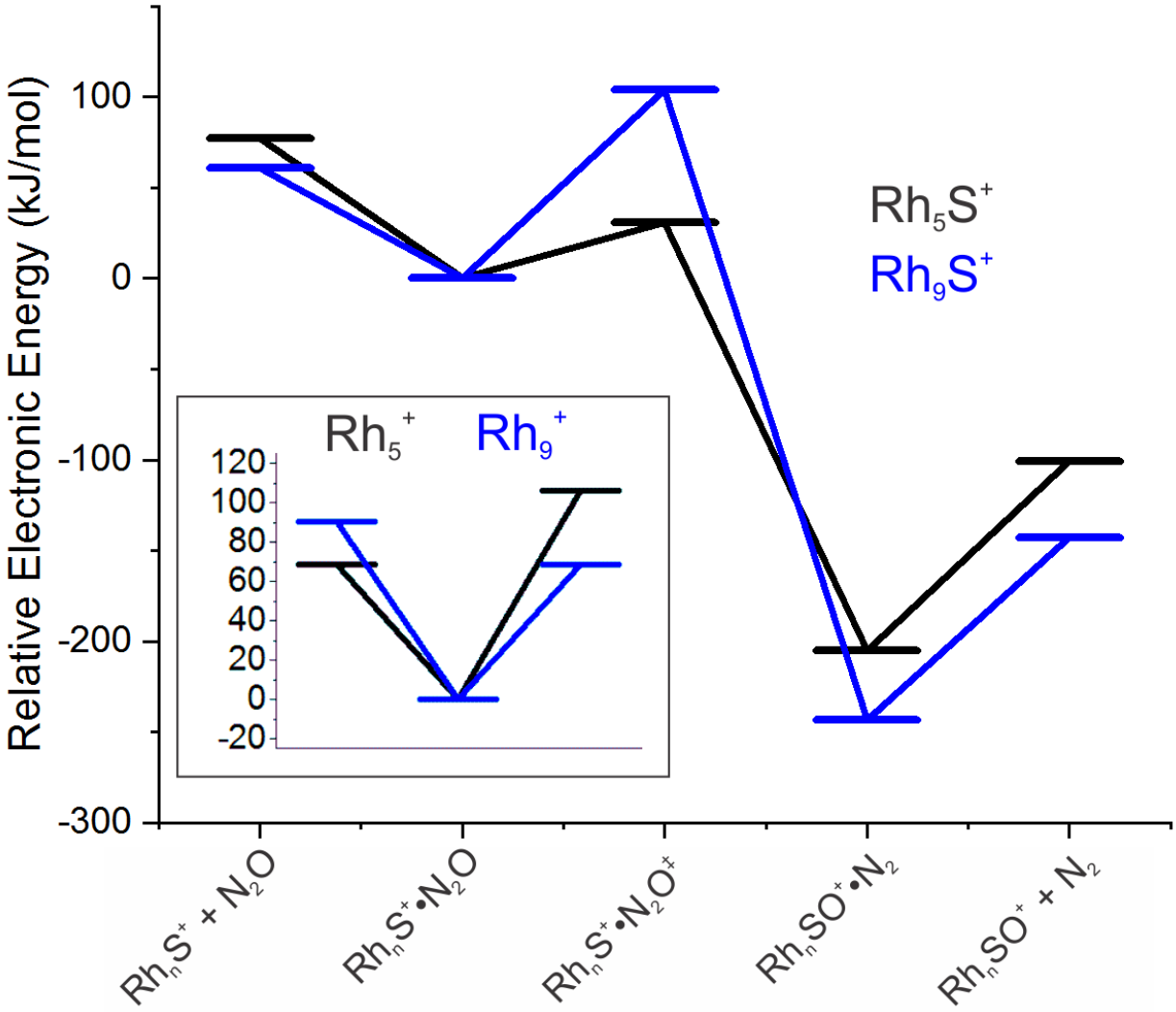

Figure 3.13 Reaction coordinate diagrams of nitrous oxide decomposing on Rh_5S^+ and Rh_9S^+. Inset: Barriers of N_2O desorption versus decomposition on Rh_5^+ and Rh_9^+. Non zero-point corrected electronic energies have been used to determine the barrier heights and were calculated at TPSSh/Def2-TZVP.

3.3.2 Electronic Structure

Results from second order perturbation theory analysis of the Fock matrix in the NBO basis of $Rh_nS^+ \bullet N_2O$ ($n = 2 – 9$) and $Rh_n^+ \bullet N_2O$ ($n = 2 – 9$) are presented in Table 3.6 and Table 3.7, respectively. This analysis reports on donor-acceptor relationships between molecular orbitals and their calculated stabilization energies. The stabilization energies over interactions which involve MOs localized on Rh_n^+ or Rh_nS^+ donating into N_2O are totaled in the second column of each table. Cluster-to-ligand interactions appear to be stronger in the sulphur analogs than in the case of pure rhodium cluster cores. This contrasts the trend observed in the electronic binding energy results presented earlier in Table 3.4 and Table 3.5, which showed nitrous oxide to bind more strongly to Rh_n^+ clusters than the Rh_nS^+ clusters. The third column of Table 3.6 and Table 3.7 contains the percentage of the total stabilization energy in which N_2O antibonding orbitals, of mostly π character, act as the acceptor. The presence of electron density in π^* orbitals would reduce bonding character, and therefore molecular rigidity of N_2O. A less rigid N_2O molecule is more likely to be capable of participating in the decomposition mechanism which requires bending and subsequent fission of the N-O bond. The involvement of these MOs as acceptor orbitals is more significant in the pure rhodium analogs.

Also examined are the MO interactions where the N_2O molecule acts as the donor, the totals of these interactions are presented in column 4. The sulphur analogs show these N_2O-donor interactions to be more stabilizing than the N_2O-acceptor interactions, for every cluster size. In the case of the pure rhodium analogs these two interactions are closer in magnitude with some instances of N_2O-acceptor interactions being greater than N_2O-donor interactions. Donation out of bonding π N_2O orbitals is consistently present and more so in the pure rhodium clusters, see

column 5. The final column presents the largest contributor to N_2O donation, the terminal nitrogen lone pair, as one could intuit.

Table 3.6 Stabilization energies of molecular orbital interactions as determined by NBO analysis. The summation of all MO interaction energies with Rh_nS^+ or N_2O acting as the donor are presented as well as the degree of involvement of chemically relevant orbitals.

Species	Rh_nS^+ Donation (kJ/mol)	Acceptor: N_2O π* (%)	N_2O Donation (kJ/mol)	Donor: N_2O π (%)	Donor: N Lone Pair (%)
$Rh_2S^+•N_2O$	246	28	387	4.4	93
$Rh_3S^+•N_2O$	374	26	376	3.7	93
$Rh_4S^+•N_2O$	223	39	430	5.4	90
$Rh_5S^+•N_2O$	218	29	423	5.3	90
$Rh_6S^+•N_2O$	216	49	360	5.4	90
$Rh_7S^+•N_2O$	293	31	339	5.4	90
$Rh_8S^+•N_2O$	303	45	408	6.3	89
$Rh_9S^+•N_2O$	256	41	402	6.0	88

Table 3.7 Stabilization energies of molecular orbital interactions as determined by NBO analysis. The summation of all MO interaction energies with Rh_n^+ or N_2O acting as the donor are presented as well as the degree of involvement of chemically relevant orbitals.

Species	Rh_n^+ Donation (kJ/mol)	Acceptor: N_2O π* (%)	N_2O Donation (kJ/mol)	Donor: N_2O π (%)	Donor: N Lone Pair (%)
$Rh_2^+•N_2O$	150	69	240	2.4	94
$Rh_3^+•N_2O$	103	51	243	5.5	90
$Rh_4^+•N_2O$	133	42	300	7.6	86
$Rh_5^+•N_2O$	203	54	169	10.1	84
$Rh_6^+•N_2O$	184	51	194	7.9	86
$Rh_7^+•N_2O$	248	43	359	7.9	86
$Rh_8^+•N_2O$	251	41	205	8.0	86
$Rh_9^+•N_2O$	275	45	386	7.8	87

Figure 3.14 shows the summation of the stabilization energies from cluster donation to nitrous oxide and nitrous oxide donation to the cluster for both the sulphur and the pure rhodium clusters. In general, more stabilization energy exists between N_2O and Rh_nS^+ as compared with Rh_n^+, supporting the lower binding energies found for $Rh_n^+•N_2O$. The change in stabilization

energy, according to NBO analysis, with cluster size bears no resemblance to the trend in binding energies reported earlier. These inconsistencies likely point to covalent interactions not being the dominant binding interaction.

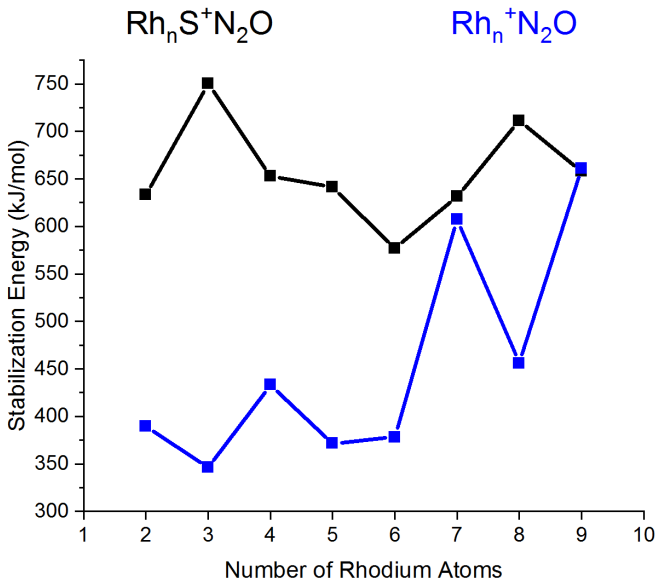

Figure 3.14 **Black** Summation of Rh_nS^+ donation and N_2O donation stabilization energies. **Blue** Summation of Rh_n^+ donation and N_2O donation stabilization energies.

Results of natural population analysis for the computation of atomic partial charges in $Rh_n^+ \bullet N_2O$ and $Rh_nS^+ \bullet N_2O$ structures are given in Figure 3.15 and Table 3.8. Summed partial charges for the Rh_n^+ and Rh_nS^+ core are plotted in Figure 3.15A. Summed partial charges for the N_2O moiety are plotted in Figure 3.15B. Values further from the nominal charges, +1*e* for the cluster core and 0*e* for N_2O, indicate a higher degree of charge transfer. The total charge for the cluster cores is less than +1*e* for every cluster size in both analogs and N_2O possesses a slightly positive charge. This points to an overall charge transfer occurring in which N_2O donates electron density to the metal cluster core. This effect appears to diminish slightly with cluster core size. When comparing the two analogs, it is obvious that the sulphur clusters are experiencing more charge transfer (*ca.* 0.022*e*) than the pure rhodium analogs for all values of *n* studied. The lower partial charge on the sulphur doped clusters compared to the pure rhodium clusters and the higher

partial charge on the N_2O moiety when bound to the Rh_nS^+ clusters versus the Rh_n^+ means there is less charge separation for sulphur clusters with the N_2O moiety, and the electrostatic binding should therefore be weaker on average.

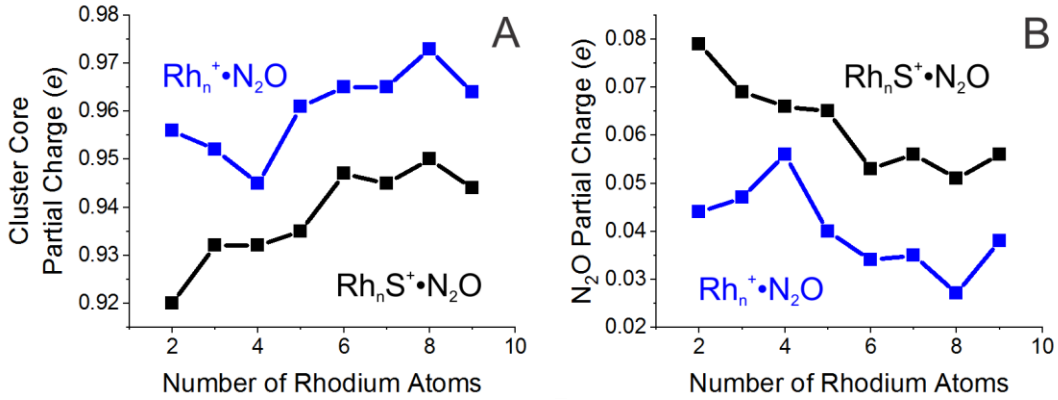

Figure 3.15 Summed atomic partial charges of (**A**) the cluster core and (**B**) the nitrous oxide moiety. In blue are the partial charges for the pure rhodium clusters and these are given for the sulphur clusters in black. The partial charges were found by using the natural populations analysis of the NBO calculations. Nominal total charge for the cluster cores are +1*e* and the N_2O moiety are 0*e*.

Table 3.8 Total of the atomic partial charges for the cluster core and the nitrous oxide moieties for the sulphur cores and pure rhodium cores.

n	$Rh_nS^+•N_2O$		$Rh_n^+•N_2O$	
	Cluster Core	N_2O	Cluster Core	N_2O
2	0.920	0.079	0.956	0.044
3	0.932	0.069	0.952	0.047
4	0.932	0.066	0.945	0.056
5	0.935	0.065	0.961	0.040
6	0.947	0.053	0.965	0.034
7	0.945	0.056	0.965	0.035
8	0.950	0.051	0.973	0.027
9	0.944	0.056	0.964	0.038

Molecular Orbital Analysis. The difference in energy between the LUMO and HOMO is a metric for the stability of a species, where larger gaps indicate a more stable complex.[76,126] The HOMO-LUMO gaps (ΔE_{H-L}) for the α and β-spin orbitals of $Rh_nS^+•N_2O$ and $Rh_n^+•N_2O$ (n = 2 – 9) have been plotted in Figure 3.16. ΔE_{H-L} for the α-spin orbitals of $Rh_n^+•N_2O$ indicate at most cluster sizes

(excluding n = 8, 9) pure rhodium analogs form a more stable complex with nitrous oxide than the sulphur doped analogs, which agrees with the computed N_2O binding energies (Table 3.4 and Table 3.5). The peaks at n = 5 in the α-spin orbitals of both analogs indicate that this cluster size is the most stable of the series which agrees with the experimental finding of anomalously inert Rh_5 clusters.[3] All four series show similar trends, peaks at n = 3 – 5, followed by a decrease in cluster stability with the lowest $\Delta E_{H\text{-}L}$ values at the largest cluster size. This also agrees with the trend in binding energies which decrease with cluster size.

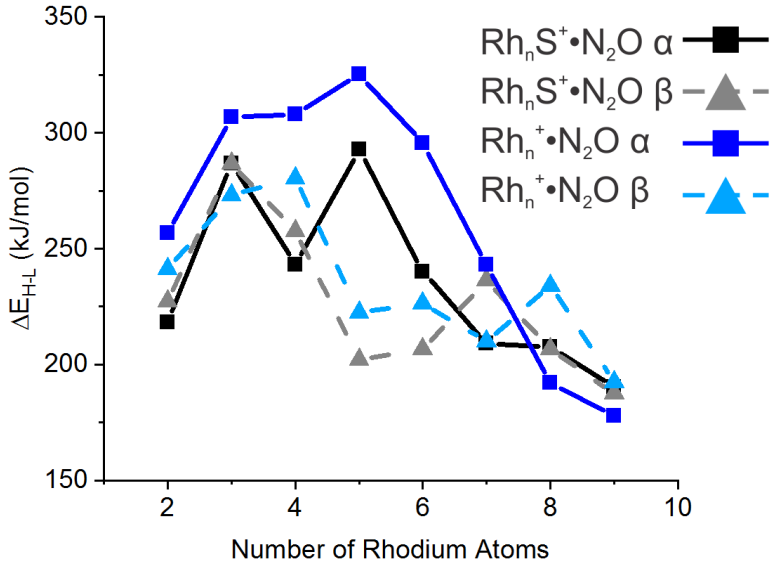

Figure 3.16 HOMO-LUMO gaps of $Rh_nS^+ \bullet N_2O$ and $Rh_n^+ \bullet N_2O$ (n = 2 – 9). The open shell nature of small rhodium clusters required the use of an unrestricted functional which calculates α and β spin orbitals separately.

As an example, the frontier molecular orbitals (FMOs) for $Rh_5S^+ \bullet N_2O$ and $Rh_5^+ \bullet N_2O$ are given in Figure 3.17. All FMOs involve the metal core interacting with the FMOs of the free N_2O molecule (see Figure 3.18). This highlights that electron density is populating the π*-system of nitrous oxide, relaxing the rigidity of N_2O. A less rigid N_2O molecule is more capable of participating in a mechanism which requires a bent transition state. Within the metal core itself the disruption caused by the inclusion of a sulphur atom is substantial. The α-HOMO of $Rh_5^+ \bullet N_2O$

consists of d-orbitals localized on each rhodium atom while the α-LUMO consists of a large π-type orbital delocalized across the entire cage with a nodal plane along the equatorial plane of the Rh_5^+ moiety (see Figure 3.17).

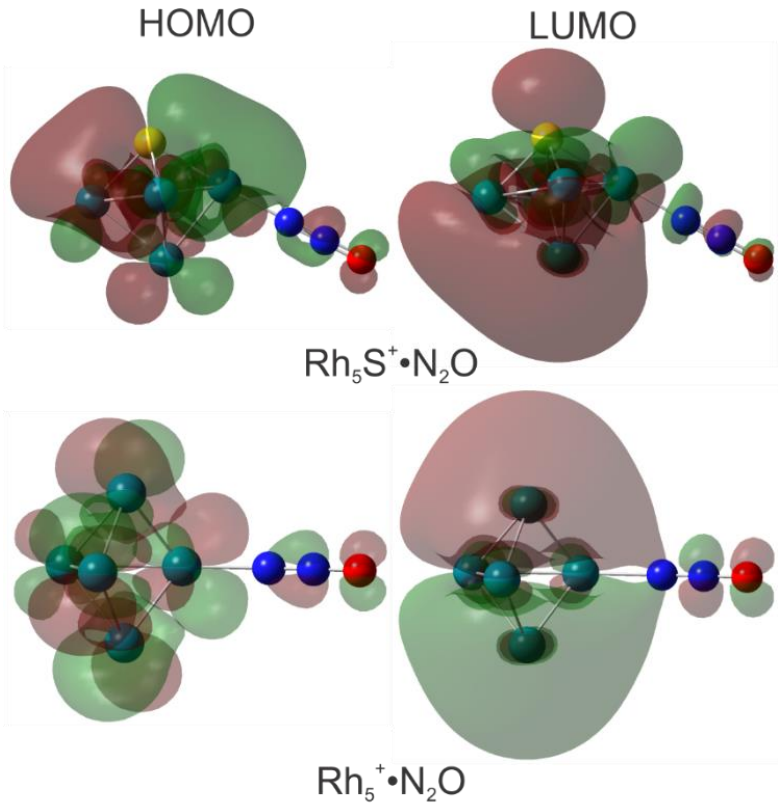

Figure 3.17 The α-HOMO (left column) and α-LUMO (right column) orbitals of $Rh_5S^+•N_2O$ (top row) and $Rh_5^+•N_2O$ (bottom row). These FMOs illustrate the overlap of the metal cores and the anti-bonding π nitrous oxide orbitals. The delocalization of the sulphur atom orbitals is also seen.

The sulphur atomic p-orbital spreads out over the rhodium atomic d-orbitals and shows a small amount of overlap with the nitrous oxide π-system. The large, delocalized cluster π-orbital of the Rh_5^+ α-LUMO is lost when the sulphur atom is included. The FMOs of the other cluster sizes can be described in a similar fashion.

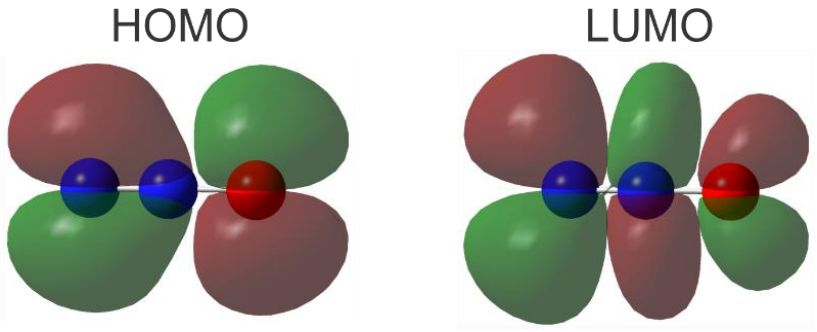

Figure 3.18 Frontier molecular orbitals of N_2O. Calculated at HF/6-31 for the purpose of qualitative discussion.

At this point it is helpful to summarize the analyses conducted and the information they reveal about $Rh_n^+ \bullet N_2O$ compared with $Rh_nS^+ \bullet N_2O$ clustering stabilities. The optimized geometries provide Rh-N bond lengths that are shorter in $Rh_nS^+ \bullet N_2O$ clusters than in $Rh_n^+ \bullet N_2O$ and NBO analysis indicates greater stabilization energies in $Rh_nS^+ \bullet N_2O$ clusters between the cluster core (Rh_nS^+) and N_2O MOs (likely due to the shorter Rh-N bond lengths which provide better overlap of the MOs). Moreover, atomic partial charges indicate more charge transfer occurring in the sulphur-doped species than in the bare rhodium species, which is not unexpected given the comparatively larger degree of MO overlap between the ligand and cluster core moieties. These results indicate that there is a greater interaction between the cluster core and the N_2O ligand in the sulphur-doped systems and suggest that the $Rh_nS^+ \bullet N_2O$ clusters are more stable than the analogous $Rh_n^+ \bullet N_2O$ clusters. However, the N_2O binding energies and the HOMO-LUMO gaps are larger in $Rh_n^+ \bullet N_2O$ clusters, suggesting a greater relative stability for the $Rh_n^+ \bullet N_2O$ clusters. Based purely on these electronic structure calculations, there is still some ambiguity with respect to relative stability / reactivity for the bare versus sulphur-doped clusters. To clarify this situation, it is necessary to consider the vibrational structure of the clusters and its impact on the reaction profiles of the sulphur-containing systems.

3.3.3 Vibrational Structure

Normal mode frequencies corresponding to each global minimum geometry and transition state structure has been predicted. These calculations verify the structures as minima, transition states, or higher order saddle points. The computed frequencies can also be used for comparison with future experimental work, such as IRMPD. Additionally, the frequencies of the molecular moieties (N_2O and N_2) can be compared when bound to the cluster or when free of the cluster to provide insight on the nature of the binding interactions. Finally, thermal corrections to the electronic energies, which include contributions from the vibrational partition function, are included to understand how the competing ligand surface reactions may behave at room temperature.

As an example, the predicted vibrational spectra for two isomers of $Rh_5S^+•N_2O$ are shown in Figure 3.19. Figure 3.19A shows all 3N-6 vibrational modes for the identified global minimum isomer and Figure 3.19B shows the 19 modes at frequencies less than 700 cm^{-1}. Figure 3.19C and D show the same data for an isomer found at 58 kJ mol^{-1} above the global minimum. Highlighted in blue are the N_2O stretching modes. The N-N stretch is predicted to appear at approximately 2471 cm^{-1} and the N-O stretch at 1403 cm^{-1} which are both blue shifted relative to the same modes of free N_2O at 2417 cm^{-1} and 1375 cm^{-1} respectively; represented by vertical dashed lines. This trend is also observed in IRMPD experiments and DFT calculations of $Rh_n^+•N_2O$ (n = 4 – 8) by Hamilton *et al.*[3] The red highlighted peaks are the degenerate bending modes of N_2O, again with dashed lines indicating the value of free N_2O at 604 cm^{-1}. When bound to the cluster the bending modes are red shifted and their degeneracy is lifted to yield two closely spaced frequencies at approximately 580 cm^{-1} and 587 cm^{-1}.

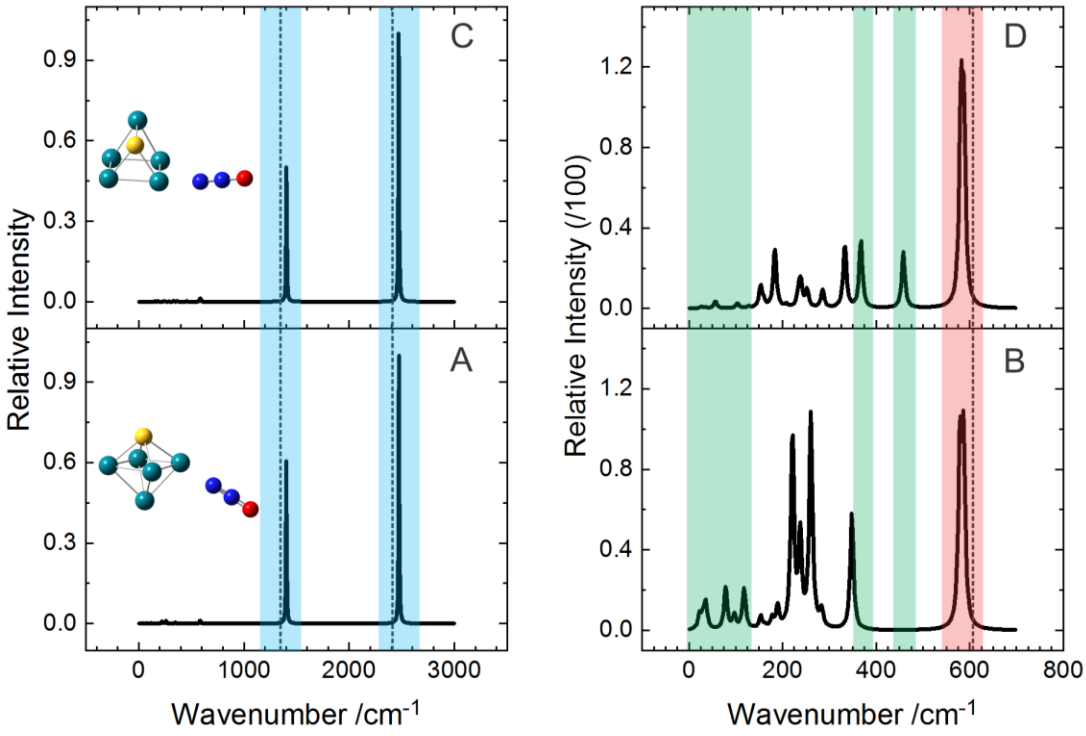

Figure 3.19 (**A)** Predicted vibrational frequencies of the $Rh_5S^+ \bullet N_2O$ global minimum. Blue highlights indicate the stretching frequencies of N_2O. (**B**) Magnification (100x) of low frequency vibrations for the global minimum. Green highlights sulphur vibrations that are unique to each isomer and red highlights N_2O bending modes. (**C**) and (**D**) The predicted vibrational frequencies of an isomer 58 kJ mol^{-1} above the global minimum. Dashed lines indicate the values of the calculated free N_2O frequencies. All frequencies computed at PBE0/Lanl2DZ(Rh), TZVP(S,N,O).

Comparison of the spectra, Figure 3.19B and Figure 3.19D, for the two isomers reveals a difference of only 2 cm^{-1} between their N_2O bending frequencies which are therefore insufficient for isomer identification. As such, the low energy vibrations will prove more useful. In Figure 3.19B and D candidate peaks are highlighted in green. The peaks at 458.14 cm^{-1} and 367.34 cm^{-1} in Figure 3.19D are assigned to sulphur stretches which are specific to coordination by 3 rhodium atoms; the arrangement found in the higher energy isomer. The vibrations predicted to occur at less than 150 cm^{-1} Figure 3.19B correspond to group breathing of the rhodium sulphur core and simultaneous wagging of the N_2O moiety. These low energy, low intensity modes would be difficult to measure using standard absorption techniques. IRMPD is known to be very sensitive,

especially when a weakly bound, typically Ar, tag is present.[3,38,39] Cluster breathing modes would be unlikely to cause fragmentation except for very high quanta of excitation, but when vibrationally redistributed to a weakly bound tag, energy absorbed at less than 150 cm^{-1} will redistribute to the tag, causing desorption for relatively low quanta of excitation. Additionally, the weak van der Waals binding associated with rare gas tags should not lead to significant differences between the bound and unbound cluster vibrational frequencies.

The wavenumbers of the fundamental bands of free N_2O (dotted lines) and the wavenumbers corresponding to the same vibrations in the cluster bound species as a function of cluster size are presented in Figure 3.20. Excellent agreement is found between the calculated and free N_2O (± 1 cm^{-1}) fundamental transitions. The N-N stretch and the N-O stretch have both been shifted to higher wavenumber. The bending modes, which are degenerate in free N_2O, are observed to be non-degenerate when bound to Rh_nS^+. These shifts agree with many experimental and computational studies and they are attributed to binding *via* the terminal nitrogen atom. [3,112–116] Notably the IRMPD and DFT study by Hamilton *et al.* on N_2O bound to Rh_n^+ ($n = 4 – 8$) found N_2O stretching frequencies blue shifted by ~40 cm^{-1} for the smaller clusters which drops to ~30 cm^{-1} for the larger cluster sizes. Hamilton was also able to exclude the possibility of N_2O binding by the oxygen atom as DFT predicted a 60 cm^{-1} red shift in the N-O stretch which was not seen in any of the IRMPD spectra.[3] A dependence on underlying cluster structure is indicated by the lack of a strong correlation of N_2O stretching frequencies to cluster size.[3] The experimentally observed bending frequencies for bound N_2O are red shifted by ~30 cm^{-1} when compared to unbound and red shift further with increasing cluster size. The bending modes were observed to maintain degeneracy within experimental error indicating the high degree of local symmetry for the N_2O binding site. The only exception was in the spectrum of $Rh_5{\bullet}N_2O^+$ which

showed the two bends separated by ~15 cm^{-1}. For our vibrational analysis, DFT predicts lifting the degeneracy of the bending modes by ~20 cm^{-1} for n > 3. This is primarily due the presence of sulphur breaking the symmetry of the cluster core.

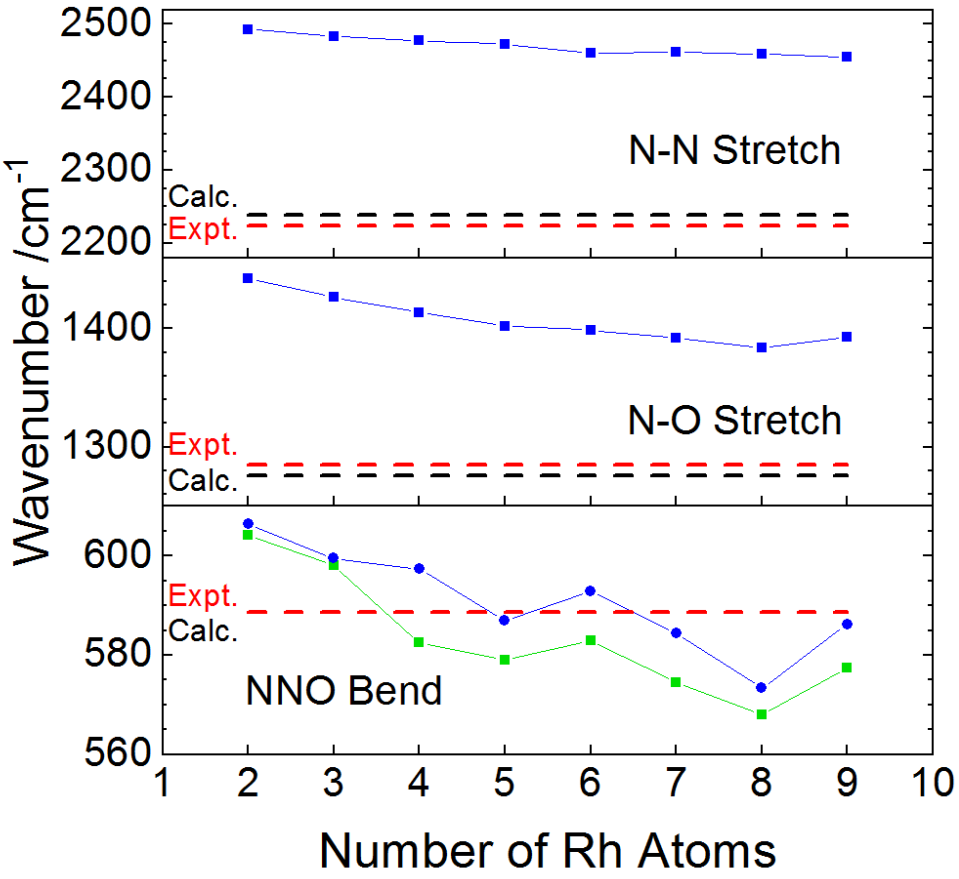

Figure 3.20 Vibrational frequencies of experimentally observed free nitrous oxide[127] (**red**) and calculated (**black**). DFT predictions for the N-N stretching, N-O stretching, and N_2O bending frequencies are presented in the top, middle, and bottom panels, respectively for $Rh_nS^+ \bullet N_2O$ ($n = 2 – 9$) (**blue** and **green**). All frequencies were calculated at PBE0/Lanl2DZ(Rh), TZVP(S,N,O).

The blue shift observed in the N-O stretching frequency (Figure 3.20 middle) relative to the same values in free-N_2O is consistent with the calculated stronger N-O bonds. This can be understood using the results of the NBO analysis and the FMOs of N_2O (see Figure 3.18). The FMOs of N_2O both possess nodal planes between the N-O bond. Donation out of the HOMO should serve to shorten and strengthen the N-O bond while donation into the LUMO should serve

to elongate and weaken the N-O bond. The NBO analysis shows that both processes are occurring however the stabilization energy of N_2O donation is larger than that of Rh_nS^+ donation implying that N_2O HOMO donation is involved to a greater extent than LUMO acceptance. Donation from N_2O to the metal cluster is also supported by the calculated partial charges which indicate reduced positive charge on the cluster and increase positive charge on N_2O. Nitrous oxide HOMO donation shortens the N-O bond length, increases the force constant, and blue shifts the stretching frequency. The involvement of the N_2O FMOs with the cluster cores also serves to disrupt the π-system of N_2O by populating internuclear nodal planes and allow the N_2O molecule to be more flexible. A more flexible N_2O will require less energy to bend and therefore display red shifting in its bending modes. Additionally, N_2O HOMO donation would result in elongation of the N-N bond and a vibrational red shift as electron density is transferred out of the N-N π-bonding orbital; however, a blue shift is observed and therefore a different explanation is required. Interactions between MOs localized on the terminal nitrogen atom and Rh_nS^+ cluster orbitals dampen the translation of the nitrogen atom therefore increasing the amount of energy required to induce the N-N stretching vibration. NBO analysis identified one such nitrogen lone pair orbital which accounted for *ca*. 90 % of the N_2O donor stabilization energy (Table 3.6). It is this blue shift that was used as a signature in experimental studies to indicate binding of the terminal nitrogen atom.[3,112–116]

Normal mode analyses are also conducted for the oxide clusters. As an example, the predicted vibrational frequencies for Rh_9S^+•O are presented in Figure 3.21. Panels A and C are showing the full vibrational spectrum for the global minimum isomer (+0 kJ mol^{-1}) and a local minimum isomer (+59.2 kJ mol^{-1}), respectively. Panels B and D show only the low frequency modes (<350 cm^{-1}) for the global and local minimum, respectively. The most intense peak at 711 cm^{-1} in the local minimum and 640 cm^{-1} in the global minimum is assigned to an oxygen

stretch during which the oxygen atom is translating along a displacement vector that is perpendicular to the Rh-Rh bond being bridged by the oxygen atom. The second red highlighted band in panels A and C at 429 cm^{-1} and 283 cm^{-1}, respectively, is assigned to the oxygen atom rocking between its two binding rhodium atoms. A third isomer distinguishing feature, in green in panels B (327 cm^{-1}) and D (250 cm^{-1}), is assigned to the sulphur atom rocking among three rhodium atoms in the high energy isomer and four rhodium atoms in the global minimum structure.

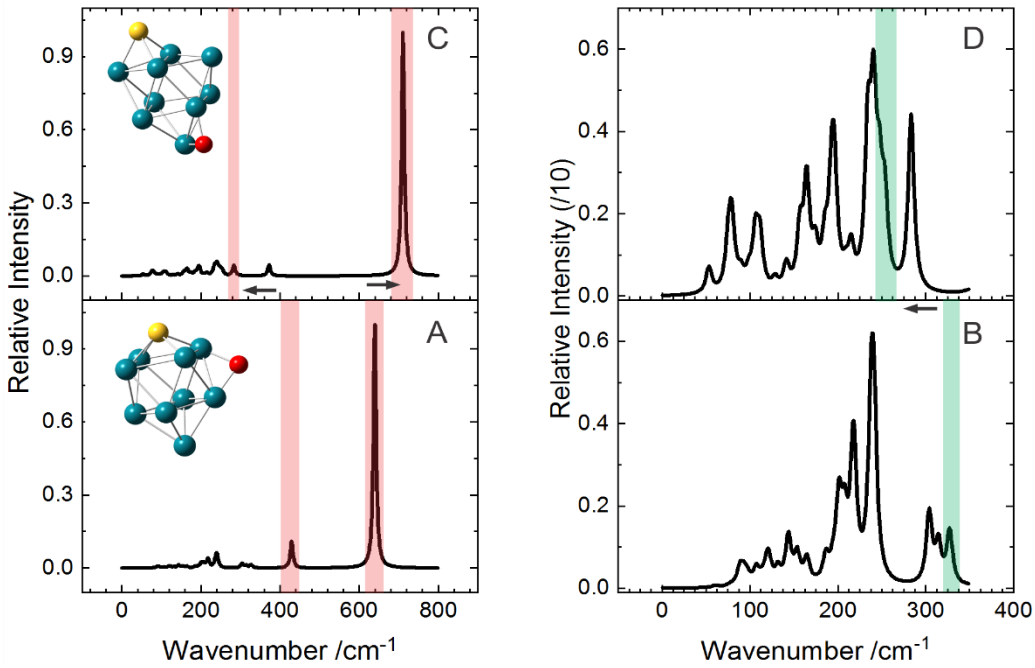

Figure 3.21 (**A**) Predicted vibrational frequencies of the Rh_9S^+•O global minimum and (**B**) x10 magnification of the low energy vibrations. (**C**) Predicted vibrational frequencies of a Rh_9S^+•O isomer lying 59.2 kJ mol^{-1} above the global minimum and (**D**) x10 magnification of the low energy vibrations. Green highlights a sulphur vibration that is unique to each isomer and red highlights unique O rocking modes. All frequencies computed at PBE0/Lanl2DZ(Rh), TZVP(S,N,O).

As a representative example of the Rh_nSO^+•N_2 vibrational analyses, predicted vibrational frequencies of Rh_5SO^+•N_2 isomers are presented in Figure 3.22. Panels A and B show the spectrum of the global minimum geometry, fundamental transitions for all 3N-6 normal modes and a 100x magnification in the region of 0 – 800 cm^{-1}, respectively. Panels C and D display the spectrum in the same manner for a higher energy isomer at 9.6 kJ/mol above the global minimum. The spectra

are dominated by the N_2 stretching frequency at 2420 cm^{-1} and 2395 cm^{-1} for the global minimum and the local minimum, respectively. The calculated stretching frequency of free N_2 is represented by the vertical dashed line. The red shift of this frequency when bound indicates a weakening of the N_2 bond which accords with the increase in the N-N bond length when N_2 is bound to Rh_nSO^+. Green highlights in panels B and D indicate features that may be used to assign potential experimental spectra to their appropriate isomers. For example, a rhodium-oxygen stretch appears at 719 cm^{-1} in the global minimum and 628 cm^{-1} in the higher energy isomer.

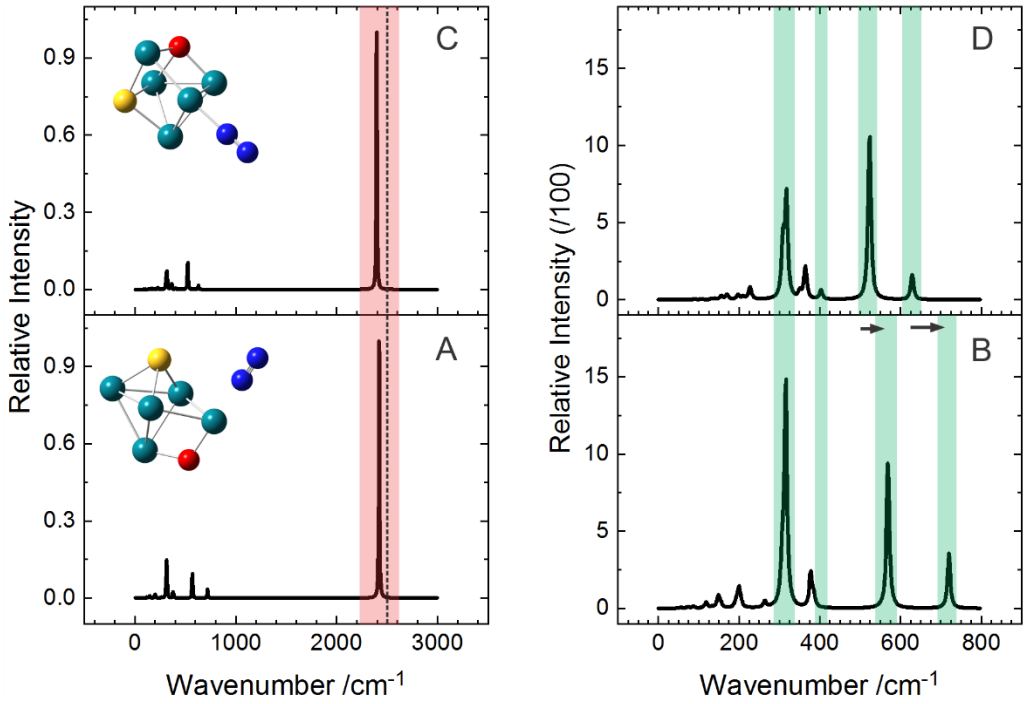

Figure 3.22 (**A**) Predicted vibrational frequencies of the $Rh_5SO^+•N_2$ global minimum and (**B**) x100 magnification of the low energy vibrations. (**C**) Predicted vibrational frequencies of a $Rh_5SO^+•N_2$ isomer lying 9.6 kJ mol^{-1} above the global minimum and (**D**) x10 magnification of the low energy vibrations. Red highlight indicates the N_2 stretching frequency and the calculated free N_2 is indicated by the dashed line. Green highlights indicate distinguishing features. All frequencies computed at PBE0/Lanl2DZ(Rh), TZVP(S,N,O).

This difference is primarily a result of the coordination of two rhodium atoms in the global minimum and three Rh atoms in the higher energy isomer. Similar behaviour is observed in a Rh-O-Rh bend occurring at 523 cm^{-1} in the higher energy isomer and 569 cm^{-1} in the global

minimum. A sulphur-rhodium stretch shows a considerably different frequency for each isomer; 403 cm^{-1} in the higher energy isomer and 307 cm^{-1} in the global minimum. The frequency of the cluster-N_2 moiety stretch occurred at very similar wavenumber for both isomers; 315 cm^{-1} and 317 cm^{-1} for the higher energy isomer and global minimum, respectively.

Figure 3.23 and Table 3.9 highlight the frequency results for select normal modes for increasing rhodium cluster size. The core-N_2 stretching frequency shows an overall increase with the number of rhodium atoms. The change in this frequency with each rhodium atom mirrors the change in the Rh-N bond length with each rhodium atom (see Figure 3.8). For instance, the contraction of the Rh-N bond length from $Rh_2SO^+•N_2$ to $Rh_3SO^+•N_2$ corresponds to the increase in the core-N_2 stretching frequency over the same change in cluster size. The same relationship exists between the N_2 stretching frequencies and the N-N bond lengths reported in Figure 3.7. The cluster bound N_2 stretching frequencies are found red shifted from the calculated free N_2 stretch at 2496.79 cm^{-1}. In an experimental study, infrared spectra were collected from RhN_2 samples that were deposited on a CsI window after generated by laser ablation of a rhodium target in excess N_2.[128] The nitrogen stretching frequency was observed at 2328.2 cm^{-1}. Our calculated red shift in the N_2 stretching frequency has been experimentally observed using infrared photodissociation on $Rh_n^+•N_2$ (n = 6 – 15).[110] The authors explain both the general red shift and the trend with increasing cluster size. The general red shift is explained by the σ-donor and π-acceptor properties of N_2, which is similar to observations for the isoelectronic compound, CO, on metal surfaces.[129] The increasing red shift with n is explained by a charge dilution model, previously used for N_2 shifts on Co and Ni. As the number of rhodium atoms increase the positive charge of the cluster is spread over more atoms. This allows for a greater degree of electron density localization at interaction sites creating greater π backdonation into the π* LUMO of the N_2 moiety.

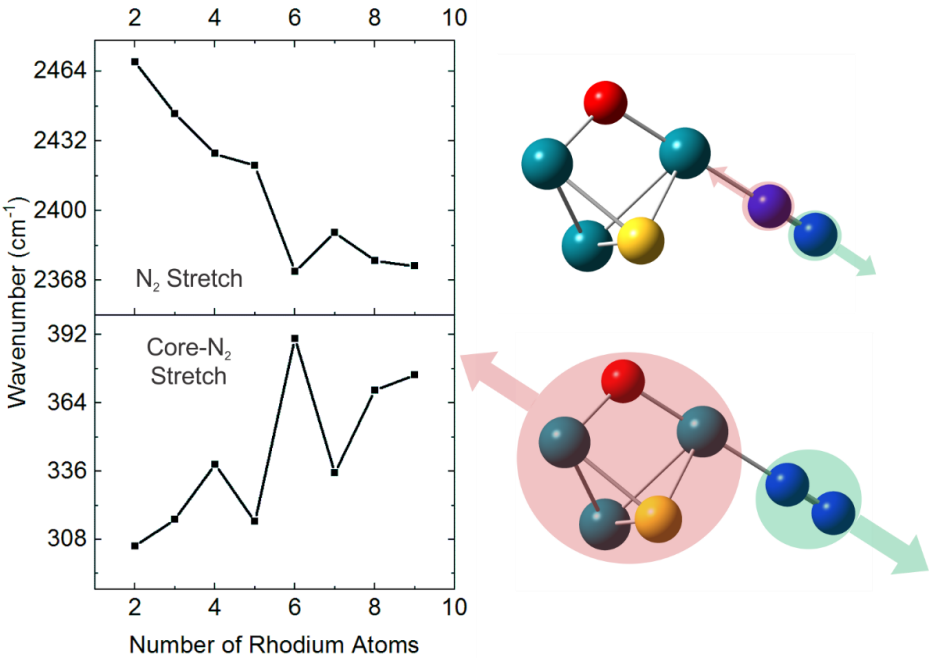

Figure 3.23 **Top** The predicted N_2 stretching frequency of $Rh_nSO^+•N_2$ (n = 2 – 9) for each value of n, calculated at PBE0/Lanl2DZ(Rh), TZVP(S,N,O). **Bottom** The predicted frequency of the core-N_2 stretching vibration along a dissociative displacement vector.

Table 3.9 Predicted vibrational frequencies of $Rh_nSO^+•N_2$ (n = 2 – 9) by DFT PBE0/Lanl2DZ(Rh), TZVP(S, N, O).

n	Core-N_2 Stretch (cm^{-1})	N_2 Stretch (cm^{-1})
2	305.16	2468.37
3	316.19	2444.58
4	338.86	2426.21
5	315.44	2420.65
6	390.45	2372.16
7	335.24	2389.94
8	369.27	2376.87
9	375.46	2374.61

Calculation of the vibrational eigenstates allows for determination of the vibrational partition function at room temperature. Determination of the electronic partition function uses the standard approximation of negligible population in the excited electronic states. This may lead to a source of error in this study as the multiplicity studies revealed numerous electronic states within

10 kJ mol^{-1} which corresponds to a Boltzmann weighting of *ca.* 2 %. The translational partition function assumes ideal gas behaviour and contributes 3/2RT = 3.72 kJ mol^{-1} to the internal energy at 298.15 K, R is the ideal gas constant. The rotational partition function contributes the same as the translational motions for nonlinear polyatomic molecules and RT = 2.48 kJ mol^{-1} as the contribution from linear molecules at room temperature. This allows for calculation of thermal corrections to the electronic energies which can be used to approximate Gibbs' energy landscapes and reaction barriers at room temperature. As an example, reaction coordinate diagrams for $Rh_2S^+ + N_2O$ and $Rh_2^+ + N_2O$ are presented in Figure 3.24. Black traces show zero-point corrected electronic energies while blue traces show Gibbs' energy corrected electronic energies. Comparison of blue and black traces for the sulpur-doped species reveal a reduction in desorption threshold while the transition state along the decomposition pathway exhibits a slight increase in energy relative to the cluster-N_2O bound state upon application of Gibbs' corrections. The inset of Figure 3.24 shows the analogous desorption and decomposition thresholds for N_2O on Rh_2^+. A decrease in both barrier heights are calculated. When thermal corrections are considered, decomposition is still the energetically preferred outcome. In the case of $Rh_2S^+ + N_2O$, Gibbs' energy corrections change the preferred reaction from N_2O decomposition (Rxn 4; Pg. 20) with thermal corrections neglected to N_2O desorption (Rxn. 3; Pg. 20) when thermal corrections are considered. This is also found for the n = 3 - 9 cluster sizes. Gibbs' energy corrected binding and activation energies are given in Figure 3.25 and Table 3.10. Desorption barriers consistently decrease by ~ 40 kJ mol^{-1} and decomposition barriers increase by ~ 5 – 15 kJ mol^{-1} with free energy corrections. The corrected new barrier heights show preference for N_2O desorption over decomposition at every cluster size, demonstrating that sulphur's ability as a catalytic poison for bulk catalysis is mirrored in calculated reactivities for gas phase nanoclusters.

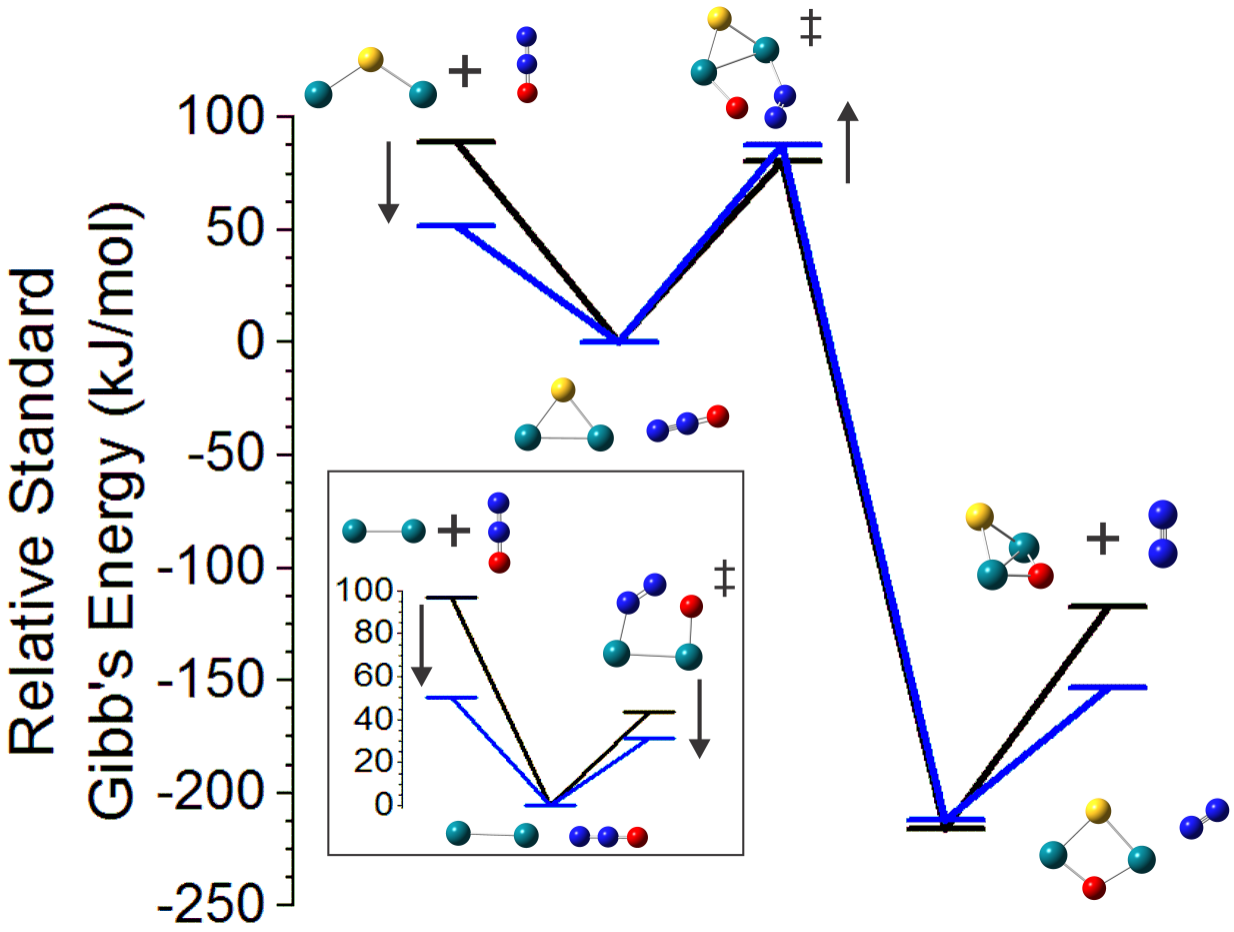

Figure 3.24 Reaction coordinate diagram of competing nitrous oxide decomposition and desorption on clusters of Rh_nS^+ (n = 2 – 9) and Rh_n^+ (n = 2 – 9) (inset). (**Black**) Energy of stationary points determined using zero-point corrected electronic energies. (**Blue**) Stationary points determined using Gibbs' energy corrected electronic energies at T = 298.15 K. Structures and frequencies calculated at TPSSh/Def2-TZVP.

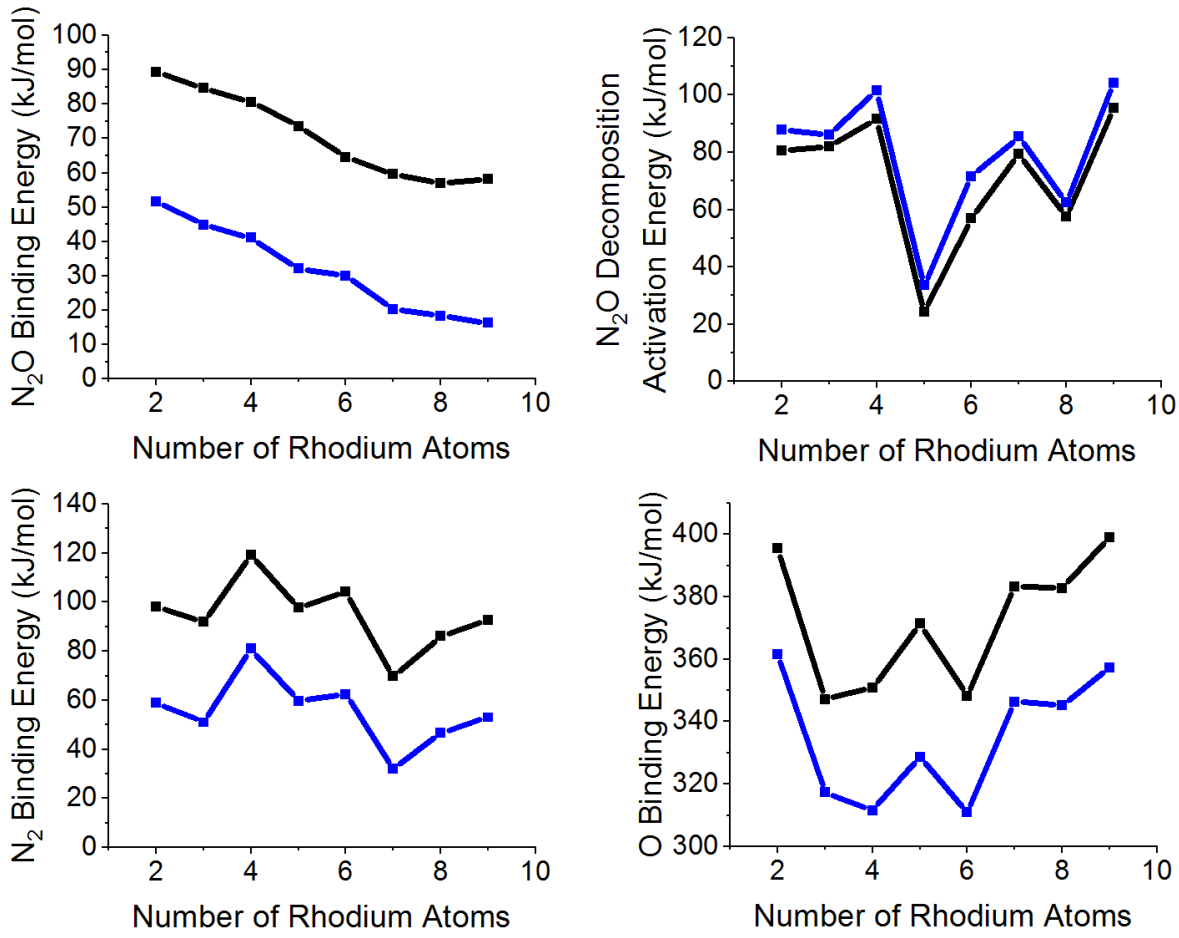

Figure 3.25 Binding energies of N_2O and O to Rh_nS^+ and N_2 to Rh_nSO^+. Energetic difference of $Rh_nS^+ \bullet N_2O$ transition state and bound minimum. (**Black**) Energies determined using zero-point corrected electronic energies. (**Blue**) Energies determined using Gibbs' energy corrected electronic energies at T = 298.15 K. Structures and frequencies calculated at TPSSh/Def2-TZVP.

Table 3.10 Binding energies of N_2O and O to Rh_nS^+ and N_2 to Rh_nSO^+. Energetic difference of $Rh_nS^+ \bullet N_2O$ transition state and bound minimum. Change in Gibbs' energy of nitrous oxide decomposition on Rh_nS^+ ($n = 2 – 9$). Energies determined using Gibbs' energy corrected electronic energies at T = 298.15 K. Structures and frequencies calculated at TPSSh/Def2-TZVP.

n	N_2O Binding Energy	Decomposition Activation Energy	N_2 Binding Energy	O Binding Energy	Decomposition ΔG^o
2	52	88	59	362	-153
3	45	86	51	317	-116
4	41	101	81	312	-113
5	32	33	60	329	-140
6	30	72	63	311	-124
7	20	85	32	346	-169
8	18	63	47	345	-170
9	16	104	53	357	-184

For completeness, Figure 3.26 illustrates the impact of thermal corrections on the reactions of N_2O with Rh_n^+ clusters. The desorption barrier is consistently reduced by *ca.* 40 kJ mol^{-1} while the changes to the decomposition barrier are less persistent and inconsistent. Most cluster sizes see a negligible increase of at most 10 kJ mol^{-1}, except $n = 2$ which sees a drop of about 15 kJ mol^{-1}. Table 3.11 compares the barriers heights of the two competing reactions and reveals no clear preference across the entire series, with three out of seven clusters sizes showing a lower barrier to decomposition.

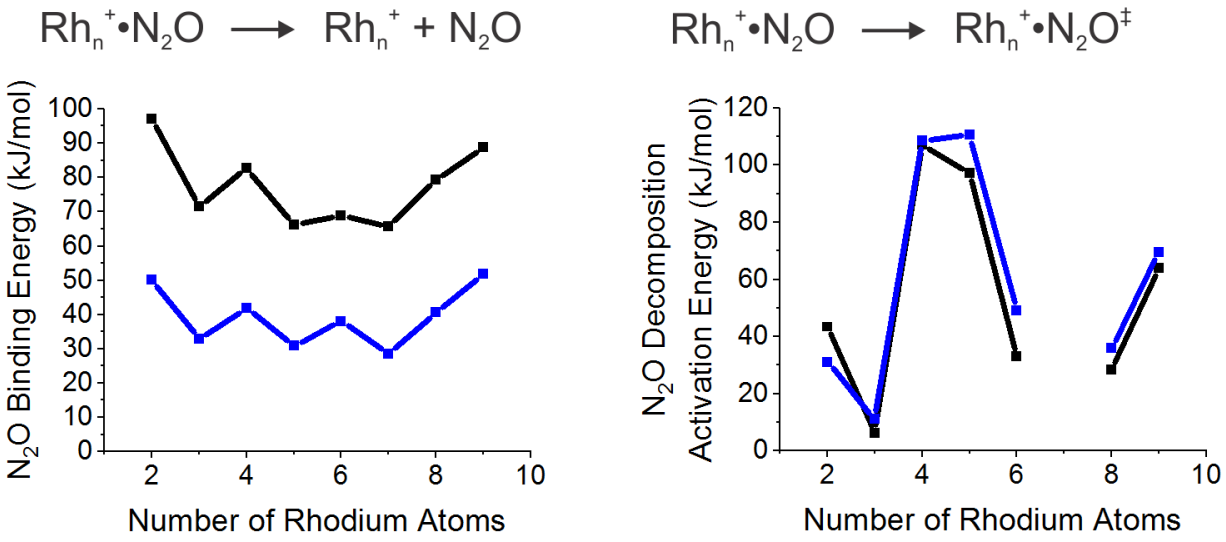

Figure 3.26 Binding energies of N_2O to Rh_n^+. Energetic difference of $Rh_n^+ \bullet N_2O$ transition state and bound minimum. (**Black**) Energies determined using zero-point corrected electronic energies. (**Blue**) Energies determined using Gibbs' energy corrected electronic energies at T = 298.15 K. Structures and frequencies calculated at TPSSh/Def2-TZVP. Starting geometries taken from Hamilton *et al.*[38] Convergence could not be obtained for $Rh_7^+ \bullet N_2O^{\ddagger}$.

Table 3.11 Binding energies of N_2O to Rh_n^+ ($n = 2 - 9$). Energetic difference of $Rh_n^+ \bullet N_2O$ transition state and bound minimum. Energies determined using Gibbs' energy corrected electronic energies at T = 298.15 K. Structures and frequencies calculated at TPSSh/Def2-TZVP. Starting geometries taken from Hamilton *et al.*[38] Convergence could not be obtained for $Rh_7^+ \bullet N_2O^{\ddagger}$.

n	N_2O Binding Energy	Decomposition Activation Energy
2	50	31
3	33	11
4	42	109
5	31	110
6	38	49
7	29	-
8	41	36
9	52	70

3.4 Conclusions

Extensive mapping of the potential energy surfaces for $Rh_nS^+•N_2O$, $Rh_nS^+•O$, and $Rh_nSO^+•N_2$ (n = 2 – 9) has been conducted. The global minimum geometries of these clusters have been identified at the DFT level of theory as well as transition states for the $Rh_nS^+ + N_2O$ decomposition reaction. Normal mode analysis confirmed the structures as stationary points, which possess only real frequencies of vibration, or transition states, which possess one imaginary frequency of vibration. The geometric, electronic, and vibrational structures of the global minimum isomers were analyzed to understand the effects of the sulphur atom on the two competing nitrous oxide reactions; decomposition and desorption. It was found that when thermal corrections are considered sulphur addition raises the barrier height for the transition state to N_2O decomposition and the desorption reaction becomes favoured at every cluster size. Inclusion of a sulphur atom effectively poisons N_2O decomposition on non-interacting, room temperature, cationic rhodium gas phase nanoclusters.

Studies of electronic structure were employed to further understand the geometric structures and to ensure the accuracy of the reaction barriers by identifying the lowest energy multiplicities. Natural population analysis identified charge transfer from N_2O to the metal clusters. Greater charge transfer in the sulphur analogs and larger stabilization energies suggest $Rh_nS^+•N_2O$ clusters should be more stable. However, greater N_2O binding energies and HOMO-LUMO gaps are found in the $Rh_n^+•N_2O$ clusters. This creates an uncertainty regarding electronic stability of $Rh_nS^+•N_2O$ clusters relative to $Rh_n^+•N_2O$ clusters. Results of these analyses were also used to explain the calculated shifts in vibrational frequencies for bound ligands relative to their unbound frequencies. The interactions realized by NBO analysis and this influence on the structure

of the N_2O and N_2 moieties indicates the existence of considerable covalent interactions. The multiplicities of the global minimum structures accord with past computational and experimental studies, finding a general increase in the multiplicity as the number of rhodium atoms increases. For example, the largest cluster studied, $Rh_9S^+ \bullet N_2O$, possessed 14 unpaired electrons, a 15-tet multiplicity. Most cluster sizes exhibited multiple spin-states within 10 kJ/mol. These results point to the need for multireference methods however current implementations are too computationally expensive. As such, a future step may employ time-dependent DFT which considers the temporal dependence of the electron density.

Geometry optimizations determined the preferred binding motifs studied clusters. The N_2O moiety prefers to bind a single rhodium atom in Rh_nS^+ *via* its terminal nitrogen atom. Binding of N_2 to Rh_nSO^+ occurs through interactions of a single nitrogen atom to a single rhodium atom. The oxygen atom preferred binding to two or three rhodium atoms depending on the underlying metal framework. The binding of oxygen was also found to be the most disruptive to the geometry of the rhodium sulphur clusters. The global minimum geometries were used to predict the harmonic vibrational spectra of each cluster and structurally identifying bands have been highlighted to guide possible IRMPD experiments.

4 Mode-Selective Laser-Control of Catalyst Decomposition

4.1 Introduction

It is generally assumed that thermal reactions which result in bond formation or bond cleavage proceed in an ergodic fashion, *i.e.*, that energy is distributed stochastically and efficiently across all internal states of the molecule(s).[130–138] In other words, the reactivities of molecules depend only on the total energy of the system and not on the means of activation (*i.e.*, the initial state of the system).[139] While there are examples of chemical systems which exhibit non-ergodic behavior, these are predominantly limited to very small molecules.[140–146] Nevertheless, non-ergodicity has been put forward as an explanation for the unexpected outcomes of electron-transfer reactions,[147–151] and rapid abstraction/dissociation reactions.[152,153] To our knowledge, there are only two examples of non-ergodic vibrational mode-selective behavior in larger molecular systems containing several 10s of atoms, both of which are weakly-bound ionic clusters. In 2012, Shaffer *et al*. reported on mode-selectivity in IRMPD of non-covalent ion pairs of triflate and bispyridinium.[134] In 2015, we demonstrated mode-specific fragmentation of amino acid-containing clusters via IR-induced transparency.[43] In the earlier case, the non-ergodic behavior was attributed to hindered IVR, which led to a localized "overheating" of the triflate moiety. The IR-induced fragmentation of the triflate-bispyridinium system was particularly noteworthy because it resulted exclusively in the production of triflic acid, indicating that the observed non-ergodic behavior occurred on a timescale longer than that required for the formation of the new O-H chemical bond. While there is some debate regarding the possible correlations between the properties of gas-phase and condensed phase species,[154–156] studies like these provide interesting

insights into molecular energy disposal / distribution and pique the imaginations of scientists who envision quantum control of chemical reactions.

To date, there have been no reports of IR mode-selective behavior in large covalently bound species. This suggests that the quantum states of molecular systems can efficiently couple and distribute energy stochastically throughout the molecule. However, if hindered IVR is a pre-requisite for non-ergodicity, one might expect mode-selective behavior to be common in chemical reactions. For example, in organometallic systems there is usually a significant energy mismatch between the ligand-localized normal modes and metal-ligand vibrations. Moreover, since these vibrational motions are associated with distinctly different regions of the molecule (*i.e.*, they occupy different regions of phase space), the anharmonic vibrational wavefunction overlap is expected to be quite small. Consequently, one might expect an IVR bottleneck to occur at the metal center, resulting in localized overheating of ligands should they be excited mode-selectively. Here, we show that such a scenario arises in palladium catalysts.

Palladium-catalyzed coupling reactions have become fundamental tools for controlled preparation of carbon–carbon and carbon-heteroatom bonds.[157–166] These reactions are tolerant of most chemical functionalities, and they are regio- and steriospecific.[167] Moreover, cross-coupling reactions are useful in condensation polymerization owing to the fact that reaction yields can be nearly quantitative.[168,169] This ease of use and breadth of applications has led to the ubiquity of Pd-catalysts in modern chemical synthesis. Pd-catalyzed reactions are initiated by oxidative addition of PdL_2, where L is commonly triarylphosphine (usually triphenylphosphine, PPh_3), with an aryl or alkyl halide (RX). This yields a $RPdL_2X$ species, which is believed to be the resting state of the catalyst in the cycle.[167,170–172] A simplified schematic of the Pd-catalyzed coupling cycle is shown in Figure 4.1.

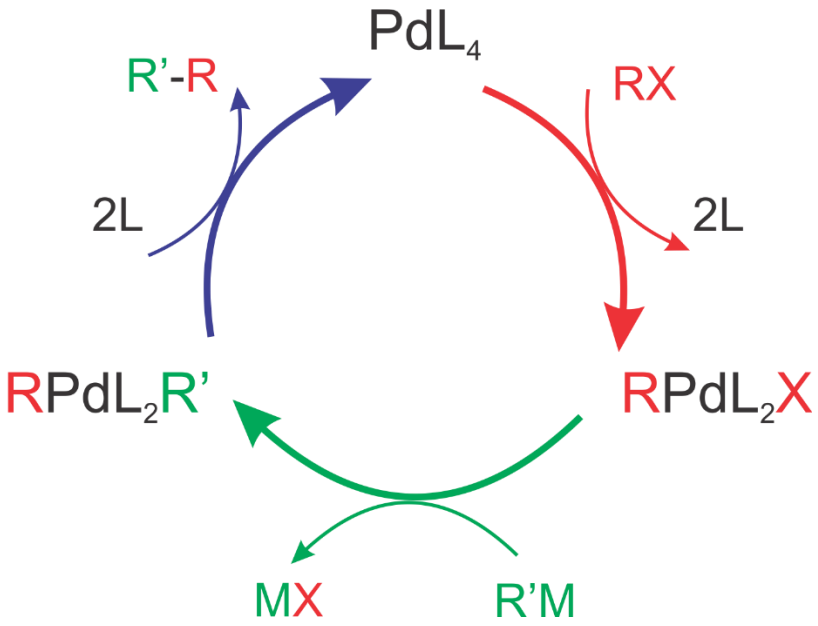

Figure 4.1 A schematic diagram of Pd-catalyzed cross-coupling reactions.

Prior to substitution of the second alky or aryl group (R′), Pd-catalysts can suffer from interchange between the Pd-bound R group and one of the phosphorus-bound aryl moieties. This allows the phosphorus-bound aryl group to enter the cross-coupling in place of the R group, which leads to unwanted product mixtures.[167,173] This "ligand scrambling" can also generate R-L products and result in the catalyst leaving the cycle. Given the synthetic importance of these Pd-catalysts, a more complete understanding of the impact of energy disposal on chemical reactivity is highly desirable, since this might lead to elimination of side products from coupling reactions.

To investigate the structure and reactivity of Pd-catalysts, five complexes were chosen for study. These are shown in Figure 4.2. Three complexes of the form $RPd(PPh_3)_2I$ (R = naphthyl (**1**), biphenyl (**2**), and isopropylphenyl (**3**)) were chosen to study the effect of varying the organic residue on the observed IRMPD behavior. Note that these species all potentially exhibit C─H•••Pd agostic interactions, which have been proposed as stabilizing interactions for the migratory insertion transition state.[173–175] We also examined the IRMPD behavior of $PhPd(P(furyl)_3)_2I$ (**4**) and $PhPd(AsPh_3)_2I$ (**5**) to study the effect of varying the ligand composition. In the case of

$PhPd(P(furyl)_3)_2I$, furyl substituents replace the phenyl rings of the phosphine group, and in $PhPd(AsPh_3)_2I$ we replace triphenylphosphine with triphenylarsine to probe the impact of the metal-heteroatom bond.

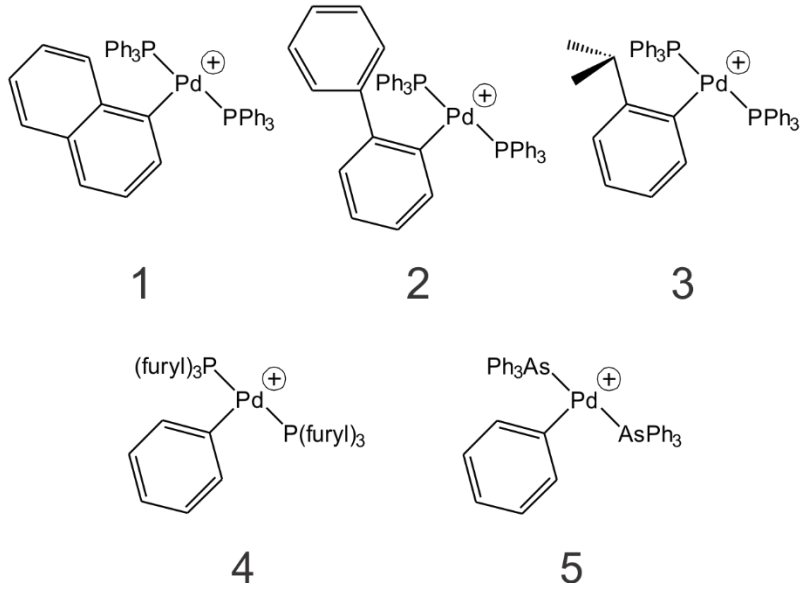

Figure 4.2 The five Pd-catalysts chosen for study. (1) trans-bis(triphenylphosphino)(1-naphthalenyl)palladium(II), (2) trans-bis(triphenylphosphino)(2-biphenyl)palladium(II), (3) trans-bis(triphenylphosphino)(2-isopropylphenyl)palladium(II), (4) trans-bis(trifurylphosphino)(1-phenyl)palladium(II), and (5) trans-bis(triphenylarseno)(1-phenyl)palladium(II).

4.2 Experimental Methods

4.2.1 Sample Preparation

Palladium complexes were prepared as outlined in E. Fillion, *et al.*, *Organomet.*, **28**, 3518-3531 (2009).[175] Electrospray ionization solutions were prepared in dry acetonitrile at a concentration of *ca*. 100 μM and were infused into the mass spectrometer at a rate of 100 μL per hour.

It should be noted that compounds **1-3** and **5** were studied as bare and acetonitrile-tagged complexes, whereas compound **4** was studied as a bare complex and one which was tagged with dibenzylacetone (dba). We were unable to produce the acetonitrile-tagged version of compound **4**.

4.2.2 Instrumentation

IRMPD experiments were carried out at the CLIO FEL facility.[47,176,177] The cationic Pd-catalysts, both bare and tagged with a molecule of acetonitrile, were prepared by electrospray ionization and were isolated within the QIT of a Bruker Esquire 3000+ mass spectrometer.[178–180] Trapped ions were then irradiated with the tunable infrared output of the FEL over a wavenumber range of 900 – 2000 cm^{-1}. As the FEL was tuned, depletion of the parent ion signal and concurrent enhancement in fragment ion signals were recorded to generate the vibrational absorption spectrum of the catalyst. A detailed description of the IR-FEL output is available in Chapter 2 Section 2.2.1.

4.3 Computational Methods

To aid in spectral assignment, a detailed computational study was conducted in parallel with the experimental work. An exhaustive search of each catalysts' potential energy surface was undertaken using the basin hopping (BH) algorithm.[14,76,178] The Pd-complexes were first optimized individually at the B3LYP/Lanl2DZ level of theory to better approximate their geometries, and atomic partial charges were calculated using the CHELPG partition scheme. The cluster PES was modeled using the Universal Force Field. To search the PES, the dihedral angles associated with single bonds were randomly distorted by $-5° \geq \theta \geq +5°$ at each iteration of the BH code. In total, approximately 40,000 geometries were sampled for each catalyst. Unique structures were then carried forward for geometry optimization at the B3LYP/Lanl2DZ level of theory where normal

mode analyses were also conducted to predict IR spectra and to ensure that each structure was a local minimum on the PES. For several of the complexes and fragments, calculations were also conducted at the B3LYP/def2-TZVPPD(Pd), 6-311++G(d,p)(C,H,P) level of theory to test the validity of the B3LYP/Lanl2DZ calculations. This computational study indicated that both calculation methods yielded similar structures and harmonic spectra (see Figure 4.19 at the end of section 4.4). Unique cluster structures were identified based on zero-point corrected energy and geometry.

4.4 Results and Discussion

4.4.1 Optimized Geometries of Palladium Complexes

For each catalyst, the BH search strategy identified a single low energy isomer, which was carried forward for calculation at the density functional level of theory to identify the most stable catalyst geometry and provide accurate predictions for harmonic vibrational spectra and thermodynamic properties. The optimized geometries of compounds **1-5** are presented in Figure 4.3. Figure 4.4D shows the calculated harmonic vibrational spectrum for the ground state of **1**•ACN. In comparing this spectrum with the experimental spectrum recorded in the acetonitrile loss channel (Figure 4.4A), we see that all major vibrational bands are reproduced by the calculation. The agreement between the calculated and measured spectra indicate that the $[RPd(PPh_3)_2]^+$ complexes adopt T-shaped geometries wherein both PPh_3 ligands are oriented orthogonal to the R─Pd bond axis.

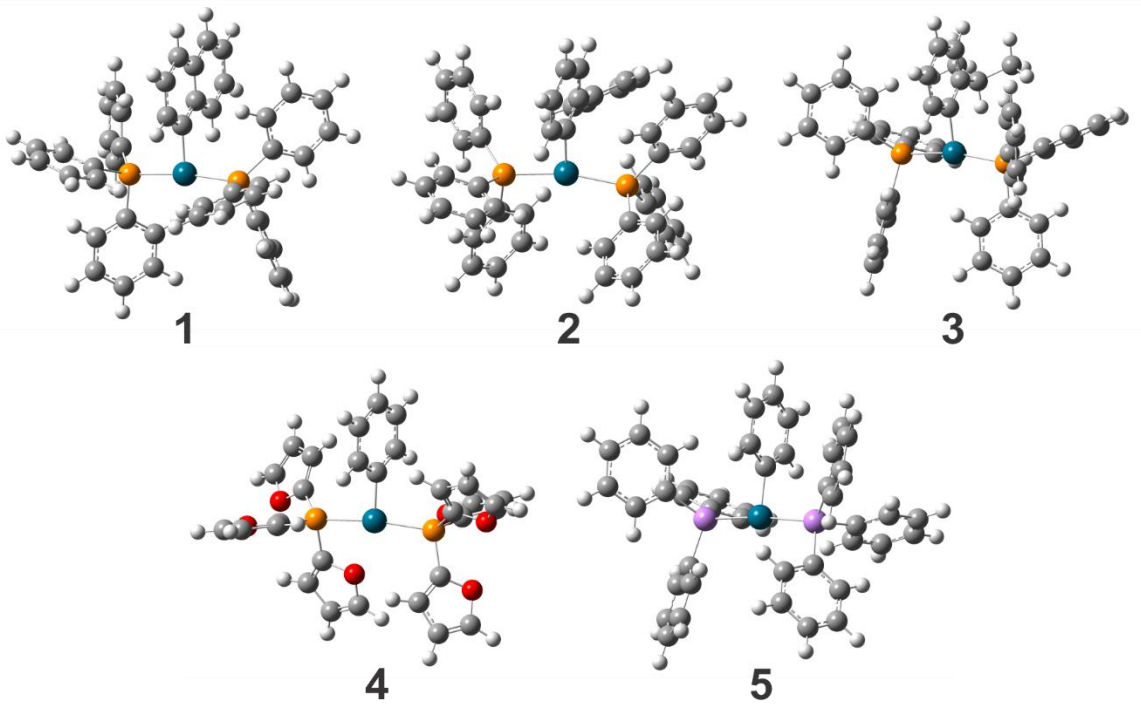

Figure 4.3 DFT B3LYP/Lanl2DZ optimized geometries of compounds 1-5.

4.4.2 Vibrational Spectroscopy

The analysis of the vibrational structure, both calculated and observed by IRMPD, of all compounds is presented. Figure 4.4, Figure 4.5, Figure 4.6, Figure 4.7, and Figure 4.8 display the vibrational data of compounds **1**, **2**, **3**, **4**, and **5**, respectively. Table 4.1 provides the assignments of the fragmentation peaks for the spectra acquired by irradiating each compound without the solvent tag and the ratio of their ion count to the total fragment ion count. Of interest for this study is the fact that fragmentation channels other than loss of acetonitrile are observed by IRMPD. For example, in the case of **1**•ACN, IR excitation also leads to formation of PPh_4^+, Naph─PPh_3^+, and loss of benzene (see Figure 4.18 at the end of this section for proposed reaction mechanisms). These product channels have been observed previously in mass spectrometry studies.[181] It should be noted that this fragmentation behavior is dependent on laser fluence; all fragmentation channels were observed when the full 1.5 W output of the FEL was utilized, but when the IR beam was

attenuated by ≥ 5 dB, loss of ACN was the only observed product channel. Production of PPh_4^+ must, by necessity, proceed via ligand migration whereby a phenyl ring associated with one of the PPh_3 moieties migrates to the opposite PPh_3 moiety via the Pd center. Such a scenario accords with expectations based on ligand scrambling in Pd-catalyzed cross-coupling reactions: should a phosphine phenyl group migrate to the Pd center during the reaction process, followed by migration of the R-group to the phosphorus center to generate a diphenyl R-phosphine, ligand scrambling can occur in the catalytic cycle. The formation of benzene arises from hydrogen abstraction during the ligand migration process. When repeating these experiments with the bare catalyst, **1**, formation of PPh_4^+, Naph─PPh_3^+, and loss of benzene was again observed (in a 58:29:12 branching ratio), but only at high laser power (*i.e.*, there was no fragmentation when attenuating the IR beam).

The key observations in this IRMPD study are shown in Figure 4.4A and B, which plot the IRMPD spectra acquired when monitoring the loss of ACN from **1**•ACN (Figure 4.4A) and the ligand migration product channels for **1**•ACN (Figure 4.4B). Whereas loss of ACN was observed following excitation of each **1**•ACN vibrational transition in the 900 – 2000 cm^{-1} region, product channels associated with ligand migration could only be accessed by exciting three vibrational bands. In other words, excitation of any vibrational band resulted in the absorption and redistribution of enough energy to access the lowest thermodynamic threshold (loss of ACN), but excitation of very specific vibrational transitions is required to access the higher energy ligand migration channels. It is interesting to note that the ligand modes do not all couple to the reactive channel with the same efficiency. For example, the phenyl ring vibration at 1490 cm^{-1} (analogous to the ν_{19A} mode of benzene) is particularly weak (see Figure 4.4B).

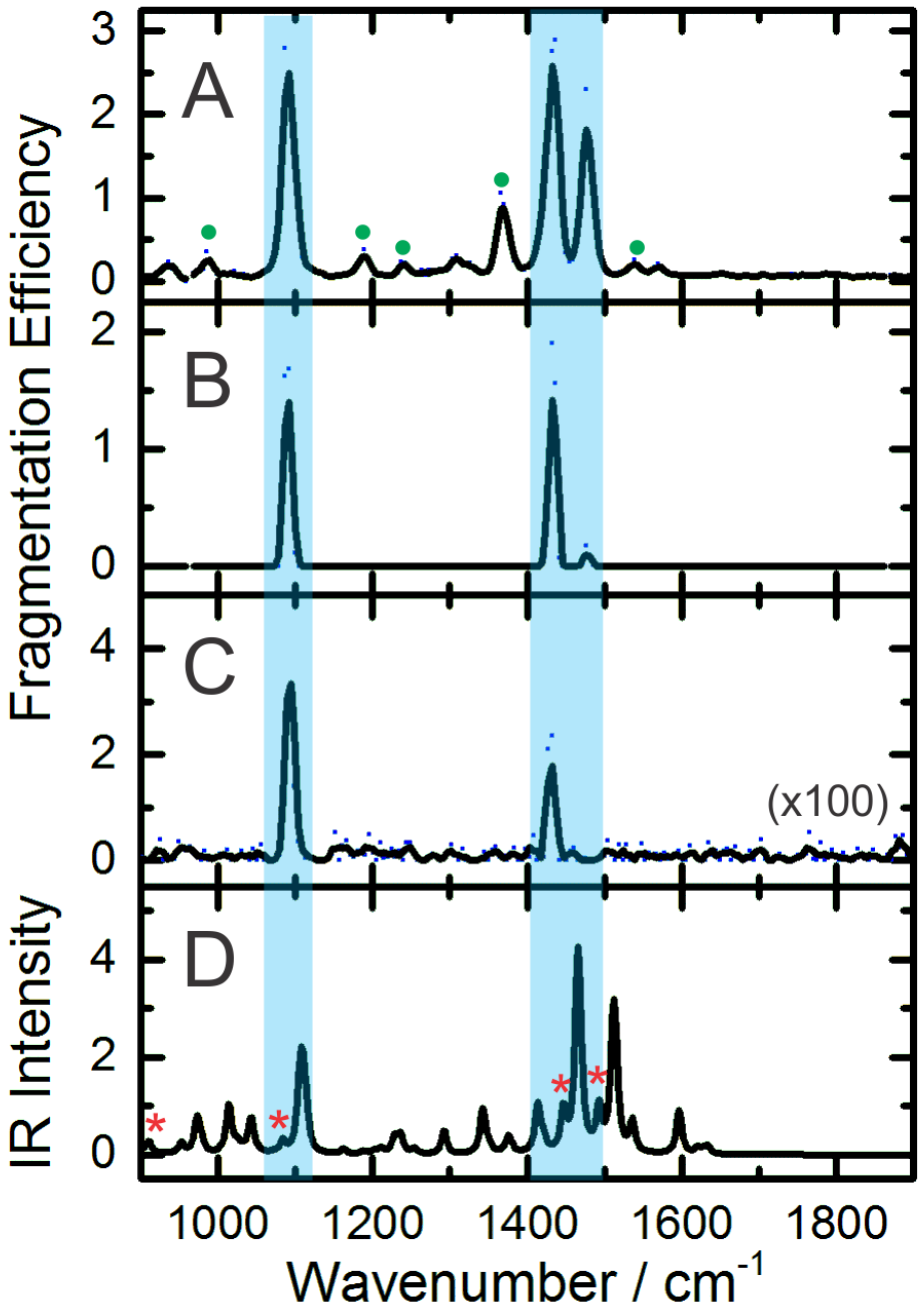

Figure 4.4 IRMPD spectra of compound **1** with (**A**, **B**) and without (**C**) the ACN tag. Measured data are plotted as blue points, and the black traces are 3-pt adjacent averages. (**A**) The IRMPD spectrum of **1**•ACN acquired by monitoring the ACN loss channel, and (**B**) when monitoring the production of (naphthyl)PPh_3^+ and PPh_4^+. (**C**) The IRMPD spectrum of bare compound **1** acquired by monitoring the production of PPh_4^+. (**D**) The calculated harmonic vibrational spectrum of compound **1**•ACN. Solvent fundamental vibrations are indicated with red asterisks, naphthyl group vibrations are indicated with green circles. Calculated IR intensities are in km mol^{-1}.

Table 4.1 Experimentally observed fragmentation assignments for each compound. The branching ratios correspond to the ion count for that particular *m/z* value divided by the total fragment ion count. The spectra that produced these branching ratios are given in the first column.

Compound (Spectrum)	Fragment Mass (amu)	Assignment	Branching Ratio
1 (4.4C)	679	**1**-C_6H_6	0.12
	389	$(C_{10}H_9)PPh_3$	0.59
	339	PPh_4	0.29
2 (4.5C)	521	**2**-PPh_3	0.24
	339	PPh_4	0.76
3 (4.6D)	381	$(C_9H_{11})PPh_3$	0.38
	339	PPh_4	0.62
4 (4.7C)	309	$(Ph)P(Furyl)_3$	0.95
	299	$PFuryl_4$	0.05
5 (4.8B)	383	$AsPh_4$	1.00

When conducting analogous experiments on the bare catalyst **1** (Figure 4.4C), the ligand migration product channels are again accessed via excitation of the two most intense features observed in Figure 4.4B. In comparing the experimental spectra and computational results, we find that the vibrational bands observed in the mode-selective process are associated with phenyl ring vibrations of the triphenyl phosphine ligands. These bands are easily resolved and distinguished from the vibrations of the naphthyl organic residue (highlighted with green dots in Figure 4.4A). This directly parallels the observations of Shaffer *et al.*, who found that non-covalent triflate/bispyridinium complexes generated triflic acid via selective excitation of SO stretching modes.[134] Here, we find that selective excitation of the PPh_3 phenyl ring vibrations in the Pd-catalysts leads to ligand migration and the formation of new covalent C-P and C-H bonds. Note that the ligand migration pathway is not accessed when exciting relatively intense absorptions associated with the ACN tag or R-group. This suggests that excitation of the phenyl moieties results in localized overheating of the triphenylphosphine ligands due to incomplete IVR, allowing the complex to access higher energy ligand migration thresholds rather than the lowest energy

ACN loss channel. It is also worth noting that ACN-tagging enhances fragmentation efficiency by a factor of fifty. This could be related to the very slight change in molecular geometry upon solvent binding; calculations show that the P–Pd–P angle opens from 171.9° to 177.6°. While this geometry change has a negligible effect on vibrational frequencies, it could affect vibrational wavefunction overlap, which would in turn influence the IVR process.

Similar mode-selective ligand scrambling is observed for compounds **2**, **3**, and **4**. Compounds **2** and **3** show the same ligand scrambling products as compound **1** $[(R)PdPPh_3]^+$ and PPh_4^+ where $R_2 = C_{12}H_9$ and $R_3 = C_9H_{11}$) and appear by using radiation of the same wavenumber as compound **1**. Figure 4.5C shows the ligand scrambling products, $[(C_{12}H_9)PdPPh_3]^+$ and PPh_4^+ appear when irradiating compound **2** with ~1090 cm^{-1} and ~1440 cm^{-1}. Figure 4.6D shows the ligand scrambling products, $[(C_9H_{11})PdPPh_3]^+$ and PPh_4^+ appear when irradiating compound **3** also with ~1090 cm^{-1} and ~1440 cm^{-1}. Compound **4** once again shows analogous ligand scrambling products $PhPdPfuryl_3^+$ and $Pfuryl_4^+$ however these ions appear at ~1000 cm^{-1}, ~1130 cm^{-1}, and ~1210 cm^{-1} showing the frequency dependence of this process on the identity of ligand X in the PX_3 groups, see Figure 4.7C.

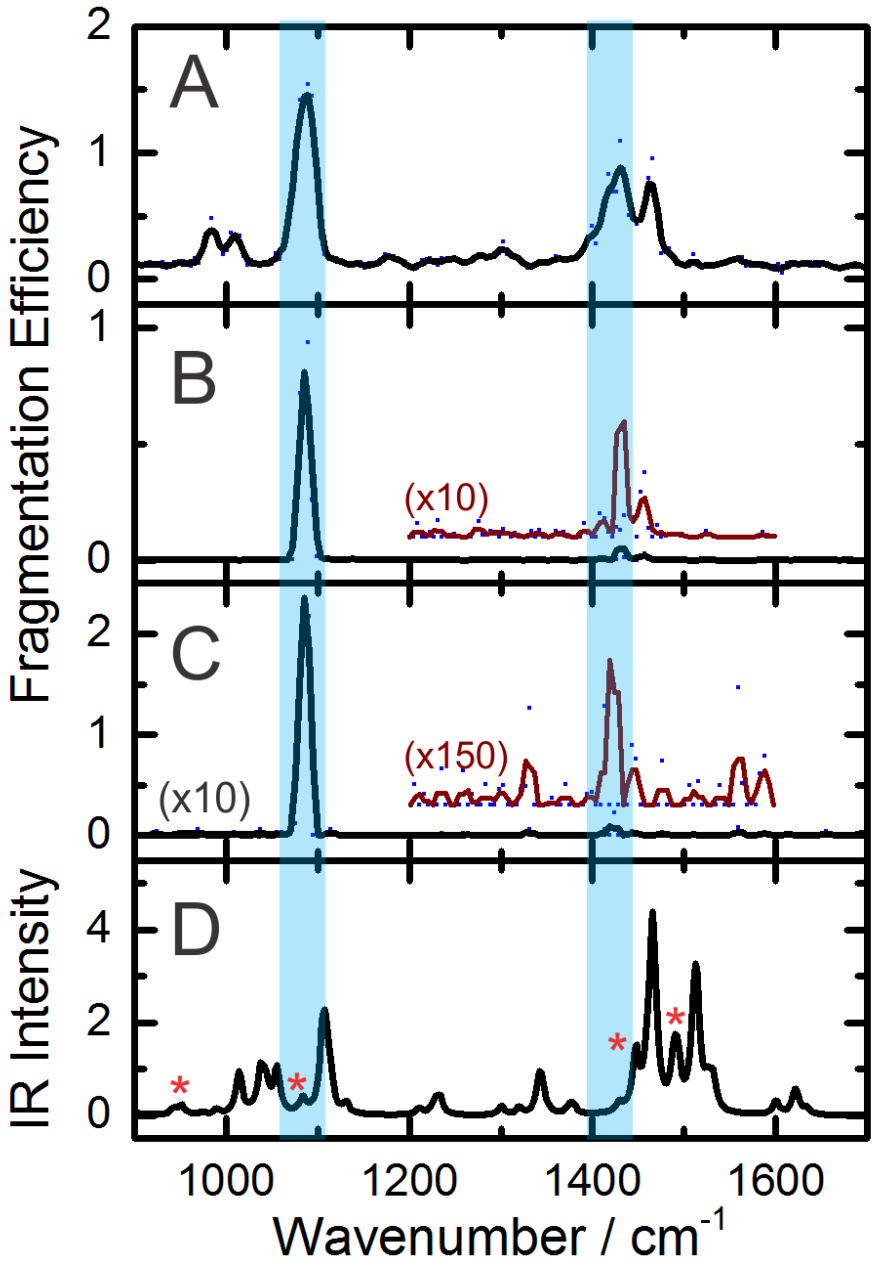

Figure 4.5 IRMPD spectra of compound **2**. Measured data are plotted as blue points, and the black traces are 3-pt adjacent averages. (**A**) The IRMPD spectrum of **2**•ACN acquired by monitoring the ACN loss channel, and (**B**) when monitoring the production of PPh_4^+. (**C**) The IRMPD spectrum of bare compound **2** acquired by monitoring the production of (biphenyl)$PdPPh_3^+$ and PPh_4^+. (**D**) The calculated harmonic vibrational spectrum of compound **2**•ACN. Solvent vibrations are indicated with red asterisks. Calculated IR intensities are in km mol^{-1}.

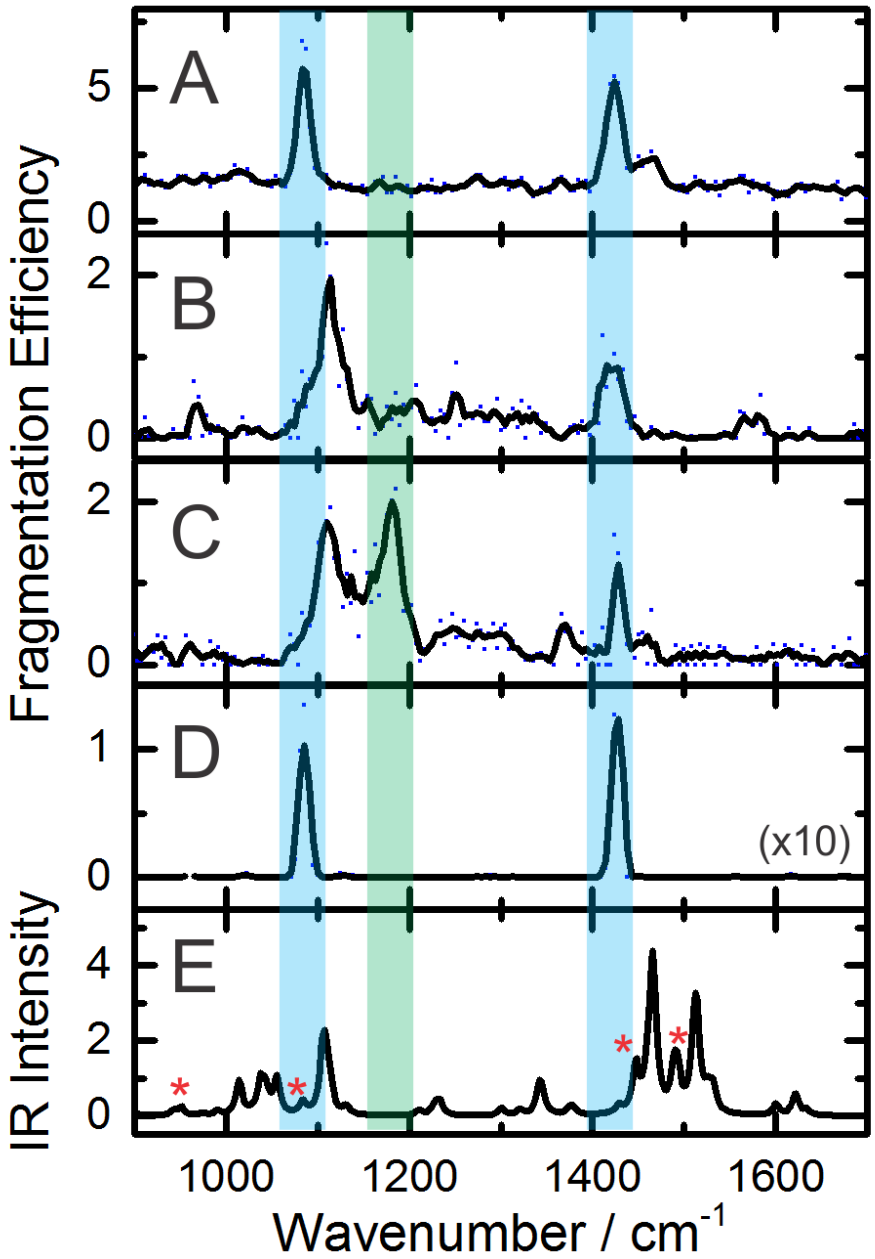

Figure 4.6 IRMPD spectra of compound **3**. Measured data are plotted as blue points, and the black traces are 3-pt adjacent averages. (**A**) The IRMPD spectrum of **3**•ACN acquired by monitoring the ACN loss channel, and (**B**) when monitoring the production of unassigned minor product channel (<1%; m/z 279) and (**C**) the production of unassigned minor product channel (~1%; m/z 579). (**D**) The IRMPD spectrum of bare compound **3** acquired by monitoring the production of (isopropylphenyl)$PdPPh_3^+$ and PPh_4^+. (**E**) The calculated harmonic vibrational spectrum of compound **3**•ACN. Solvent vibrations are indicated with red asterisks. Calculated IR intensities are in km mol^{-1}.

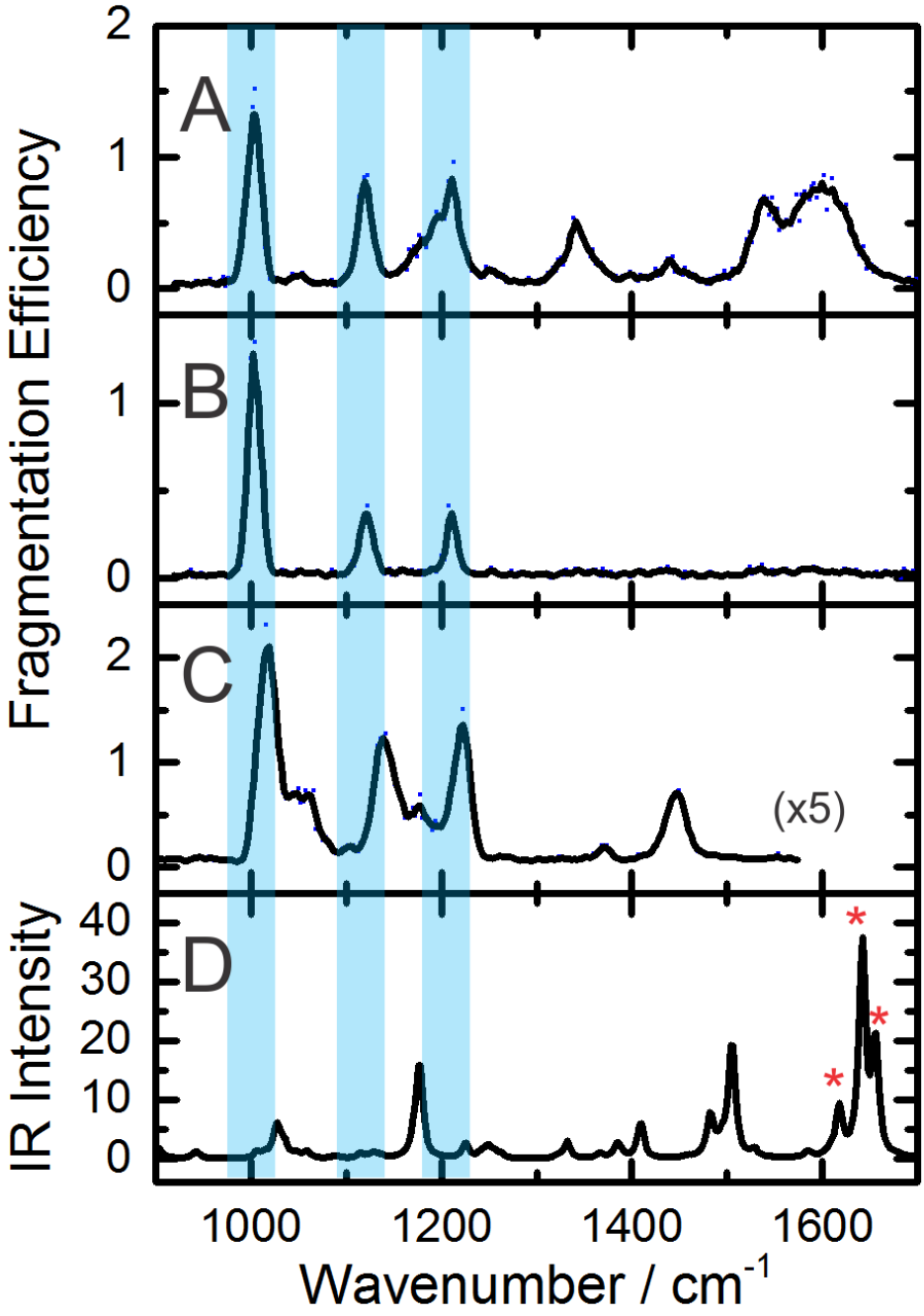

Figure 4.7 IRMPD spectra of compound **4**. Measured data are plotted as blue points, and the black traces are 3-pt adjacent averages. (**A**) The IRMPD spectrum of **4**•dba acquired by monitoring the dba loss channel, and (**B**) when monitoring the production of $PhP(furyl)_3^+$ and $P(furyl)_4^+$. (**C**) The IRMPD spectrum of bare compound **4** acquired by monitoring the production of $PhP(furyl)_3^+$ and $P(furyl)_4^+$. (**D**) The calculated harmonic vibrational spectrum of compound **4**•dba. Solvent vibrations are indicated with red asterisks. Calculated IR intensities are in km mol^{-1}.

Compounds **2**, **3**, and **4** exhibited similar mode-selective behavior to **1.** This suggests that that the observed mode-selective behavior of the Pd-catalysts is invariant with respect to the organic residue. These observations are consistent with mode-selective localized overheating of the phosphine ligand due to hindered IVR arising from poor coupling with Pd-P vibrational modes. To test this hypothesis, the triphenylarsine derivative of compound **4** (*i.e.*, compound **5**) was studied. By substituting arsenic for phosphorus, one shifts the Pd-L vibrational levels to lower energy. Consequently, this chemical substitution should impact coupling between vibrational modes, and therefore IVR efficiency in the catalyst. Indeed, when probing the IRMPD behavior of compound **5**, we see no evidence for mode-selectivity; we only observe loss of ACN from **5**•ACN, and we observe the same IRMPD spectrum (with the exception of the ACN vibrations) for all product channels of the bare catalyst, **5**.

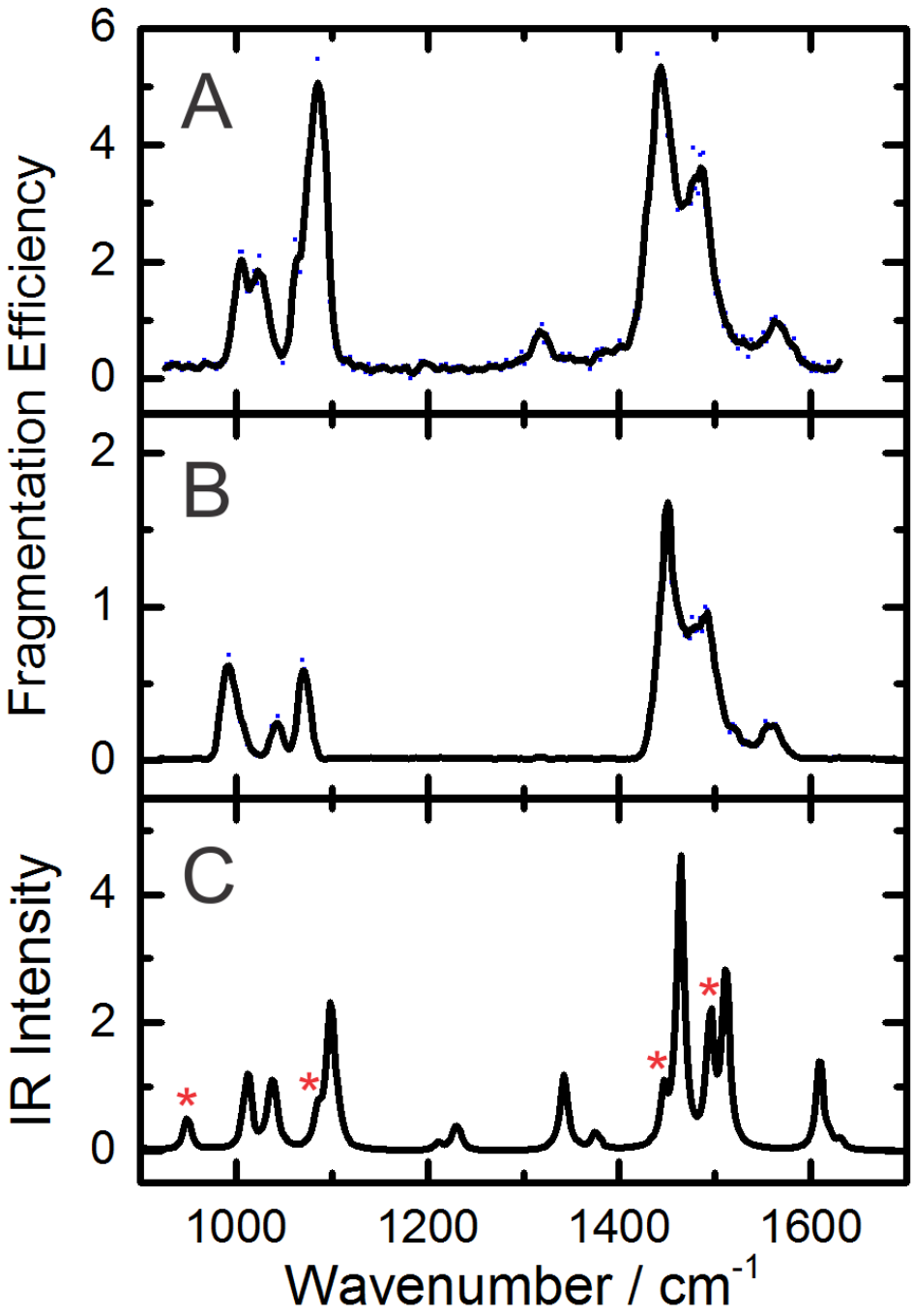

Figure 4.8 IRMPD spectra of compound **5**. Measured data are plotted as blue points, and the black traces are 3-pt adjacent averages. (**A**) The IRMPD spectrum of **5**•ACN acquired by monitoring the ACN loss channel. (**B**) The IRMPD spectrum of bare compound **5** acquired by monitoring the production of $AsPh_4^+$. (**C**) The calculated harmonic vibrational spectrum of compound **5**•ACN. Solvent vibrations are indicated with red asterisks. Calculated IR intensities are in km mol^{-1}.

Figure 4.8 shows the IRMPD spectrum for compound **5**•ACN in panel A and compound **5** when monitoring for the analogous $AsPh_4^+$ seen previously in panel B. The spectrum in panel B completely reproduced the spectrum in panel A indicating that mode-selective ligand scrambling was not observed in compound **5**.

Figure 4.9 provides an energy level diagram showing the observed IRMPD product channels for the bare catalyst **1**. These results are also tabulated in Table 4.2. For IR excitation at *ca*. 1000 cm^{-1}, the energy of eight photons is required to access the lowest energy product channel (production of Naph-PPh_3^+), nine are required to produce PPh_4^+, and the energy of fourteen IR photons are required to produce benzene. Here, it is important to distinguish between multiple photon and multiphoton processes. In a multiple photon process, photons are absorbed sequentially one at a time and photon energy is redistributed via intramolecular vibrational energy redistribution (IVR) prior to the next absorption event.[46,182–184] In contrast, multiphoton processes are non-linear processes wherein absorption of N photons occurs simultaneously at the N-photon level. Consequently, IRMPD is analogous to a thermal process whereby a molecule is "heated" a single photon at a time. It is interesting to note that production of PPh_3 and production of the naphthyl radical, which are both lower in energy than the benzene product channel, and which require simple impulsive fragmentation of the Pd-PPh_3 or Pd-Naph bonds, are not observed. In other words, excitation of the triphenylphosphine ligands results in selective cleavage of a P-Ph bond. This observation also supports the conclusion that the absorbed IR energy is initially localized to the triphenylphosphine ligand and does not immediately access the dissociative coordinate associated with the Pd-P or Pd-Naph bonds. Analogous energy level diagrams and tabulated data of the product and reactant free energy differences for compounds **2 – 5** are presented in Figure

4.10, Figure 4.11, Figure 4.12, and Figure 4.13 and Table 4.3, Table 4.4, Table 4.5, and Table 4.6, respectively.

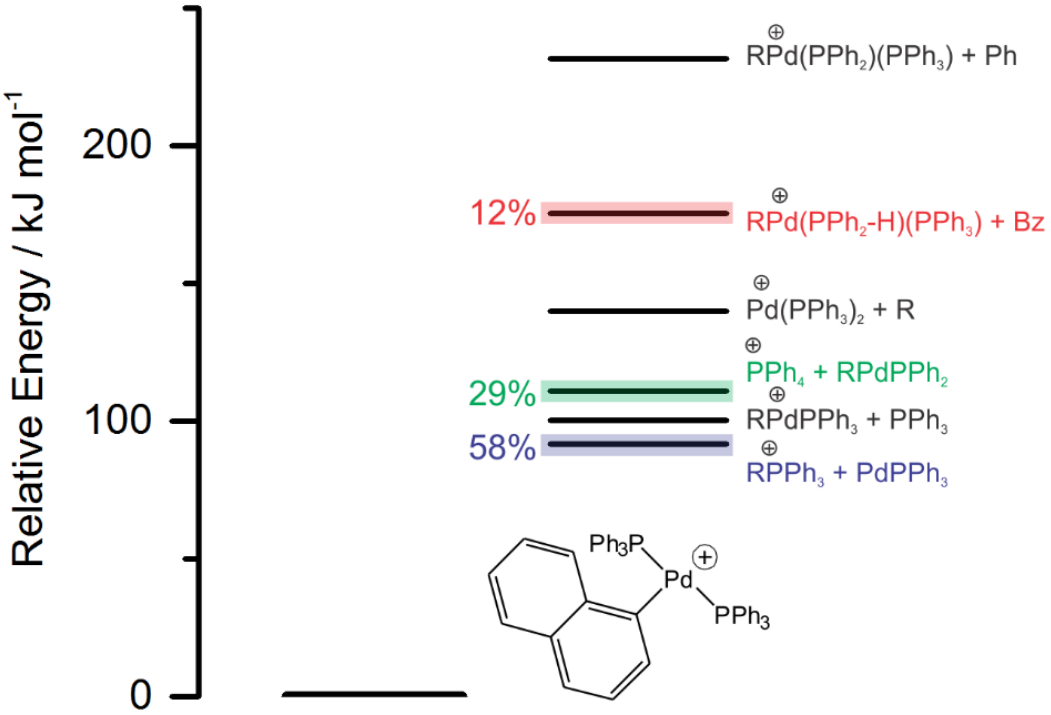

Figure 4.9 The relative standard Gibbs energies of fragmentation product channels for compound **1**. The channels highlighted with color are observed via IRMPD, with branching ratios as indicated. Calculations were conducted at the B3LYP/Lanl2DZ level of theory.

Table 4.2 Energetic barriers for various ligand migration reactions of compound **1**. Barriers were calculated using B3LYP/Lanl2DZ. The given branching ratios correspond to the IRMPD interrogation of the non-solvent cluster compound.

Parent		Cationic Fragment		Neutral Fragment	ΔD_0 /eV (kJ/mol)	ΔG_0 /eV (kJ/mol)	Branching Ratio
1•ACN	→	**1**	+	ACN	1.01 (97.4)	0.48 (46.0)	N/A
1	→	$Pd(PPh_3)_2$	+	$C_{10}H_9$	2.16 (208)	1.45 (140)	0
	→	$(C_{10}H_9)Pd(PPh_3)$	+	PPh_3	1.58 (152)	1.04 (100)	0
	→	$(C_{10}H_9)PPh_3$	+	$PdPPh_3$	1.39 (134)	0.95 (91.7)	0.59
	→	PPh_4	+	$(C_{10}H_9)Pd(PPh_2)$	1.64 (158)	1.15 (111)	0.29
	→	$(C_{10}H_9)Pd(PPh_3)(PPh_2)$	+	C_6H_5	3.03 (292)	2.40 (232)	0
	→	$(C_{10}H_9)Pd(PPh_3)(PPh_2)$-H	+	C_6H_6	2.42 (233)	1.82 (176)	0.12

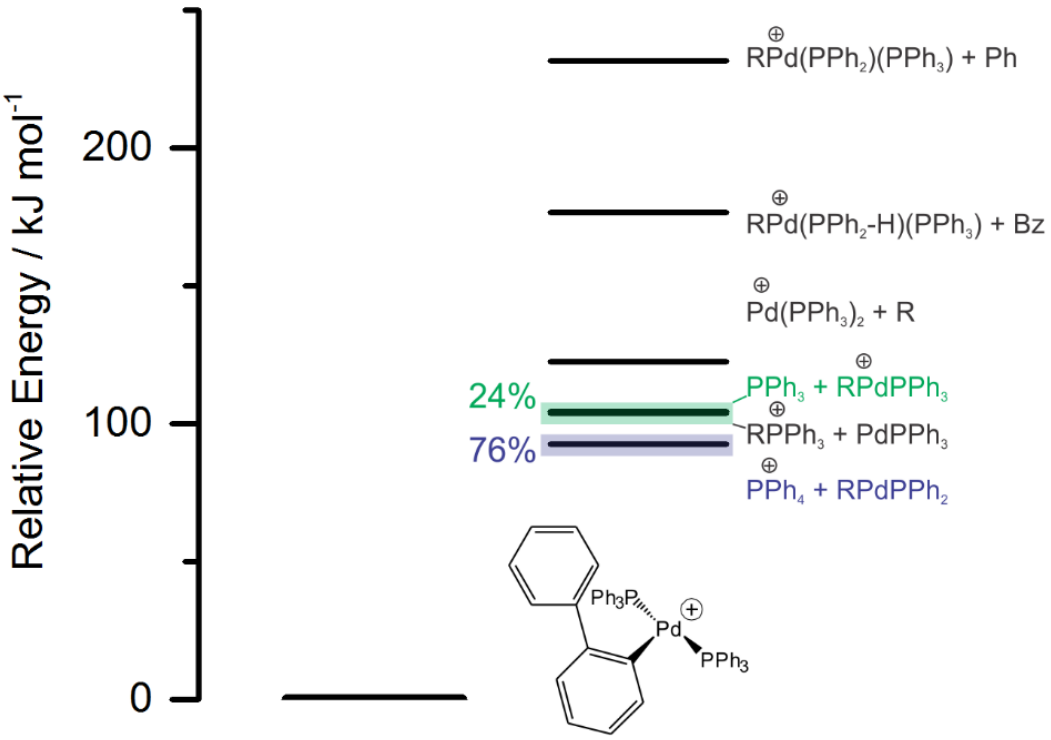

Figure 4.10 The relative standard Gibbs energies of fragmentation product channels for compound **2**. The channels highlighted with color are observed via IRMPD, with branching ratios as indicated. Calculations were conducted at the B3LYP/Lanl2DZ level of theory.

Table 4.3 Energetic barriers for various ligand migration reactions of compound **2**. Barriers were calculated using B3LYP/Lanl2DZ. The given branching ratios correspond to the IRMPD interrogation of the non-solvent cluster compound.

Parent		Cationic Fragment		Neutral Fragment	ΔD_0 /eV (kJ/mol)	ΔG_0 /eV (kJ/mol)	Branching Ratio
2•ACN	→	**2**	+	ACN	0.98 (94.6)	0.45 (43.4)	N/A
	→	$Pd(PPh_3)_2$	+	$C_{12}H_9$	2.08 (201)	1.27 (123)	0
	→	$(C_{12}H_9)Pd(PPh_3)$	+	PPh_3	1.66 (160)	1.08 (104)	0.24
	→	$(C_{12}H_9)PPh_3$	+	$PdPPh_3$	1.60 (154)	1.08 (104)	0
2	→	PPh_4	+	$(C_{12}H_9)Pd(PPh_2)$	1.50 (145)	0.96 (92.6)	0.76
	→	$(C_{12}H_9)Pd(PPh_3)(PPh_2)$	+	C_6H_5	3.03 (292)	2.40 (232)	0
	→	$(C_{12}H_9)Pd(PPh_3)(PPh_2)$-H	+	C_6H_6	2.41 (233)	1.82 (177)	0

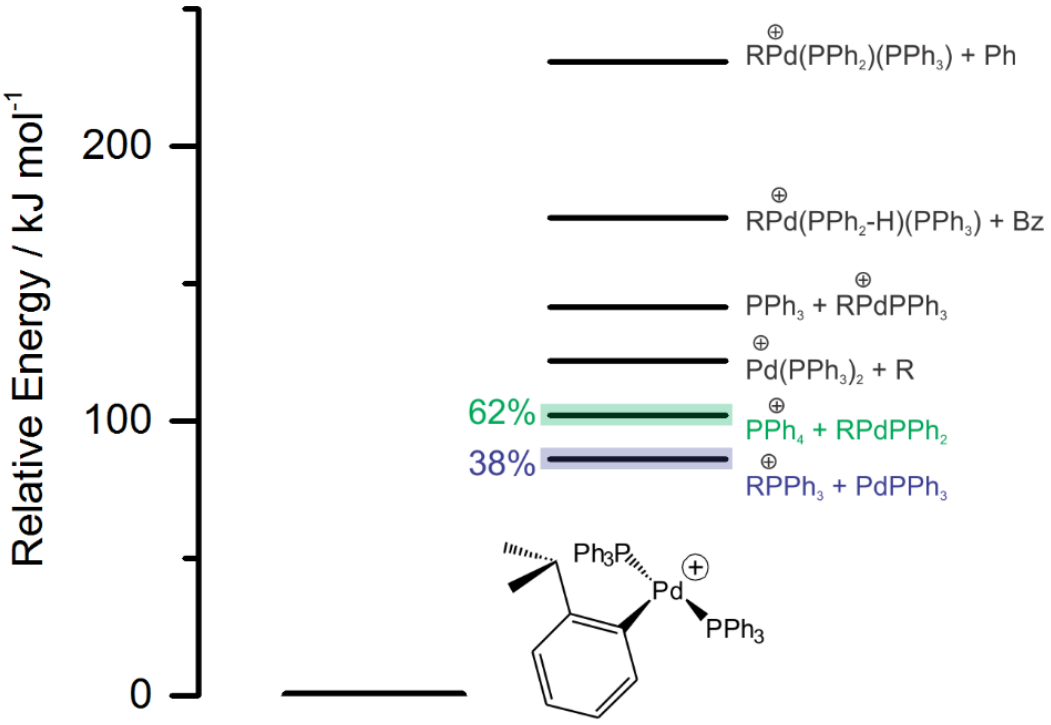

Figure 4.11 The relative standard Gibbs energies of fragmentation product channels for compound **3**. The channels highlighted with color are observed via IRMPD, with branching ratios as indicated. Calculations were conducted at the B3LYP/Lanl2DZ level of theory.

Table 4.4 Energetic barriers for various ligand migration reactions of compound **3**. Barriers were calculated using B3LYP/Lanl2DZ. The given branching ratios correspond to the IRMPD interrogation of the non-solvent cluster compound.

Parent		Cationic Fragment		Neutral Fragment	ΔD_0 /eV (kJ/mol)	ΔG_0 /eV (kJ/mol)	Branching Ratio
3•ACN	→	**3**	+	ACN	0.98 (94.6)	0.55 (53.0)	N/A
	→	$Pd(PPh_3)_2$	+	C_9H_{11}	2.05 (198)	1.26 (122)	0
	→	$(C_9H_{11})Pd(PPh_3)$	+	PPh_3	2.04 (197)	1.47 (142)	0
	→	$(C_9H_{11})PPh_3$	+	$PdPPh_3$	1.38 (133)	0.89 (85.9)	0.38
3	→	PPh_4	+	$(C_9H_{11})Pd(PPh_2)$	1.61 (155)	1.06 (102)	0.62
	→	$(C_9H_{11})Pd(PPh_3)(PPh_2)$	+	C_6H_5	3.00 (289)	2.40 (231)	0
	→	$(C_9H_{11})Pd(PPh_3)(PPh_2)$-H	+	C_6H_6	2.38 (230)	1.81 (175)	0

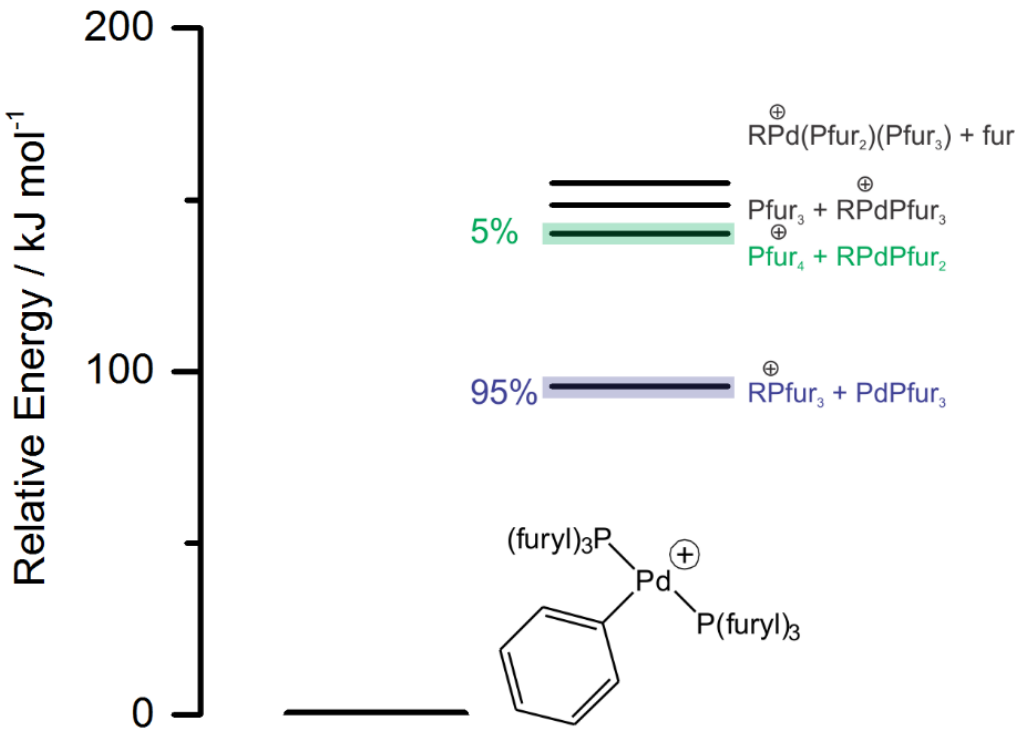

Figure 4.12 The relative standard Gibbs energies of fragmentation product channels for compound **4**. The channels highlighted with color are observed via IRMPD, with branching ratios as indicated. Calculations were conducted at the B3LYP/Lanl2DZ level of theory.

Table 4.5 Energetic barriers for various ligand migration reactions of compound **4**. Barriers were calculated using B3LYP/Lanl2DZ. The given branching ratios correspond to the IRMPD interrogation of the non-solvent cluster compound.

Parent		Cationic Fragment		Neutral Fragment	ΔD_0 /eV (kJ/mol)	ΔG_0 /eV (kJ/mol)	Branching Ratio
4•DBA	→	**4**	+	DBA	1.06 (102)	0.43 (41.5)	N/A
	→	$Pd(Pfuryl_3)_2$	+	C_6H_5	2.30 (222)	1.06 (102)	0
	→	$(C_6H_5)Pd(Pfuryl_3)$	+	$Pfuryl_3$	2.06 (199)	1.54 (149)	0
4	→	$(C_6H_5)Pfuryl_3$	+	$PdPfuryl_3$	1.52 (147)	0.99 (95.5)	0.95
	→	$Pfuryl_4$	+	$(C_6H_5)Pd(Pfuryl_2)$	2.00 (193)	1.45 (140)	0.05
	→	$(C_6H_5)Pd(Pfuryl_3)(Pfuryl_2)$	+	C_4H_3O	3.10 (299)	2.53 (244)	0

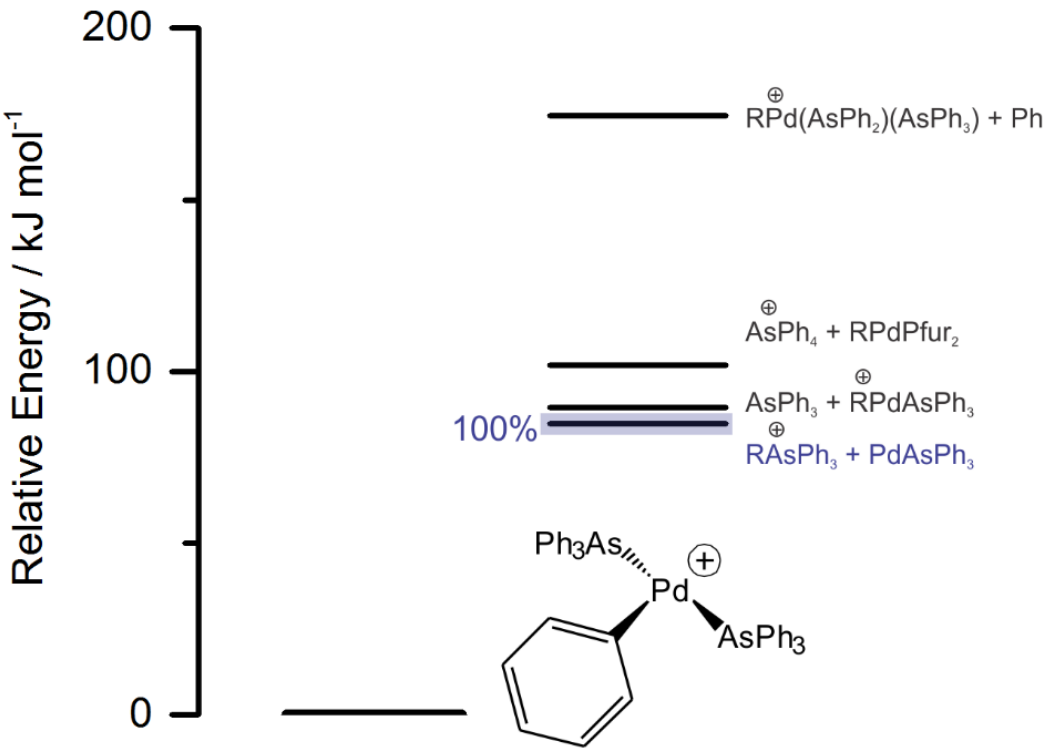

Figure 4.13 The relative standard Gibbs energies of fragmentation product channels for compound **5**. The channels highlighted with color are observed via IRMPD, with branching ratios as indicated. Calculations were conducted at the B3LYP/Lanl2DZ level of theory.

Table 4.6 Energetic barriers for various ligand migration reactions of compound **5**. Barriers were calculated using B3LYP/Lanl2DZ. The given branching ratios correspond to the IRMPD interrogation of the non-solvent cluster compound.

Parent		Cationic Fragment		Neutral Fragment	ΔD_0 /eV (kJ/mol)	ΔG_0 /eV (kJ/mol)	Branching Ratio
5•ACN	→	**5**	+	ACN	1.10 (106)	0.55 (53.1)	N/A
	→	$Pd(AsPh_3)_2$	+	C_6H_5	2.37 (229)	1.81 (175)	0
	→	$(C_6H_5)Pd(AsPh_3)$	+	$AsPh_3$	1.45 (140)	0.93 (89.7)	0
5	→	$AsPh_4$	+	$PdAsPh_3$	1.34 (129)	0.89 (85.9)	1
	→	$AsPh_4$	+	$(C_6H_5)Pd(AsPh_2)$	1.54 (149)	1.05 (101)	0
	→	$(C_6H_5)Pd(AsPh_3)(AsPh_2)$	+	C_6H_5	2.97 (287)	2.38 (230)	0

Some insight into the hindered IVR interpretation of the observed mode-selective behavior is provided by our quantum chemical calculations. Figure 4.14 shows the harmonic vibrational spectra of compounds **1** and **5**. See Figure 4.15, Figure 4.16, and Figure 4.17 for compounds **2**, **3**, and **4**, respectively. While these approximate the actual vibrational structure of the respective

Pd-catalysts, the fact that the computed spectra agree so well with the observed ACN-tagged spectra suggests that the vibrational normal modes are relatively harmonic. The vibrational transitions associated with relatively large amplitude Pd-L motion are indicated with dashed blue lines in Figure 4.14. As expected, these vibrations are lower in energy in compound **5** ($AsPh_3$) than in compound **1** (PPh_3). The PPh_3 phenyl ring vibrational bands that exhibit mode-selective behavior are highlighted in green in Figure 4.14; the position of these bands remains largely unaffected when arsenic is substituted for phosphorus. The IVR lifetimes of room temperature aromatic molecules are typically much less than 1 ns.[185–189] Thus, it is likely that the rate of IVR within the triphenylphosphine ligand is less than 1 ns, which is well within the micropulse spacing of the IR-FEL (see Section 2.2.1). As shown by high-resolution experiments on CH stretching modes of hydrocarbon molecules,[185,189] the IVR rate is not directly determined by the density of states, but rather by the presence of *doorway states* which efficiently couple the vibrational mode of interest to the bath states of the molecule;[184] this defines the statistical limit and irreversibility of vibrational energy redistribution.[46] Thus, to explain the observed non-ergodic behavior of compound **1**, we must consider the doorway states which can potentially couple with the phenyl ring vibrations and thus provide a pathway for IVR throughout the catalyst.[46] The most likely doorway states are combination levels composed of the large amplitude Pd-L modes (highlighted in blue) and the lower energy ligand vibrations in the 700 –1000 cm^{-1} region. These combination levels lie within the 900 – 2000 cm^{-1} region that was probed with IRMPD and are plotted as red dashed lines in Figure 4.14. Note that the combination energy level structure is significantly different for the arsenic derivative compared to the phosphorus derivative. Since these combination levels involve motion of the ligand phenyl (or furyl) rings, it is possible that they might exhibit non-zero coupling with the v = 1 levels in the 900 – 2000 cm^{-1} region due to system anharmonicity.

Consequently, the combined ligand and Pd-L vibration provides an IVR pathway through the metal center. However, given the excellent match between the measured IRMPD spectrum and the calculated harmonic spectrum, one might expect that anharmonic wavefunction overlap between the v = 1 levels and the combination levels is poor. Moreover, the density of the potential doorway states in the 900 – 2000 cm^{-1} region is low – there are significant energy gaps between adjacent combination levels (see Figure 4.14). This has important bearing on IVR efficiency since the coupling between vibrational levels is dependent on wavefunction overlap and on the energy difference between the interacting states: a modest shift in doorway state energy, as would be expected following substitution of As for P, would dramatically impact IVR efficiency.

IR multiphoton electronic excitation, which could also result in the apparent mode-selective behavior, is unlikely to occur in these complexes. In the bare Pd^{2+} cation, the lowest energy electronic excitation is a spin-forbidden $^4F_{7/2} - {}^2D_{3/2}$ transition at 27,097.084 cm^{-1} (324 kJ mol^{-1}).[190] The lowest energy allowed transition from the ground electronic state of Pd^{2+} is the $^2F_{7/2} - {}^2D_{3/2}$ transition at 32,280.538 cm^{-1} (386 kJ mol^{-1}).[190] To reach these electronic states with IR excitation of 1000 cm^{-1} requires *ca*. 30 photons, approximately twice the energy requirement to reach the highest observed fragmentation threshold. Note that these two lowest energy electronic transitions have been observed in UV-Vis spectra of similar Pd coordination complexes,[191,192] which exhibit weak bands near 400 nm and strong absorptions near 350 nm.

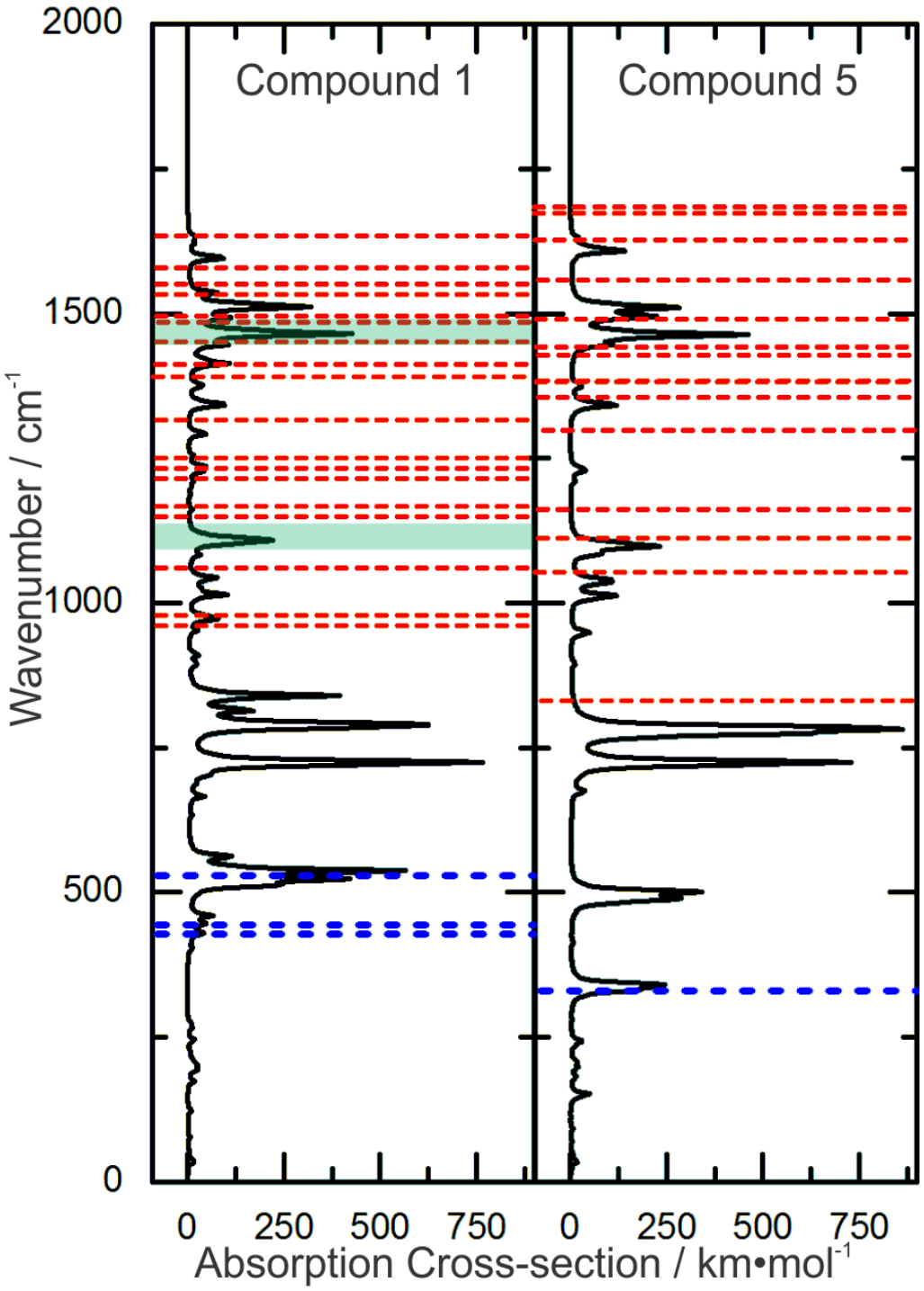

Figure 4.14 The calculated harmonic vibrational spectra of (left) compound **1** and (right) compound **5**. The mode-selective PPh_3 phenyl ring vibrations are highlighted in green. Blue dashed lines indicate the location of large amplitude Pd-L vibrations. Red dashed lines indicate the location of ligand/Pd-L combination levels.

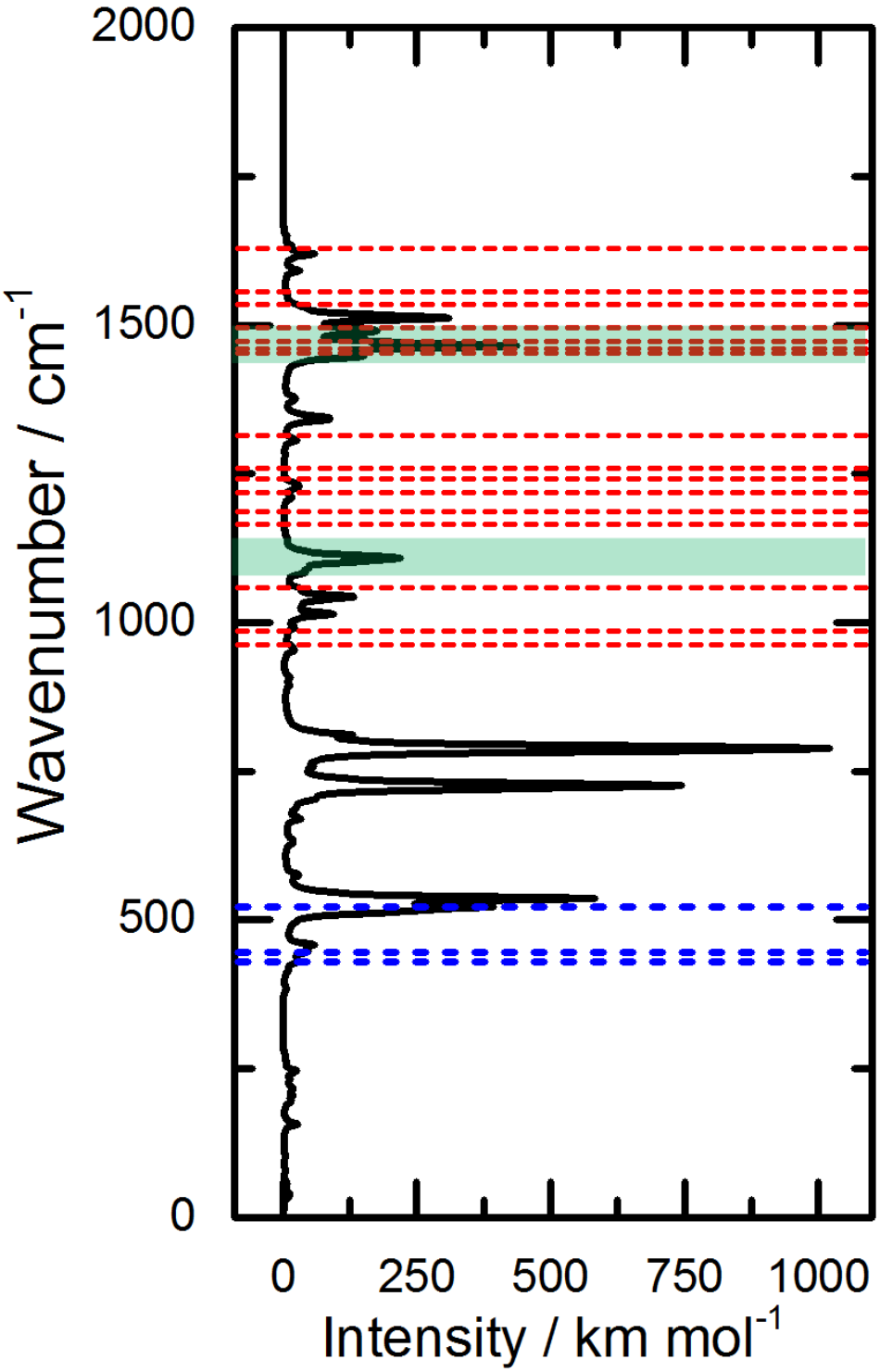

Figure 4.15 The calculated harmonic vibrational spectra of compound **2**. The mode-selective PPh_3 phenyl ring vibrations are highlighted in green. Blue dashed lines indicate the location of large amplitude Pd-L vibrations. Red dashed lines indicate the location of ligand/Pd-L combination levels.

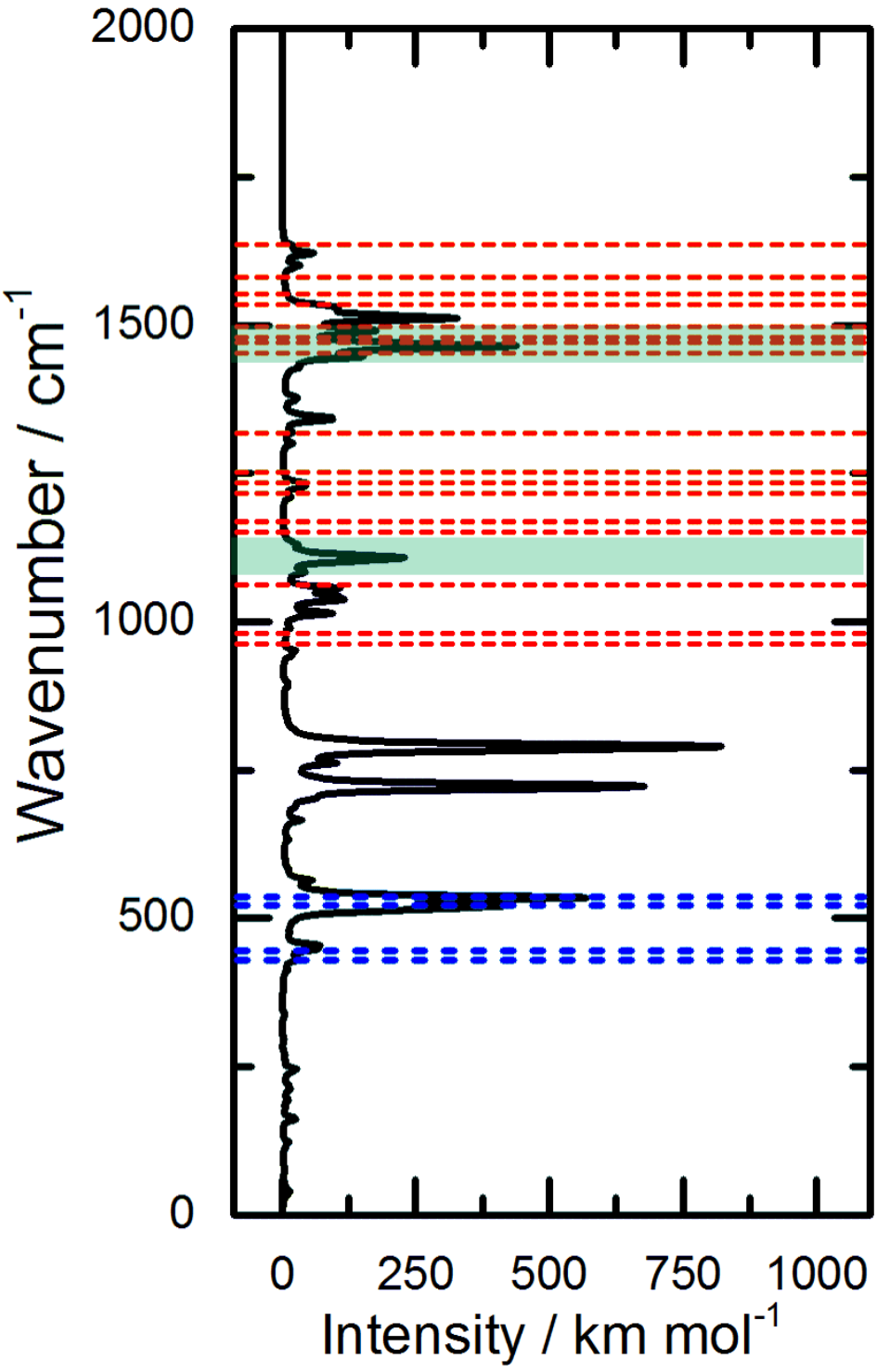

Figure 4.16 The calculated harmonic vibrational spectra of compound **3**. The mode-selective PPh3 phenyl ring vibrations are highlighted in green. Blue dashed lines indicate the location of large amplitude Pd-L vibrations. Red dashed lines indicate the location of ligand/Pd-L combination levels.

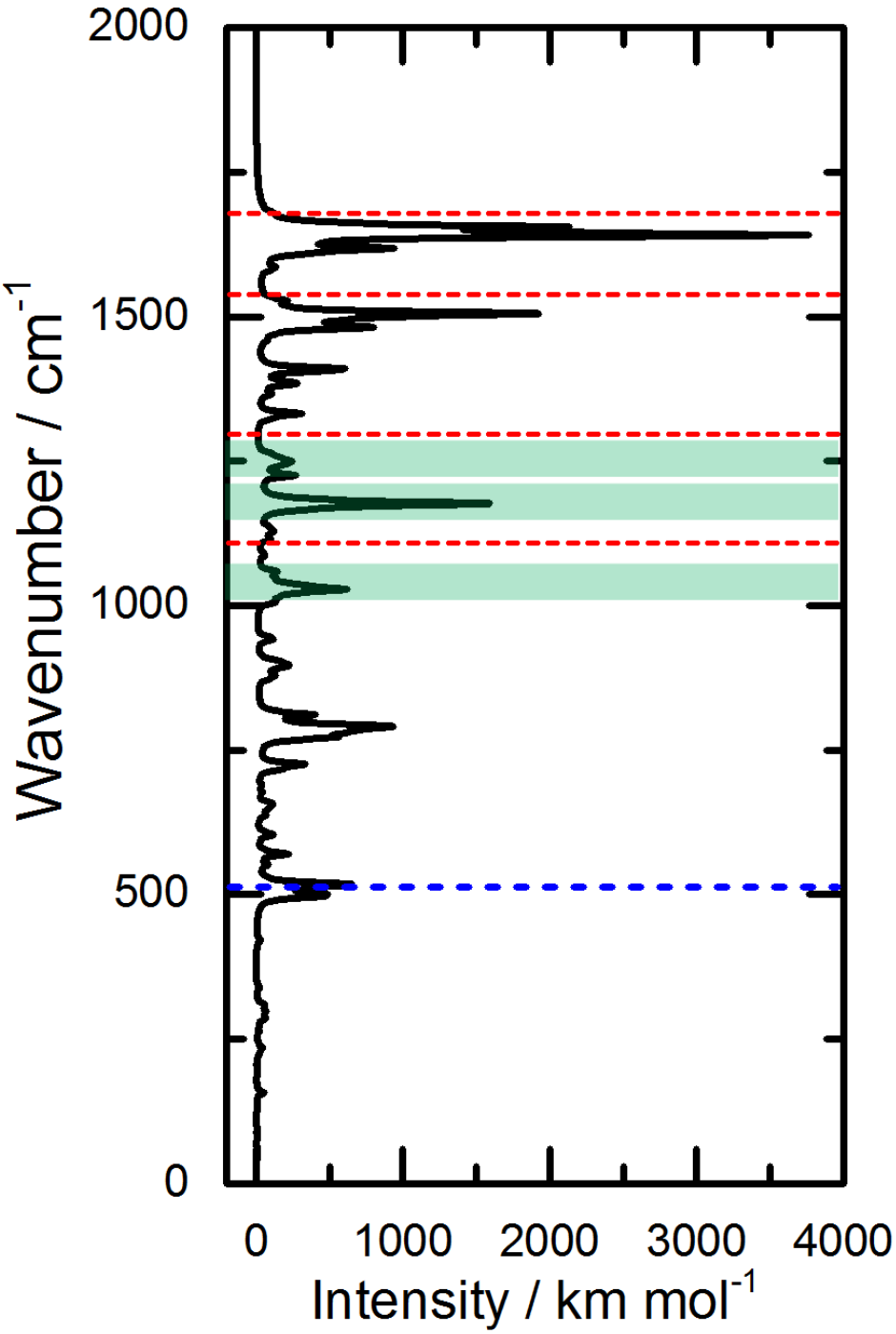

Figure 4.17 The calculated harmonic vibrational spectra of compound **4**. The mode-selective $P(furyl)_3$ furyl ring vibrations are highlighted in green. Blue dashed lines indicate the location of large amplitude Pd-L vibrations. Red dashed lines indicate the location of ligand/Pd-L combination levels.

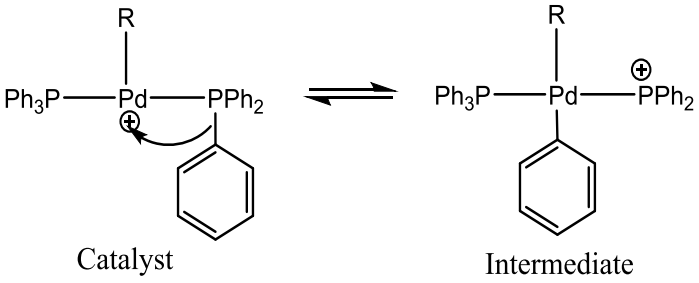

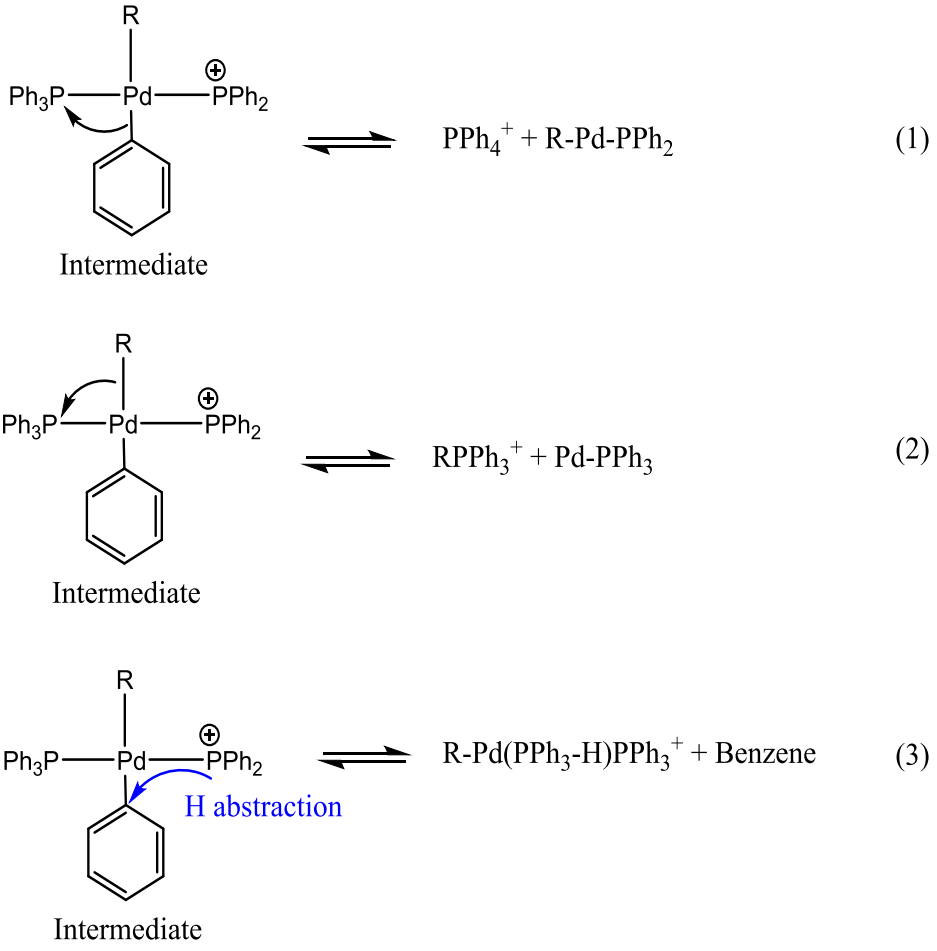

Figure 4.18 Proposed mechanisms for decomposition pathways.

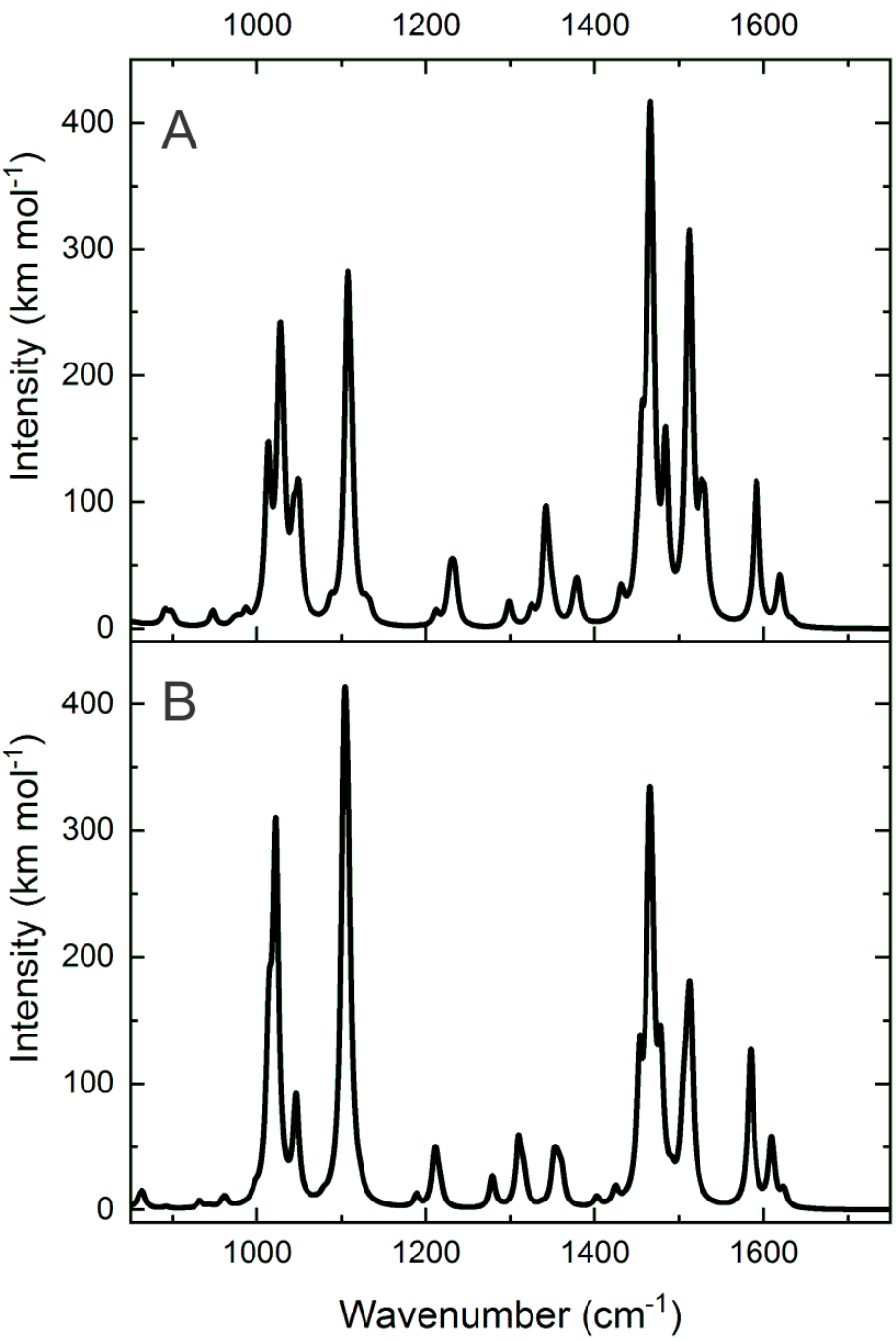

Figure 4.19 Results of frequency calculations of the optimized structure of $Pd(PPh_3)_2$ using (**A**) Lanl2DZ and (**B**) def2-TZVPPD (Pd), 6-311++G(d,p) (C, H, P).

4.5 Conclusions

To conclude, while the focus of this study is on Pd-containing catalysts, it seems likely that these species are archetypal of organometallic systems, since similar IVR bottlenecks are likely to occur at other heavy-metal centers. For example, the quantized vibrational structure of analogous Rh- or Pt-containing complexes should not be too dissimilar to the Pd-complexes discussed here. Thus, it is an interesting open question as to how IVR influences energy disposal within, and chemical reactivity of, this class of compounds. Finally, it is worth underscoring that these are gas phase observations and that the solution phase IVR behavior of these catalysts may be modified by vibrational shifts due to interactions between solvent and solute molecules. Moreover, vibrational excitation can potentially be damped within a few picoseconds by coupling with the solvent bath modes. How this affects the vibrational mode-selective behavior of these catalysts, and therefore the efficacy of employing IR excitation to control solution phase reactions, is currently unknown.

5 Clusters of $B_{12}X_{12}^{2-}$ (X = H, F, Cl)

5.1 Introduction

5.1.1 The All-halogenated or All-hydrogenated Icosahedral Dodecaborate Dianion

Small boron-containing clusters have received an increasing amount of attention owing to the promise of new boron-based nanomaterials. Anionic elemental boron clusters, for example, are known to be planar up to approximately B_{39}, suggesting that cluster deposition may provide a route to extended atomically thin boron sheets (*i.e.*, borophene).[193–202] The transition to three-dimensional anionic structures at B_{40} results in borospherene, the recently (and as of yet only) observed all-boron analogue of Buckminster Fullerene, C_{60}.[203–206] It is hoped that these advances will unlock a new facet of boron chemistry, as occurred with carbon chemistry through the 1990s and 2000s.[207]

The structural evolution from 2D to quasi-planar to 3D boron cluster geometries can be influenced by addition of hydrogen, fluorine, or heavier halides.[208–214] For example, the quasi-planar B_{12} cluster is significantly lower in energy than the icosahedral isomer, however, the icosahedral $B_{12}H_{12}^{2-}$ cluster is the most stable known polyhedral borane.[212,215] In recent years, a great deal of progress has been made in studying a variety of small boron clusters, especially those which incorporate hydrogen or halogen atoms.[2,7,36,41,193,198–201,206,211,216–222] For example, the polyhedral dodecaborate ions, *closo*-$B_{12}X_{12}^{2-}$ (with X being a variety of different substituents), have been found to exhibit outstanding structural and electronic stability, and have consequently found use in a variety of fundamental and applied research fields, including neutron capture cancer therapy, energy storage, self-organization processes, and as weakly coordinating anions for the

stabilization of highly reactive cations used in synthesis and catalysis.[216,220,223–230] However, despite the variety and importance of these applications, a detailed understanding of the interaction of these ions with other molecules and counterions is still lacking. Further insight is required to allow the rational selection of a specific *closo*-borate species for a target property and application (*e.g.*, solubility, reactive ion delivery). To obtain a fundamental understanding of the interaction of dodecaborates with certain molecules or ions, we are investigating these interactions in the gas phase, where they can be studied without the perturbing influence of other molecules. For this purpose, we have investigated the gas phase interaction of different *closo*-dodecaborates with metal cations,[2,36,41] large organic host molecules like cyclodextrine,[219] strong dipoles,[7] tetraalkylammonium ions,[221] and protons.[231]

$B_{12}X_{12}^{2-}$ [X = H, F, Cl] dianions have quadruply-degenerate cage-centered HOMOs of g_u symmetry. The HOMO is mainly localized on the boron cage and separated from complexing counterions by the intervening hydrogen/halogen atoms (note that halogen lone pair electron density increasingly contributes to the HOMO with increasing halogen size).[222] The –2*e* charge is always spherically delocalized, so that the Coulomb-interaction of a cation with the unpolarized anion may be approximated by the center of the sphere, resulting in a relatively large distance over which charge separation occurs (*ca*. 3–4 Å).[36,41] The electrostatic interaction between the boron cage and coordinating cations is therefore relatively weak in comparison with common dianionic species like SO_4^{2-} or HPO_4^{2-}. For this reason, $B_{12}H_{12}^{2-}$ and its halogenated derivatives are often referred to as "weakly coordinating" or "superweak" anions.[216,224–227]

5.1.2 Transition Metal Clusters

Owing to the quasi-spherical shape, large size, and high rotational mobility of $B_{12}H_{12}^{2-}$, metal-$B_{12}H_{12}$ salts have been found to exhibit superionicity, and $Na_2B_{12}H_{12}$ has recently been proposed

as a solid-state Na superionic conductor for use in sodium-based batteries.[223] Research focus is now also being directed towards the fluorinated analogues, $M^{n+}(B_{12}F_{12})_m$, since the strong B–F bonds are expected to be very weakly basic with respect to forming BF•••M^{n+} bridging bonds.[224] As such, the fluorine atoms act to separate the metal centre and the g_u-symmetry HOMO of the boron cage,[232] thereby preventing charge-transfer. Consequently, the reactivity of metal ions in $M^{n+}(B_{12}F_{12})_m$ salts might approach that of the corresponding gas-phase M^{n+} cation, thus creating new opportunities for delivery of highly reactive catalysts in solution or supported catalysts in, *e.g.*, microporous zeolites.[224]

While a good deal is known about the structures and properties of polyboron chlorides, bromides, and iodides,[210] the literature concerning experimental investigation of polyboron fluoride clusters is relatively sparse.[208,210–214] For the most part, structural characterization of small boron halide clusters has been achieved by gas-phase electron diffraction or X-ray crystallography of low-temperature B_nF_m crystals.[211,213,214,224,227] The structures that have been characterized to date typically have a high degree of fluorination and consist of a tightly bound central polyboron unit with BF_2 groups or atomic fluorine bound to the central boron cluster's surface. While there have been some reports of elemental boron clusters complexed with metal atoms,[197,233–236] we are not aware of any publications that investigate the interactions within isolated clusters of M•B_nF_m (where M is a metal ion/atom). Here, we describe a combined computational and experiment study of gas-phase ionic clusters of transition metals (TMs) and the superweak $B_{12}F_{12}^{2-}$ anions.

5.1.3 Triethylammonium Clusters

Here, we study the complexes formed between the $B_{12}X_{12}^{2-}$ [X = F, Cl] dianions and triethylammonium (Et_3NH^+) to increase our knowledge of the role of protic hydrogens in the interaction with halogenated dodecaborates. These results deepen and complement the insights of

a 2015 study that examines the collision-induced dissociation (CID) of $[(CH_3)_3NH{\bullet}B_{12}X_{12}]^-$ [X = F, Cl, Br, I].[231] It was found for these species that the major products of dissociation at low collision energies were $[H{\bullet}B_{12}X_{12}]^-$ [X = F, Cl, Br, I] protic anions that acted as Bronsted acids in the gas phase. The formation of hydronium was demonstrated following complexation of the protonated anions with trace water vapor in the ion trap. These protic anions could also be obtained by fragmentation of *N*-tetraalkylammonium complexed with $B_{12}X_{12}^{2-}$ [X = F, Cl, Br, and I].[221] In this case, fragmentation was shown to result in the loss of neutral trialkylammonia and the production of the alkylated *closo*-dodecaborate anion. CID of the nascent $[B_{12}X_{12} + C_nH_{2n+1}]^-$ (X = Cl, Br, I) species yielded the protic anions by alkene loss. Interestingly, $[B_{12}F_{12} + C_nH_{2n+1}]^-$ exhibited different chemistry, yielding $B_{12}F_{12}^-$ via charge transfer and $B_{12}F_{11}^-$ via fluoride abstraction.[221] While the structure of $[R_3NH{\bullet}B_{12}X_{12}]^-$ [X = F, Cl], which produces the protic anions in a proton transfer process, has been studied previously computationally, direct experimental evidence for this structure is still lacking. To address this, we employ IRMPD to determine the geometric structures of the isolated clusters and to probe fragmentation as a function of laser wavelength and power. Experimental outcomes are interpreted with the aid of DFT calculations.

5.1.4 All-*cis* Hexafluorocyclohexane Clusters

First synthesized by Keddie *et al.* and more recently by Wiesenfeldt *et al.*, all-cis 1,2,3,4,5,6-hexafluorocyclohexane, hereafter **1**, possesses the largest reported dipole (6.2 D) of any aliphatic compound.[6,237] This high polarity leads to considerable dispersive and electrostatic interactions between **1** and ions, both anionic and cationic.[7,8,238] Figure 5.1 presents a DFT optimization of the chair conformation for **1**. A recent publication of $[B_{12}F_{12}]^{2-}$ regarded clustering with **1** where DFT and IRMPD was employed to study $[\mathbf{1}_n{\bullet}B_{12}F_{12}]^{2-}$ (n = 1-4).[7] This study revealed the presence of a

solvation shell completing at $n = 3$ in a trigonal planar geometry around $[B_{12}F_{12}]^{2-}$. Unexpectedly, it was also revealed that the charge-dipole interaction binds **1** to $B_{12}F_{12}^{2-}$ as strongly as it does to Cl^- despite the fact that $B_{12}F_{12}^{2-}$ is viewed as a superweak anion, and an unusual C-H•••F-B hydrogen bond was facilitated.[8]

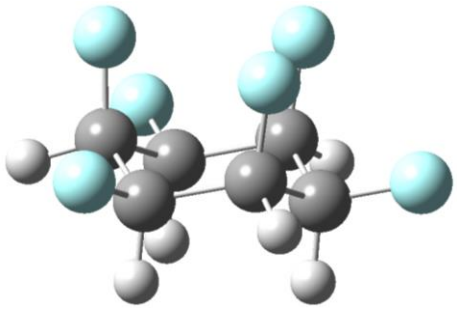

Figure 5.1 Chair conformation of **1**, All-cis 1,2,3,4,5,6-hexafluorocyclohexane. Optimized using DFT at B3LYP/6-311++G(d,p).

Moving forward with the study of $[B_{12}X_{12}]^{2-}$ complexes, we exploit this opportunity to investigate the intriguing and exotic dihydrogen bonding likely to exist when $[B_{12}H_{12}]^{2-}$ clusters with the partial positive face of **1**. An account by Crabtree *et al.* investigated literature and the Cambridge Crystallographic Database (CSD) for characteristics of the unconventional H•••H dihydrogen bond.[239] They rationalized a high melting point of H_3BNH_3 relative to isoelectronic ethane as evidence for strong B-H•••H-N dihydrogen bonding in H_3BNH_3. A search of the CSD for short intermolecular B-H•••H-N distances revealed 26 such interactions in the range of 1.7 – 2.2 Å, which is shorter than twice the van der Waals radius of hydrogen (2.4 Å) suggesting an attractive interaction between the H atoms. In addition to HH bond lengths they also found that the B-H•••(HN) angles in those 26 intermolecular bonds to fall in the range of 95° - 120°, unlike standard hydrogen bonds which are typically linear. Finally, they conducted DFT optimization of the H_3BNH_3 dimer. The geometry closely reproduced the crystallographic geometric parameters and provided an estimate of the interaction energy for a B-H•••H-N dihydrogen bond of 25.5 kJ mol^{-1}.

We have taken advantage of our expertise in joint IRMPD and DFT studies to determine cluster geometry and predict binding energies, ionization energies, bond/cage critical points, donor/acceptor relationships among molecular orbitals, and many other physical properties. Vibrational IRMPD spectra have been collected by use of the CLIO facility in France. Additionally, a new collaboration has been established with researchers at the Pacific Northwest National Labs (PNNL) in Richland, WA, USA who have previously investigated halogenated dodecaboron clusters.[219,222,231] The researchers at PNNL have produced and recorded photoelectron spectra of $[\mathbf{1}_n \bullet B_{12}X_{12}]^{2-}$ (X = H, F; *n* = 1-5) which will allow for evaluation of the electronic structure and assessment of our employed DFT method for predicting vertical detachment energies.

5.2 Experimental Methods

5.2.1 Preparation of Transition Metal $B_{12}F_{12}^{2-}$ Clusters

Clusters of TMs and the $B_{12}F_{12}^{2-}$ dianion were produced via electrospray ionization (ESI) of acetonitrile solutions containing the associated $TM(solv.)_nB_{12}F_{12}$ salt. See reference [224] for a detailed description of the synthetic procedure for making some of these salts. Briefly, a 0.5 mmol solution of commercially available $K_2B_{12}F_{12}$ in acetonitrile was quickly added to 1.0 mmol of anhydrous $AgNO_3$ in acetonitrile and stirred for 20 minutes. The resulting white KNO_3 precipitate was removed and the filtrate was evaporated under vacuum to yield $Ag_2(CH_3CN)_4B_{12}F_{12}$, which was dissolved in dry dichloromethane and the insoluble residue filtered. The filtrate was then evaporated to give a white solid. This silver salt precursor was then used in ion exchange reactions with the TM chloride salts of Co(II), Ni(II), Cu(I), Cu(II), Zn(II), Rh(III), Pd(II), Ag(I), Cd(II), Ir(III), Pt(II), Au(I), Au(III), and Hg(II) in acetonitrile, water, or a mixture of acetonitrile and water. Following removal of the AgCl precipitate, the filtrate was evaporated under vacuum to

yield the associated $TM(CH_3CN)_nB_{12}F_{12}$ or $TM(H_2O)_nB_{12}F_{12}$ salt. The $TM(solv.)_nB_{12}F_{12}$ salts were all isolated as solids with the exception of the $Au(I)(CH_3CN)_nB_{12}F_{12}$ salt, which yielded a viscous yellow liquid. Since ESI of the 5d TM salts yielded only B_nF_m fragments (*i.e.*, metal-cage clusters could not be isolated), they will not be discussed further.

5.2.2 Preparation of Triethylammonium $B_{12}X_{12}^{2-}$ (X = F, Cl) Clusters

$[(CH_2CH_3)_3NH{\bullet}B_{12}X_{12}]^-$ (X = F, Cl) clusters were produced via electrospray ionization of *ca*. 100 μM solutions of triethylammonium chloride (Sigma Aldrich; Oakville, ON) and $K_2B_{12}X_{12}$ (X = F, Cl) in a 50:50 methanol/water mixture. The cluster salts $K_2B_{12}X_{12}$ (X = F, Cl) were prepared according to literature procedures.[240]

5.2.3 Preparation of all-*cis* Hexafluorocyclohexane $B_{12}H_{12}^{2-}$ Clusters

Cluster of $[\mathbf{1}{\bullet}B_{12}H_{12}]^{2-}$ n = 1 – 5 were introduced into the gas phase by electrospray ionization of a solution containing a 1:1 mixture of **1** and $K_2B_{12}H_{12}$ (Sigma Aldrich; Oakville, ON) each with a concentration of 100 μg/mL in a solvent of 50:50 methanol/water. Samples of **1** were supplied by the O'Hagan group at the University of St. Andrews, UK.

5.2.4 Instrumentation

IRMPD experiments were performed at the CLIO FEL facility. All experiments were run with solutions of *ca.* 100 μmol were injected into vacuum at a rate of 100 μL/hour via an ESI source operating in negative ion mode. The resulting gas phase clusters were transferred to a Bruker Esquire 3000+ ion trap mass spectrometer where they were mass-selected, trapped, and irradiated with the tunable infrared output of the FEL.

Photoelectron spectroscopy was conducted by researchers at the Pacific Northwest National Labs (PNNL) in Richland, WA, USA. The instrumentation has been described in detail

elsewhere.[241] Briefly, solution is introduced to the gas phase by electrospray ionization, a species is selected by a quadrupole mass selector, the ions are accumulated and cooled in a Paul type ion trap which is cryogenically controlled (10 K – 350 K), cooled ions travel down a 2 m time-of-flight (TOF) mass spectrometer, then ions are interrogated with a detachment laser and the ejected electrons are collected using a magnetic bottle and analyzed by a 5.2 m TOF electron tube. The TOFs of the photoelectrons are used to construct a kinetic energy spectrum by comparison with the TOFs of ejected electrons from known calibrants. Finally, the binding energy of the electrons is deduced by subtraction of the electron kinetic energy from the photon energy of the detachment laser.

5.3 Computational Methods

To support the experimental work, DFT calculations were conducted using the Gaussian 09 suite for computational chemistry.[16] Owing to the icosahedral symmetry of the $B_{12}X_{12}^{2-}$ cages, relatively few geometric isomers exist, so cluster isomers can be generated manually with confidence. For example, the Cu(I)•$(B_{12}F_{12})^-$ cluster can have the copper cation located at an apex site (*i.e.*, 180° B–F•••Cu bond angle), an edge site (adjacent to two F atoms), or a facial site (adjacent to three F atoms). The same three possible isomers of the charge carrying proton in triethylammonium clusters were used as input geometries with all three converging on the proton adjacent to a facial site as the global minimum. For completeness structures with the charge carrying proton was pointing away from the dianion cage and with one of the ethyl branches is adjacent to the cage were sampled and found to be lie within 15 – 60 kJ mol^{-1} of the global minimum. Electronic structure calculations were undertaken at the B3LYP/6-311++G(d.p) level of theory for 3d TMs, triethylammonium, and **1** as this method has been demonstrated to be reliable for boron cluster calculations.[212,213,242,243] Note, however, that several other DFT methods have

been shown to yield reliable results in computational studies of other boron-containing systems.[197,206] Since the 6-311++G(d,p) basis set is not available for atoms that are larger than Kr, the Def2-TZVPPD/ECP-28 basis set and effective core potential were used for the 4d TMs.[244,245] Owing to the fact that clusters containing 5d TMs could not be isolated and studied via IRMPD (*vide supra*), these species were not studied computationally. Since $[B_{12}X_{12}]^{2-}$ (X = H, F, Cl) are closed shell species, cluster multiplicities were set to those of the free non-cage moiety ground state. Empirical dispersion corrections were applied to energy calculations of triethylammonium and **1** with the intent of focusing the investigation on the weak non-covalent intermolecular interactions.

To improve numerical integration and ensure convergence of the calculations, an integration grid with 225 radial shells and 974 angular points per shell was employed. This resulted in 219,150 integration grid points for each atom.[16] Following geometry optimization, normal mode analyses were completed to ensure that each cluster structure was a local minimum on the potential energy surface. This also served to calculate the harmonic vibrational frequencies of each cluster. Natural bonding orbital (NBO) analysis was then conducted for the ground state of each cluster to calculate the natural partial charge of the metal ion and the interaction energies between the various moieties and $B_{12}X_{12}^{2-}$ cages.[22] Quantum theory of atoms in molecules (QTAIM) analyses were also undertaken to investigate intermolecular interactions.[23,31] On the basis of previous work,[2,7,36,41] we expect that this computational approach is valid for the complexes studied here.

5.4 Transition Metal $B_{12}F_{12}^{2-}$ Clusters

5.4.1 Results and Discussion

Interestingly, TM•$(B_{12}F_{12})_m$ clusters, where m = 1 or 2, could only be isolated for the 3d TMs (Co, Ni, Cu(I), Cu(II), Zn), Ag and Cd. ESI of the Rh, Pd, and 5d TM salts yielded no evidence of TM•$(B_{12}F_{12})_m$ cluster formation, nor production of any other metal-containing cluster or the bare TM cation. This suggests that the Rh, Pd, and 5d TM cations are neutralized during the ESI process. More interesting still, ESI of the Rh, Pd, and 5d TM solutions produced a range of $B_nF_m^-$ clusters from n = 10 – 24 and m = 10 – 24, where in general (n — m) = 0, ±1. The same $B_nF_m^-$ fragments were also produced from the TM = Co, Ni, and Cd solutions, but not from solutions of TM = Cu, Ag, or Zn salts. These observations suggest that, with the exception of TM = Cu, Ag, and Zn, the ESI process drives charge-transfer from the $B_{12}F_{12}^{2-}$ cage to the metal counterion, thereby destabilizing the boron cage and leading to fragmentation/reaction. Here, we will focus on the single cage $[TM•B_{12}F_{12}]^-$ (TM = Cu(I), Ag(I)) and double cage $[TM•(B_{12}F_{12})_2]^{2-}$ (TM = Co(II), Ni(II), Zn(II), Cd(II)) clusters.

Single Cage Clusters Boron occurs naturally in a 4:1 ratio as ^{11}B and ^{10}B, respectively, which produces an isotopic distribution for boron cage clusters that facilitates unambiguous identification by mass spectrometry. With the exception of cobalt, which exists naturally as ^{59}Co in 100% abundance, all other isolable $[TM•B_{12}F_{12}]^-$ and $[TM•(B_{12}F_{12})_2]^{2-}$ clusters exhibit at least two appreciably abundant naturally occurring isotopologues. For the single cage $[TM•B_{12}F_{12}]^-$ species, for example, TM = ^{63}Cu, ^{65}Cu, ^{107}Ag or ^{109}Ag.

Figure 5.2 shows the IRMPD spectrum recorded for $[Cu(I)•B_{12}F_{12}]^-$ in the 1000 - 1450 cm^{-1} region when gating on the mass channel associated with production of $B_{12}F_{12}^-$.

The intense band at *ca*. 1225 cm^{-1} is associated with excitation of the triply degenerate T_{1u} vibrational normal mode of the $B_{12}F_{12}$ cage. Owing to the fact that the Cu(I) cation occupies a facial site on the $B_{12}F_{12}$ icosahedron (see Figure 5.3), the degeneracy of the T_{1u} mode is lifted and the band is split into a component associated with vibration along the Cu(I)–$B_{12}F_{12}$ axis and a doubly degenerate component associated with off-axis cage vibration. This is most easily seen experimentally in the m/z = 360 amu mass channel, which corresponds to production of $^{11}B_{12}{}^{19}F_{12}$ by IRMPD of $[^{63}Cu(I)\bullet{}^{11}B_{12}{}^{19}F_{12}]^-$ and $[^{65}Cu(I)\bullet{}^{11}B_{12}{}^{19}F_{12}]^-$. The apparent broadening of the lower wavenumber (*ca.* 1207 cm^{-1}) component is due to the vibrational isotope effect associated with the Cu(I)–$B_{12}F_{12}$ axial motion of the two Cu(I) isotopologues. In comparing with the calculated harmonic vibrational spectrum shown in Figure 5.2F, we see a wavenumber shift that corresponds to a scaling factor of 0.9798, which is in good general agreement with commonly used scaling factors found in the literature.[246] Since the application of a scaling factor was not needed for spectral assignment, we report unscaled computed frequencies here.

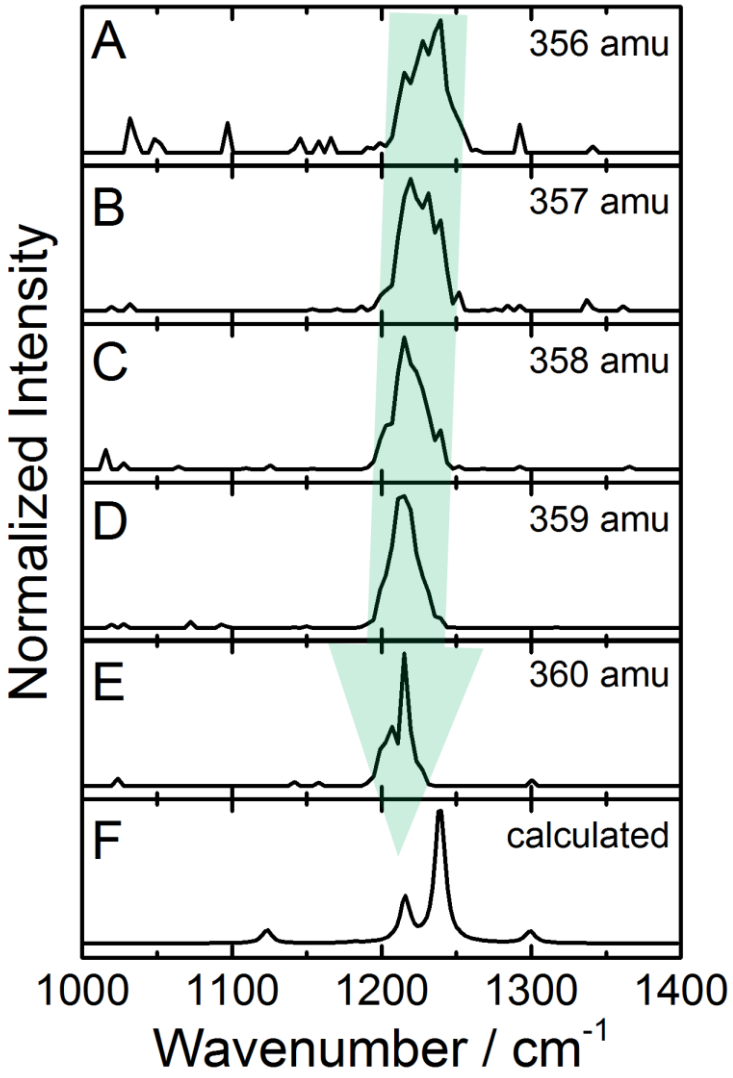

Figure 5.2 IRMPD spectrum of $[Cu(I)•B_{12}F_{12}]^-$ as observed in the (A) m/z = 356 amu, (B) m/z = 357 amu, (C) m/z = 358 amu, (D) m/z = 359 amu, and (E) m/z = 360 amu mass channels corresponding to production of the five most abundant isotopologues of $B_{12}F_{12}^{2-}$. (F) Calculated harmonic vibrational spectrum of $[Cu(I)•B_{12}F_{12}]^-$. Calculations were conducted at the B3LYP/6-311++G(d,p) level of theory.

Product channels of m/z = 359 amu and lighter exhibit an intense broad peak in the 1200 – 1250 cm^{-1} region owing to the fact that each isotopologue has several associated isotopomers (*i.e.*, isotopic isomers) contributing to the observed spectrum. For example, the m/z = 359 amu product, which corresponds to production of $^{10}B^{11}B_{11}{}^{19}F_{12}$, could have the ^{10}B atom located at one of four different symmetry sites of the boron cage in the parent $[Cu(I)•^{10}B^{11}B_{11}{}^{19}F_{12}]^-$ cluster. As a result, the spectrum acquired in the m/z = 359 amu channel is

composed of eight isotopomeric variants of $[Cu(I)\bullet B_{12}F_{12}]^-$, each of which exhibits a slightly different vibrational spectrum owing to the vibrational isotope effect. In comparing the spectra recorded for the m/z = 356 – 360 amu product channels, which correspond to formation of $^{10}B_m{}^{11}B_{12-m}{}^{19}F_{12}$ (m = 4–0), the expected trend for the vibrational isotope effect is apparent.

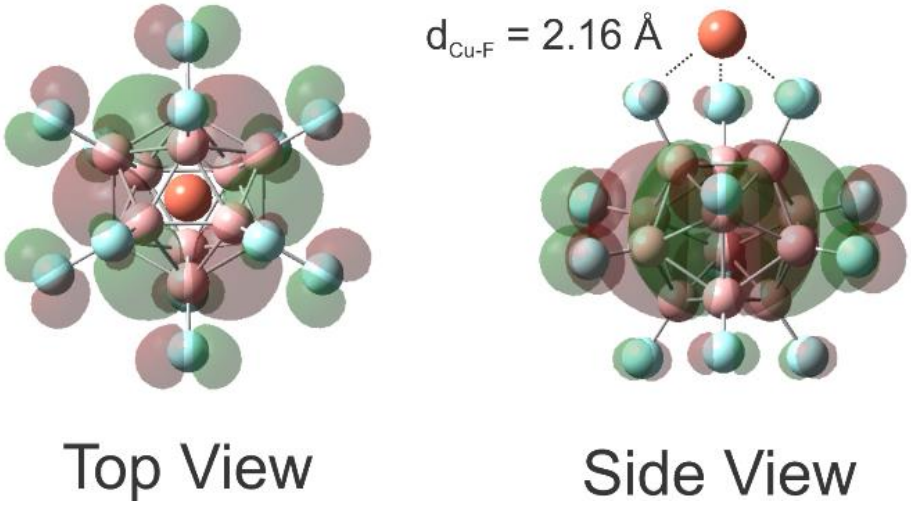

Figure 5.3 The geometry optimized structure of $[Cu(I)\bullet B_{12}F_{12}]^-$ shown (left) along the $Cu(I)–B_{12}F_{12}$ axis and (right) perpendicular to the $Cu(I)–B_{12}F_{12}$ axis. Also shown in the quadruply degenerate HOMO. Calculations were conducted at the B3LYP/6-311++G(d,p) level of theory.

Formally, $[TM(I)\bullet B_{12}F_{12}]^-$ (TM = Cu, Ag) clusters exist as $TM^+\bullet B_{12}F_{12}{}^{2-}$. Indeed, a major source of interest in these superweak ion systems is the view that the weak $BF\bullet\bullet\bullet M^{n+}$ interactions should lead to reactive metal ions that behave as pseudo gas-phase species in the solid or solution phases. It is therefore perhaps surprising that formation of $TM^0 + B_{12}F_{12}{}^-$ was the only observed product channel for IRMPD of $[Cu(I)\bullet B_{12}F_{12}]^-$ and $[Ag(I)\bullet B_{12}F_{12}]^-$. This, of course, implies that charge-transfer from the $B_{12}F_{12}{}^{2-}$ cage g_u HOMO to the valence *s* atomic orbital of the metal cation occurs during the dissociation process. The observed charge-transfer process can be rationalized if we draw analogy with the textbook example of NaCl, which exists as $Na^{\delta+}\bullet Cl^{\delta-}$ in its ground electronic state, but which dissociates to form neutral products via its lowest thermodynamic threshold in the gas-phase. This, of course, is due to the imbalance between the electron affinity

of Cl (3.51 eV) and the ionization energy of Na (5.14 eV).[247] Given the ionization energies of Cu (7.73 eV) and Ag (7.58 eV), and the expected electron affinity of $B_{12}F_{12}^-$ (1.6 eV), observation of charge-transfer during IRMPD of $[TM(I)•B_{12}F_{12}]^-$ (TM = Cu, Ag) is not unreasonable.[247] Here, however, charge-transfer must occur over a distance of *ca*. 3.5 Å and via the intervening fluorine layer that separates the metal cation and the quadruply degenerate HOMO of the anionic boron cage (see Figure 5.3).

To investigate the charge-transfer properties of the clusters, NBO calculations were conducted for the geometrically optimized electronic ground states. Subsequent population analysis shows that *ca*. 0.1*e* of charge density is transferred from $B_{12}F_{12}^{2-}$ to the Ag(I) cation in $[Ag(I)•B_{12}F_{12}]^-$. For the ground electronic state of $[Cu(I)•B_{12}F_{12}]^-$, a charge transfer of *ca*. 0.5*e* to the metal cation is calculated. This supports the chemically intuitive view that the metal centers retain a high partial positive charge for these ground state clusters. Second order perturbation theory analysis of the Fock matrix in the NBO basis facilitates calculation of the dominant interactions associated with the transfer of charge density to the metal cation.[42,76] These are summarized for $[Cu(I)•B_{12}F_{12}]^-$ and $[Ag(I)•B_{12}F_{12}]^-$ in Table 5.1. Charge-transfer and incipient chemical bond formation between Ag^+ and $B_{12}F_{12}^{2-}$ accounts for *ca*. 411.7 kJ mol^{-1} worth of stabilization energy in $[Ag(I)•B_{12}F_{12}]^-$. The dominant interactions are charge-transfer from the boron cage and the F atoms adjacent to the Ag(I) cation, and back donation from Ag(I) to the boron cage. A minor degree of back donation from Ag(I) to the adjacent F atoms was also calculated. These four interactions were found in all of the $TM•(B_{12}F_{12})_n$ clusters studied. In the case of $[Cu(I)•B_{12}F_{12}]^-$, charge-transfer interactions account for ca. 824 kJ mol^{-1} worth of stabilization energy. More than half of the interaction energy (487.4 kJ mol^{-1}) is provided by charge-transfer from the MOs associated with the B_{12} cage. It should be noted that, since different basis sets were

used for the Cu(I) and Ag(I), there will be some small error introduced when drawing comparison between charge-transfer properties in $[Cu(I)\bullet B_{12}F_{12}]^-$ and $[Ag(I)\bullet B_{12}F_{12}]^-$. Nevertheless, we are confident that these calculations capture a qualitative view of the specific charge-transfer interactions in these clusters.

Table 5.1 Natural partial charges and interaction energies calculated for charge-transfer interactions in the ground electronic states of $[Cu(I)\bullet B_{12}F_{12}]^-$ and $[Ag(I)\bullet B_{12}F_{12}]^-$. Calculations were conducted at the B3LYP/6-311++G(d,p) level of theory. A Def2-TZVPPD/ECP-28 basis set and effective core potential combination was employed for Ag.

Cluster	Metal Partial Charge	Interaction Energy (kJ/mol)	
$[Cu(I)\bullet B_{12}F_{12}]^-$	+ 0.4 *e*	Cage → Cu^+	487.4
		F → Cu^+	243.1
		Cage ← Cu^+	57.7
		F ← Cu^+	37.7
$[Ag(I)\bullet B_{12}F_{12}]^-$	+ 0.9 *e*	Cage → Ag^+	103.3
		F → Ag^+	150.2
		Cage ← Ag^+	135.1
		F ← Ag^+	23.0

Figure 5.4 shows the calculated change in standard Gibbs energy for production of $B_{12}F_{12}^{2-}$ and $B_{12}F_{12}^-$ following dissociation of the various $TM\bullet(B_{12}F_{12})_n$ clusters studied. Numerical values are tabulated in Table 5.2. For the two coinage metal clusters, the dissociation processes are:

$$[TM\bullet B_{12}F_{12}]^- \rightarrow TM^+ + B_{12}F_{12}^{2-} \qquad \text{Rxn. 1}$$

$$[TM\bullet B_{12}F_{12}]^- \rightarrow TM^0 + B_{12}F_{12}^- \qquad \text{Rxn. 2}$$

Where TM = Cu or Ag. In both cases, dissociation via the charge-transfer threshold (Rxn. 2) is favoured by *ca*. 627.6 kJ mol^{-1} over formation of $TM^+ + B_{12}F_{12}^{2-}$, which is consistent with experimental observations. The energy difference between these thresholds is, of course, equal to IE(TM) – EA($B_{12}F_{12}^{2-}$), where IE(TM) is the ionization energy of the transition metal and

$EA(B_{12}F_{12}^{2-})$ is the electron affinity of $B_{12}F_{12}^{2-}$. Importantly, the charge-transfer dissociation threshold is the lowest thermodynamic dissociation threshold for $TM•(B_{12}F_{12})_n$ clusters. The highest calculated charge-transfer dissociation threshold amongst the species studied here is $\Delta G° = 160$ kJ mol^{-1} for $[Cu(I)•B_{12}F_{12}]^-$, with most of the other cluster species exhibiting significantly smaller (or negative) values of $\Delta G°$ for dissociation. Thus, accessing the charge-transfer dissociation threshold via IRMPD at *ca*. 1225 cm^{-1} requires at most 11 photons (usually many fewer).

Double Cage Clusters $TM•(B_{12}F_{12})_n$ clusters for TM = Co(II), Ni(II), Zn(II), and Cd(II) were observed as $[TM•(B_{12}F_{12})_2]^{2-}$. As was mentioned above, the Rh(III) and Pd(II) analogues, which were stable in the solid and solution phases, were not isolable as gas-phase clusters. Nevertheless, DFT calculations were conducted for $[Rh(III)•(B_{12}F_{12})_n]^-$ and $[Pd(II)•(B_{12}F_{12})_n]^{2-}$ for comparison with the observed 3d TM analogues. Calculations show that all but one of the double cage clusters exhibit a geometric structure wherein the metal atom is sandwiched between eclipsed trigonal faces of the two $B_{12}F_{12}$ cages (see Figure 5.5). Interestingly, $[Pd(II)•(B_{12}F_{12})_n]^{2-}$ adopts a geometry wherein the central metal atom is bound between edge sites of the two $B_{12}F_{12}$ cages. This might not be unexpected given the propensity of palladium to form square planar complexes. This geometry is, however, suggestive of relatively strong chemical interactions in addition to the expected electrostatic bonding.

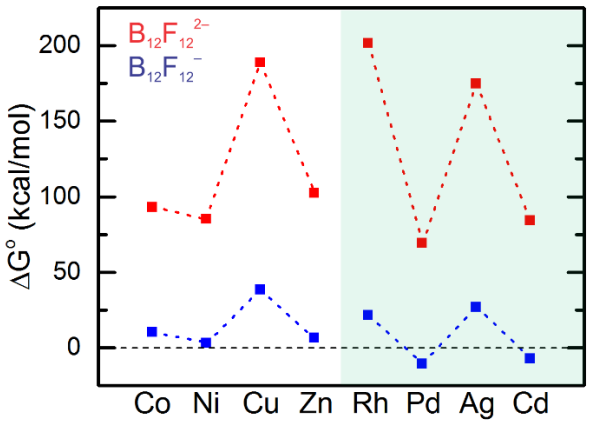

Figure 5.4 Calculated ΔG° for unimolecular dissociation of $[TM•B_{12}F_{12}]^-$ (TM = Cu(I), Ag(I)) and $[TM•(B_{12}F_{12})_2]^{2-}$ (TM = Co(II), Ni(II), Zn(II), Rh(III), Pd(II), Cd(II)) to yield (red) $B_{12}F_{12}^{2-}$ and (blue) $B_{12}F_{12}^-$. Calculations were conducted at the B3LYP/6-311++G(d,p) level of theory for 3d metals. The Def2-TZVPPD/ECP-28 basis set and effective core potential was employed for 4d metals. (1 kcal mol^{-1} = 4.184 kJ mol^{-1})

Table 5.2 Calculated ΔG° for unimolecular dissociation of $[TM•B_{12}F_{12}]^-$ (TM = Cu(I), Ag(I)) and $[TM•(B_{12}F_{12})_2]^{2-}$ (TM = Co(II), Ni(II), Zn(II), Rh(III), Pd(II), Cd(II)) to yield $B_{12}F_{12}^{2-}$ and $B_{12}F_{12}^-$. Calculations were conducted at the B3LYP/6-311++G(d,p) level of theory for 3d metals. The Def2-TZVPPD/ECP-28 basis set and effective core potential was employed for 4d metals.

Cluster Dissociation Process	ΔG° ($kJ•mol^{-1}$)
$[Co•(B_{12}F_{12})_2]^{2-} \rightarrow Co•B_{12}F_{12} + B_{12}F_{12}^{2-}$	389.5
$[Co•(B_{12}F_{12})_2]^{2-} \rightarrow [Co•B_{12}F_{12}]^- + B_{12}F_{12}^-$	43.1
$[Ni•(B_{12}F_{12})_2]^{2-} \rightarrow Ni•B_{12}F_{12} + B_{12}F_{12}^{2-}$	356.5
$[Ni•(B_{12}F_{12})_2]^{2-} \rightarrow [Ni•B_{12}F_{12}]^- + B_{12}F_{12}^-$	12.1
$[Cu•(B_{12}F_{12})]^- \rightarrow Cu^+ + B_{12}F_{12}^{2-}$	789.5
$[Cu•(B_{12}F_{12})]^- \rightarrow Cu + B_{12}F_{12}^-$	160.2
$[Zn•(B_{12}F_{12})_2]^{2-} \rightarrow Zn•B_{12}F_{12} + B_{12}F_{12}^{2-}$	428.0
$[Zn•(B_{12}F_{12})_2]^{2-} \rightarrow [Zn•B_{12}F_{12}]^- + B_{12}F_{12}^-$	26.8
$[Rh•(B_{12}F_{12})_2]^- \rightarrow [Rh•B_{12}F_{12}]^+ + B_{12}F_{12}^{2-}$	843.5
$[Rh•(B_{12}F_{12})_2]^- \rightarrow [Rh•B_{12}F_{12}] + B_{12}F_{12}^-$	89.1
$[Pd•(B_{12}F_{12})_2]^{2-} \rightarrow Pd•B_{12}F_{12} + B_{12}F_{12}^{2-}$	289.1
$[Pd•(B_{12}F_{12})_2]^{2-} \rightarrow [Pd•B_{12}F_{12}]^- + B_{12}F_{12}^-$	-44.4
$[Ag•(B_{12}F_{12})]^- \rightarrow Ag^+ + B_{12}F_{12}^{2-}$	731.4
$[Ag•(B_{12}F_{12})]^- \rightarrow Ag + B_{12}F_{12}^-$	111.7
$[Cd•(B_{12}F_{12})_2]^{2-} \rightarrow Cd•B_{12}F_{12} + B_{12}F_{12}^{2-}$	351.9
$[Cd•(B_{12}F_{12})_2]^{2-} \rightarrow [Cd•B_{12}F_{12}]^- + B_{12}F_{12}^-$	-31.0

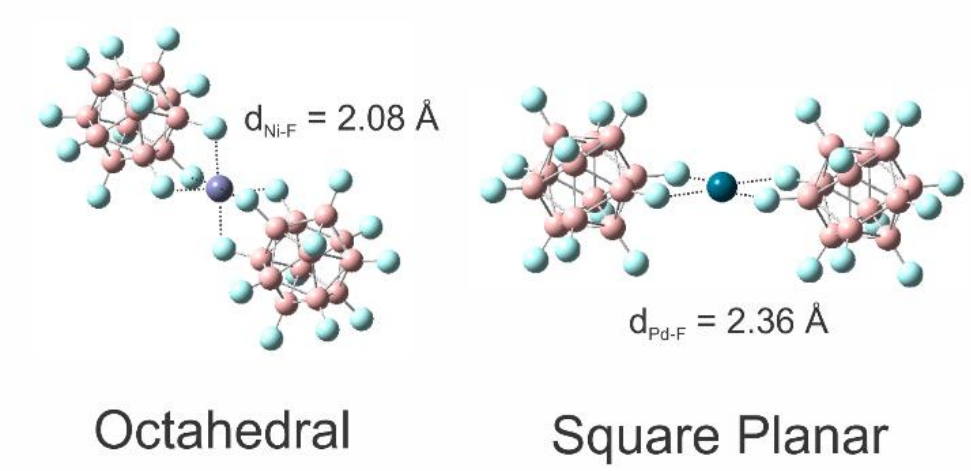

Figure 5.5 Optimized structures for (left) $[Ni(II)\bullet(B_{12}F_{12})_2]^{2-}$ and (right) $[Pd(II)\bullet(B_{12}F_{12})_2]^{2-}$, where the local geometry about the TM is octahedral and square planar, respectively. Calculations were conducted at the B3LYP/6-311++G(d,p) level of theory for 3d metals. The Def2-TZVPPD/ECP-28 basis set and effective core potential was employed for 4d metals.

The IRMPD spectra obtained for the $[TM\bullet(B_{12}F_{12})_2]^{2-}$ (TM = Co(II), Ni(II), Zn(II), Cd(II)) clusters are shown in Figure 5.6. Relatively little variation in the $B_{12}F_{12}$ T_{1u} normal mode peak position is observed as a function of TM substitution. The vibrational band associated with the $[Co(II)\bullet(B_{12}F_{12})_2]^{2-}$ cluster is noticeably narrower than the analogous bands for the heavier TMs owing to the fact that Co(II) is monoisotopic and therefore has fewer isotopologues contributing to the spectrum. In principle, the IRMPD spectra for the various isotopologues can (to some degree) be deconvoluted by gating on specific parent and daughter mass peaks. However, owing to the complexity of the isotopomer/isotopologue structures and the fact that the isotopically pure $[Co(II)\bullet(^{10}B_{12}F_{12})_2]^{2-}$ and $[Co(II)\bullet(^{11}B_{12}F_{12})_2]^{2-}$ species were only minor components in the statistical distribution, spectral deconvolution was not possible.

In all cases, DFT calculations predicted weak bands to slightly higher and lower wavenumber of the intense $B_{12}F_{12}$ cage T_{1u} vibration. The transition at *ca*. 1300 cm^{-1} is associated with the $B_{12}F_{12}$ cage breathing mode, while the peak at *ca*. 1115 cm^{-1} corresponds to excitation of

the $B_{12}F_{12}$–TM–$B_{12}F_{12}$ asymmetric stretch (reminiscent of the CO_2 asymmetric stretching motion). The IRMPD spectrum of $[Cd(II)\bullet(^{11}B_{12}F_{12})_2]^{2-}$ was the only one in which the 1115 cm^{-1} peak was observed (see Figure 5.6D). Of course, the non-observation of weak vibrational transitions in IRMPD spectra is not unusual.[42,45,178,248,249]

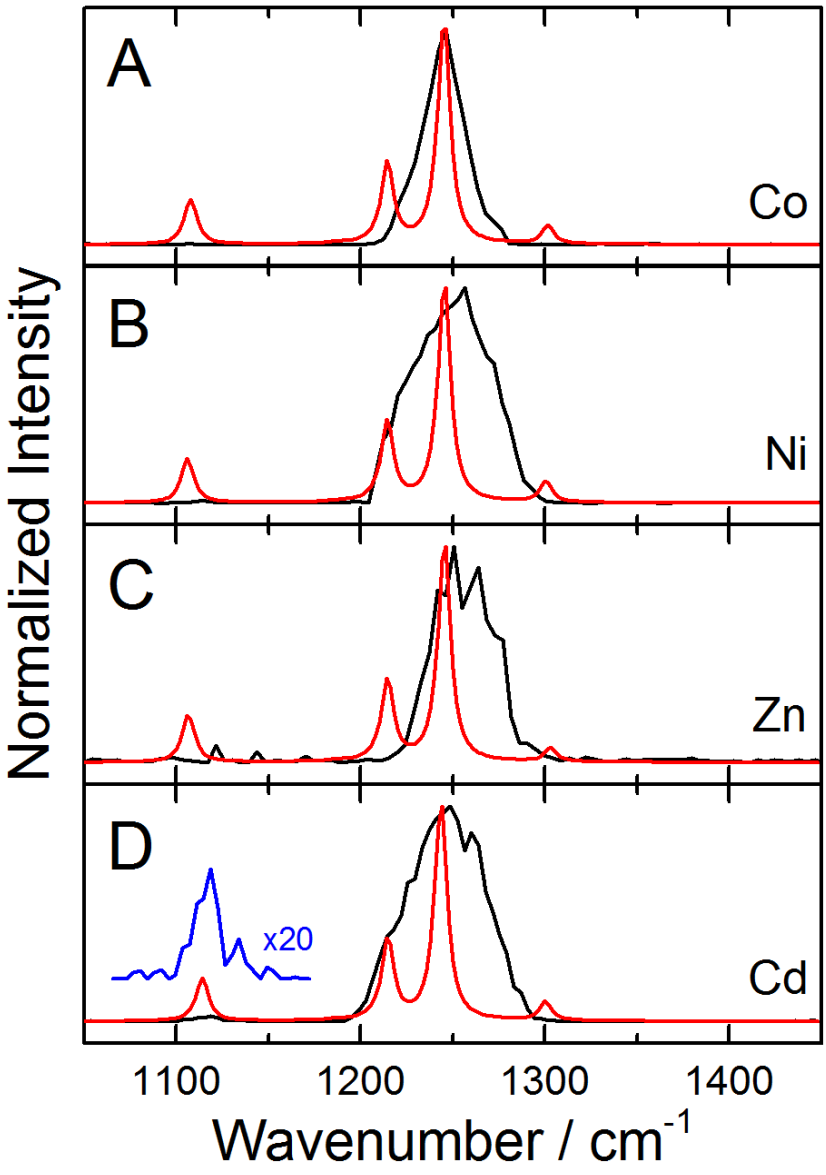

Figure 5.6 (**black**) Experimental and (**red**) calculated vibrational spectra for (**A**) $[Co(II)\bullet(B_{12}F_{12})_2]^{2-}$, (**B**) $[Ni(II)\bullet(B_{12}F_{12})_2]^{2-}$, (**C**) $[Zn(II)\bullet(B_{12}F_{12})_2]^{2-}$, (**D**) $[Cd(II)\bullet(B_{12}F_{12})_2]^{2-}$. Calculations were conducted at the B3LYP/6-311++G(d,p) level of theory for 3d metals. The Def2-TZVPPD/ECP-28 basis set and effective core potential was employed for 4d metals.

Figure 5.4 also shows the binding energies of the double cage clusters for dissociation via:

$$[TM\bullet(B_{12}F_{12})_2]^{2-} \rightarrow TM\bullet B_{12}F_{12} + B_{12}F_{12}^{2-} \qquad \text{Rxn. 3}$$

$$[TM\bullet(B_{12}F_{12})_2]^{2-} \rightarrow [TM\bullet B_{12}F_{12}]^{-} + B_{12}F_{12}^{-} \qquad \text{Rxn. 4}$$

Where TM = Co(II), Ni(II), Zn(II), Pd(II), Cd(II). In the case of the $[Rh(III)\bullet(B_{12}F_{12})_2]^-$ cluster, the transition metal-containing products are $[Rh(III)\bullet(B_{12}F_{12})]^+$ and $Rh(II)\bullet(B_{12}F_{12})$, respectively. With the exception of $[Rh(III)\bullet(B_{12}F_{12})_2]^-$ (where $\Delta G°_{dissociation}$ = 89.1 kJ mol^{-1}), the double cage species exhibit $\Delta G°$ values for dissociation via the charge-transfer channel that are all less than 43.9 kJ mol^{-1}. Thus, IRMPD to access the charge-transfer dissociation threshold is expected to be at most a three-photon process. This, again, is consistent with the observation of $B_{12}F_{12}^-$ as the major product channel. As was done for the single cage clusters, NBO analysis was conducted for each of $[TM\bullet(B_{12}F_{12})_2]^{2-}$ (TM = Co(II), Ni(II), Zn(II), Pd(II), Cd(II)) and $[Rh(III)\bullet(B_{12}F_{12})_2]^-$. The results of these calculations are summarized in Table 5.3. In all cases, significant interactions associated with charge-transfer were observed, both in terms of electron density donation from the $B_{12}F_{12}$ cages to the metal ion, and back donation from the metal to the $B_{12}F_{12}$ cages. Calculated natural charges for Co, Ni, Zn, and Cd were all in the range of +1.3 – 1.6, implying electron density donation in the range from 0.4*e* – 0.7*e* to the metal centres for the ground electronic states of these clusters. Interestingly, in addition to the dominant $B_{12}F_{12}^-$ product channel, IRMPD of mass-selected $[Co(II)\bullet(B_{12}F_{12})_2]^{2-}$ (*ca*. 0.6*e* donation) and $[Ni(II)\bullet(B_{12}F_{12})_2]^{2-}$ (*ca*. 0.7*e* donation) also resulted in production of $B_nF_m^-$ fragments ranging in size from $B_6F_4^-$ up to $B_{18}F_{18}^-$. The production of these $B_nF_m^-$ fragments can be rationalized in terms of the charge-transfer process since removal of electron density from the quadruply degenerate highest occupied molecular orbital of the $B_{12}F_{12}^{2-}$ cage yields a reactive radical species.

Table 5.3 TM natural partial charges and calculated interaction energies for charge-transfer interactions in the ground electronic states of $[TM•(B_{12}F_{12})_2]^{2-}$ (TM = Co(II), Ni(II), Zn(II), Pd(II), and Cd(II)) and $[Rh•(B_{12}F_{12})_2]^{-}$. Calculations were conducted at the B3LYP/6-311++G(d,p) level of theory. A Def2-TZVPPD/ECP-28 basis set and effective core potential combination was employed for the 4d TMs.

Cluster	Metal Partial Charge	Interaction Energy (kJ/mol)	
$[Co(II)•(B_{12}F_{12})_2]^{2-}$	+ 1.4 *e*	Cage → Co^{2+}	435.1
		F → Co^{2+}	1818.8
		Cage ← Co^{2+}	950.6
		F ← Co^{2+}	815.9
$[Rh(III)•(B_{12}F_{12})_2]^{-}$	+ 0.8 *e*	Cage → Rh^{3+}	604.2
		F → Rh^{3+}	429.7
		Cage ← Rh^{3+}	202.1
		F ← Rh^{3+}	162.8
$[Ni(II)•(B_{12}F_{12})_2]^{2-}$	+ 1.3 *e*	Cage → Ni^{2+}	477.8
		F → Ni^{2+}	1929.2
		Cage ← Ni^{2+}	916.7
		F ← Ni^{2+}	793.7
$[Pd(II)•(B_{12}F_{12})_2]^{2-}$	+ 0.8 *e*	Cage → Pd^{2+}	747.3
		F → Pd^{2+}	320.1
		Cage ← Pd^{2+}	138.5
		F ← Pd^{2+}	134.7
$[Zn(II)•(B_{12}F_{12})_2]^{2-}$	+ 1.5 *e*	Cage → Zn^{2+}	429.3
		F → Zn^{2+}	1397.0
		Cage ← Zn^{2+}	619.2
		F ← Zn^{2+}	418.4
$[Cd(II)•(B_{12}F_{12})_2]^{2-}$	+ 1.6 *e*	Cage → Cd^{2+}	707.5
		F → Cd^{2+}	783.7
		Cage ← Cd^{2+}	274.1
		F ← Cd^{2+}	120.9

The fact that two such species are in close proximity in the cobalt- and nickel-bound $B_{12}F_{12}^{2-}$ dimers facilitates reactions associated with the fusion and fragmentation of the $B_{12}F_{12}$ cages. Indeed, the electrospray process itself generated B_nF_m ionic fragments up to $B_{24}F_{24}^{2+}$ when employing solutions containing the Ni(II), Rh(II), and Pd(II) salts. This, too, can be rationalized in terms of charge-transfer since clusters of these three metals exhibit the highest degree of charge density donation from the $B_{12}F_{12}$ cages. In the case of Pd (*ca*. 1.2*e* donated) and Rh (*ca*. 2.2*e*

donated) so much charge density is donated that the metals are neutralized and the $B_{12}F_{12}$ cages undergo reaction during the electrospray process.

5.4.2 Conclusions

Six TM•$(B_{12}F_{12})_n$ clusters (TM = Co(II), Ni(II), Cu(I), Zn(II), Ag(I), Cd(II)) have been prepared by ESI of solutions containing their respective salts. IRMPD spectra show strong absorptions in the 1200 – 1250 cm^{-1} region, which are associated with the triply degenerate T_{1u} vibrational mode of the $B_{12}F_{12}$ cage. Excitation of this mode leads predominantly to production of $B_{12}F_{12}^-$, indicating that charge-transfer from the boron cage to the TM plays a major role in the ground state electronic structure. This conclusion is supported by DFT calculations, where in all cases studied the charge-transfer dissociation threshold was lower than that of simple ionic dissociation. Thus, the $B_{12}F_{12}^{2-}$ cage may be viewed as a "superatom" in the larger clusters.[1] The degree of charge-transfer in, and how charge-transfer might influence the physicochemical properties of, the solid state of TM•$(B_{12}F_{12})$ compounds (which could all be isolated) are interesting open questions. Our group has recently published results of an analogous study on $B_{12}H_{12}$-transition metal clusters.[36]

When electrosprayed, several of the TM•$(B_{12}F_{12})$ salts generate a broad distribution of B_nF_m clusters. Calculations show that production of B_nF_m clusters occurs for TM species that exhibit the highest degrees of charge-transfer. This suggests that charge-transfer to the metal center generates highly reactive open shell $B_{12}F_{12}$ cages, which subsequently undergo fusion and fragmentation reactions. The precise mechanism by which these reactions occur is not known. Nevertheless, this method might offer a new, efficient production technique for studying isolated or deposited B_nF_m clusters, with potential applications in nanofabrication of boron-based materials.

5.5 Triethylammonium $B_{12}X_{12}^{2-}$ (X = F, Cl) Clusters

5.5.1 Results and Discussion

Figure 5.7 plots the IRMPD spectrum for total fragmentation efficiency at four FEL power settings. By comparing the experimental spectra to the calculated IR absorption spectrum for the lowest energy isomeric cluster structures, we can confidently assign the band at ~ 1250 cm^{-1} to the T_{1u} vibrational mode of the $B_{12}F_{12}$ moiety. The spectral width of this feature (~ 50 cm^{-1}) is larger than the *ca*. 25 cm^{-1} band width normally observed at the CLIO facility.[33,49,176,179] As was the case in analogous $B_{12}X_{12}$-containing clusters, we attribute this difference to: (1) lifting of the T_{1u} degeneracy and splitting of the associated vibrational band upon complexation (*ca*. 15 cm^{-1} for the fluorine derivative), and (2) vibrational isotope shifts due to the presence of multiple $^{10}B/^{11}B$ isotopologues (*ca*. 50 cm^{-1} for the fluorine derivative).[36,41,49,250] The remaining vibrational bands observed at 1035 cm^{-1}, 1160 $cm^{-1,}$ 1325 $cm^{-1,}$ 1400 cm^{-1}, and 1470 cm^{-1} are all associated with the triethylammonium moiety in the global minimum isomer (see Figure 5.7B). The bands at 1400 cm^{-1} and 1470 cm^{-1}, which arise from motion of the charge-carrying proton and the CH_2 scissoring / CH_3 umbrella modes of the ethyl groups, are particularly sensitive to the binding mode of the complex. For example, for the global minimum structure, the NH wag is predicted at 1400 cm^{-1}, whereas in isomers 2 and 3, the band wavenumber is at 1477 cm^{-1} and 1442 cm^{-1}, respectively. Comparison of these band positions with those calculated at the B3LYP/6-311++G(d,p) level of theory indicate that the N–H bond is oriented towards one of the triangular faces of the $B_{12}F_{12}^{2-}$ moiety, with the three F atoms and the H atom creating a distorted tetrahedral cage. This structural motif has also been found in the crystal structures of $[(n\text{Bu}_3\text{NH})(HCB_{11}I_{11})]$ and $[(Et_3NH)_2(B_{12}Cl_{12})]\bullet 2NCCH_3$.[231,251] The average H•••F (H•••Cl)

distance was 2.25 Å (2.78 Å) and the distance from the H atom to the center of the F_3 (Cl_3) triangular face was 1.35 Å (1.68 Å). A recent paper by Fedorova *et al.* computationally studied $HN(C_2H_5)_3^+$ complexed with ten different acidic anions of the form RXO_n (X = S, P; n = 3, 4).[252] The preferred binding of $HN(C_2H_5)_3^+$ to the acid occurred via the charge carrying proton to an oxygen atom, forming a conventional hydrogen bond (N-H•••O). The shortest H-bond length found was 1.421 Å with the acid H_2PO_3 and the longest was 1.589 Å with the acid CF_3HSO_3. At 55.9 kJ mol^{-1} above the global minimum a second binding motif is computed wherein the N–H bond is oriented away from the $B_{12}F_{12}^{2-}$ moiety; the calculated IR spectrum for this geometric isomer has a significantly poorer agreement with the experimental spectrum (see Figure 5.8). It is worth noting that the bands associated with the $HN(C_2H_5)_3^+$ moiety are observed only at relatively high FEL powers. This is likely due to the relatively low IR absorption cross-sections of $HN(C_2H_5)_3^+$ moiety compared to that of the $B_{12}F_{12}^{2-}$ moiety (see Figure 5.7B); at low FEL power (125 mW), there is insufficient IR absorption via the $HN(C_2H_5)_3^+$ vibrational transitions to induce cluster fragmentation. The vibrational bands of the chlorinated derivative exhibit similar power dependence (see Figure 5.9).

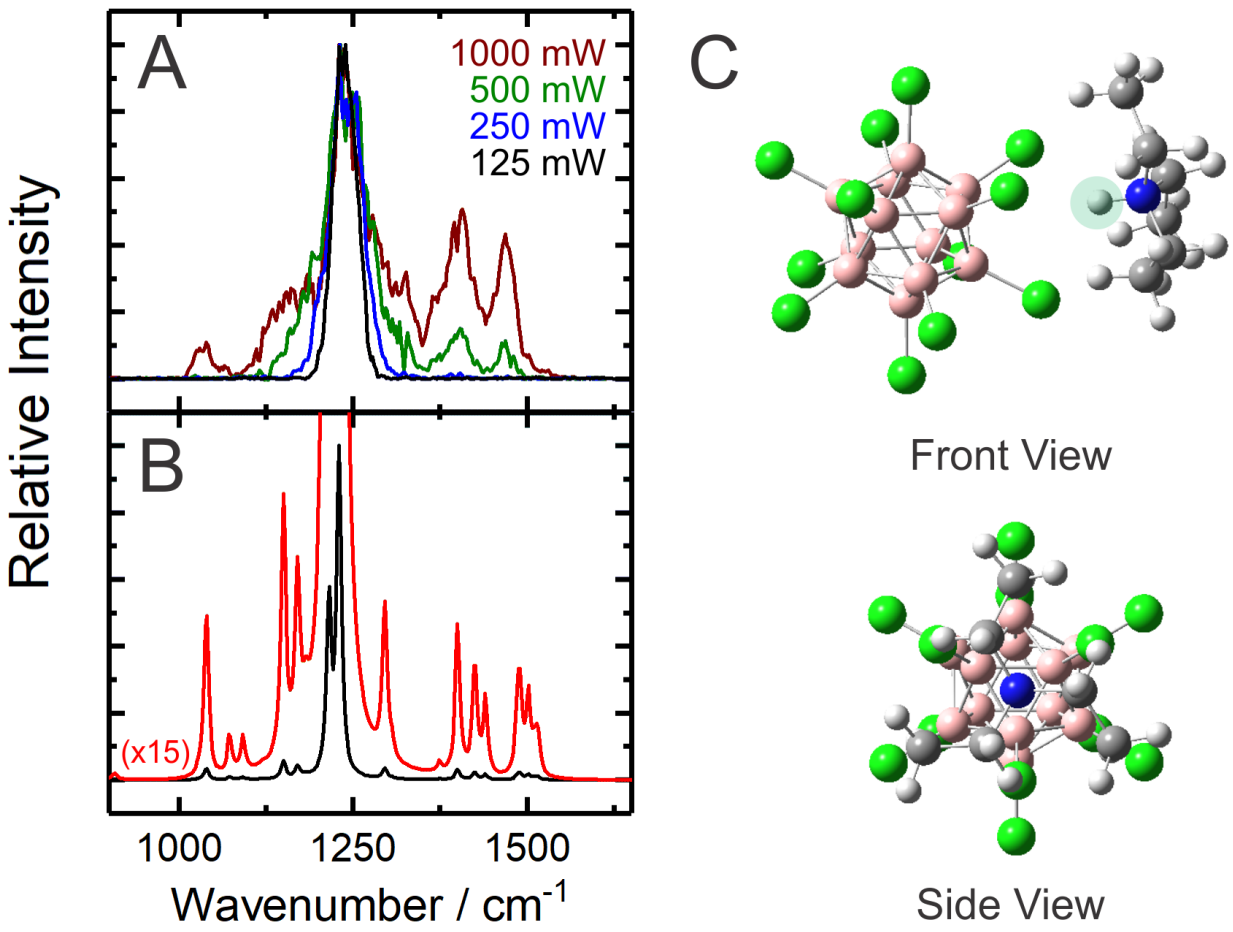

Figure 5.7 (**A**) The IRMPD spectrum of $[(CH_2CH_3)_3NH{\bullet}B_{12}F_{12}]^-$ as a function of FEL power. Note that the band at 1250 cm^{-1} associated with the $B_{12}F_{12}^{2-}$ moiety is saturated at powers above 125 mW. (**B**) The calculated IR absorption spectrum for the global minimum geometry of the ion. (**C**) The optimized geometry of the complex. The ammonium proton is highlighted in green in the front view.

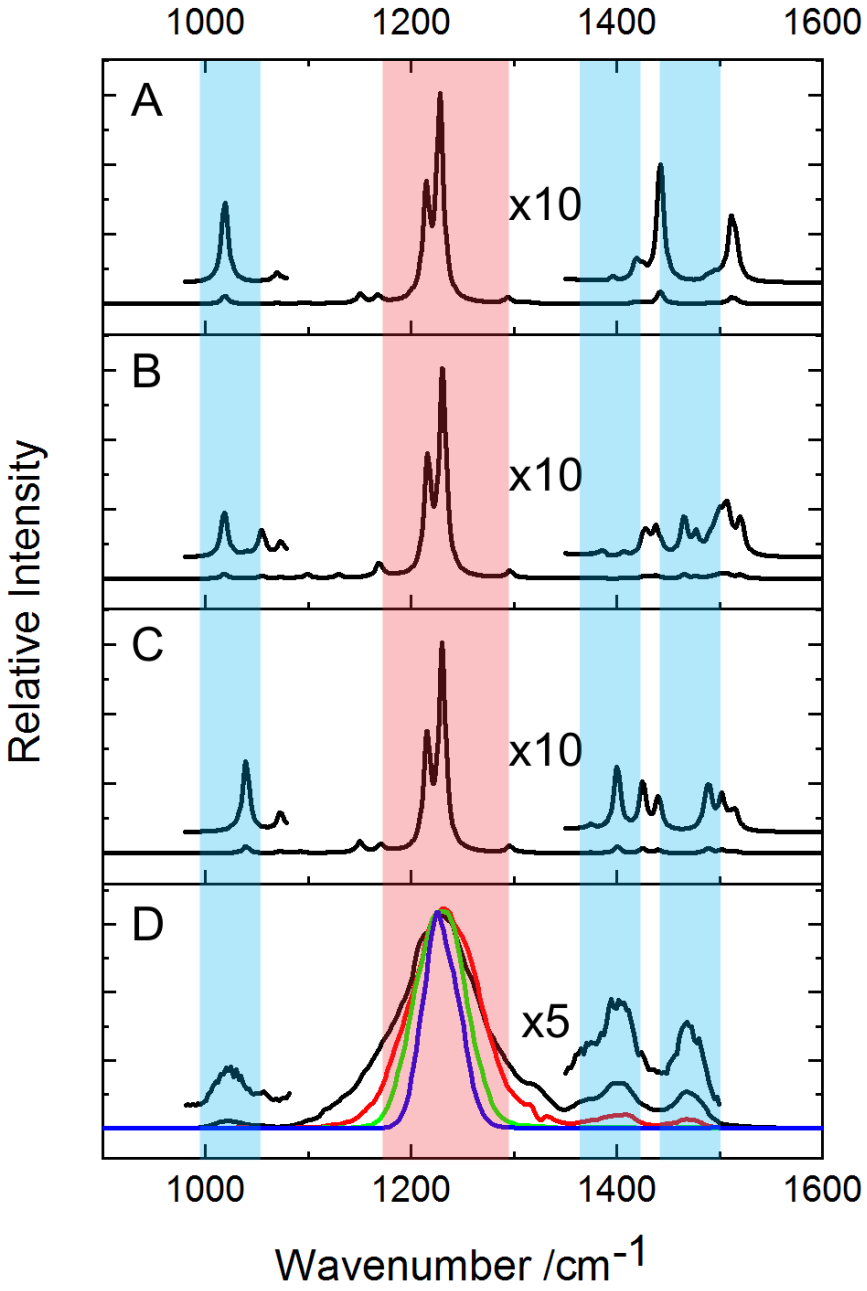

Figure 5.8 Vibrational spectra of $B_{12}F_{12}TEA$. (**A**, **B**) DFT predicted spectra of higher energy isomer 3 (+55.9 kJ mol^{-1}) and isomer 2 (+16.4 kJ mol^{-1}), respectively. (**C**) DFT predicted spectrum of the global minimum isomer. (**D**) IRMPD Experimental spectrum; black – 1000 mW, red – 500 mW, green – 250 mW, blue – 125 mW. Blue highlighted bands are assigned to TEA group vibrations, red highlighted band assigned to asymmetric breathing of the boron atoms.

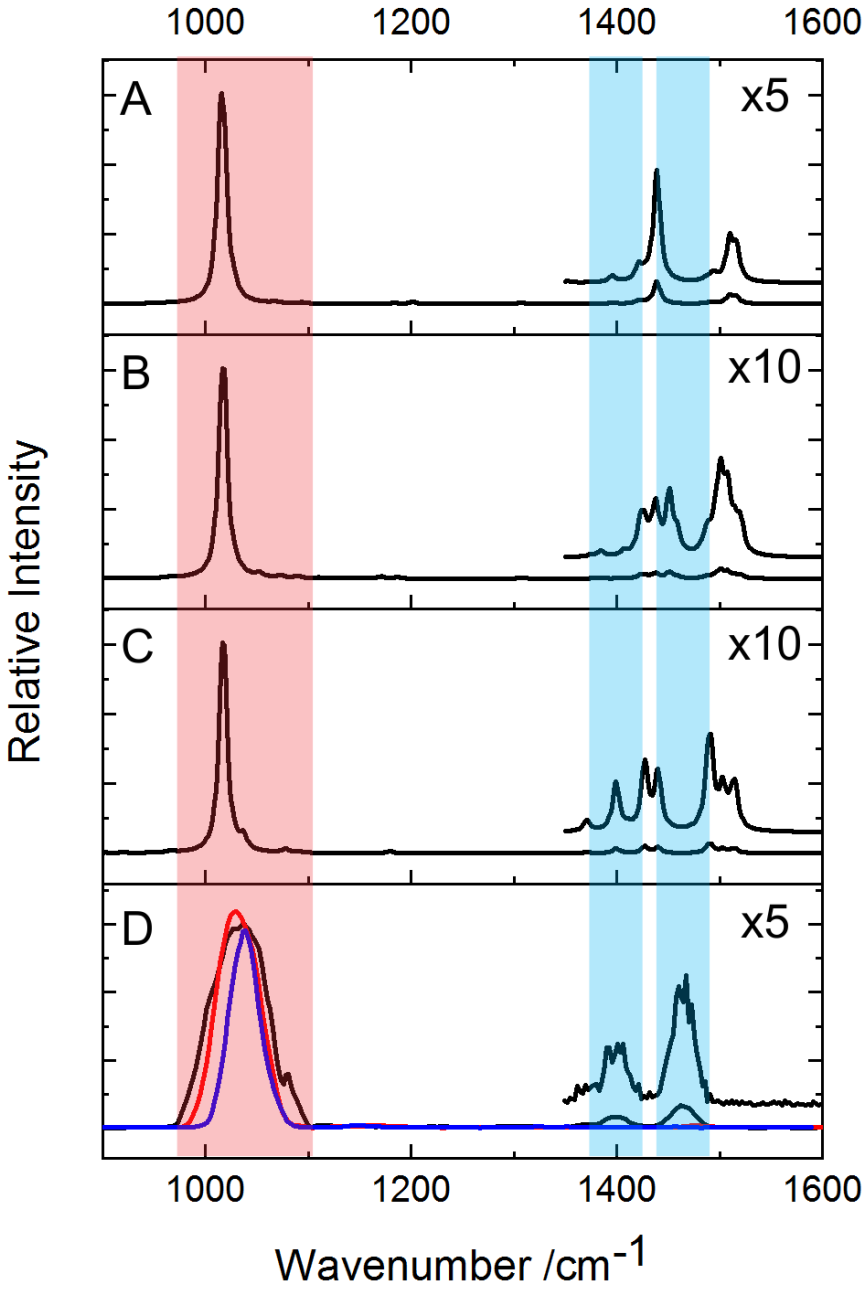

Figure 5.9 Vibrational spectra of $B_{12}Cl_{12}TEA$. (**A**, **B**) DFT predicted spectra of higher energy isomer 3 (+53.4 kJ mol^{-1}) and isomer 2 (+18.6 kJ mol^{-1}), respectively. (**C**) DFT predicted spectrum of the global minimum isomer. (**D**) IRMPD Experimental spectrum; black – 1000 mW, red – 500 mW, green – 250 mW, blue – 125 mW. Blue highlighted bands are assigned to TEA group vibrations, red highlighted band assigned to asymmetric breathing of the boron atoms.

Figure 5.10A shows the mass spectrum of $[(CH_2CH_3)_3NH{\bullet}B_{12}F_{12}]^-$ as observed when irradiating the trapped ions non-resonantly with 1000 mW at 940 cm^{-1}. Because the parent cluster does not absorb at this wavenumber, fragmentation is negligible. In contrast, irradiation at a wavenumber of 1250 cm^{-1} resulted in substantial fragmentation of the parent ion. The observed product ions accord well with those assigned in the collision induced dissociation (CID) studies described previously.[221] A full assignment of the fragmentation products are given in Table 5.4 for the experiments involving the fluorine analog and Table 5.5. for the experiments involving the chlorine analog.

At low FEL power (1250 cm^{-1}, 125 mW; Figure 5.9A), the major products of IRMPD are $B_{12}F_{12}^-$ (*m/z* ~ 358), $B_{12}F_{11}^-$ (*m/z* ~ 339), and $B_{11}F_8^-$ (*m/z* ~ 271). As the FEL power is increased, additional low *m/z* fragments become dominant contributors to the observed mass spectrum (*e.g.*, see Figure 5.10C and D; highlighted in orange). The formation of these small species is attributed to fragmentation of B_nF_m ($n \leq 12$, $m \leq 12$) moieties. It is possible that the formation of the small B_nF_m species proceeds via sequential fragmentation of larger fragments following absorption of multiple photons, or instead by IRMPD of the nascent products from a previous fragmentation event. We favour the former interpretation based on Figure 5.10E, which plots the ion signal as a function of *m/z* and IRMPD wavenumber as observed at a FEL power of *ca*. 1000 mW. The spectral regions associated with $HN(C_2H_5)_3^+$ vibrational transitions are highlighted in blue and the $B_{12}F_{12}^{2-}$ vibrational transition is highlighted in red (*vide infra*). There are two observations of note for Figure 5.10E. First, it is clear upon inspection that some mass channels exhibit a different IR wavenumber dependence than others (*e.g.*, *m/z* 112 versus *m/z* 358). The IRMPD spectrum as acquired in the *m/z* 112 and *m/z* 358 product channels are plotted in Figure 5.12A and B, respectively. Whereas the *m/z* 112 product channel exhibits a single vibrational band associated

with the $B_{12}F_{12}^{2-}$ cage vibration, the *m/z* 358 product channel exhibits vibrational bands associated with both the $B_{12}F_{12}^{2-}$ cage and the $HN(C_2H_5)_3^+$ moiety. Analogous plots for the chlorinated species (see Figure 5.13) use *m/z* 255 ($B_7Cl_5^-$), 283 ($B_{10}Cl_5^-$), and 555 ($B_{12}Cl_{12}^-$) product channels. $B_7Cl_5^-$ is produced from $B_{12}Cl_{12}^-$ *via* loss of multiple BCl/BCl_3 fragments. The appearance of the $HN(C_2H_5)_3^+$ bands in the $B_7Cl_5^-$ spectrum indicates that $B_7Cl_5^-$ may be fragmented from $[(CH_2CH_3)_3NH{\bullet}B_{12}Cl_{12}]^-$ to a small extent. $B_{10}Cl_5^-$ is produced from $B_{12}Cl_{11}^-$ *via* loss of multiple BCl/BCl_3 fragments. Absence of the $HN(C_2H_5)_3^+$ bands indicates $B_{10}Cl_5^-$ cannot be produced from $[(CH_2CH_3)_3NH{\bullet}B_{12}Cl_{12}]^-$. To produce $B_{10}Cl_5^-$, $[(CH_2CH_3)_3NH{\bullet}B_{12}Cl_{12}]^-$ must fragment to $B_{12}Cl_{11}^-$, the fragment $B_{12}Cl_{11}^-$ then subsequently absorbs IR photons and fragments to $B_{10}Cl_5^-$. Recently, similar observations for other ionic complexes have been interpreted in the context of mode-selective behavior.[33,134] Here, however, the second notable observation from Figure 5.10E suggests otherwise. When exciting $[(CH_2CH_3)_3NH{\bullet}B_{12}F_{12}]^-$ via the $HN(C_2H_5)_3^+$ bands at 1400 cm^{-1} and 1470 cm^{-1}, one observes products at *m/z* 358 ($B_{12}F_{12}^-$), *m/z* 339 ($B_{12}F_{11}^-$), *m/z* 271 ($B_{11}F_8^-$), and *m/z* 172 ($B_9F_4^-$); excitation of the $HN(C_2H_5)_3^+$ moiety clearly leads to fragmentation of the boron cage. In other words, when deposited in the $HN(C_2H_5)_3^+$ moiety, the energy flow to the $B_{12}F_{12}^{2-}$ moiety is apparently sufficient so as to access fragmentation channels associated with loss of F^- and BF_3^- (and larger $B_nF_m^-$ species differing in mass by one BF unit). Similar behavior was observed for the chlorinated analogue (see Figure 5.11 and Table 5.5). This is notable because CID was found to yield $B_{12}Cl_{11}^-$ and fragments produced from $B_{12}Cl_{11}^-$,[220,221] whereas IRMPD also produced $B_{12}Cl_{12}^-$ and smaller species associated with fragmentation of the oxidized cage. Fragmentation pathways are given for loss of BX and BX_3 from $B_{12}X_{11}$ and $B_{12}X_{12}$ in Figure 5.14 and Figure 5.15 for X = F and Figure 5.16 and Figure 5.17 for X = Cl.

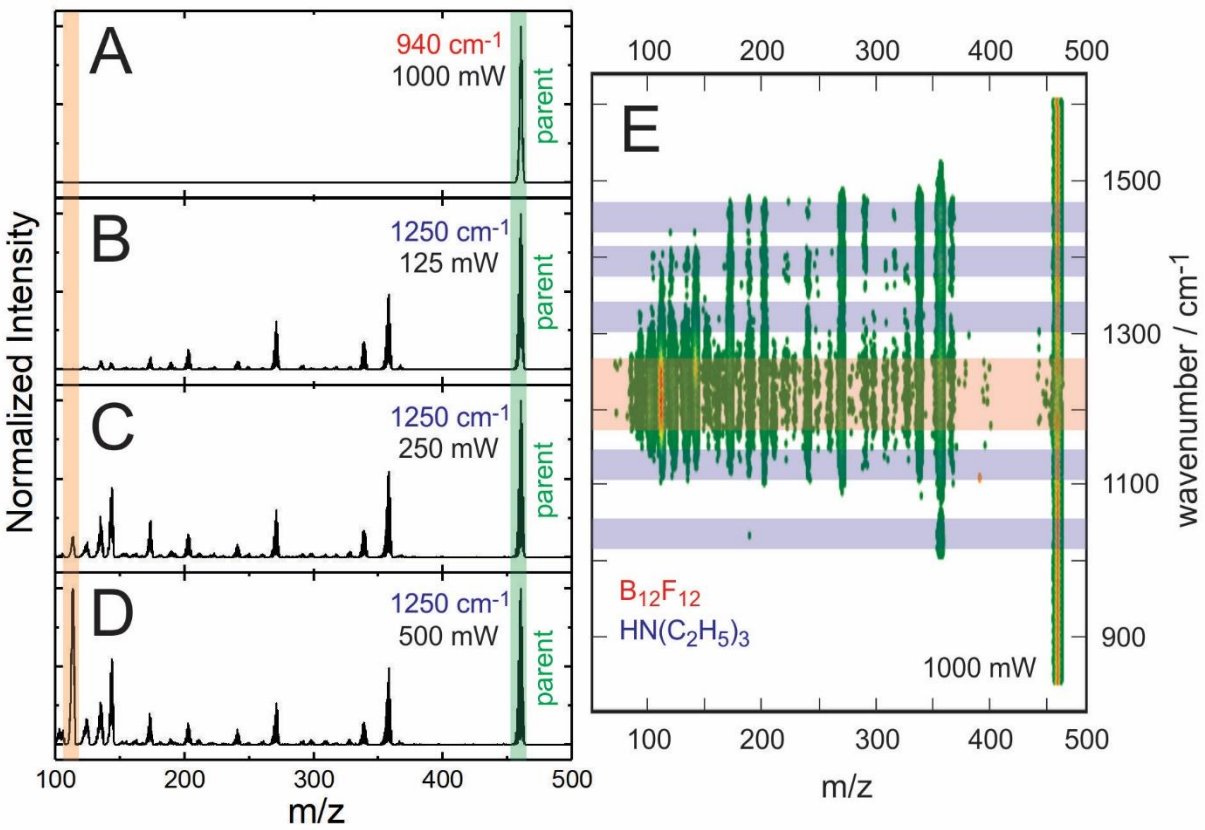

Figure 5.10 (**A**) The mass spectrum observed for isolated $[(CH_2CH_3)_3NH{\bullet}B_{12}F_{12}]^-$ when interrogating with 1000 mW at 940 cm^{-1} (non-resonant); only the parent ion is observed. The mass spectrum observed when the FEL is resonant with the $B_{12}F_{12}$ transition at 1250 cm^{-1} and the FEL power is (**B**) 125 mW, (**C**) 250 mW, and (**D**) 500 mW. The orange bar in **A-D** highlights the production of small mass ions (e.g., $B_6F_2^-$) with increasing laser power when resonant with an absorption. (**E**) A 2-D IR/MS plot showing the mass spectrum as a function of FEL wavenumber across the 800 - 1600 cm^{-1} region when interrogating at 1000 mW. Low ion intensities are shown in green, high intensities in red. The blue highlighted regions indicate vibrational bands associated with the triethylammonium moiety, and the red highlighted region indicates the vibrational band(s) associated with the $B_{12}F_{12}$ cage.

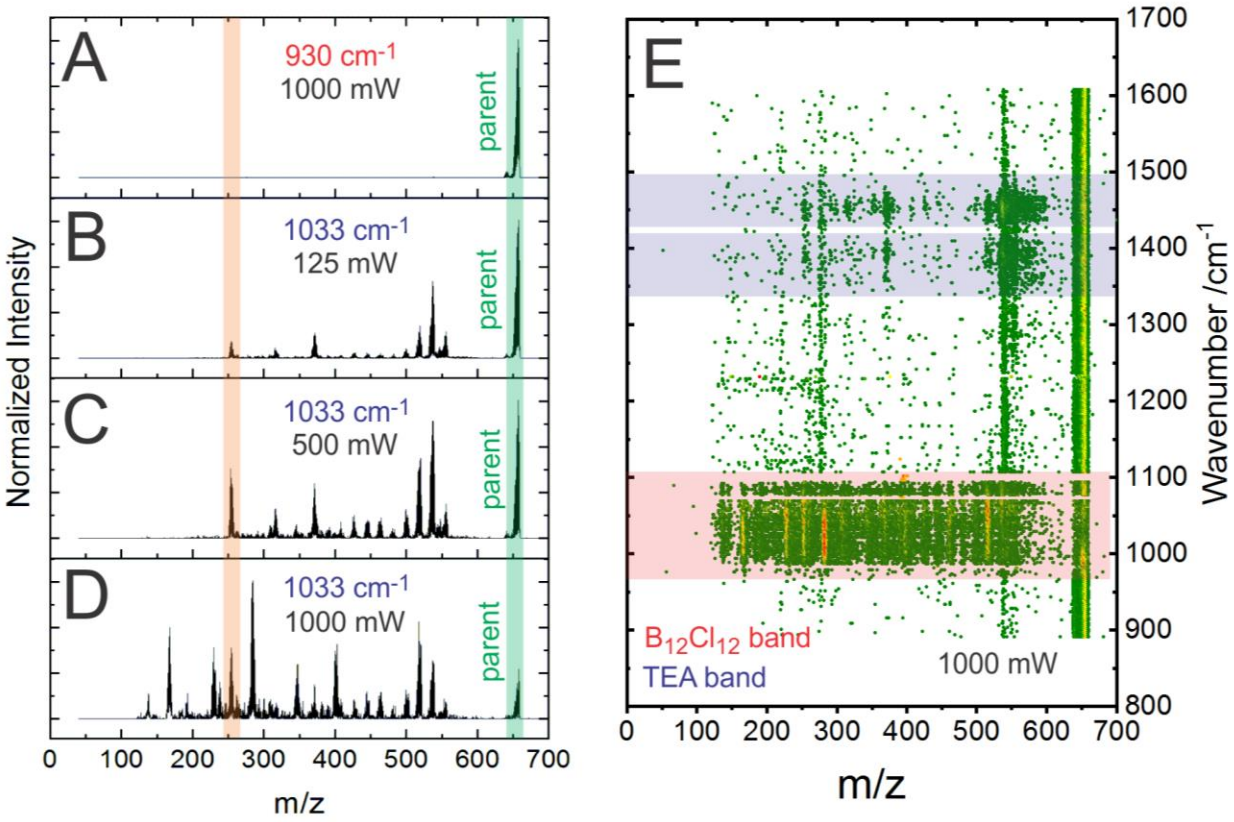

Figure 5.11 (**A**) The mass spectrum observed for isolated $[(CH_2CH_3)_3NH{\bullet}B_{12}Cl_{12}]^-$ when interrogating with 1000 mW at 930 cm^{-1} (non-resonant); only the parent ion is observed. The mass spectrum observed when the FEL is resonant with the $B_{12}Cl_{12}$ transition at 1033 cm^{-1} and the FEL power is (**B**) 125 mW, (**C**) 500 mW, and (**D**) 1000 mW. (**E**) A 2-D IR/MS plot showing the mass spectrum as a function of FEL wavenumber across the 800 – 1600 cm^{-1} region when interrogating at 1000 mW. Low ion intensities are shown in green, high intensities in red. The blue highlighted regions indicate vibrational bands associated with the triethylammonium moiety, and the red highlighted region indicates the vibrational band(s) associated with the $B_{12}Cl_{12}$ cage.

Table 5.4 Peak assignments for $[B_{12}F_{12}TEA]^-$ mass spectrum when radiated with 1000 mW of 1228 cm^{-1}. m/z values are given for the most intense peak of the isotopic distribution. Most isotopic distributions do not match one assignment perfectly and likely consist of multiple species with similar nominal mass. Hydroxide and water clusters likely contributing to peak intensities but are difficult to assign due to similar nominal mass with fluorine and overlapping isotopic distributions due to the presence of boron. (OH=17 amu, H_2O=18 amu, F=19 amu)

m/z	Assignment	Parent
460	$[B_{12}F_{12}\cdot TEA]^-$	-
368	$[B_{12}F_{11}\cdot N_2]^-$	$[B_{12}F_{11}]^-$
358	$[B_{12}F_{12}]^-$	$[B_{12}F_{12}\cdot TEA]^-$
	$[B_{12}F_{11}\cdot H_2O]^-$	$[B_{12}F_{11}]^-$
338	$[B_{12}F_{11}]^-$	$[B_{12}F_{12}\cdot H]^-$
328	$[B_{11}F_{11}]^-$	$[B_{12}F_{12}]^-$
317	$[B_{10}F_{10}\cdot H_2O]^-$	$[B_{12}F_{12}]^-$
309	$[B_{11}F_{10}]^-$	$[B_{12}F_{11}]^-$
298	$[B_{10}F_{10}]^-$	$[B_{12}F_{12}]^-$
291	$[B_{11}F_9]^-$	$[B_{12}F_{12}]^-$
271	$[B_{11}F_8]^-$	$[B_{12}F_{11}]^-$
260	$[B_{10}F_8]^-$	$[B_{12}F_{12}]^-$
250	$[B_9F_8]^-$	$[B_{12}F_{11}]^-$
241	$[B_{10}F_7]^-$	$[B_{12}F_{11}]^-$
221	$[B_{10}F_6]^-$	$[B_{12}F_{12}]^-$
	$[B_8F_7]^-$	$[B_{12}F_{11}]^-$
211	$[B_9F_6]^-$	$[B_{12}F_{11}]^-$
204	$[B_{10}F_5]^-$	$[B_{12}F_{11}]^-$
191	$[B_9F_5]^-$	$[B_{12}F_{12}]^-$
	$[B_7F_6]^-$	$[B_{12}F_{11}]^-$
181	$[B_8F_5]^-$	$[B_{12}F_{11}]^-$
173	$[B_9F_4]^-$	$[B_{12}F_{11}]^-$
163	$[B_8F_4]^-$	$[B_{12}F_{12}]^-$
153	$[B_9F_3]^-$	$[B_{12}F_{12}]^-$
	$[B_7F_4]^-$	$[B_{12}F_{11}]^-$
144	$[B_8F_3]^-$	$[B_{12}F_{11}]^-$
135	$[B_7F_3]^-$	$[B_{12}F_{12}]^-$
	$[B_9F_2]_-$	$[B_{12}F_{11}]^-$
124	$[B_8F_2]^-$	$[B_{12}F_{12}]^-$
113	$[B_7F_2]^-$	$[B_{12}F_{11}]^-$
103	$[B_6F_2]^-$	$[B_{12}F_{12}]^-$

Table 5.5 Peak assignments for $[B_{12}Cl_{12}TEA]^-$ mass spectrum when radiated with 1000 mW of 1032 cm^{-1}. m/z values are given for the most intense peak of the isotopic distribution. Most isotopic distributions do not match one assignment perfectly and likely consist of multiple species with similar nominal mass. Hydroxide and water dimer clusters likely contributing to peak intensities but are difficult to assign due to similar nominal mass with chlorine and overlapping isotopic distributions due to the presence of boron. ($(OH)_2$=34 amu, $(H_2O)_2$=36 amu, Cl=35 amu)

m/z	Assignment	Parent
658	$[B_{12}Cl_{12}\cdot TEA]^-$	-
555	$[B_{12}Cl_{12}]^-$	$[B_{12}Cl_{12}\cdot TEA]^-$
538	$[B_{12}Cl_{11}\cdot H_2O]^-$	$[B_{12}Cl_{11}]^-$
519	$[B_{12}Cl_{11}]^-$	$[B_{12}Cl_{12}\cdot H]^-$
	$[B_{12}Cl_{10}OH\cdot H_2O]^-$	$[B_{12}Cl_{11}\cdot H_2O]^-$
500	$[B_{12}Cl_{10}OH]^-$	$[B_{12}Cl_{11}\cdot H_2O]^-$
483	$[B_{12}Cl_{10}]^-$	$[B_{12}Cl_{12}]^-$
	$[B_{12}Cl_9(OH)_2]^-$	$[B_{12}Cl_{11}\cdot H_2O]^-$
464	$[B_{10}Cl_{10}]^-$	$[B_{12}Cl_{12}]^-$
	$[B_{12}Cl_8(OH)_3]^-$	$[B_{12}Cl_{11}\cdot H_2O]^-$
445	$[B_{10}Cl_9\cdot H_2O]^-$	$[B_{12}Cl_{11}]^-$
	$[B_{12}Cl_7(OH)_4]^-$	$[B_{12}Cl_{11}\cdot H_2O]^-$
427	$[B_{10}Cl_9]^-$	$[B_{12}Cl_{11}]^-$
	$[B_{12}Cl_6(OH)_5]^-$	$[B_{12}Cl_{11}\cdot H_2O]^-$
409	$[B_{12}Cl_5(OH)_6]^-$	$[B_{12}Cl_{11}\cdot H_2O]^-$
401	$[B_{11}Cl_8]^-$	$[B_{12}Cl_{11}]^-$
390	$[B_{10}Cl_8]^-$	$[B_{12}Cl_{12}]^-$
	$[B_{12}Cl_4(OH)_7]^-$	$[B_{12}Cl_{11}\cdot H_2O]^-$
382	$[B_9Cl_8]^-$	$[B_{12}Cl_{11}]^-$
371	$[B_8Cl_8]^-$	$[B_{12}Cl_{12}]^-$
	$[B_{12}Cl_3(OH)_8]^-$	$[B_{12}Cl_{11}\cdot H_2O]^-$
348	$[B_9Cl_7]^-$	$[B_{12}Cl_{12}]^-$
317	$[B_8Cl_6\cdot H_2O]^-$	$[B_{12}Cl_{12}]^-$
	$[B_{12}(OH)_{11}]^-$	$[B_{12}Cl_{11}\cdot H_2O]^-$
310	$[B_9Cl_6]^-$	$[B_{12}Cl_{11}]^-$
301	$[B_8Cl_6]^-$	$[B_{12}Cl_{12}]^-$
285	$[B_{10}Cl_5]^-$	$[B_{12}Cl_{11}]^-$
255	$[B_7Cl_5]^-$	$[B_{12}Cl_{12}]^-$
230	$[B_9Cl_4]^-$	$[B_{12}Cl_{11}]^-$
193	$[B_8Cl_3]^-$	$[B_{12}Cl_{11}]^-$
168	$[B_9Cl_2]^-$	$[B_{12}Cl_{11}]^-$
138	$[B_6Cl_2]^-$	$[B_{12}Cl_{12}]^-$

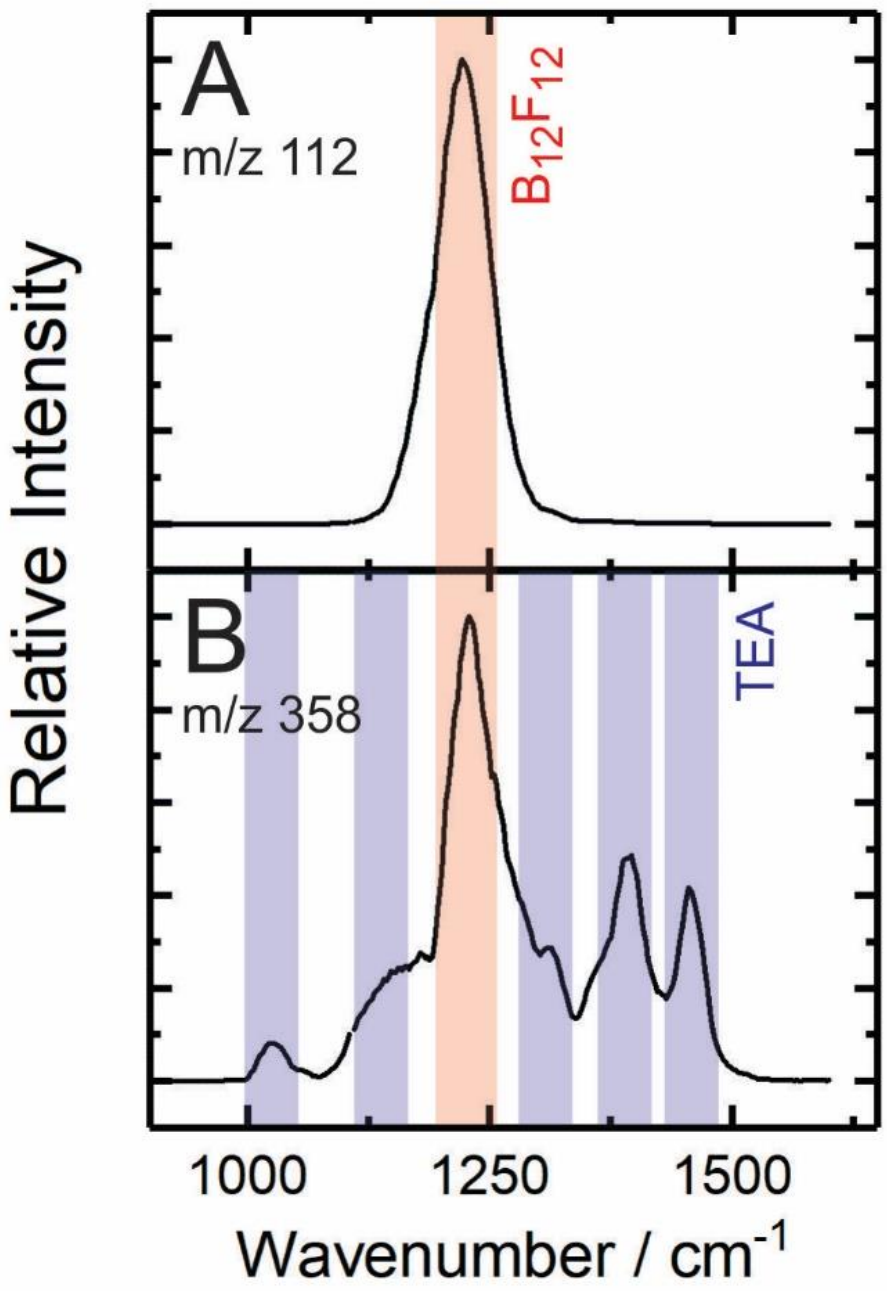

Figure 5.12 The IRMPD spectrum of $[(CH_2CH_3)_3NH{\bullet}B_{12}F_{12}]^-$ as monitored via the (**A**) m/z 112 and (**B**) m/z 358 product channels. Triethylammonium (TEA) bands are highlighted in blue and the $B_{12}F_{12}^{2-}$ band is highlighted in red. The FEL power was set to 1000 mW.

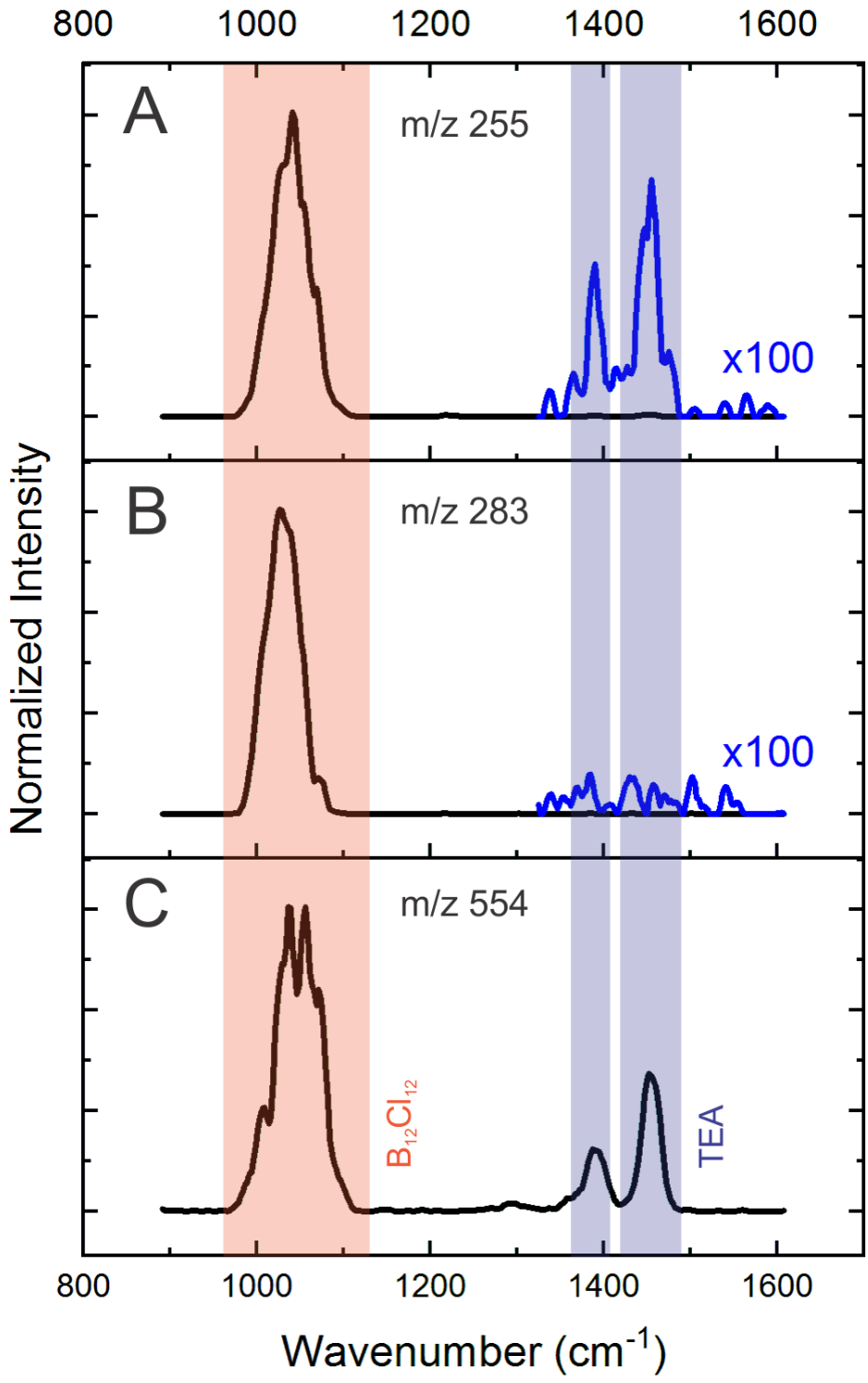

Figure 5.13 The IRMPD spectrum of $[(CH_2CH_3)_3NH{\bullet}B_{12}Cl_{12}]^-$ as monitored via the (**A**) m/z 255, (**B**) m/z 283, and (**C**) m/z 554 product channels. Triethylammonium (TEA) bands are highlighted in blue and the $B_{12}F_{12}^{2-}$ band is highlighted in red. The FEL power was set to 1000 mW.

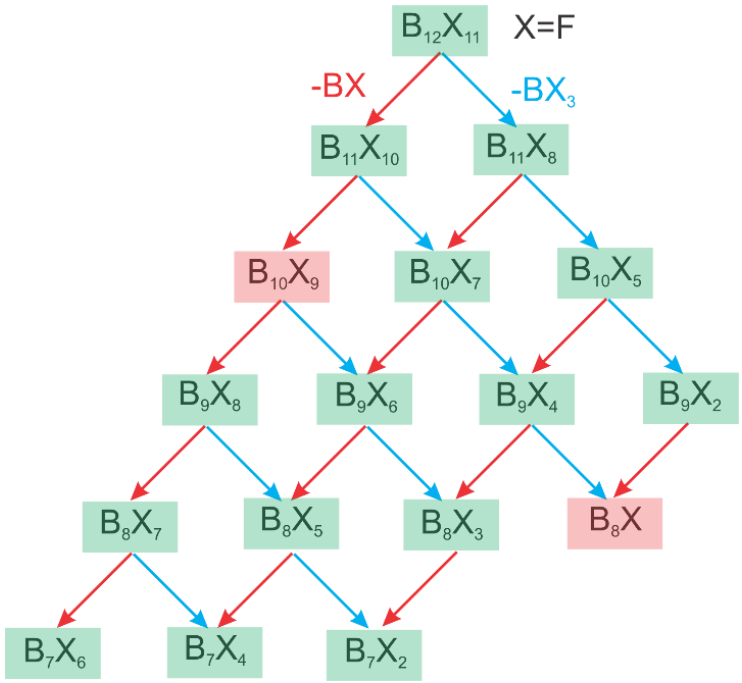

Figure 5.14 Fragmentation pathways of $B_{12}F_{11}$ by loss of BF and/or BF_3. Species highlighted in green were observed while those highlighted in red were not observed.

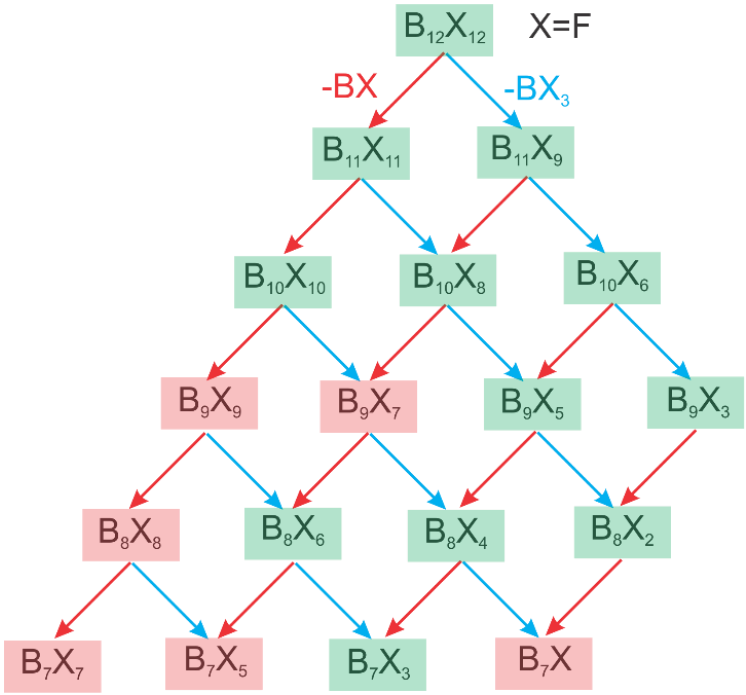

Figure 5.15 Fragmentation pathways of $B_{12}F_{12}$ by loss of BF and/or BF_3. Species highlighted in green were observed while those highlighted in red were not observed.

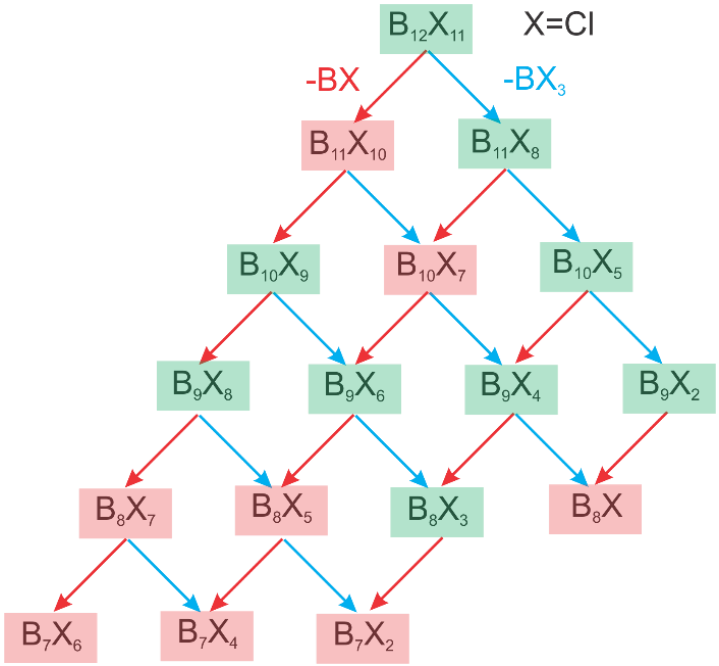

Figure 5.16 Fragmentation pathways of $B_{12}Cl_{11}$ by loss of BCl and/or BCl_3. Species highlighted in green were observed while those highlighted in red were not observed.

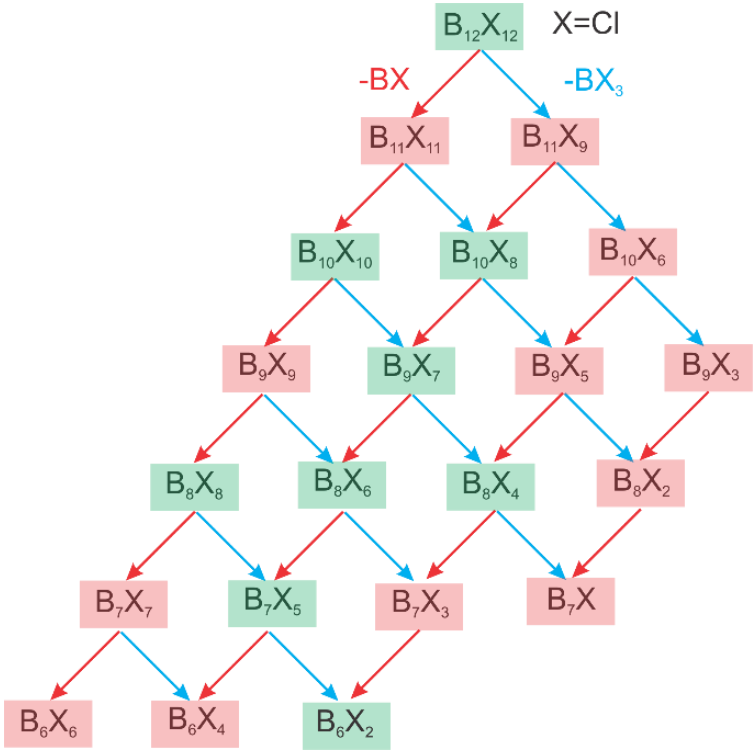

Figure 5.17 Fragmentation pathways of $B_{12}Cl_{12}$ by loss of BCl and/or BCl_3. Species highlighted in green were observed while those highlighted in red were not observed.

To further investigate the observed fragmentation of the $[(CH_2CH_3)_3NH{\bullet}B_{12}X_{12}]^-$ (X = F, Cl) complexes, detailed electronic structure calculations were conducted at the density functional level of theory. Table 5.6 provides an overview of the three lowest-energy fragmentation thresholds for the $[(CH_2CH_3)_3NH{\bullet}B_{12}X_{12}]^-$ (X = F, Cl) complexes. Channels IIIa and IIIb are the binding energies of $HN(C_2H_5)_3^+$ to $[B_{12}F_{12}]^{2-}$ and $[B_{12}Cl_{12}]^{2-}$. The study of $HN(C_2H_5)_3^+$ clustering with acidic anions provides a comparison for $HN(C_2H_5)_3^+$ binding energies. The largest binding energy they reported was 503.7 kJ mol^{-1} to H_2PO_3.[252] The larger binding energy in $[(CH_2CH_3)_3NH{\bullet}B_{12}X_{12}]^-$ (X = F, Cl) are a result of the larger charge of the cages. In both the fluorinated and chlorinated derivatives, proton transfer from the $HN(C_2H_5)_3^+$ moiety to the $B_{12}X_{12}^{2-}$ cage followed by dissociation to yield neutral triethylamine and $B_{12}X_{12}H^-$ is the most thermodynamically favored pathway (channel Ia/b in Table 5.6). This accords with expectation based on the observed CID behavior of $[(CH_3)_3NH{\bullet}B_{12}X_{12}]^-$ (X = F, Cl).[221] However, upon IRMPD of $[(CH_2CH_3)_3NH{\bullet}B_{12}F_{12}]^-$ the isotope pattern of the ion signal observed at ~ *m/z* 359 does not match that of $B_{12}X_{12}H^-$ (see Figure 5.18). Instead, the signal at ~*m/z* 359 is best modelled by a *ca.* 70:30 contribution of $B_{12}F_{12}^-$ and $[B_{12}F_{11} + H_2O]^-$.

Table 5.6 Calculated low-energy dissociation thresholds of $[(CH_2CH_3)_3NH{\bullet}B_{12}X_{12}]^-$ (X = F, Cl).

Parent	Products		D_0 kJ/mol	ΔH^0 kJ/mol	ΔG^0 kJ/mol
	$\rightarrow [B_{12}F_{12}]^{2-} + [N(CH_2CH_3)_3+H]^+$	(IIIa)	589.5	587.3	540.9
$[B_{12}F_{12}{\bullet}N(CH_2CH_3)_3+H]^-$	$\rightarrow [B_{12}F_{12}]^- + N(CH_2CH_3)_3+H$	(IIa)	445.1	445.0	392.6
	$\rightarrow [B_{12}F_{12}H]^- + N(CH_2CH_3)_3$	(Ia)	278.0	276.6	228.6
	$\rightarrow [B_{12}Cl_{12}]^{2-} + [N(CH_2CH_3)_3+H]^+$	(IIIb)	538.8	537.0	488.0
$[B_{12}Cl_{12}{\bullet}N(CH_2CH_3)_3+H]^-$	$\rightarrow [B_{12}Cl_{12}]^- + N(CH_2CH_3)_3+H$	(IIb)	483.6	481.9	432.4
	$\rightarrow [B_{12}Cl_{12}H]^- + N(CH_2CH_3)_3$	(Ib)	229.5	227.7	179.5

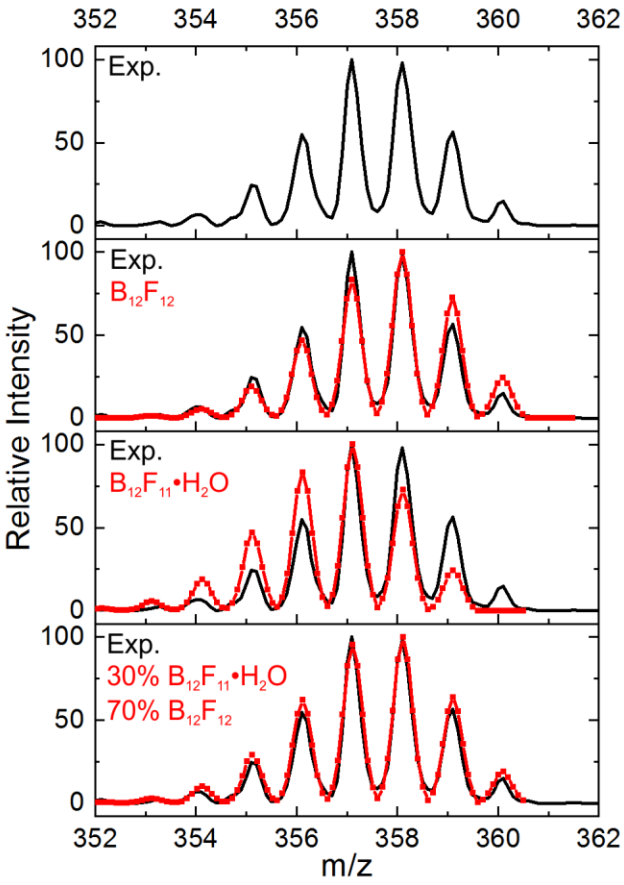

Figure 5.18 Experimental mass spectrum of an isotopic distribution summitting at 357 amu compared to simulated mass spectra for $B_{12}F_{12}^-$, $B_{12}F_{11}{\cdot}H_2O^-$ and a 70:30 combination of $B_{12}F_{12}^-$ and $B_{12}F_{11}{\cdot}H_2O^-$. The intensities of the simulated spectra were computed using a binomial distribution for the isotopic distribution of $^{10}B/^{11}B$ multiplied by a gaussian factor for each mass. See Eq. 5.1 and Eq. 5.2.

A binomial probability distribution was used to simulate the relative intensities of different isotopologues of $B_{12}F_{12}$ from boron isotopes ^{10}B with a natural abundance of approximately 0.2 and ^{11}B with a natural abundance of approximately 0.8.

$$P_r = \frac{n!}{k!\,(n-k)!} p^k q^{n-k} \qquad \text{Eq. 5.1}$$

In the above equation; n = 12 the number of boron atoms in the cluster, k = 0 to 12 the number of ^{10}B atoms in the cluster, p = 0.2 the natural abundance of ^{10}B, and q = 0.8 the natural abundance of ^{11}B.

Table 5.7 Raw probabilities of $(^{10}B_n{}^{11}B_m)F_{12}{}^{2-}$ (n + m = 12) isotopologues according to the binomial distribution, Eq. 5.1.

^{10}B	^{11}B	$(^{10}B^{11}B)_{12}F_{12}$ Mass	P_r
12	0	348.1	4.10E-09
11	1	349.1	1.97E-07
10	2	350.1	4.33E-06
9	3	351.1	5.77E-05
8	4	352.1	5.19E-04
7	5	353.1	3.32E-03
6	6	354.1	1.55E-02
5	7	355.1	5.32E-02
4	8	356.1	1.33E-01
3	9	357.1	2.36E-01
2	10	358.1	2.83E-01
1	11	359.1	2.06E-01
0	12	360.1	6.87E-02

A simulated intensity for every 0.1 amu was generated by multiplying the result of P_r by a scaling factor generated by a Gaussian distribution.

$$f = \frac{1}{\sigma\sqrt{2\pi}} e^{\frac{-(x-\mu)^2}{2\sigma^2}} \qquad \text{Eq. 5.2}$$

In the above equation: σ = 0.184 is the experimental FWHM, μ is the appropriate P_r for the current 1 amu mass range (*i.e.*, when predicting intensities for the 347.6 – 348.6 range $P_r = 4.10 \times 10^{-9}$), and x is the mass for which the intensity is being predicted.

The appearance of $B_{12}F_{12}^-$ indicates that IR excitation accesses the charge transfer threshold (channel IIa; Table 5.6). The formation of $[B_{12}F_{11} + H_2O]^-$, on the other hand, is a result of complexation of $B_{12}F_{11}^-$ with trace water vapor in the ion trap as observed previously.[221] This is supported by the observation of a signal at ~*m/z* 339, which corresponds to formation of $B_{12}F_{11}^-$ following either HF elimination from $B_{12}F_{12}H^-$ or tetra-alkylammonium-fluoride abstraction to produce the $[(CH_2CH_3)_3NH^+ + F^-]$ ion pair. Subsequent elimination of BF and BF_3 units from

$B_{12}F_{12}^-$ and $B_{12}F_{11}^-$ yield the features to lower *m/z* in the mass spectrum. Similar observations were previously made in CID studies.[221] The formation of a water adduct is also observed in the case of the chlorinated analogue (as expected based on previous work).[220] Moreover, there are numerous peaks in the low *m/z* region of the mass spectrum indicating the production of $[B_{12}Cl_n(OH)_{n-m}]^-$ ($n+m = 11$) fragments owing to HCl elimination following complexation with water.

At the density functional level of theory, the computed ground states of $[(CH_2CH_3)_3NH{\bullet}B_{12}F_{12}]^-$ (see Figure 5.19) and $[(CH_2CH_3)_3NH{\bullet}B_{12}Cl_{12}]^-$ both exhibit localization of the charge carrying proton at the lone pair of the triethylamine nitrogen. Furthermore, in both complexes, the N–H bond is oriented towards the perhalogenated cage participating in what appears to be N–H•••X hydrogen bonding. This is supported by the fact that N–H•••F–B internuclear separation of 2.25 Å in $[(CH_2CH_3)_3NH{\bullet}B_{12}F_{12}]^-$ is substantially less than the sum of the van der Waals radii for F (1.47 Å) and H (1.20 Å).[253,254] Similarly, in $[(CH_2CH_3)_3NH{\bullet}B_{12}Cl_{12}]^-$, the N–H•••Cl–B internuclear separation of 2.78 Å is significantly less than the sum of the van der Waals radii for Cl (1.75 Å) and H. Of course, binding in these complexes is expected to be predominantly associated with the Coulombic attraction between the dianion and the monocation. To investigate this further, NBO analyses were conducted for both the fluorinated and chlorinated complexes. Within the NBO framework, one can estimate the energy of hydrogen bonding / charge transfer interactions via a second order perturbation theory treatment of the Fock matrix as per Eq. 2.5 (Section 2.1.4). Using this approach, H-bonding interaction energies of 42.4 kJ mol^{-1} and 63.7 kJ mol^{-1} are calculated for $[(CH_2CH_3)_3NH{\bullet}B_{12}F_{12}]^-$ and $[(CH_2CH_3)_3NH{\bullet}B_{12}Cl_{12}]^-$, respectively. Figure 5.19 shows an overlap of the HOMO and LUMO+6 orbitals, which contribute to H-bonding in the fluorinated derivative. Subtracting these values from the calculated electronic dissociation energies for production of $B_{12}X_{12}^{2-}$ +

$HN(CH_2CH_3)_3^+$ yields the electrostatic contributions to binding in the respective complexes. for $[(CH_2CH_3)_3NH{\bullet}B_{12}F_{12}]^-$, where $D_e = 593.7$ kJ mol^{-1} to the charge separated threshold, electrostatic interactions contribute 551.5 kJ mol^{-1} to the total binding energy of the complex. This is in decent agreement with a rough approximation of the energy of attraction (eqn. 4) between a charge of $-2e$ at the center of the boron cage and a charge of $+1e$ at the center of mass for the triethylammonium moiety (separation of 5.08 Å; interaction energy of 547.4 kJ mol^{-1}). In the chlorine analog D_e = 542.4 kJ mol^{-1} and therefore electrostatic interactions contribute 478.7 kJ mol^{-1}. Once again approximating the system as two point-charges separated by the distance between the chlorine cage center of mass and the triethylammonium center of mass (5.83 Å) we find agreement with Coulomb's law of electrostatic attraction (Eq. 5.3) which estimates an interaction energy of 476.7 kJ mol^{-1}.

$$U_E(r) = \frac{1}{4\pi\varepsilon_0}\frac{q_1 q_2}{r} \qquad \text{Eq. 5.3}$$

In Eq. 5.3, $\varepsilon_0 = 8.854187817\text{x}10^{-12}$ C^2 J^{-1} m^{-1} is vacuum permittivity, $q_1 = 2e$ C and $q_1 = 1e$ C are the charges on the two particles of interest, $e = 1.602176634\text{x}10^{-19}$ C is the absolute value of the charge of an electron, and r is the separation distance of the two particles.

Additional support for H-bonding between the $B_{12}X_{12}^{2-}$ and $HN(CH_2CH_3)_3^+$ moieties is provided by QTAIM analyses.[23,31] Figure 5.19 provides a plot showing bond critical points (BCPs; light green), ring critical points (RCPs; red), and cage critical points (CCPs; blue) as determined via topological analysis of the electron density of $[(CH_2CH_3)_3NH{\bullet}B_{12}F_{12}]^-$. The charge densities ($\rho$) and the Laplacians ($\nabla^2\rho$) of the BCPs are provided in Table 5.8. For covalent interactions, electron densities on the order of $\rho > 10^{-1}$ a.u. and a negative value of $\nabla^2\rho$ is expected: a negative value of $\nabla^2\rho$ indicates a concentration of electron density at the BCP, as expected for a covalent (shared electron density) interaction.[26] In contrast, hydrogen bonding and van der Waals

interactions exhibit positive values of $\nabla^2\rho$ and lower electron densities at the BCP; typically $\rho \approx 10^{-3} - 10^{-2}$ a.u. for H-bonds. It is clear from Table 5.8 that AIM analyses yield ρ in the appropriate range and the correct sign of $\nabla^2\rho$ for H-bonding interactions between the $B_{12}X_{12}^{2-}$ and $HN(CH_2CH_3)_3^+$ moieties. The study by Fedorova *et al.* determined an electron density of 0.096 a.u. and sum of the Laplacian of 0.137 a.u. at the BCP of the N-H•••O hydrogen bond found between $HN(CH_2CH_3)_3^+$ and H_2PO_3. This is substantially larger than the values reported below, even when one considers that the N-H is participating in three simultaneous H-bonds with the X atoms on $[B_{12}X_{12}]^{2-}$.

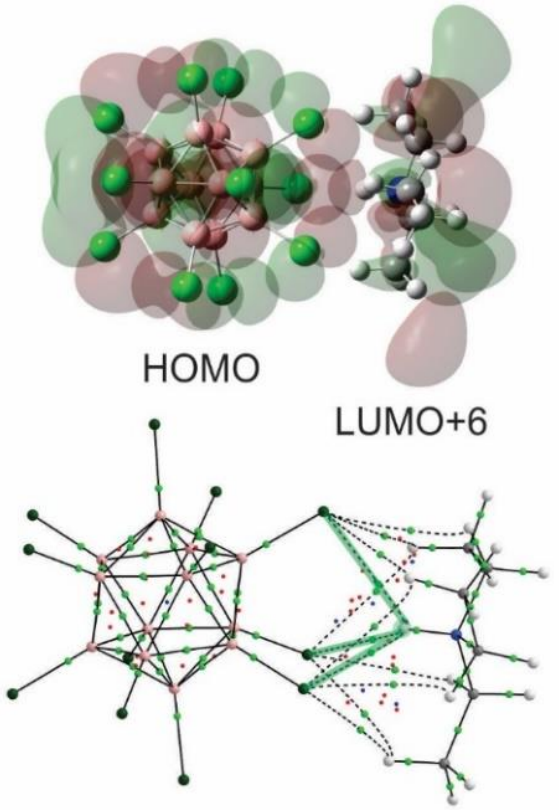

Figure 5.19 (Top) An overlay of the HOMO and LUMO+6 of $[(CH_2CH_3)_3NH{\bullet}B_{12}F_{12}]^-$, which contribute to hydrogen bonding between the $B_{12}F_{12}^{2-}$ and $(CH_2CH_3)_3NH^+$ moieties. Note the orbital overlap near the charge-carrying proton. (Bottom) A plot showing bond critical points (BCPs; light green), ring critical points (RCPs; red), and cage critical points (CCPs; blue) as yielded via QTAIM analysis. NH•••BF hydrogen bonds are highlighted in green. Dashed lines show non-covalent bond paths between the $B_{12}F_{12}^{2-}$ and $(CH_2CH_3)_3NH^+$ moieties.

Table 5.8 Analysis of hydrogen bond critical points in $[(CH_2CH_3)_3NH{\bullet}B_{12}X_{12}]^-$ (X = F, Cl). Electron densities (ρ) and the Laplacians ($\nabla^2\rho$) are reported as averages of multiple similar interactions.

Complex	Interaction	ρ	$\nabla^2\rho$
$[(CH_2CH_3)_3NH{\bullet}B_{12}F_{12}]^-$	NH•••FB	0.0085	0.0256
	CH_3•••FB	0.0063	0.0193
	CH_2•••FB	0.0081	0.0271
$[(CH_2CH_3)_3NH{\bullet}B_{12}Cl_{12}]^-$	NH•••ClB	0.0127	0.0480
	CH_3•••ClB	0.0083	0.0303
	CH_2•••ClB	0.0102	0.0420

5.5.2 Conclusions

The IRMPD action spectra and supporting DFT calculations of $[(CH_2CH_3)_3NH{\bullet}B_{12}X_{12}]^-$ (X = F, Cl) shows that the triethylammonium moiety is oriented so as to direct the N–H bond towards a triangular face of the dodecaborate cage. Fragmentation of the complexes proceeds via the two lowest energy dissociation pathways, namely, proton-transfer to produce $[HB_{12}X_{12}]^-$ (X = F, Cl) and charge-transfer to yield $[B_{12}X_{12}]^-$ (X = F, Cl). In the case of the proton-transfer dissociation channel, HX elimination yields electrophilic $[B_{12}X_{11}]^-$ (X = F, Cl) species that subsequently react with trace water vapor in the ion trap to form water adducts and hydroxylated dodecaborates. One can exercise some control over the fragmentation of these species by tuning the power of the interrogating laser and/or selecting the vibrational transition utilized for IRMPD; lower laser powers and weaker transitions (*viz*. triethylammonium bands) favor the lowest energy proton-transfer dissociation channel, whereas higher laser powers and stronger transitions facilitate production of $[B_{12}X_{12}]^-$ (X = F, Cl) and associated fragments via the second-lowest charge-transfer (*i.e.*, redox) threshold. Under no conditions were the products of the impulsive, charge separated product channel observed (*i.e.*, formation of $B_{12}X_{12}^{2-}$). This is consistent with the observations of analogous transition metal-containing clusters, where IRMPD resulted in charge transfer from the dodecaborate to the metal ion. The fact that $B_{12}X_{12}^{2-}$ (X = H, F, Cl, Br, I) species

behave as weakly coordinating anions in the solution phase suggests that the local interactions of solvent molecules substantially affects the physicochemical properties of these ions in the condensed phase.

NBO and QTAIM analyses of the geometry optimized global minima for $[(CH_2CH_3)_3NH{\bullet}B_{12}X_{12}]^-$ (X = F, Cl) indicate that charge separation persists in the electronic ground state – charges of *ca*. –1.95*e* and +0.95*e* are calculated for the $B_{12}X_{12}$ (X = F, Cl) and $(CH_2CH_3)_3NH$ moieties, respectively – and that hydrogen bonding provides stabilization in both complexes. Nevertheless, bonding in the complexes is dominated by Coulombic and higher multipolar (*e.g.*, charge-dipole) interactions, which account for in excess of 90 % of the interaction energies in the clusters.

5.6 All-*cis* 1,2,3,4,5,6-Hexafluorocyclohexane $B_{12}H_{12}^{2-}$ Clusters

5.6.1 Results and Discussion

Injection of a solution containing $K_2B_{12}H_{12}$ and **1** into the electrospray ionization source produced the mass spectrum shown in Figure 5.20. The spectrum shows clusters of $[\mathbf{1}_n \bullet B_{12}H_{12}]^{2-}$ n = 1 – 4, with no evidence of the production of clusters with n ≥ 5 suggesting the completion of a solvation shell at n = 4. This mixture also did not produce any intensity for bare $[B_{12}H_{12}]^{2-}$ or $[B_{12}H_{12}]^{-}$ species. These observations contrast the observations of the analogous study on $[\mathbf{1}_n \bullet B_{12}F_{12}]^{2-}$ n = 1 – 3 by Lecours *et al.*[7] The observed mass spectrum in that study showed $[B_{12}F_{12}]^{2-}$ and $[\mathbf{1}_n \bullet B_{12}F_{12}]^{2-}$ n = 1 – 3; the lack of a n = 4 cluster led to the conclusion that the solvation shell of **1** around $[B_{12}F_{12}]^{2-}$ was completed at n = 3. DFT binding energies for loss of one molecule of **1** from $[\mathbf{1}_n \bullet B_{12}X_{12}]^{2-}$ (X = H, F) (n = 1 – 5) provide insight for these observations; these results are discussed below.

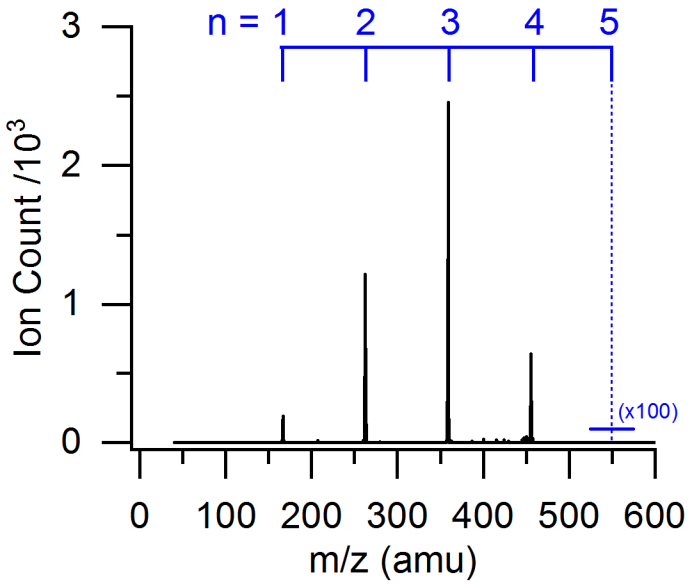

Figure 5.20 Mass Spectrum of $[\mathbf{1}_n \bullet B_{12}H_{12}]^{2-}$ (n = 1 – 4) clusters obtained from a Bruker Esquire 3000+ QIT. $[\mathbf{1}_5 \bullet B_{12}H_{12}]^{2-}$ was not observed.

The clusters observed in the mass spectrum shown in Figure 5.20 were isolated and interrogated with the output of the CLIO FEL in the range of 800 cm^{-1} – 1500 cm^{-1}. Figure 5.21 shows how the mass spectrum of isolated $[\mathbf{1}_4 \bullet B_{12}H_{12}]^{2-}$ changes as a function of the FEL wavenumber. When the FEL is off resonance with a normal mode, the $[\mathbf{1}_4 \bullet B_{12}H_{12}]^{2-}$ parent ion is observed as well as $[\mathbf{1}_3 \bullet B_{12}H_{12}]^{2-}$ at 20 % of the parent ion intensity presumably produced by in trap fragmentation *via* collision induced dissociation and/or blackbody infrared dissociation.[31,85-88] The presence of $[\mathbf{1}_3 \bullet B_{12}H_{12}]^{2-}$ when off resonance indicates a weak binding energy of **1** in $[\mathbf{1}_4 \bullet B_{12}H_{12}]^{2-}$, suggesting that the fourth **1** molecule is actually part of the second solvation shell or perhaps there are two binding motifs. When the FEL output is resonant with any vibrational transition of the cluster in the probed spectral region, an increased amount of $[\mathbf{1}_3 \bullet B_{12}H_{12}]^{2-}$ is observed. Excitation of specific vibrational bands are required to produce $[\mathbf{1}_2 \bullet B_{12}H_{12}]^{2-}$ and $[\mathbf{1} \bullet B_{12}H_{12}]^{2-}$ fragments. However, given that IR excitation to produce $n = 1$ clusters also produces $n = 2$ and 3 clusters, it is likely that excitation at these wavenumbers deposits enough energy in the parent to induce sequential loses of **1**. Alternatively, owing to spectral similarities amongst the clusters, it could be that the product cluster absorbs at the same wavenumber as the parent (see Figure 5.23). A substantial number of photons may be required to induce the loss of three **1** molecules. In order to absorb many photons, either a high intensity IR field or a high absorption cross section is required. The latter suggests a normal mode with a large transition dipole moment may be responsible for bands at *ca.* 1050 cm^{-1} and *ca.* 1250 cm^{-1}. To model IR absorption, vibrational spectra were calculated for the global minimum geometries identified by DFT. Furthermore, thresholds for the loss of a single **1** molecule from $[\mathbf{1}_n \bullet B_{12}H_{12}]^{2-}$ to produce $[\mathbf{1}_{n-1} \bullet B_{12}H_{12}]^{2-}$ have been calculated and are discussed below.

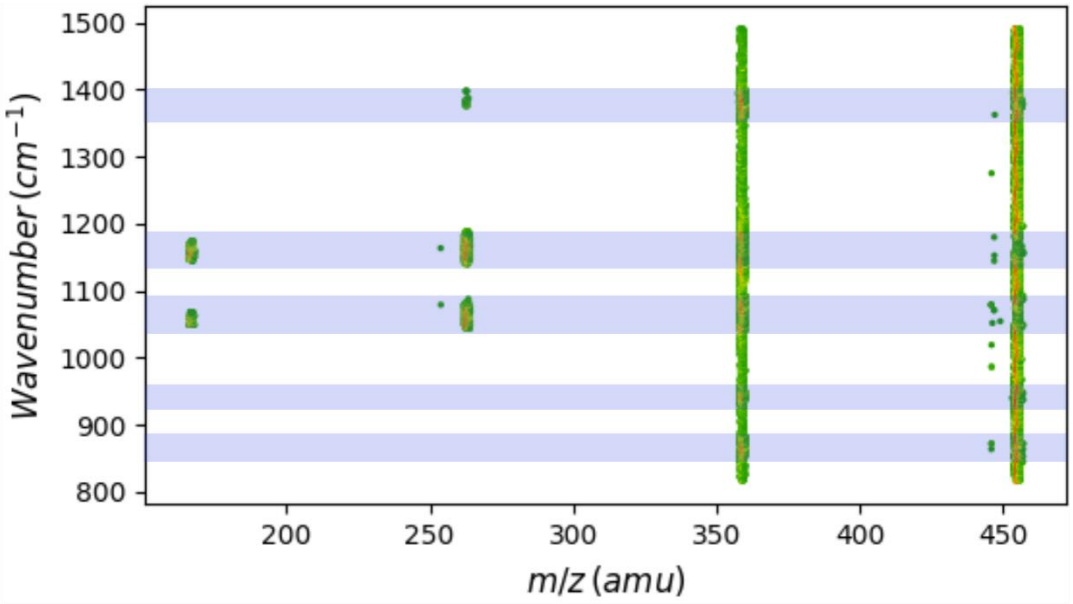

Figure 5.21 A 2-D IR/MS plot showing mass spectrum as a function of FEL wavenumber in the region of 800 cm^{-1} – 1500 cm^{-1} of [**1**$_4$•$B_{12}H_{12}$]$^{2-}$. Normalized ion count is represented by the colour scale with 1.0 represented by red and 0.05 representing by green. Blue highlights indicate resonant absorption of photons which leads to fragmentation.

IRMPD interrogation of $[B_{12}H_{12}]^{2-}$ was also conducted to record the spectrum of the uncomplexed dianion. The mass spectrum of $[B_{12}H_{12}]^{2-}$ when irradiated with 1050 cm^{-1} photons is given in Figure 5.22 and assignment of the fragmentation peaks is given in Table 5.9. The fragmentation peaks, which are singly charged, are assigned to species which have exchanged a hydrogen atom for a hydroxide group or a molecular nitrogen group, both of which are likely to exist in the ion trap. This behaviour has been observed previously by Warneke *et al.* who studied the gas phase reactivity of $[B_{12}X_{12}]^{2-}$ X = F, Cl, Br, and I.[221] They reported a tendency of $[B_{12}X_{12}]^{2-}$ to undergo exchange reactions in which halogen atoms are traded for N_2, OH, and/or a combination of both.

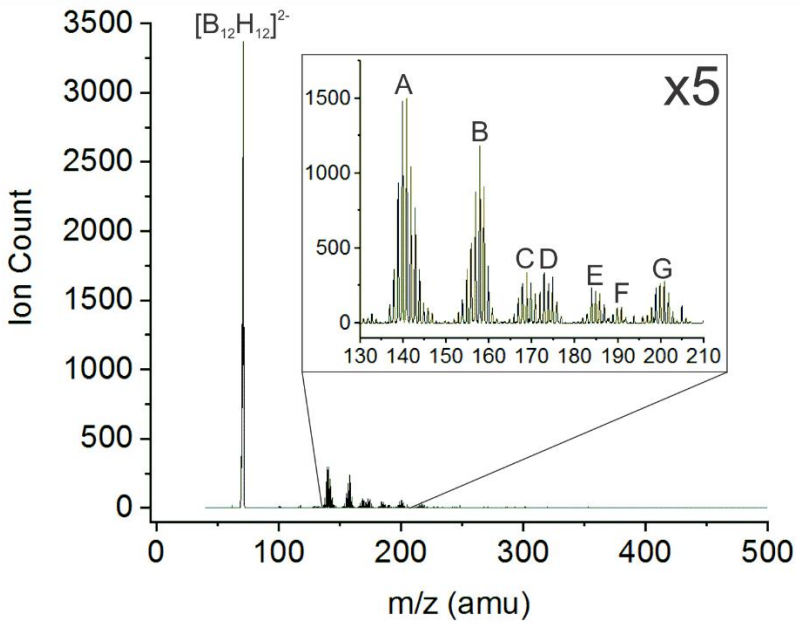

Figure 5.22 Trapped $[B_{12}H_{12}]^{2-}$ ions of m/z = 71 amu irradiated with 1050 cm^{-1} photons. All peaks in inset are singly charged and assigned in Table 5.9.

Table 5.9 Assignment of fragment peaks resulting during irradiation of $[B_{12}H_{12}]^{2-}$. All assignments are for singly charged ions.

Peak	Assignment	Nominal Mass (amu)
A	$B_{12}H_{12}$	142
B	$B_{12}H_{11}OH$	158
C	$B_{12}H_{11}N_2$	169
D	$B_{12}H_{10}(OH)_2$	174
E	$B_{12}H_{10}N_2(OH)$	185
F	$B_{12}H_9(OH)_3$	190
G	$B_{12}H_9N_2(OH)_2$	201

The IRMPD spectrum of un-complexed $[B_{12}H_{12}]^{2-}$, the black trace in the n = 0 panel of Figure 5.23, shows only one broad (50 cm^{-1}) feature centered at 1054 cm^{-1}. This spectrum was reasonably well predicted by the DFT calculations which show only one unscaled peak at 1066 cm^{-1} within the probed IR region. DFT has assigned the peak to the triply degenerate T_{1u} cage breathing mode. As previously mentioned, the width of this feature in the experimental spectrum is due to the presence of isotopologues. The ^{11}B:^{10}B ratio is approximately 4:1 which

results in numerous isotopologues and isotopomers with slightly different vibrational frequencies. Calculation of the vibrational frequencies for $[^{10}B_{12}H_{12}]^{2-}$ and $[^{11}B_{12}H_{12}]^{2-}$ predict the T_{1u} mode of the lighter all ^{10}B cage to be blue shifted by 50 cm^{-1} compared to the T_{1u} mode of the heavier all ^{11}B cage.

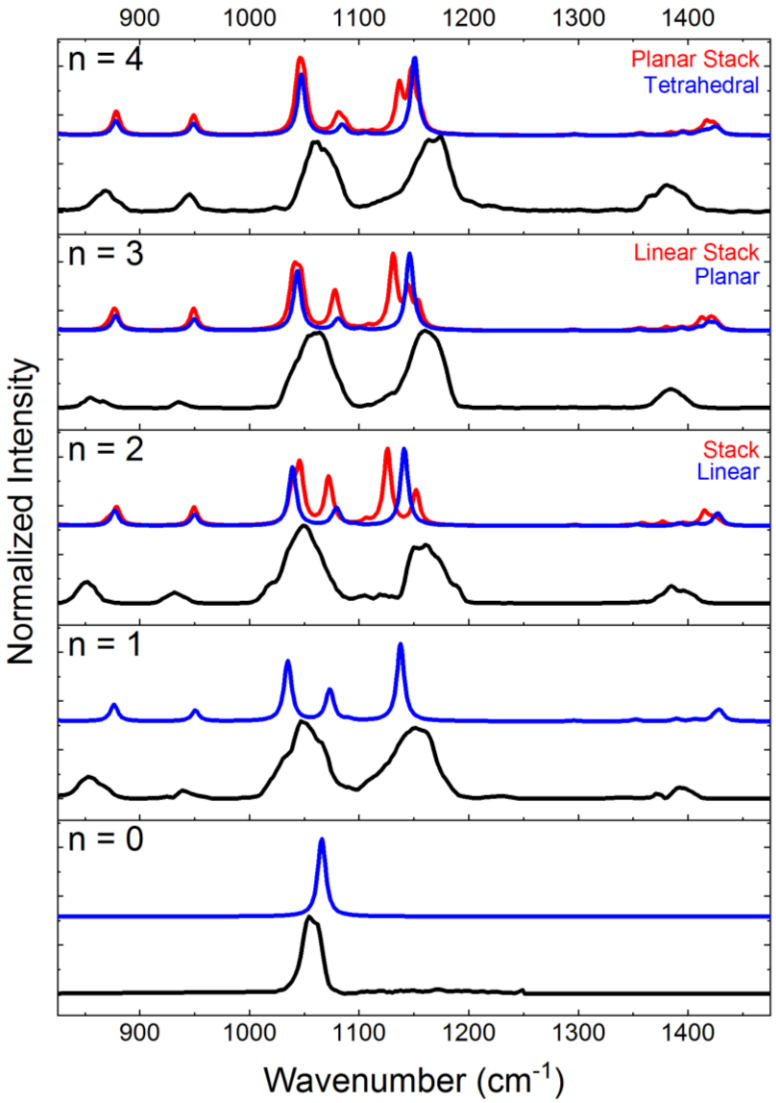

Figure 5.23 (**Black**) IRMPD spectra of $[\mathbf{1}_n \bullet B_{12}H_{12}]^{2-}$ (n = 0 – 4). (**Blue**) Predicted vibrational spectra of the DFT identified global minimum geometries for the same species. (**Red**) Predicted vibrational spectra of higher energy isomers involving the stacking of **1**. All calculations were performed at the B3LYP/6-311++G(d,p) level of theory.

The IRMPD spectra for $[\mathbf{1}_n \bullet B_{12}H_{12}]^{2-}$ (n = 1 – 4) are also provided in Figure 5.23. The four spectra are similar to one another differing only by relative bound intensity. We may therefore hypothesize that binding of **1** to $[B_{12}H_{12}]^{2-}$ occurs in a similar manner across all cluster sizes. DFT calculations allow us to test this hypothesis by energetically comparing isomers with different binding motifs and predicting the associated IR spectra for comparison with experiment. The blue traces in Figure 5.23 are the calculated spectra for the lowest energy isomers which adopt similar geometries to those identified by Lecours *et al.* for $[\mathbf{1}_n \bullet B_{12}F_{12}]^{2-}$ n = 1 – 3. Molecules of **1** prefer to bind to $[B_{12}F_{12}]^{2-}$ by the hydrogen face, which possesses a partial positive charge; the dipole moment is calculated to be *ca.* 7.3 Debye.[7] Complexed molecules of **1** adopt the chair conformation rather than the twist boat conformation, which is energetically disfavoured by 20 kJ mol^{-1}. The chair conformation of **1** allows for the three axial hydrogen atoms to interlock with three fluorine atoms of $[B_{12}F_{12}]^{2-}$ creating six hydrogen bonding interactions. This same binding motif is also adopted by the analogous $[B_{12}H_{12}]^{2-}$ complexes as this arrangement facilitates stabilizing dihydrogen bonding interactions (see Figure 5.24).

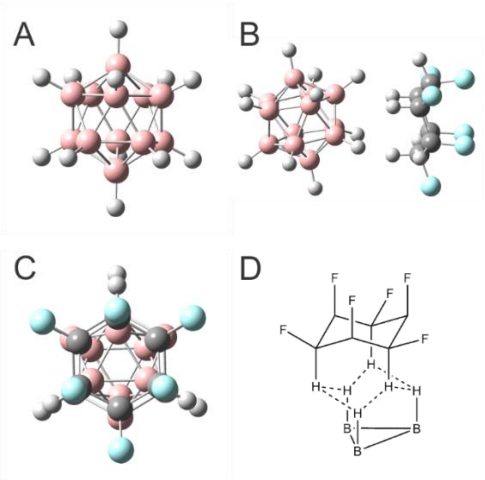

Figure 5.24 **A** Geometry optimized $B_{12}H_{12}^{2-}$ **B** Side and **C** Front views of the $[\mathbf{1} \bullet B_{12}H_{12}]^{2-}$ cluster **D** Binding motif between **1** and $B_{12}H_{12}^{2-}$ which involves CH•••HB interactions. All structures have been optimized at the B3LYP/6-311++G(d,p) level of theory.

Experimental results from Lecours *et al.* suggested the completion of the first solvation shell of **1** around $[B_{12}F_{12}]^{2-}$ occurred at $n = 3$. They found no evidence of $[1_4 \bullet B_{12}F_{12}]^{2-}$ in the QIT at the CLIO facility. Their computational study revealed a $[1_4 \bullet B_{12}F_{12}]^{2-}$ cluster with all four **1** molecules interacting directly with $[B_{12}F_{12}]^{2-}$ is geometrically feasible. However, the solvation shell became kinetically trapped at $n = 3$ due to the rigidity of the intermolecular bonding. What was absent in that study was an investigation of the second solvation shell. Here, we study a possible arrangement of the second solvation shell in which molecules of **1** are stacked on one another (see Figure 5.27). The predicted vibrational spectra for the lowest energy stack isomers of $[1_n \bullet B_{12}H_{12}]^{2-}$ $n = 2 – 4$ appear in Figure 5.23 as red traces.

Comparison of the theoretical DFT frequencies for different isomers to the experimentally collected spectra allows for identification of the geometric isomers being probed by IRMPD. It is clear from Figure 5.23 that the experimental spectra of each cluster size best matches the calculated spectrum of the global minimum geometries identified by DFT. Stacking **1** molecules is computationally predicted to lift the degeneracy of fundamental transitions occurring in the region of 1110 cm^{-1} to 1160 cm^{-1}. The presence of stack isomers is unlikely as the experimental peak in that region does not show any splitting. However, due to the large width of the experimental peak, stack isomers cannot be ruled out based on the IRMPD spectra reported here.

The frequency calculations conducted on the global minimum isomers have been useful in assigning the experimental IRMPD spectra. The band at *ca.* 850 cm^{-1} in the IRMPD spectra is assigned to several overlapping transitions which involve group CH wagging motions (calculated at 877 cm^{-1}). At *ca.* 940 cm^{-1} in the IRMPD spectra, a peak appears and is assigned to a symmetric stretch of the CH_{axial} groups away from the center of the ring (calculated to occur at 950 cm^{-1}). The band at 1049 cm^{-1} has a width of *ca.* 100 cm^{-1} for $n = 1$ and shifts to 1060 cm^{-1} (narrowing

to FWHM ≈ 60 cm^{-1}) by n = 4. The CLIO bandwidth is typically ~ 25 cm^{-1}.[49,176,179] The larger bandwidth observed here is due to overlapping bands and isotopic effects. Overlapping bands in this region are group stretching of the bonds between carbon and equatorial fluorine atoms (C-F_{eq}) in **1** and the three breathing modes of $[B_{12}H_{12}]^{2-}$ which compose the T_{1u} mode in the bare cage. In $[\mathbf{1}\bullet B_{12}H_{12}]^{2-}$ the fundamental transitions of the C-F_{eq} modes are calculated to form a band at 1035 cm^{-1} (see Figure 5.23, n = 1, blue trace). In free **1** (*i.e.* not complexed to $[B_{12}H_{12}]^{2-}$ or another **1**) the C-F_{eq} band is calculated to occur at 1070 cm^{-1}; complexation of $[B_{12}H_{12}]^{2-}$ red shifts the frequency of this transition by 35 cm^{-1}. Every **1** molecule added to $[\mathbf{1}_n\bullet B_{12}H_{12}]^{2-}$ increases the frequency of the C-F_{eq} stretching modes by 3 – 5 cm^{-1} (see Table 5.10) blue shifting the frequency towards that in free **1**. This indicates a reduction of the interactions between **1** and $[B_{12}H_{12}]^{2-}$, a pattern that is observed for most of the vibrational bands (see Table 5.10). The three breathing modes in the bare dianion are calculated to have a degenerate fundamental transition at 1066 cm^{-1}. Complexation of **1** to $[B_{12}H_{12}]^{2-}$ blue shifts the wavenumber of the fundamental transition from 1066 cm^{-1} to 1073 cm^{-1} and slightly (< 5 cm^{-1}) lifts the degeneracy. Each additional **1** causes a further blue shift of the fundamental band by 3 – 6 cm^{-1}. At 1160 cm^{-1} a transition associated with stretching of the C-F_{axial} bonds of **1** is observed. This transition behaves in the same manner as the C-F_{eq} transition with respect to its wavenumber in free **1** and how the wavenumber changes with the number of **1** molecules bound to the cage. The highest wavenumber band observed in the probed region, centered at 1390 cm^{-1}, is assigned to group wagging of the hydrogen atoms on **1**. The wavenumber equatorial hydrogen wag adheres to the same pattern as the C-F_{eq} and C-F_{ax} stretches. The wavenumber of the axial hydrogen wag fundamental transition is blue shifted from its value in free **1**, 1397 cm^{-1}, to 1428 cm^{-1} in $[\mathbf{1}\bullet B_{12}H_{12}]^{2-}$. The wavenumber of this transition decreases, heading toward the value in free **1**, as the number of **1**s around $[B_{12}H_{12}]^{2-}$ increases.

This vibration is dampened due to the engagement of the axial hydrogen atoms by the hydrogen atoms of the $[B_{12}H_{12}]^{2-}$ cage and this engagement lessens as more **1** surround the cage. These observations of the change in computed wavenumber with n lead to the expectation that the magnitude of bonding interactions between **1** and $[B_{12}H_{12}]^{2-}$ in $[\mathbf{1}_n \bullet B_{12}H_{12}]^{2-}$ should similarly decrease with increasing n.

Table 5.10 DFT predicted frequencies for vibrational normal modes in $[\mathbf{1}_n \bullet B_{12}H_{12}]^{2-}$ $n = 1 - 4$, $[B_{12}H_{12}]^{2-}$, and **1**. Calculations were done at the B3LYP/6-311++G(d,p) level of theory and all values are in units of cm^{-1}.

n	$C\text{-}F_{eq}$ stretch	$C\text{-}F_{ax}$ stretch	H_{eq} wag	H_{ax} wag	$[B_{12}H_{12}]^{2-}$ T_{1u} Components		
1	1035	1137	1390	1428	1071	1074	1074
2	1039	1141	1392	1427	1076	1080	1080
3	1044	1150	1390	1420	1079	1080	1083
4	1047	1151	1395	1418	1084	1084	1086
Free **1**	1070	1180	1410	1397			
Free $[B_{12}H_{12}]^{2-}$					1066	1066	1066

An explanation for the behaviour of the $[B_{12}H_{12}]^{2-}$ T_{1u} components in $[\mathbf{1}_n \bullet B_{12}H_{12}]^{2-}$ $n = 0 - 4$ comes from consideration of the dependence of vibrational spacings in the Morse potential on the energy at a displacement of the normal mode coordinate, q. In Figure 5.25, a red Morse potential represents the T_{1u} normal mode of bare $[B_{12}H_{12}]^{2-}$. When **1** is bound to the cage the energy of the Morse potential is increased at coordinates larger than equilibrium due to a repulsive energy term. The repulsive energy is caused by the nuclei of the cage-bound hydrogen atoms translating well within the van der Waals radii of the **1**-bound hydrogen atoms. As a result, the red Morse potential narrows to become the blue Morse potential. A narrower potential possesses relatively higher energy vibrational states and increased spacing between them, see Figure 5.25. The change in the potential as n increases is observed as blue shifts of the calculated fundamental transition in each cluster.

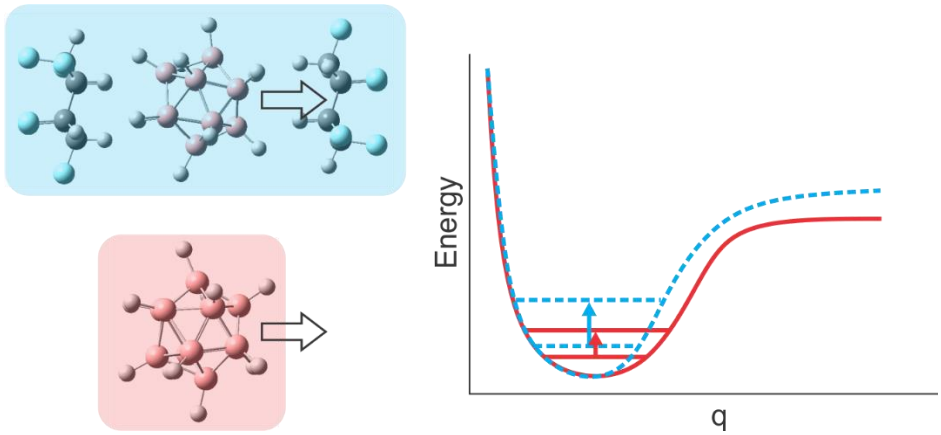

Figure 5.25 Simplification of the T_{1u} normal mode component in $[\mathbf{1}_n \bullet B_{12}H_{12}]^{2-}$ $n = 0$ (**red**) and an analogous mode in $n = 2$ (**blue**) to a Morse potential where q is the normal mode coordinate and the energy is in arbitrary units. The structures are shown at their maximum displacement along the normal mode coordinate, indicated by arrows.

Photoelectron (PE) spectroscopy of $[\mathbf{1}_n \bullet B_{12}F_{12}]^{2-}$ $n = 0 - 4$ and $[\mathbf{1}_n \bullet B_{12}H_{12}]^{2-}$ $n = 0 - 5$ was conducted in collaboration with Jonas Warneke at Pacific Northwest National Laboratories. Figure 5.26 presents the PE spectra of the fluorinated and hydrogenated boron cage complexes as black traces and the computed density of electronic states as red traces. Single point energy calculations were conducted on the $[\mathbf{1}_n \bullet B_{12}X_{12}]^-$ anion using the global minimum geometry of the dianion. The energy of each anion MO is relative to the HOMO of the dianion and are shifted by the difference in the total electronic energy between the anion and the dianion. The intensities are generated by convolution of Gaussian distributions (width of 0.25 eV) centered on the relative energies of the anion MOs. The onset of a feature in the PE spectra indicates the lowest energy ionization threshold and they are consistently predicted by our simulations. Only one broad feature appeared in the PE spectra of the fluorinated clusters while two features were present in the hydrogenated spectra. The ionization threshold increases consistently by ~ 0.7 – 0.8 eV with each additional **1** molecule until $n = 4$ where the increase in ionization threshold is reduced to ~ 0.5 eV. This change in ionization behaviour suggests that the fourth moiety of **1** binds in a different environment than that the first three molecules for both the fluorinated cage and hydrogenated cage clusters. A

different environment maybe provided by a new solvation shell beginning at $n = 4$. The simulations in no way account for transition probabilities (*i.e.*, vibrational wave function overlap) and therefore the number of features is overestimated as some transitions from the dianion HOMO to a particular anion MO will have a transition probability of zero. Work on more intensive methods for predicting PES is underway in the Hopkins group such as; reoptimizing the geometry at the −1 charge, use of time-dependent DFT, and calculation of the Franck-Condon factors which should govern the transition intensity.

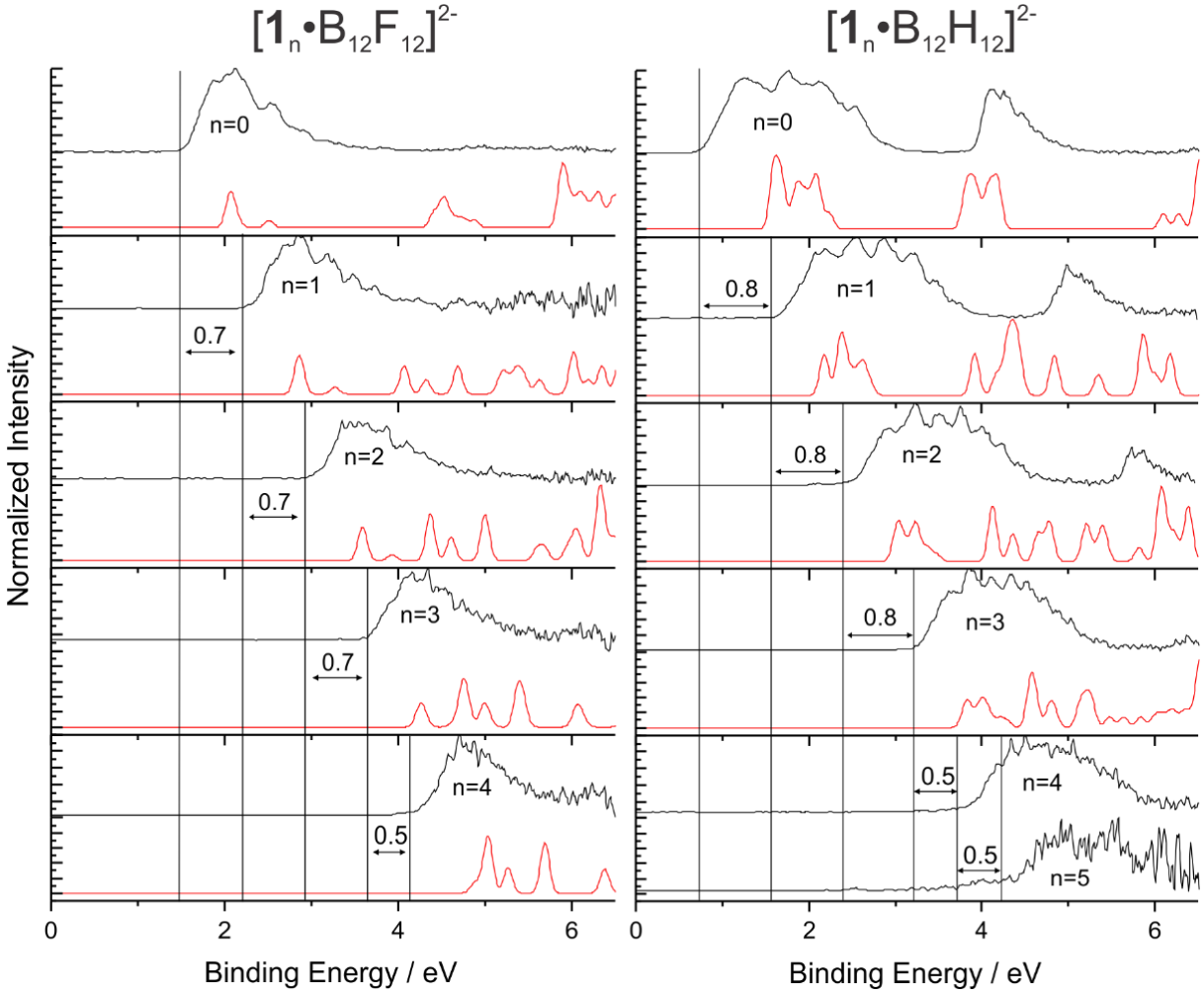

Figure 5.26. Photoelectron spectra of (left) $[\mathbf{1}_n{\bullet}B_{12}F_{12}]^{2-}$ n = 0 – 4 and (right) $[\mathbf{1}_n{\bullet}B_{12}H_{12}]^{2-}$ n = 0 – 5. Computational data (red) are predicted vertical detachment energies from the HOMO of the global minimum dianion to the MOs of the geometrically identical monoanion.

The study of $[\mathbf{1}_n \bullet B_{12}F_{12}]^{2-}$ (n = 1 – 3) Lecours *et al*. provided a starting point for the search of the global minimum geometries of $[\mathbf{1}_n \bullet B_{12}H_{12}]^{2-}$ (n = 1 – 5); $[B_{12}H_{12}]^{2-}$ moieties were swapped with the fluorine cages and optimization with frequency calculations were conducted using the latest revision of Gaussian 09, Rev. E. For comparison purposes, the fluorine cage clusters also required optimization using this latest revision. The energetic ordering of the isomers was consistent between the $[\mathbf{1}_n \bullet B_{12}H_{12}]^{2-}$ and $[\mathbf{1}_n \bullet B_{12}F_{12}]^{2-}$ n = 1 – 3 studies; the geometric structures of these species are provided in Figure 5.24, Figure 5.27, and Figure 5.28, respectively. The global minimum linear structure of $[\mathbf{1}_2 \bullet B_{12}H_{12}]^{2-}$ was favoured over the bent structure with a difference in Gibbs' energy of 2.2 kJ mol^{-1} at 298 K (see Figure 5.27). As was the case in the fluorinated cage clusters, the second molecule of **1** prefers to bind three trigonal facial sites away from the first molecule of **1** in $[\mathbf{1}_2 \bullet B_{12}H_{12}]^{2-}$. The higher energy "bent" isomer is generated when the **1** moieties are closer together by only one trigonal facial site. The third molecule of **1** may only bind to the bent geometry which will have a Boltzmann population of 0.41. Binding to the linear geometry is not possible because no trigonal facial site exists with all three cage-hydrogen atoms free from binding with the preexisting **1** moieties. A third isomer, also of "linear" orientation but in this case consisting of stacked **1** moieties bound to the $[B_{12}H_{12}]^{2-}$ dianion, is calculated to lie $\Delta G°$ = 31.8 kJ mol^{-1} above the global minimum (see Figure 5.27).

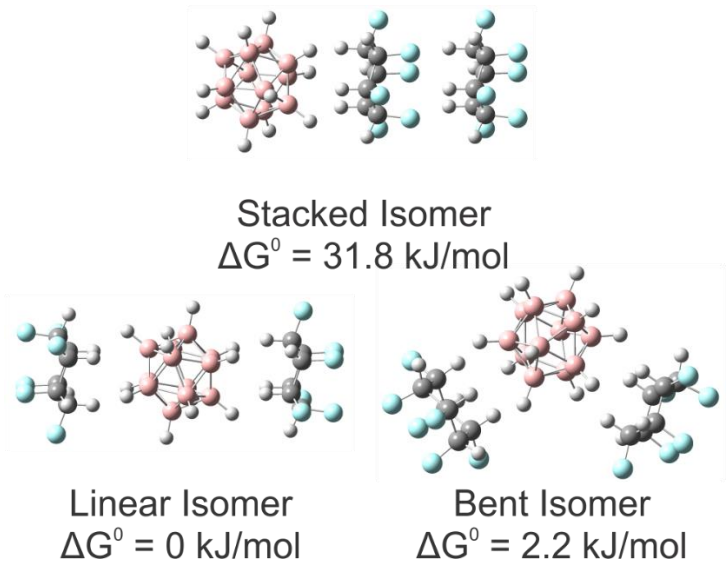

Figure 5.27 Isomers of $[\mathbf{1}_2 \bullet B_{12}H_{12}]^{2-}$ optimized at B3LYP/6-311++G(d,p).

Figure 5.28 presents the geometries and relative free energies for clusters of $[\mathbf{1}_3 \bullet B_{12}H_{12}]^{2-}$. The trigonal planar global minimum was found to be nearly isoenergetic with the trigonal pyramidal isomer (+0.2 kJ/mol) for the fluorine cage analog this difference was found to be 1.4 kJ/mol.[7] Assuming sequential binding of **1**, the route to $[\mathbf{1}_4 \bullet B_{12}H_{12}]^{2-}$ requires the higher energy bent isomer of $[\mathbf{1}_2 \bullet B_{12}H_{12}]^{2-}$ and the higher energy trigonal planar isomer of $[\mathbf{1}_3 \bullet B_{12}H_{12}]^{2-}$ (*i.e.*, the structures with open binding sites) to have appreciable populations. Given that these isomers, which exist above their respective global minimum isomer, are more accessible for $[\mathbf{1}_n \bullet B_{12}H_{12}]^{2-}$ (n = 2 and 3 have Boltzmann populations of 0.41 and 0.92, respectively) than $[\mathbf{1}_n \bullet B_{12}F_{12}]^{2-}$ (n = 2 and 3 have Boltzmann populations of 0.22 and 0.57, respectively), production of $[\mathbf{1}_4 \bullet B_{12}H_{12}]^{2-}$ is conceivable. Stacked isomers for $[\mathbf{1}_3 \bullet B_{12}H_{12}]^{2-}$ are considerably higher in energy. Note that the calculated vibrational spectrum of the trigonal pyramid n = 3 isomer was essentially indistinguishable from that of the trigonal planar isomer (shown in Figure 5.23).

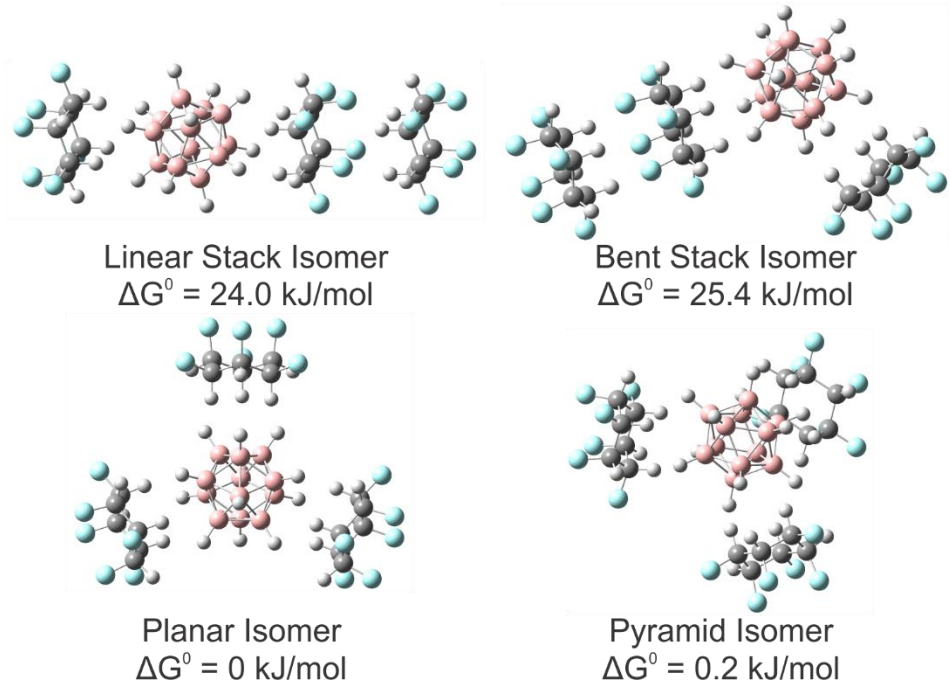

Figure 5.28 Isomers of $[\mathbf{1}_3 \bullet B_{12}H_{12}]^{2-}$ optimized at B3LYP/6-311++G(d,p). Frequency calculations determined the linear stack isomer to be a transition state.

The geometries and relative free energies for isomers of $[\mathbf{1}_4 \bullet B_{12}H_{12}]^{2-}$ are shown in Figure 5.29. The global minimum geometry consists of a tetrahedral arrangement of the four **1** moieties around the $[B_{12}H_{12}]^{2-}$ dianion. Binding of **1** to $[B_{12}H_{12}]^{2-}$ occurs *via* the same interlocking pattern as observed for the smaller cluster sizes. Stacked isomers of $[\mathbf{1}_4 \bullet B_{12}H_{12}]^{2-}$ are much closer in energy to the global minimum than for the smaller cluster sizes. Based on calculated Gibbs' energies (and assuming a Boltzmann population distribution), the tetrahedral isomer is expected to account for 21 % of the cluster population distribution. Meanwhile the planar stacked isomer of $[\mathbf{1}_4 \bullet B_{12}H_{12}]^{2-}$ should only account for 0.6 %. The reported relative energies from the fluorinated study are used to predict a population of the tetrahedral isomer for $[\mathbf{1}_4 \bullet B_{12}F_{12}]^{2-}$ of *ca.* 10 %.

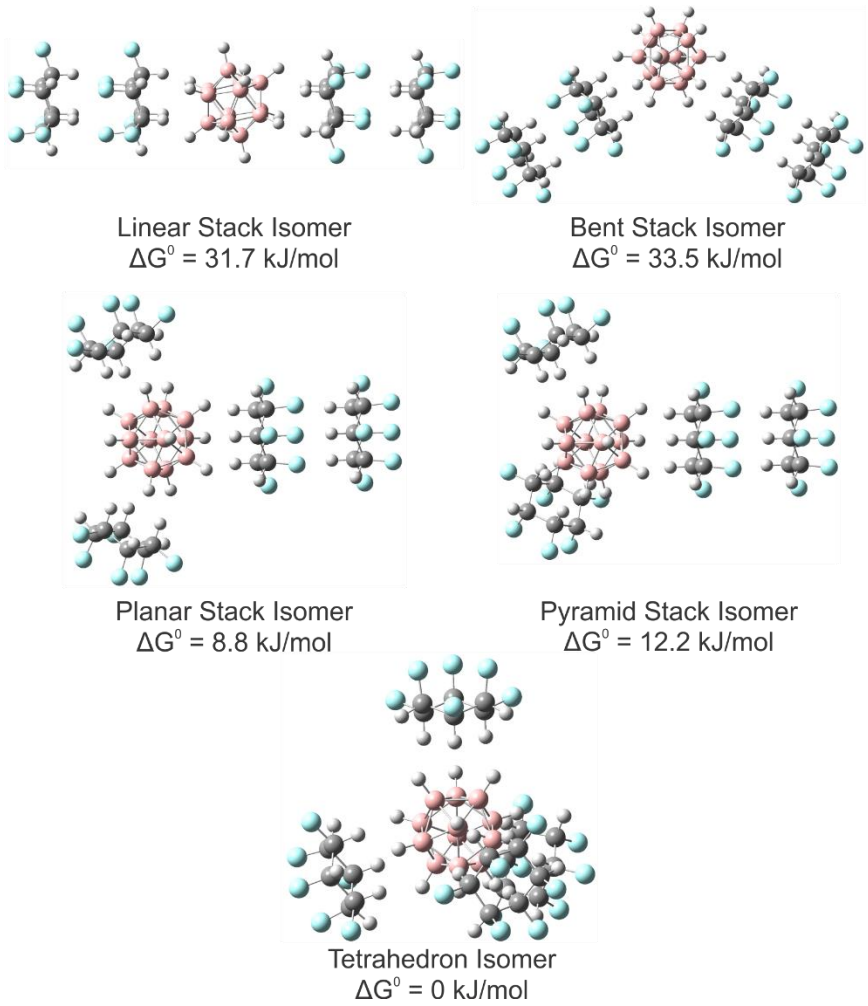

Figure 5.29 Isomers of $[\mathbf{1}_4 \bullet B_{12}H_{12}]^{2-}$ optimized at B3LYP/6-311++G(d,p). Frequency calculations determined the linear stack isomer to be a transition state.

Figure 5.30 provides the optimized geometries and relative electronic energies of $[\mathbf{1}_5 \bullet B_{12}H_{12}]^{2-}$. Here we report electronic energies because frequency calculations would not converge for this cluster size at the level of theory employed. In particular, the presence of imaginary frequencies associated with twisting of the **1** molecules relative to the $[B_{12}H_{12}]^{2-}$ cage was found to cause problems with identifying stable local minima.

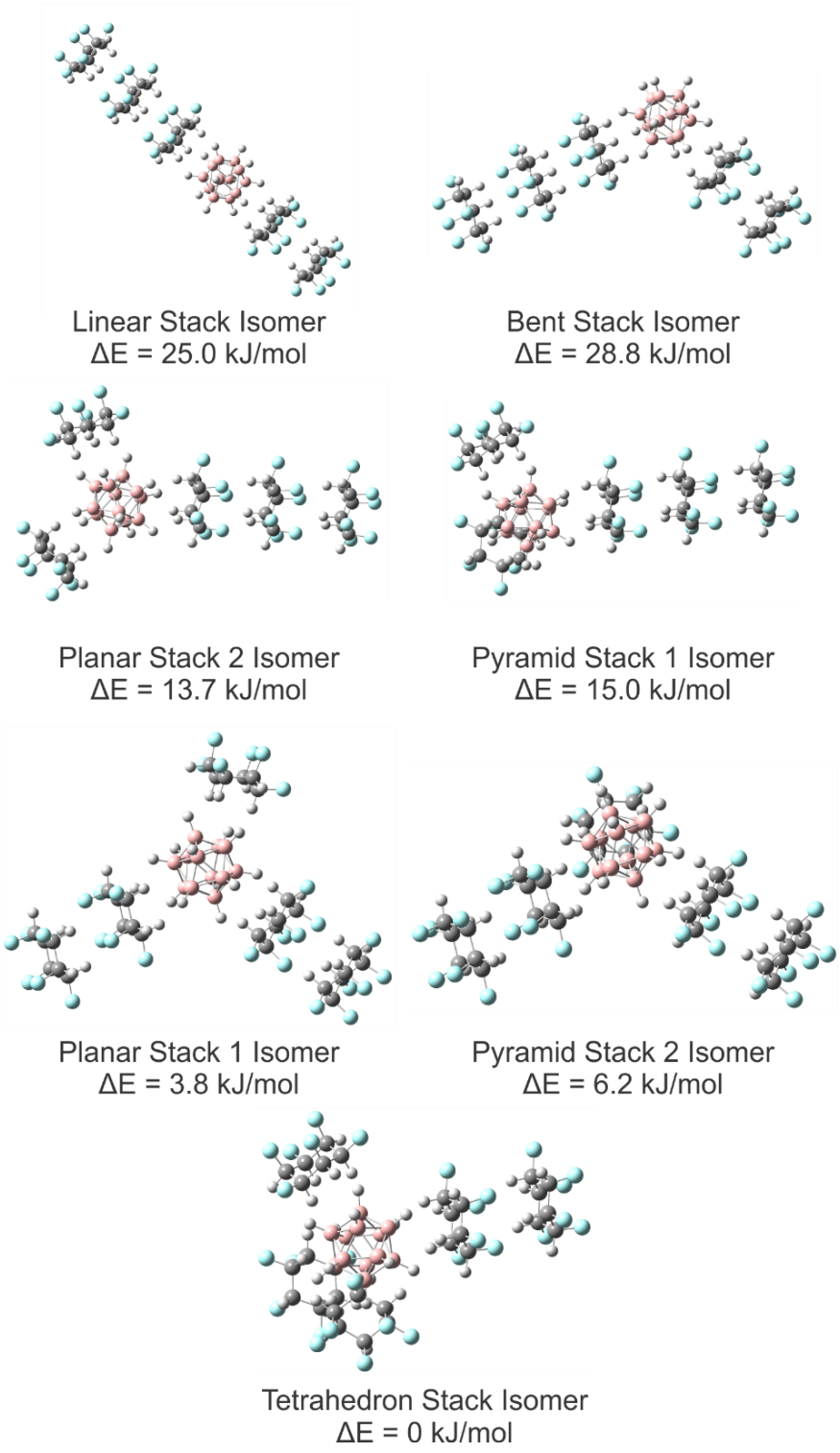

Figure 5.30 Isomers of $[\mathbf{1}_5 \bullet B_{12}H_{12}]^{2-}$ optimized at B3LYP/6-311++G(d,p). Electronic energies relative to the tetrahedron stack isomer are reported as frequency calculations are still in progress.

The dissociation reaction where a single molecule of **1** is lost from $[\mathbf{1}_n \bullet B_{12}H_{12}]^{2-}$ to form $[\mathbf{1}_{n-1} \bullet B_{12}H_{12}]^{2-}$ provides insight into the stability of the $[\mathbf{1}_n \bullet B_{12}H_{12}]^{2-}$ cluster. The calculated energies of these reactions are provided in Table 5.11. In the analogous fluorinated cage study, **1** binds to $B_{12}F_{12}^{2-}$ with a molecular binding enthalpy of $\Delta H° = 160.1$ kJ/mol. To put this binding strength in context, the enthalpy of binding of Cl^- to **1** is $\Delta H° = 156.5$ kJ/mol[8] and to *p*-cyanophenol is $\Delta H^0 = 148$ kJ/mol, which is the largest enthalpy of binding listed on NIST for the chlorine anion.[44,257,258] The enthalpy of binding of $[\mathbf{1} \bullet B_{12}H_{12}]^{2-}$ was found to be $\Delta H° = 177.1$ kJ mol^{-1}.

Table 5.11 Calculated binding energies for loss of a single **1** from $[\mathbf{1}_n \bullet B_{12}H_{12}]^{2-}$ (n = 1 - 5). The B3LYP/6-311++G(d,p) level of theory with empirical dispersion corrections has been used. Thermodynamic corrections were computed using T = 298 K.

Species	D_0 (kJ/mol)	ΔH^0 (kJ/mol)	ΔG^0 (kJ/mol)	S^0 (J/mol•K)
$[\mathbf{1} \bullet B_{12}H_{12}]^{2-}$	179.4	177.1	128.8	606.3
linear $[\mathbf{1}_2 \bullet B_{12}H_{12}]^{2-}$	158.6	155.7	109.3	868.5
bent $[\mathbf{1}_2 \bullet B_{12}H_{12}]^{2-}$	156.6	153.8	106.7	865.9
stack $[\mathbf{1}_2 \bullet B_{12}H_{12}]^{2-}$	128.3	125.6	75.9	857.1
planar $[\mathbf{1}_3 \bullet B_{12}H_{12}]^{2-}$	138.8	135.3	92.3	1139.6
pyramid $[\mathbf{1}_3 \bullet B_{12}H_{12}]^{2-}$	137.3	133.6	92.1	1144.5
linear stack $[\mathbf{1}_3 \bullet B_{12}H_{12}]^{2-}$	120.2	119.2	65.7	1106.5
bent stack $[\mathbf{1}_3 \bullet B_{12}H_{12}]^{2-}$	118.9	116.1	66.9	1118.6
tetrahedral $[1_4 \bullet B_{12}H_{12}]^{2-}$	119.0	116.0	69.2	1405.2
planar stack $[1_4 \bullet B_{12}H_{12}]^{2-}$	111.4	108.6	60.2	1394.8
pyramid stack $[1_4 \bullet B_{12}H_{12}]^{2-}$	110.9	108.4	57.0	1389.8
linear stack $[1_4 \bullet B_{12}H_{12}]^{2-}$	115.2	112.7	61.3	1352.0
bent stack $[1_4 \bullet B_{12}H_{12}]^{2-}$	114.5	112.1	60.9	1364.8
tetra stack $[1_5 \bullet B_{12}H_{12}]^{2-}$	105.5	102.3	56.4	1668.8

Geometric properties were studied to understand the higher binding energies of **1** to $[B_{12}H_{12}]^{2-}$ cages compared to $[B_{12}F_{12}]^{2-}$ cages. The distances between axial hydrogen atoms of **1** and the H or F atoms of $[B_{12}X_{12}]^{2-}$ (X = H, F) were averaged for each cage-ring interface. At each cage-ring interface there exists six B-X•••H-C interaction distances (refer to the binding motif in Figure 5.24 D). Average B-H•••H-C and B-F•••H-C distances in $[\mathbf{1}_n \bullet B_{12}H_{12}]^{2-}$ n = 1 – 5 clusters and in $[\mathbf{1}_n \bullet B_{12}F_{12}]^{2-}$ n = 1 – 4 clusters, respectively, are tabulated in Table 5.12 and plotted in Figure 5.31. Note that the B-H•••H-C in the cluster $[\mathbf{1}_5 \bullet B_{12}H_{12}]^{2-}$ are calculated in two different ways; either (a) including the three **1** moieties which are not impacted by the second solvation shell (excluding two **1** moieties) or (b) excluding only the moiety of **1** in the secondary solvation shell (*i.e.*, the exterior moiety participating in the stacking interaction). These two calculations highlight the reduced distance at the cage-ring interface of the stacked species; this is a result of the attraction of the moiety of the stacked pair outer **1** to the dianion cage, which nudges the inner **1** moiety closer to the cage. Overall, the **1** molecules are bound more closely to the $[B_{12}H_{12}]^{2-}$ cage than they are the $[B_{12}F_{12}]^{2-}$ cage by ~ 0.13 Å. This is in general accordance with the smaller van der Waals radius of hydrogen (1.20 Å) relative to that of fluorine (1.47 Å). The B-H•••H-C distances, which are less than 2.40 Å (*i.e.*, two times the van der Waals radii of hydrogen), indicates the possible presence of attractive interactions between the H atoms. We find the average B-H•••(H) angle to be 103°. The B-H•••H-C distances increase by 0.02 Å (0.9 %) with each additional **1** moiety for n < 5 whereas, the binding energies of **1** to $[\mathbf{1}_n \bullet B_{12}H_{12}]^{2-}$ decrease by 15 – 25 % with each additional **1** molecule. These results accord with the work on B-H•••H-N dihydrogen bonds by Crabtree *et al.*[239]

Table 5.12 Averaged interaction distances between axial hydrogen atoms of **1** and the nearest X = H or X = F atoms in $[\mathbf{1}_n \bullet B_{12}X_{12}]^{2-}$ calculated at the B3LYP/6-311++G(d,p) level of theory. The geometry of $[\mathbf{1}_5 \bullet B_{12}H_{12}]^{2-}$ involves a tetrahedral arrangement of four **1**s and the fifth **1** is stacked directly in line with another **1**.
a. Includes only the three **1** moieties not impacted by the second solvation shell.
b. All four **1** molecules in the tetrahedral arrangement are included in the average.
c. Optimization had not converged. The optimization step with the lowest electronic energy was used.

n	$r_{(B\text{-}H\cdots H\text{-}C)}$ (Å)	$r_{(B\text{-}F\cdots H\text{-}C)}$ (Å)
1	2.18	2.32
2	2.20	2.33
3	2.22	2.35
4	2.24	2.37[c]
5[a]	2.25	
5[b]	2.24	

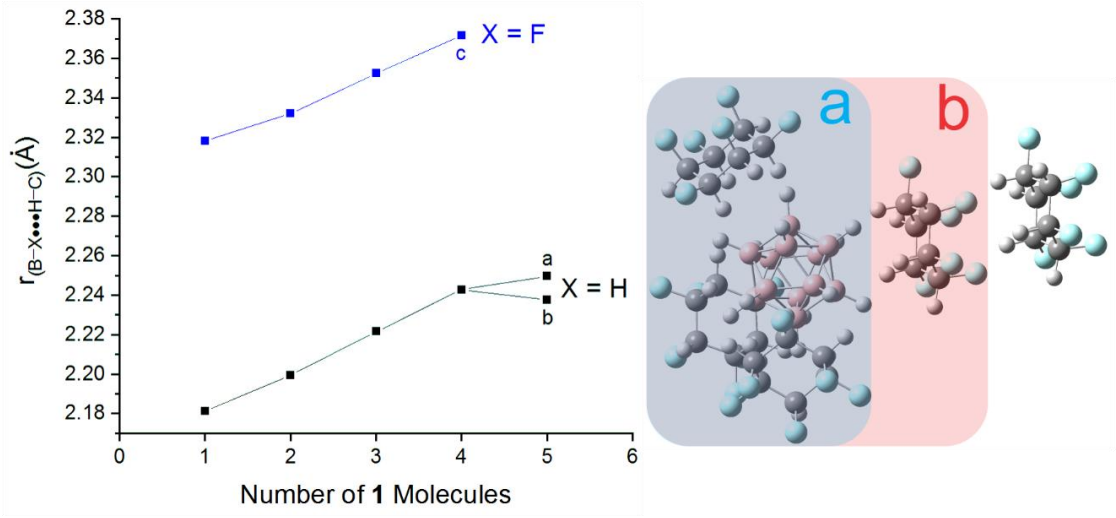

Figure 5.31 Distances between interacting H•••F or H•••H atoms in complexes of $[\mathbf{1}_n \bullet B_{12}X_{12}]^{2-}$ (X = F, H; *n* = 1-5). Illustration of which **1** moieties are included in the average for $n = 5^a$ and 5^b.

The relationship between B-H•••H-C distance in $[\mathbf{1} \bullet B_{12}H_{12}]^{2-}$ and the zero-point corrected dissociation energy is plotted in Figure 5.32; a linear fit of the data shows a nearly perfect correlation. We begin our study of intermolecular interactions with classical electrostatic interactions as they are expected to dominate the binding in these clusters.

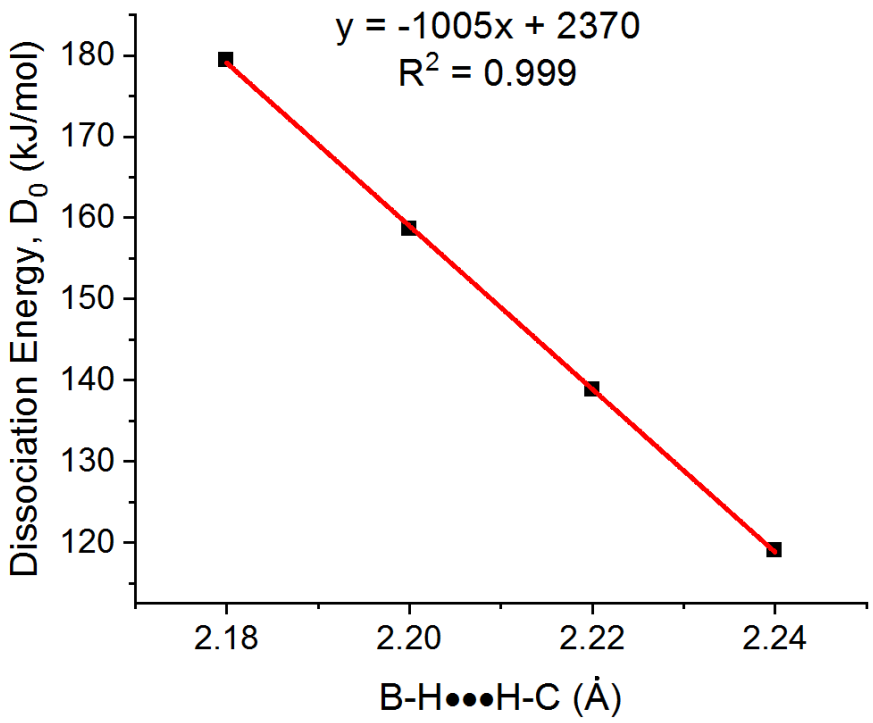

Figure 5.32 Zero-point corrected electronic energy required to dissociate $[\mathbf{1}_n{\bullet}B_{12}H_{12}]^{2-}$ into **1** and $[\mathbf{1}_{n-1}{\bullet}B_{12}H_{12}]^{2-}$ at the average B-H•••H-C distances found in the global minimum geometries of $[\mathbf{1}_n{\bullet}B_{12}H_{12}]^{2-}$ (n = 1 – 4) optimized at B3LYP/6-311++G(d,p) (black squares). Empirically fit linear function (red line).

An estimate of the electrostatic contribution from ion-dipole attraction to the binding energy is found using Eq. 5.4.

$$U_{ion-dipole}(r) = \frac{1}{4\pi\varepsilon_0}\frac{q_1\mu cos\theta}{r^2} \qquad \text{Eq. 5.4}$$

Where, ε_0 = 8.854187817x10^{-12} C^2 J^{-1} m^{-1} is vacuum permittivity, $q_1 = 2e$ C is the charge of the $[B_{12}H_{12}]^{2-}$ dianion, μ = 7.3 Debye is the dipole moment, θ is the angle of the dipole moment vector relative to axis connecting the centers of mass (equal to zero), e = 1.602176634x10^{-19} C is the absolute value of the charge of an electron, and r is the separation distance of the two species.[259] Eq. 5.4 was utilized in the analogous study of $[\mathbf{1}_n{\bullet}B_{12}F_{12}]^{2-}$ where D_0 = 163.5 kJ mol^{-1} and an ion-dipole energy of 134 kJ mol^{-1}, was used to estimate a contribution of 29.5 kJ mol^{-1} for covalent interactions to total binding.[7] In comparison, NBO analysis indicated a stabilization energy of

30.9 kJ mol^{-1} for charge-transfer (*i.e.*, incipient covalent interactions). This shows that classical ion-dipole electrostatic interactions dominate [**1**$_n$•$B_{12}F_{12}$]$^{2-}$, but that quantum covalent interactions must be considered for an accurate description. Application of the same analysis here, with a center of mass separation between [$B_{12}H_{12}$]$^{2-}$ and **1** of 5.09 Å, a charge of −2, and a dipole moment of 7.3 Debye yields an ion-dipole potential energy of 164.2 kJ mol^{-1}. When subtracted from the electronic dissociation energy, D_0 = 179.4 kJ mol^{-1}, an estimate is provided for the energy of the covalent interactions (*i.e.*, 15.2 kJ mol^{-1}). Figure 5.33 provides the results of computing the ion-dipole potential energy at the differing distances between the centers of mass of the dianion cage and **1** (averaged when n > 1) for [**1**$_n$•$B_{12}H_{12}$]$^{2-}$ (n = 1 – 4). Also plotted are the zero-point corrected dissociation energies for the corresponding clusters. When these results are compared to the dissociation energies it is clear that further analysis of the non-covalent and covalent interactions must be conducted.

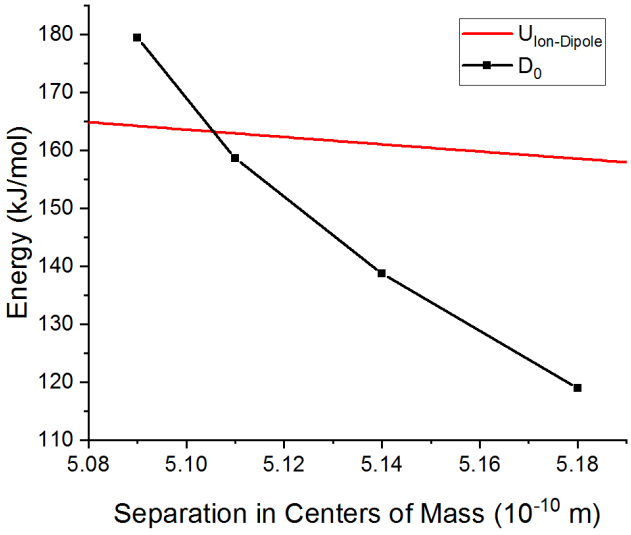

Figure 5.33 (red) Ion-dipole potential energy function r = 5.08 – 5.19 Å (Eq. 5.4). (black) Zero-point corrected dissociation energies for n = 1 – 4 plotted against the average distance between the [$B_{12}H_{12}$]$^{2-}$ center of mass and the **1** center of mass in [**1**$_n$•$B_{12}H_{12}$]$^{2-}$ (n = 1 – 4).

Natural population analysis was performed to investigate the atomic partial charges of the interacting atoms. In their 2017 photoelectron spectroscopy study, Warneke *et al.* calculated the atomic partial charges on $[B_{12}X_{12}]^{2-}$ X = F, Cl, Br, I.[222] They reported the partial charges on boron atoms in $[B_{12}F_{12}]^{2-}$ summed to a value of +3.6*e* and those of the fluorine atoms to ─5.6*e*. We arrive at a similar result for $[B_{12}F_{12}]^{2-}$, a positive boron cage (+4.05*e*) and a negative fluorine shell (─6.05*e*). In contrast, in the results for $[B_{12}H_{12}]^{2-}$ we observed a negatively charged boron cage (─2.05*e*) and an essentially neutral shell of hydrogen atoms (+0.05*e*). These results are visualized in electrostatic charge distribution maps in Figure 5.34.

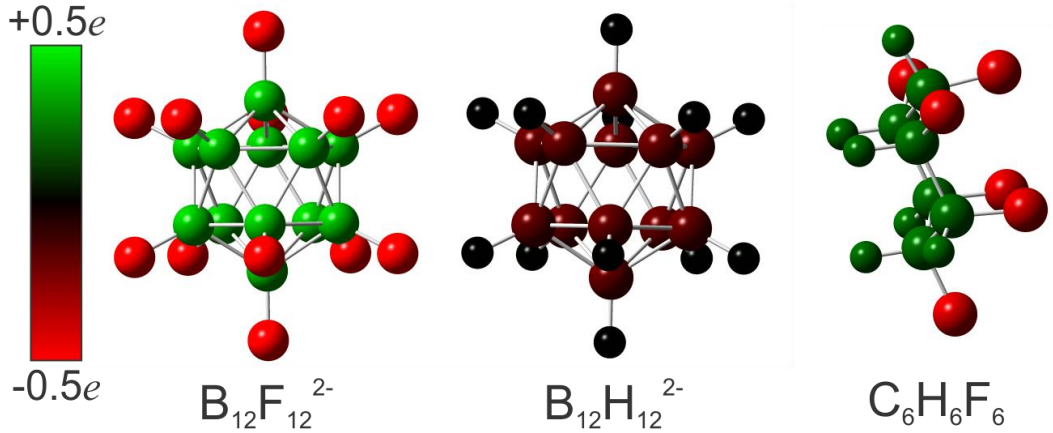

Figure 5.34 Atomic partial charges determined using Natural Population Analysis

In hydrogen bonding systems, the electron rich species are labelled the hydrogen bond acceptor (A) and the electron poor species are labelled the hydrogen bond donor (D). For example, in a water dimer the covalently bound O-H participating in the hydrogen bond is referred to as the D group while the electron rich oxygen atom of the other H_2O molecule is considered the A group. Applying these labels to the $[\mathbf{1}_n \bullet B_{12}X_{12}]^{2-}$ X = H, F clusters, the B-X moieties are the A groups while the H_{axial}-C bonds are considered the D groups. Table 5.13 provides the average partial charges found on the hydrogen bond participants in $[\mathbf{1}_n \bullet B_{12}X_{12}]^{2-}$ X = H, F clusters. In both analogs, the differences in partial charges between the A group X atoms and D group H_{axial} atoms

decrease as n increases. This trend correlates with the trend of B-X•••H-C distances and dissociation energies of **1** from $[\mathbf{1}_n \bullet B_{12}X_{12}]^{2-}$ X = H, F as a function of n. When comparing partial charges on the A groups, a larger negative partial charge is found on the fluorine atoms than the hydrogen atoms, as expected. Comparing the D group partial charges, we find larger positive partial charges on the H_{axial} atoms in complexes with $[B_{12}H_{12}]^{2-}$ than in complexes with $[B_{12}F_{12}]^{2-}$ implying a greater depletion of electron density. This accords with the fact that **1** is closer to the dianion cage; the −2 charge has repelled the electron density to a greater extent.

Table 5.13 Partial charges of H, F atoms in the BX•••HC hydrogen bonds at the $[\mathbf{1}_n \bullet B_{12}X_{12}]^{2-}$ (X = H, F) and **1** for n < 5. Values were determined using the Natural Population Analysis from the NBO treatment. Acceptor (A) represents the average partial charge on the "X" atoms adjacent to a **1** moiety. Donor (D) represents the average partial charge on the axial hydrogen atoms of **1** when adjacent to $[\mathbf{1}_n \bullet B_{12}X_{12}]^{2-}$ (X = H, F). Re-optimization of $[\mathbf{1}_4 \bullet B_{12}F_{12}]^{2-}$ is ongoing.

	$[\mathbf{1}_n \bullet B_{12}H_{12}]^{2-}$		$[\mathbf{1}_n \bullet B_{12}F_{12}]^{2-}$	
	A	D	A	D
n	δ (H)	δ (H)	δ (F)	δ (H)
1	-0.0110	0.263	-0.517	0.238
2	-0.0023	0.254	-0.510	0.233
3	0.0012	0.244	-0.505	0.226
4	0.0102	0.217		

The calculated B-H•••H-C distances (discussed earlier) suggested that incipient chemical bonding may be occurring between **1** and $[B_{12}X_{12}]^{2-}$ X = H, F. To investigate this possibility, NBO analysis was conducted to assess the magnitude of charge-transfer interactions between $[B_{12}X_{12}]^{2-}$ and **1**. Discussion of stabilization energies within NBO analysis is always with respect a lower energy, electron rich, donor orbital interacting with a higher energy, electron poor, acceptor orbital. In these clusters, donor orbitals were supplied by the $[B_{12}X_{12}]^{2-}$ cages and acceptor orbitals were supplied by the **1** moieties. The stabilization energies of the $[B_{12}X_{12}]^{2-}$ and **1** interactions are reported in Table 5.14. To obtain the values given in Table 5.14, a summation of all stabilization energies from the $[B_{12}X_{12}]^{2-}$ moiety to a specific **1** moiety is computed, then these values are

averaged for each molecule of **1** in the complex. Hydrogen bonding is predominantly associated with the acceptance of electron density by the σ* orbital of the hydrogen bond donor.[260] Here, the σ* orbital is associated with the C-H_{axial} bonds of **1**. NBO analysis indicated a larger charge-transfer stabilization energy in the hydrogen cage clusters than in the fluorine cage clusters, which accords with the higher dissociation energies found in the hydrogen cage clusters. This can be rationalized based on cluster geometries; shorter interaction distances provide better overlap between interacting orbitals. The stabilization energies found were substantially larger than expected from the estimate of 15.2 kJ mol^{-1} for $[\mathbf{1}\bullet B_{12}H_{12}]^{2-}$ determined by subtracting the ion-dipole energy from the D_0 value. The relationship between stabilization energy and X•••H separation in B-X•••H-C (X = H, F) is shown in Figure 5.35. At each $[B_{12}X_{12}]^{2-}$/**1** interface there are three interacting H_{axial} atoms, each of which accepts the majority of the total donated electron density into the σ* orbital of the C-H_{axial} bond. Other orbitals found to accept electron density include hydrogen Rydberg orbitals and C-F σ* orbitals. In the $B_{12}H_{12}^{2-}$ clusters, this electron density is donated by lone pair orbitals on the boron atoms and B-H bonding orbitals. In the $B_{12}F_{12}^{2-}$ clusters, this electron density is donated exclusively by lone pair orbitals on the fluorine atoms. In Figure 5.35, the sum stabilization energies for interactions wherein a σ* orbital from the C-H_{axial} bond is acting as the acceptor orbital is plotted against the average of the two X•••H distances, the stabilization energy correlates strongly with $1/r_{(X\cdots H)}$. Crabtree *et al.* found an interaction energy of 25.5 kJ mol^{-1} per B-H•••H-N dihydrogen bond in the H_3BNH_3 dimer.[239] Here we find σ* C-H_{axial} acceptor interactions of 28.7 kJ mol^{-1} for each H_{axial} in $[\mathbf{1}\bullet B_{12}H_{12}]^{2-}$.

Table 5.14 Total stabilization energies for $B_{12}X_{12}^{2-}$ donor to **1** acceptor interactions averaged across all molecules of **1** in the considered cluster. Also reported is the percent of the total stabilization energy where the C-H_{axial} σ* orbital is the acceptor.

	$[\mathbf{1}_n \bullet B_{12}H_{12}]^{2-}$		$[\mathbf{1}_n \bullet B_{12}F_{12}]^{2-}$	
n	$E_{interact}$ (kJ mol^{-1})	% Accepted by σ^*_{C-H}	$E_{interact}$ (kJ mol^{-1})	% Accepted by σ^*_{C-H}
1	113.9	76	38.8	62
2	87.3	77	31.1	72
3	73.2	71	29.1	74
4	52.9	67		
5	52.3	68		

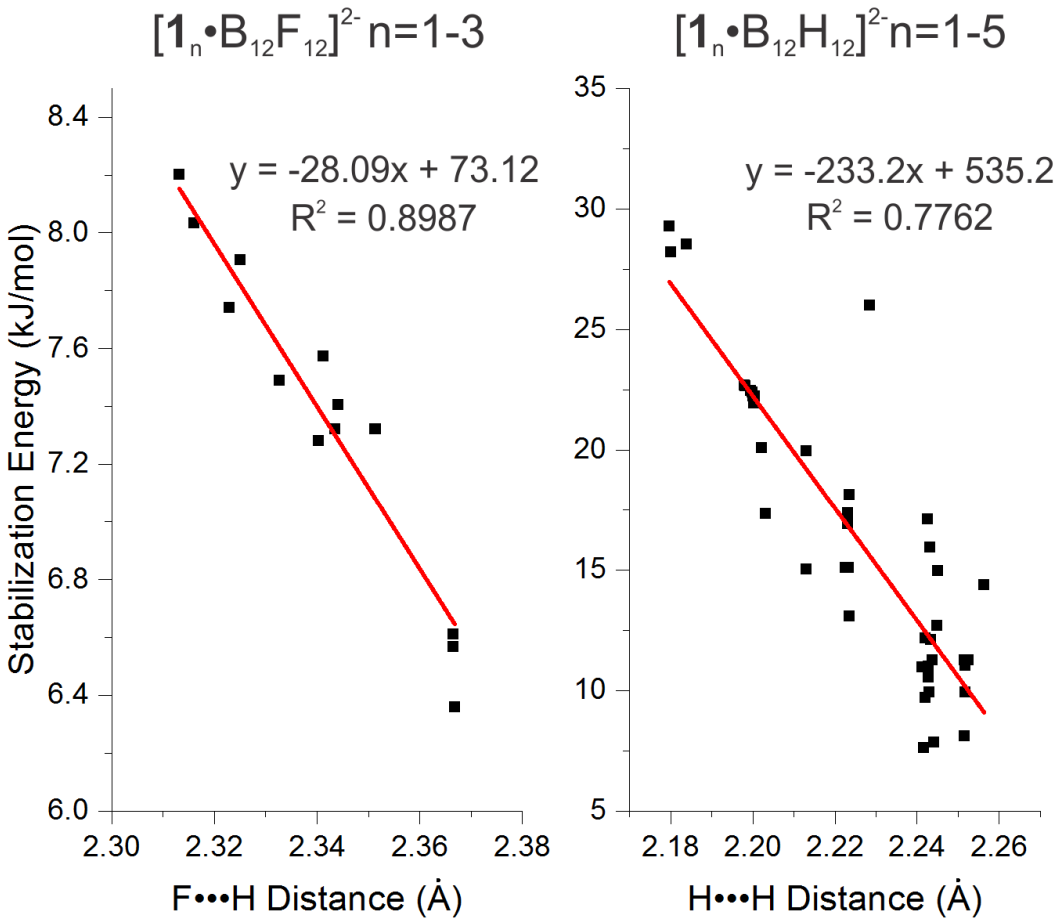

Figure 5.35 Variation of stabilization energy for $[B_{12}X_{12}]^{2-}$ donor to σ* C-H_{axial} acceptor interactions with the distance between the hydrogen bonding atoms.

To further characterize and quantify interactions between $[B_{12}H_{12}]^{2-}$ and **1** moieties, the quantum theory of atoms in molecules (QTAIM) analysis was conducted.[23] Figure 5.36 shows bond, ring, and cage critical points, where the gradient of the electron density equals zero, for inter-moiety interactions in $[\mathbf{1}\bullet B_{12}F_{12}]^{2-}$. Six bond critical points (BCP) are associated with the F atoms and the H_{axial} atoms. A ring critical points (RCP) is found on each of the six triangular faces of the interface; formed by either two F atoms and one H atom or one F atom and two H atoms. In addition to this, one single cage critical point (CCP) is found at the center of the $B_{12}F_{12}^{2-}$/**1** interface. Similar critical points were found for all $B_{12}X_{12}^{2-}$/**1** interfaces in all clusters analyzed.

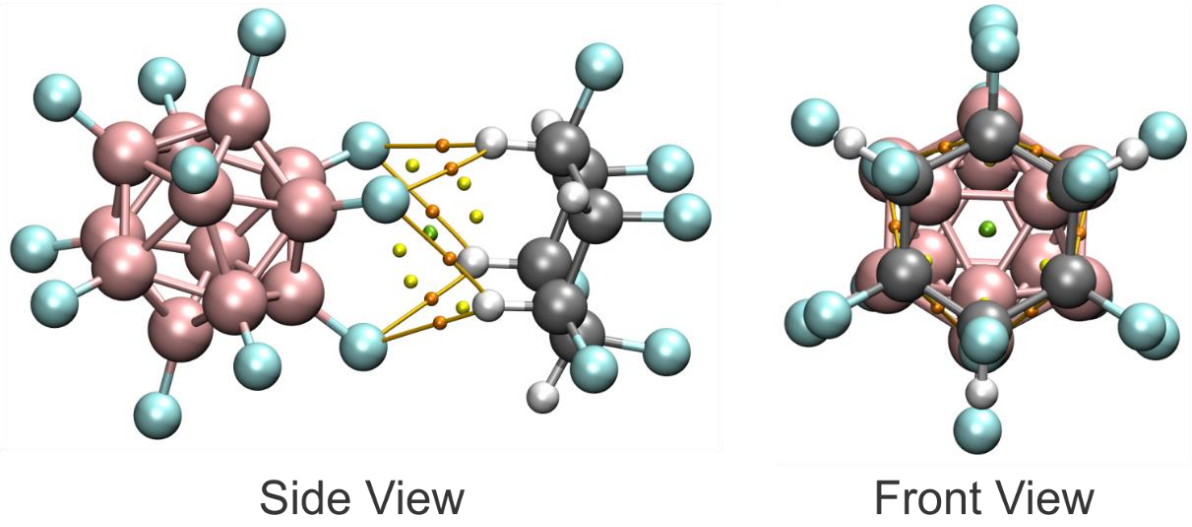

Figure 5.36 Bond paths (orange lines), bond critical points (orange spheres), ring critical points (yellow spheres), and cage critical point (green sphere) found at the site of interaction between **1** and $[B_{12}F_{12}]^{2-}$ in the $[\mathbf{1}\bullet B_{12}F_{12}]^{2-}$ cluster.

Average electron densities and the Laplacian of the electron densities for each critical point associated with $B_{12}X_{12}^{2-}$/**1** interfaces of $[\mathbf{1}_n\bullet B_{12}H_{12}]^{2-}$ (n = 1 – 5) and $[\mathbf{1}_n\bullet B_{12}F_{12}]^{2-}$ (n = 1 – 4) are provided in Table 5.15 and Table 5.16, respectively. Kock and Popelier established that the values of the BCP electron densities for hydrogen bonds are in the range of 0.021 – 0.002 a.u.[26] More recently, Kumar *et al.* determined the electron density for the hydrogen bond in the water dimer to be 0.0219 a.u. and the Laplacian to be 0.0396 a.u.[24] As shown in Table 5.15 and Table 5.16, similar

values are calculated for $B_{12}X_{12}^{2-}$/**1** interactions, providing further support that dihydrogen bonds are a key contributor to the binding of **1** and $[B_{12}H_{12}]^{2-}$. Additionally, we also find a positive sign for the sum of the Laplacian. The sign for the sum of the Laplacian for a critical point indicates if there is a depletion of electron density (*i.e.*, a non-covalent interaction) or a concentration of electron density (*i.e.*, a covalent interaction). Comparatively higher electron density is found at the fluorinated cage BCPs than at the hydrogenated cage BCPs. This result is unsurprising simply because of the existence of lone pair electron density on the fluorine atoms. The magnitude of the electron densities and Laplacian values decreases as more moieties of **1** are added to the clusters (see Figure 5.37), once again in line with many of the previous physical properties discussed above. When the electron density of every BCP is plotted against its corresponding B-X•••H-C distance, a linear relationship is observed (see Figure 5.38) again suggesting a non-covalent nature for these dihydrogen bonds.

Table 5.15 Average electron densities and the sum of the Laplacian of the electron densities for cage, ring, and bond critical points found at the interface of the $B_{12}H_{12}^{2-}$ cage and the axial hydrogen atoms of **1**.
a. Excludes both molecules of **1** participating in the stack arrangement
b. Includes the four **1** molecules directly interacting with the $B_{12}H_{12}^{2-}$ cage

n	ρ CCP (a.u.)	ρ RCP (a.u.)	ρ BCP (a.u.)	$\nabla^2\rho$ CCP (a.u.)	$\nabla^2\rho$ RCP (a.u.)	$\nabla^2\rho$ BCP (a.u.)
1	3.43E-03	7.32E-03	1.06E-02	1.28E-02	2.48E-02	3.02E-02
2	3.32E-03	7.01E-03	1.01E-02	1.24E-02	2.37E-02	2.89E-02
3	3.21E-03	6.70E-03	9.62E-03	1.20E-02	2.26E-02	2.76E-02
4	3.12E-03	6.41E-03	9.15E-03	1.16E-02	2.16E-02	2.63E-02
5[a]	3.09E-03	6.32E-03	9.01E-03	1.15E-02	2.13E-02	2.59E-02
5[b]	2.89E-03	6.30E-03	9.52E-03	1.15E-02	2.27E-02	2.94E-02

Table 5.16 Electron densities and the sum of the Laplacian of the electron densities for cage, ring, and bond critical points found at the interface of the $B_{12}F_{12}^{2-}$ cage and the axial hydrogen atoms of **1**.
c. The optimization step with the lowest electronic energy was used.

n	ρ CCP (a.u.)	ρ RCP (a.u.)	ρ BCP (a.u.)	$\nabla^2\rho$ CCP (a.u.)	$\nabla^2\rho$ RCP (a.u.)	$\nabla^2\rho$ BCP (a.u.)
1	1.85E-03	5.42E-03	1.16E-02	9.10E-03	2.67E-02	4.24E-02
2	1.82E-03	5.28E-03	1.12E-02	8.94E-03	2.58E-02	4.10E-02
3	1.78E-03	5.09E-03	1.07E-02	8.69E-03	2.47E-02	3.92E-02
4[c]	1.80E-03	4.94E-03	1.03E-02	8.53E-03	2.38E-02	3.77E-02

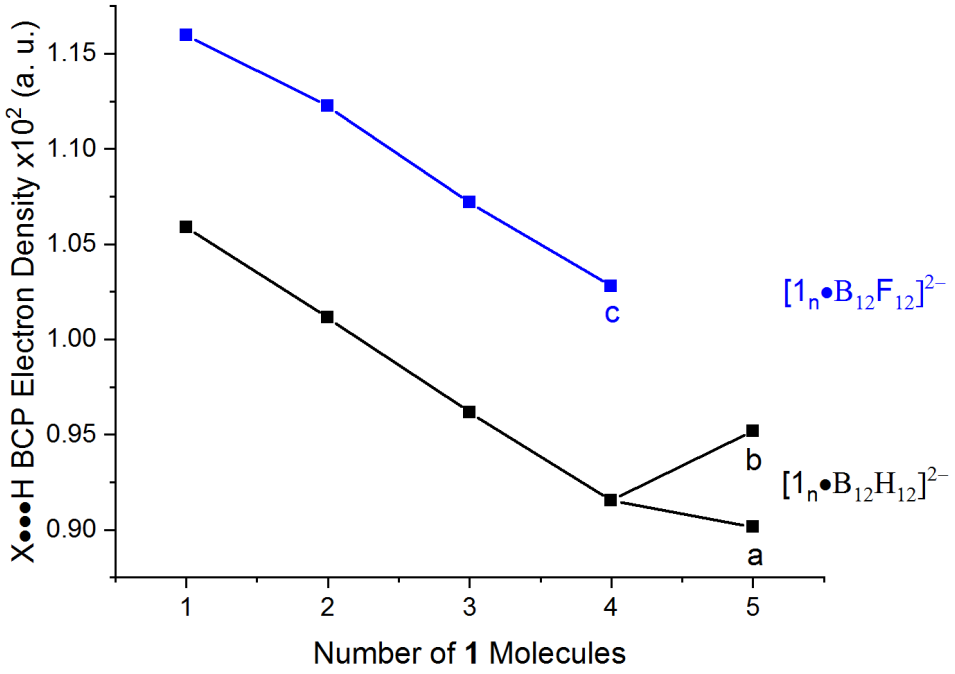

Figure 5.37 Electron density found at the bond critical points located between the interacting X = F (blue) or X = H (black) atoms of $B_{12}X_{12}^{2-}$ and the axial hydrogen atoms of **1** in complexes of $[1_n \bullet B_{12}X_{12}]^{2-}$ (X = H, F; n = 1 – 5).
a. Excludes both molecules of **1** participating in the stack arrangement
b. Includes the four **1** molecules directly interacting with the $B_{12}H_{12}^{2-}$ cage
c. The optimization step with the lowest electronic energy was used.

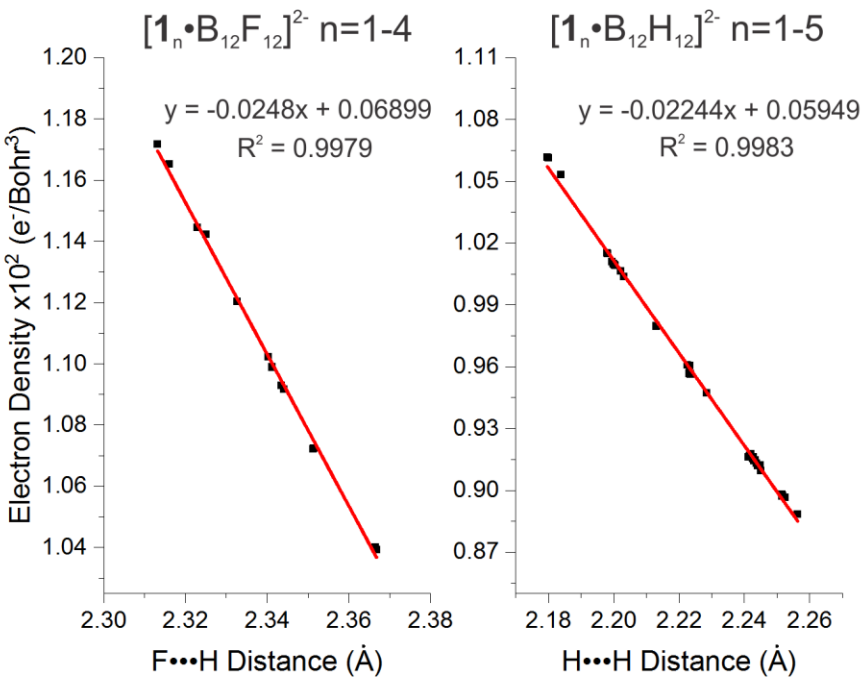

Figure 5.38 Electron density at the bond critical points between the axial hydrogen atoms of **1** and X = F, H atoms of $B_{12}X_{12}^{2-}$.

5.6.2 Conclusions

A combined theoretical and spectroscopic approach has been used to investigate the intermolecular interactions in clusters of $[\mathbf{1}_n \bullet B_{12}H_{12}]^{2-}$ (n = 1 – 5). IRMPD spectra have been collected for $[\mathbf{1}_n \bullet B_{12}H_{12}]^{2-}$ (n = 1 – 4), a species with the corresponding m/z ratio for $[\mathbf{1}_5 \bullet B_{12}H_{12}]^{2-}$ could not be isolated using the QIT at the CLIO facility. DFT calculations were conducted on various isomers of $[\mathbf{1}_n \bullet B_{12}H_{12}]^{2-}$ (n = 1 – 5) and comparison of the predicted IR spectra to the experimental spectra identified the DFT global minimum isomers as the most abundant species in the ensemble. The calculated frequencies of the fundamental transitions for each vibrational normal mode of vibration were used to assign the IRMPD spectra in the region of 800 – 1500 cm^{-1}. Analysis of the dependence of calculated transition frequencies on the number of **1** moieties in the cluster revealed that the $B_{12}H_{12}^{2-}$/**1** interactions were diminishing with each additional **1**. This analysis

also indicated the engagement of the axial hydrogen atoms of **1** by the hydrogen atoms of $B_{12}H_{12}^{2-}$, likely *via* the formation of dihydrogen bonds.

Kinetic trapping of the first solvation shell at $n = 3$ has been proposed in the case of $[\mathbf{1}_n \bullet B_{12}F_{12}]^{2-}$ clusters. [7] At the CLIO facility, formation of $n \geq 4$ was not observed in these fluorinated cage clusters and DFT calculations found that sequential addition of **1** to produce $[\mathbf{1}_4 \bullet B_{12}F_{12}]^{2-}$ clusters must utilize higher energy isomers at the $n = 2$ and 3 cluster sizes. Additionally, the binding energy of **1** to $[\mathbf{1}_3 \bullet B_{12}F_{12}]^{2-}$ was calculated to be relatively weak with $\Delta G° = 38.6$ kJ mol^{-1}. Here, in our study of analogous hydrogenated clusters, formation of $[\mathbf{1}_4 \bullet B_{12}H_{12}]^{2-}$ was observed. However, the cluster spontaneously fragmented (*i.e.*, non-resonantly) during IRMPD experiments indicating a weak binding energy of **1** to $[\mathbf{1}_3 \bullet B_{12}H_{12}]^{2-}$ which was calculated to be $\Delta G° = 69.2$ kJ mol^{-1}. The production of $[\mathbf{1}_4 \bullet B_{12}H_{12}]^{2-}$ was possible because the isomers required to sequentially form the $n = 4$ cluster were closer in energy to their respective global minimum isomers. A complete solvation shell of **1** around $B_{12}X_{12}^{2-}$ is preferred, kinetically, to complete at $n = 3$ but is geometrically capable of expanding to $n = 4$. The results of the PE spectroscopy experiments yielded further support of a complete solvation shell at $n = 3$.

NBO and QTAIM analyses have quantified MO stabilization energies, atomic partial charges, and electron densities. The stabilization energies of MO interactions, in which $B_{12}X_{12}^{2-}$ donates electron density and **1** accepts electron density, were found to be significantly larger in $[\mathbf{1}_n \bullet B_{12}H_{12}]^{2-}$ compared to $[\mathbf{1}_n \bullet B_{12}F_{12}]^{2-}$ which is primarily a result of the shorter X•••H distances in the hydrogenated clusters. In the hydrogenated clusters it was found that dihydrogen bonding accounted for 76 % of the total stabilization energy. Natural population analysis produced atomic partial charges of the interacting atoms at the $B_{12}X_{12}^{2-}$/**1** interface. The difference between the charges of the interacting atoms was far greater when X = F and this difference decreases with

additional moieties of **1**. The electrostatic attraction of these atoms appears to play a minor role given that **1** binds with greater strength to $B_{12}H_{12}^{2-}$ ($\Delta G° = 128.8$ kJ mol^{-1}) than $B_{12}F_{12}^{2-}$ ($\Delta G° = 84.6$ kJ mol^{-1}). Electron density at the BCPs in the fluorinated clusters was larger than that in the hydrogenated clusters due to the increased lone pair electron density associated with the fluorine atoms. The quantity of the electron density within the dihydrogen bonds of the hydrogenated clusters is on the order a typical hydrogen bond. When one considers that each hydrogen atom at the $B_{12}H_{12}^{2-}$/**1** interface is involved in two dihydrogen bonds, the amount of electron density split between those two bonds is on the order of the electron density found in the hydrogen bond of the water dimer.

6 Conclusions

In this thesis, the intermolecular interactions which exist between moieties within a cluster system were studied using a combination of experimental and theoretical techniques. In general, the best theoretical model (*i.e.*, choice of functional and basis set within DFT) has chosen based on literature pertaining to similar species. The validity of the model is assessed by comparisons of a predicted property to the experimental observations of that property. With successful experimental validation of a given computational approach, additional physico-chemical properties predicted by the theoretical model can be further analyzed to provide a deeper understanding of the observed physical behaviour of the cluster system under investigation and guide future experimental work.

A pure computational study of competing nitrous oxide decomposition and desorption reactions on Rh_nS^+ $n = 2 – 9$ was conducted. A custom written basin hopping algorithm generated potential energy surface minima candidate structures of three stationary points on the decomposition reaction profile. Optimization with DFT was perform to identify the global minimum geometry and multiplicity of each stationary point at each cluster size. A transition state structure was optimized for each cluster size to obtain the kinetic barriers to N_2O decomposition. Comparisons have been made with the analogous pure rhodium system to understand the role of the sulphur atom in the cluster size regime given its reputation as a catalytic poison in the bulk phase. Analysis of the global minimum geometric properties of $Rh_nS^+•N_2O$, $Rh_nSO^+•N_2$, and $Rh_nS^+•O$ revealed the binding preferences of the moieties to the metal cluster core. Multiplicity studies revealed that these clusters have an appreciable density of electronic states that are thermally accessible at room temperature. Electronic reaction barriers were computed and did not show any preference for N_2O decomposition versus desorption in the presence of sulphur, but when taking considering the Gibbs energy of the clusters we found that desorption was preferred

in all cases. It is also worth noting that different reaction minima along the decomposition profile possessed different multiplicities, indicating that these reactions likely proceed through crossings of the electronic surfaces. An inconsistency between the computed stability of the $Rh_nS^+•N_2O$ clusters relative to the analogous bare rhodium clusters was observed. The bonds between the Rh_nS^+ ($n = 1 – 9$) cluster cores and N_2O were found to be short relative to the bare cluster analogues,[3,38] and NBO analysis identified greater stabilization energies and a greater degree of charge transfer in the sulphur-containing species, all pointing to a greater stability of the Sulphur-doped analogs. In contrast, larger N_2O binding energies and larger HOMO-LUMO gaps, two traditional metrics for cluster stability, were calculated for the $Rh_n^+•N_2O$ species.[76,126]

Harmonic vibrational frequency calculations facilitated prediction of vibrational spectra and thermal corrections for the stationary points along reaction pathways. The predicted vibrational spectra are available to guide future experimental studies (*e.g.*, IRMPD or velocity map imaging). They show blue shifting of the N-N and N-O stretches and red shifting in the bending modes of N_2O on Rh_nS^+ relative to the calculated frequencies of these modes in free N_2O. The N_2 stretching frequency in $Rh_nSO^+•N_2$ was calculated to be red shifted relative to free N_2. Inclusion of thermal energy corrections results in a lower $Rh_nS^+•N_2O$ desorption threshold than the decomposition reaction barrier for every cluster size studied. Thus, at room temperature, DFT predicts nitrous oxide desorption as the preferred pathway showing qualitative agreement with the known bulk phase property of Sulphur to poison catalytic processes.

The challenges presented by the rhodium clusters are in part due to the large density of electronic states. Current theoretical approaches, such as multireference techniques, for treatment of excited electronic states are too computationally expensive to treat such systems. This has directed our studies toward the less electronically, but more geometrically complicated

organometallic palladium complexes. These species can be thought of as covalent clusters owing to the strength of chelation between the organic ligands and the Pd centre. We utilized the CLIO FEL facility to collect IRMPD spectra of five different palladium complexes, which were selected to study the impact of electronic and geometric structure on IVR. Basin hopping was once again employed to generate global minimum candidates that were subsequently treated with DFT. Calculated vibrational spectra of the global minimum isomers were in excellent agreement with the experimental IRMPD spectra. Absorption of multiple IR photons lead to the loss of solvent molecule messenger tags and the formation of products associated with ligand scrambling reactions. Products of the solvent tag loss were observed at every absorbing wavelength. Products of higher energy ligand scrambling thresholds were only observed for absorptions resonant with phenyl ring vibrations in the PPh_3 or $P(furyl)_3$ ligands. This mode-selective behaviour is a result of inefficient coupling of the ligand vibrational mode to the bath states. Incomplete intermolecular vibrational energy redistribution (IVR) leads to localized overheating of the PPh_3 (or $P(furyl)_3$) ligands, raising the internal energy of the molecule in a specific region of phase space so as to access the higher energy ligand scrambling thresholds on that part of the potential energy surface. Like the triphenylphosphine species, complexes with $P(furyl)_3$ ligands showed mode selectivity at frequencies which correspond to the phosphorus-containing ligand vibrational transitions. However, the IRMPD induced fragmentation of the complex with $AsPh_3$ ligands did not show mode-selective behavior, indicating that the P–Pd acted as a bottleneck for energy flow leading to incomplete energy redistribution via IVR. When considering vibrational levels that are combinations of low frequency palladium-ligand vibrations and ligand vibrations, a greater density of vibrational states is calculated for the arsenic-containing compounds. This analysis indicates

that IVR is hindered for the phosphorus-containing species due to a lack of doorway states in fortuitous energy windows that correspond with the ligand v = 1 levels.

Finally, to study a limiting case of intermolecular interactions, we chose to investigate weakly coordinating the dodecaborate derivatives, $B_{12}X_{12}^{2-}$ X = H, F, Cl. These species were complexed with a series of cationic transition metals, a protonated amine, and the very polar hexafluorocyclohexane species, $C_6H_6F_6$. $B_{12}F_{12}^{2-}$ and $B_{12}H_{12}^{2-}$ have been identified as superweak anions in solution, a property that arises due to their relatively large size and the fact that the electron density associated with their frontier molecular orbitals is contained in the cage center, thereby making it unavailable for localized interactions with chelating species. Understanding the forces between $B_{12}X_{12}^{2-}$ cages and cationic and neutral species will provide insights for tailoring applications such as the utilization of these systems in reactive cation delivery.[216,223–228]

In initial studies of complexation between $B_{12}F_{12}^{2-}$ and a single transition metal cation, twelve different transition metals were considered. These clusters were produced by electrospray ionization and the isolable species were probed using IRMPD at the CLIO facility. Interestingly, clusters containing the heaviest of the transition metals could not be isolated in the ion trap, and non-complexed metal cations were not observed in positive mode. Even more peculiar was the observation of $B_nF_m^-$ fragments from $B_{12}F_{12}^{2-}$, which is known for being a very stable species (refer to Section 5.1.1). DFT calculations showed charge transfer occurring from the cage to the transition metal atoms. The observed charge transfer was due to the imbalance between the ionization energy of the neutral metal atom and the comparatively low electron affinity of $B_{12}F_{12}^-$. In the cases of the heavier transition metals, charge transfer was so significant that it resulted in production of neutral metal atoms (which cannot be observed by mass spectrometric techniques) and the $B_{12}F_{12}^-$ monoanion, a species which is unstable and loses units of BF and BF_3. The lighter

transition metals, which were calculated to have lesser degrees of charge transfer with $B_{12}F_{12}^{2-}$, could be studied using IRMPD. These systems, which exhibit charge-separation in the ground vibronic state, were found to undergo dissociative charge transfer during IRMPD. Calculation show that the charge-transfer dissociative threshold is favoured by 630 kJ mol^{-1} over the impulsive ionic separation threshold. The highest dissociative charge transfer threshold was calculated to be $\Delta G° = 160$ kJ mol^{-1} for the $[Cu(I)•B_{12}F_{12}]^-$ cluster. This work shows that the $TM•B_{12}F_{12}^{2-}$ clusters are too reactive for gas phase delivery of transition metals – the TM = Cu(I), Ag(I), and Zn(II) were the only species to not exhibit cage fragmentation. Thus, solvent effects are expected to play a significant role in stabilizing these species and giving rise to the superweak anion behavior in solution.

With regard to spectroscopic characterization, complexes containing one and two $B_{12}F_{12}^{2-}$ moieties were studied. The IR spectra of the single-cage species showed only one wide band corresponding to the degenerate T_{1u} breathing mode of the uncomplexed $B_{12}F_{12}^{2-}$ cage. The relatively large bandwidth observed was due to isotope effects associated with the 4:1 ratio of ^{11}B:^{10}B. One additional peak appeared in the double-cage spectra, which corresponded to symmetric stretching of the cluster (similar to the symmetric stretch of CO_2). In general, the optimized structures of the double cage species showed the metal atom positioned between the two cages and engaged by six fluorine atoms (three from each cage) in an octahedral binding motif. In the Pd (II) double cage cluster, the metal atom was engaged by four fluorine atoms (two from each cage) in a square planar arrangement, as is typical of palladium complexes. Similar observations were made for the analogous $B_{12}H_{12}^{2-}$–containing species.[36]

The unexpected reactivities of the transition metal $B_{12}F_{12}^{2-}$ clusters motivated further exploration of $B_{12}X_{12}^{2-}$ intermolecular interactions. To investigate interactions with closed-shell

organic molecules, we introduced triethylammonium (TEA), an organic molecule that contains an ideal hydrogen bond donor (N-H^+ group). Clusters of $[TEA{\bullet}B_{12}X_{12}]^-$ X = F, Cl were studied using IRMPD and DFT calculations. The global minimum structure exhibits a geometry wherein the charge-carrying proton points towards the center of a triangular face of the dianion cage. Fragmentation of the $[TEA{\bullet}B_{12}X_{12}]^-$ X = F, Cl clusters occurred by two pathways: (1) dissociative charge transfer to produce neutral TEA, $B_{12}X_{12}^-$, and $B_nF_m^-$ species consistent with the loss of BX/BX_3 units from $B_{12}X_{12}^-$ And (2) proton transfer to produce neutral triethylammonia and $B_{12}X_{12}H^-$. The $B_{12}X_{11}^-$ fragment was also observed, presumably by loss of HX from $B_{12}X_{12}H^-$, as was a large variety of $B_nF_m^-$ species consistent with the loss of BX/BX_3 units from $B_{12}X_{11}^-$. DFT calculations indicate that the proton transfer reaction has the lowest thermodynamic barrier, followed by dissociative charge transfer; well above both of those thresholds is the threshold corresponding to separation of the ions. Ion separation is also ruled out by experiment because no $B_{12}X_{12}^{2-}$ was observed.

To evaluate MO interactions between TEA and $B_{12}X_{12}^{2-}$, NBO analysis was conducted. The primary interaction between TEA and the $B_{12}X_{12}^{2-}$ X = F, Cl species is a hydrogen bond involving the charge-carrying proton. Geometric parameters and analysis of the electron density topology by QTAIM both indicate that the B-X•••H-N interactions are hydrogen bonding in nature. The stabilization energy of the hydrogen bond is estimated to be 42.4 kJ mol^{-1} in the fluorinated cage cluster and 63.7 kJ mol^{-1} in the chlorinated cage cluster. The combination of the hydrogen bond stabilization energy and the electrostatic interaction between the two moieties (~ 547.4 kJ mol^{-1} and ~ 476.7 kJ mol^{-1}; calculated using Coulomb's law for $[TEA{\bullet}B_{12}X_{12}]^-$ X = F, Cl, respectively) accounts for 99% of the dissociation energy as determined via DFT

calculations. This shows that electrostatic interactions dominate the binding between $B_{12}X_{12}^{2-}$ X = F, Cl and organic ligands in the gas phase.

Finally, intermolecular interactions between $B_{12}X_{12}^{2-}$ X = F, H and neutral all-*cis* 1,2,3,4,5,6-hexafluorocyclohexane, **1**, were studied. IRMPD spectra that were collected for $[\mathbf{1}_n \bullet B_{12}H_{12}]^{2-}$ $n = 1 - 4$ in the 800 – 1500 cm^{-1} region were in excellent agreement with those calculated for the global minima with DFT. As the clusters grow, the interaction distances between **1** and $B_{12}H_{12}^{2-}$ increase. Associated with the larger separations are lower electron densities at the critical points, lower stabilization energies for the complex, and lower dissociation energies. These analyses also identified six dihydrogen bonds B-H•••H-C interactions at each $B_{12}H_{12}^{2-}$/**1** interface. To further study this phenomenon, photoelectron spectra were collected for $[\mathbf{1}_n \bullet B_{12}X_{12}]^{2-}$ X = F, H; $n = 1 - 5$. The first photoelectron band in each spectrum is reasonably predicted by the calculated vertical electron detachment energy. Both the experimental photoelectron spectra and IRMPD spectra indicate that a change in the binding of **1** occurs at $n = 4$ for $[\mathbf{1}_n \bullet B_{12}X_{12}]^{2-}$ X = F, H.[7] DFT results indicate that this change is associated with kinetic trapping of three **1** moieties in a planar geometry around $B_{12}X_{12}^{2-}$ X = F, H; higher energy isomers of $n = 2$ and $n = 3$ are necessary for the sequential addition of **1** to produce the global minimum geometry of the $n = 4$ cluster. In both the fluorinated and hydrogenated clusters, hydrogen bonding was found to make significant contributions to the overall stabilization energy. However, in the case of the $B_{12}H_{12}^{2-}$ derivative, the use of a simple electrostatic model for ion-dipole interactions in combination with NBO stabilization energies fails to predict the dissociation energy as accurately as was possible for the TEA complexes. Moreover, the calculated dissociation energies for these species are large in comparison with other ion-organic molecule complexes.[8,257,258] Thus, future work is still required to elucidate the complex interactions of the $B_{12}X_{12}^{2-}$ systems.

Many future directions exist for the investigations discussed herein. Chapter 3 concluded with noting inconsistencies among relative cluster stabilities. Treatment of these species with more recently developed methods (*i.e.*, functional/basis set) and multireference theories which more rigorously treat electronic structure may help resolve some inconsistencies. Electronic structure may also be investigated experimentally using a velocity map imaging spectrometer which is currently under development in the Hopkins Lab. In Chapter 4 it was understood that replacement of a phosphorous atom for an arsenic atom removed the observed mode selectivity. Further studies may vary the identity of this atom to perhaps gain a better understanding of the IVR process and why in some instances this process is inefficient. Our gas phase studies in Chapter 5 identified $[B_{12}X_{12}]^{2-}$ as non-viable for delivery of cationic transition metals or protonated TEA. Computational work using solvation models, the polarizable continuum model for example, could be applied to probe how the energetics of the various dissociation thresholds are affected.

Taken as a whole, this thesis provides a detailed investigation of intermolecular interactions between moieties that exhibit complex electronic and/or geometric structures. The interactions studied range from essentially covalent through to essentially ionic in nature, and we very clearly see how the interplay between electronic and geometric structure gives rise to interesting, and oftentimes unexpected, behavior such as mode-selectivity, catalyst poisoning, and dihydrogen bonding. While non-covalent interactions have for many years been implicated in determining the physicochemical properties of systems such as biological macromolecules and catalysts,[2,9–12] a deep understanding of the physics underpinning these phenomena is still being developed. With the research described herein, we hope to have provided a little more clarity and direction for this fascinating subject.

7 References

(1) Luo, Z.; Castleman, A. W. Special and General Superatoms. *Acc. Chem. Res.* **2014**, *47* (10), 2931–2940. https://doi.org/10.1021/ar5001583.

(2) Hopkins, W. S. Determining the Properties of Gas-Phase Clusters. *Mol. Phys.* **2015**, *113* (21), 3151–3158. https://doi.org/10.1080/00268976.2015.1053545.

(3) Hamilton, S. M.; Hopkins, W. S.; Harding, D. J.; Walsh, T. R.; Haertelt, M.; Kerpal, C.; Gruene, P.; Meijer, G.; Fielicke, A.; Mackenzie, S. R. Infrared-Induced Reactivity of N_2O on Small Gas-Phase Rhodium Clusters. *J. Phys. Chem. A* **2011**, *115* (12), 2489–2497. https://doi.org/10.1021/jp201171p.

(4) Jabłońska, M.; Palkovits, R. It Is No Laughing Matter: Nitrous Oxide Formation in Diesel Engines and Advances in Its Abatement over Rhodium-Based Catalysts. *Catal. Sci. Technol.* **2016**, *6* (21), 7671–7687. https://doi.org/10.1039/C6CY01126H.

(5) Mancino, G.; Cimino, S.; Lisi, L. Sulphur Poisoning of Alumina Supported Rh Catalyst during Dry Reforming of Methane. *Catal. Today* **2016**, *277*, 126–132. https://doi.org/10.1016/j.cattod.2015.10.035.

(6) Keddie, N. S.; Slawin, A. M. Z.; Lebl, T.; Philp, D.; O'Hagan, D. All-Cis 1,2,3,4,5,6-Hexafluorocyclohexane Is a Facially Polarized Cyclohexane. *Nat. Chem.* **2015**, *7* (6), 483–488. https://doi.org/10.1038/nchem.2232.

(7) Lecours, M. J.; Marta, R. A.; Steinmetz, V.; Keddie, N.; Fillion, E.; O'Hagan, D.; McMahon, T. B.; Hopkins, W. S. Interaction of $B_{12}F_{12}^{2-}$ with All-*Cis* 1,2,3,4,5,6-Hexafluorocyclohexane in the Gas Phase. *J. Phys. Chem. Lett.* **2017**, *8* (1), 109–113. https://doi.org/10.1021/acs.jpclett.6b02629.

(8) Ziegler, B. E.; Lecours, M.; Marta, R. A.; Featherstone, J.; Fillion, E.; Hopkins, W. S.; Steinmetz, V.; Keddie, N. S.; O'Hagan, D.; McMahon, T. B. Janus Face Aspect of All-Cis 1,2,3,4,5,6-Hexafluorocyclohexane Dictates Remarkable Anion and Cation Interactions In the Gas Phase. *J. Am. Chem. Soc.* **2016**, *138* (24), 7460–7463. https://doi.org/10.1021/jacs.6b02856.

(9) Le Bourvellec, C.; Renard, C. M. G. C. Interactions between Polyphenols and Macromolecules: Quantification Methods and Mechanisms. *Crit. Rev. Food Sci. Nutr.* **2012**, *52* (3), 213–248. https://doi.org/10.1080/10408398.2010.499808.

(10) Kryscio, D. R.; Peppas, N. A. Critical Review and Perspective of Macromolecularly Imprinted Polymers. *Acta Biomat.* **2012**, *8* (2), 461–473. https://doi.org/10.1016/j.actbio.2011.11.005.

(11) Chakraborty, P.; Nag, A.; Chakraborty, A.; Pradeep, T. Approaching Materials with Atomic Precision Using Supramolecular Cluster Assemblies. *Acc. Chem. Res.* **2019**, *52* (1), 2–11. https://doi.org/10.1021/acs.accounts.8b00369.

(12) Hobza, P.; Zahradník, R.; Müller-Dethlefs, K. The World of Non-Covalent Interactions: 2006. *Collect. Czech. Chem. Commun.* **2006**, *71* (4), 443–531. https://doi.org/10.1135/cccc20060443.

(13) Wales, D. J.; Scheraga, H. A. Review: Chemistry - Global Optimization of Clusters, Crystals, and Biomolecules. *Science* **1999**, *285* (5432), 1368–1372. https://doi.org/10.1126/science.285.5432.1368.

(14) Wales, D. J.; Doye, J. P. K. Global Optimization by Basin-Hopping and the Lowest Energy Structures of Lennard-Jones Clusters Containing up to 110 Atoms. *J. Phys. Chem. A* **1997**, *101* (28), 5111–5116. https://doi.org/10.1021/jp970984n.
(15) Cramer, C. J. *Essentials of Computational Chemistry: Theories and Models*, 2nd ed.; Wiley: Chichester, West Sussex, England ; Hoboken, NJ, 2004.
(16) Frisch, M. J.; Trucks, G. W.; Schlegel, H. B.; Scuseria, G. E.; Robb, M. A.; Cheeseman, J. R.; Scalmani, G.; Barone, V.; Mennucci, B.; Petersson, G. A.; et al. Gaussian 09 Revision D.01. 2009.
(17) Hehre, W. J. *A Guide to Molecular Mechanics and Quantum Chemical Calculations*; Wavefunction, Inc: Irvine, CA, 2003.
(18) Breneman, C. M.; Wiberg, K. B. Determining Atom-Centered Monopoles from Molecular Electrostatic Potentials. The Need for High Sampling Density in Formamide Conformational Analysis. *J. Comput. Chem.* **1990**, *11* (3), 361–373. https://doi.org/10.1002/jcc.540110311.
(19) Wiberg, K. B.; Rablen, P. R. Comparison of Atomic Charges Derived via Different Procedures. *J. Comput. Chem.* **1993**, *14* (12), 1504–1518. https://doi.org/10.1002/jcc.540141213.
(20) Glendening, E. D.; Badenhoop, J. K.; Reed, A. E.; Carpenter, J. E.; Bohmann, J. A.; Morales, C. M.; Landis, C. R.; Weinhold, F. *NBO 6.0*; Theoretical Chemistry Institute: University of Wisconsin, Madison, 2013.
(21) Glendening, E. D.; Landis, C. R.; Weinhold, F. Natural Bond Orbital Methods: Natural Bond Orbital Methods. *WIREs Comput Mol Sci* **2012**, *2* (1), 1–42. https://doi.org/10.1002/wcms.51.
(22) Glendening, E. D.; Landis, C. R.; Weinhold, F. NBO 6.0: Natural Bond Orbital Analysis Program. *J. Comput. Chem.* **2013**, *34* (16), 1429–1437. https://doi.org/10.1002/jcc.23266.
(23) Bader, R. F. W. A Quantum Theory of Molecular Structure and Its Applications. *Chem. Rev.* **1991**, *91* (5), 893–928. https://doi.org/10.1021/cr00005a013.
(24) Kumar, P. S. V.; Raghavendra, V.; Subramanian, V. Bader's Theory of Atoms in Molecules (AIM) and Its Applications to Chemical Bonding. *J. Chem. Sci.* **2016**, *128* (10), 1527–1536. https://doi.org/10.1007/s12039-016-1172-3.
(25) Popelier, P. L. A. Characterization of a Dihydrogen Bond on the Basis of the Electron Density. *J. Phys. Chem. A* **1998**, *102* (10), 1873–1878. https://doi.org/10.1021/jp9805048.
(26) Koch, U.; Popelier, P. L. A. Characterization of C-H-O Hydrogen Bonds on the Basis of the Charge Density. *J. Phys. Chem.* **1995**, *99* (24), 9747–9754. https://doi.org/10.1021/j100024a016.
(27) Matta, C. F. Hydrogen–Hydrogen Bonding: The Non-Electrostatic Limit of Closed-Shell Interaction Between Two Hydro. In *Hydrogen Bonding—New Insights*; Grabowski, S. J., Ed.; Springer Netherlands, 2006; pp 337–375. https://doi.org/10.1007/978-1-4020-4853-1_9.
(28) Duarte, D. J. R.; Angelina, E. L.; Peruchena, N. M. Physical Meaning of the QTAIM Topological Parameters in Hydrogen Bonding. *J. Mol. Model.* **2014**, *20* (11). https://doi.org/10.1007/s00894-014-2510-3.
(29) Grabowski, S. J.; Sokalski, W. A.; Dyguda, E.; Leszczyński, J. Quantitative Classification of Covalent and Noncovalent H-Bonds. *J. Phys. Chem. B* **2006**, *110* (13), 6444–6446. https://doi.org/10.1021/jp0600817.

(30) Rozenberg, M. The Hydrogen Bond – Practice and QTAIM Theory. *RSC Adv.* **2014**, *4* (51), 26928–26931. https://doi.org/10.1039/C4RA03889D.
(31) Keith, T. A. *AIMALL*; TK Gristmill Software, Overland Parks KS, USA, 2017.
(32) Lu, T.; Chen, F. Multiwfn: A Multifunctional Wavefunction Analyzer. *J. Comput. Chem.* **2012**, *33* (5), 580–592. https://doi.org/10.1002/jcc.22885.
(33) Carr, P. J. J.; Lecours, M. J.; Burt, M. J.; Marta, R. A.; Steinmetz, V.; Fillion, E.; Hopkins, W. S. Mode-Selective Laser Control of Palladium Catalyst Decomposition. *J. Phys. Chem. Lett.* **2018**, *9* (1), 157–162. https://doi.org/10.1021/acs.jpclett.7b03030.
(34) Carr, P. J. J.; Warneke, J.; Featherstone, J.; Jenne, C.; Loire, E.; Hopkins, W. S. The Structure of Proton-Bound Triethylammonia $B_{12}X_{12}^{2-}$ (X = F, Cl) Clusters. *Mol. Phys.* **2019**, 1–8. https://doi.org/10.1080/00268976.2019.1595203.
(35) Fu, W.; Carr, P. J. J.; Lecours, M. J.; Burt, M.; Marta, R. A.; Steinmetz, V.; Fillion, E.; McMahon, T. B.; Hopkins, W. S. Intramolecular Cation–π Interactions in Protonated Phenylalanine Derivatives. *Phys. Chem. Chem. Phys.* **2017**, *19* (1), 729–734. https://doi.org/10.1039/C6CP07337A.
(36) De Vlugt, I. J. S.; Lecours, M. J.; Carr, P. J. J.; Anwar, A.; Marta, R. A.; Fillion, E.; Steinmetz, V.; Hopkins, W. S. Infrared-Driven Charge-Transfer in Transition Metal-Containing $B_{12}X_{12}^{2-}$ (X = H, F) Clusters. *J. Phys. Chem. A* **2018**, *122* (35), 7051–7061. https://doi.org/10.1021/acs.jpca.8b05750.
(37) Fu, W.; Xiong, J.; Lecours, M. J.; Carr, P. J. J.; Marta, R. A.; Fillion, E.; McMahon, T.; Steinmetz, V.; Hopkins, W. S. The Structures of Proton-Bound Dimers of Glycine with Phenylalanine and Pentafluorophenylalanine. *J. Mol. Spec.* **2016**, *330*, 194–199. https://doi.org/10.1016/j.jms.2016.07.004.
(38) Hamilton, S. M.; Hopkins, W. S.; Harding, D. J.; Walsh, T. R.; Gruene, P.; Haertelt, M.; Fielicke, A.; Meijer, G.; Mackenzie, S. R. Infrared Induced Reactivity on the Surface of Isolated Size-Selected Clusters: Dissociation of N_2O on Rhodium Clusters. *J. Am. Chem. Soc.* **2010**, *132* (5), 1448–1449. https://doi.org/10.1021/ja907496c.
(39) Harding, D. J.; Gruene, P.; Haertelt, M.; Meijer, G.; Fielicke, A.; Hamilton, S. M.; Hopkins, W. S.; Mackenzie, S. R.; Neville, S. P.; Walsh, T. R. Probing the Structures of Gas-Phase Rhodium Cluster Cations by Far-Infrared Spectroscopy. *J. Chem. Phys.* **2010**, *133* (21), 214304. https://doi.org/10.1063/1.3509778.
(40) Hermes, A. C.; Hamilton, S. M.; Hopkins, W. S.; Harding, D. J.; Kerpal, C.; Meijer, G.; Fielicke, A.; Mackenzie, S. R. Effects of Coadsorbed Oxygen on the Infrared Driven Decomposition of N_2O on Isolated Rh_5^+ Clusters. *J. Phys. Chem. Lett.* **2011**, *2* (24), 3053–3057. https://doi.org/10.1021/jz2012963.
(41) Hopkins, W. S.; Carr, P. J. J.; Huang, D.; Bishop, K. P.; Burt, M.; McMahon, T. B.; Steinmetz, V.; Fillion, E. Infrared-Driven Charge Transfer in Transition Metal $B_{12}F_{12}$ Clusters. *J. Phys. Chem. A* **2015**, *119* (31), 8469–8475. https://doi.org/10.1021/acs.jpca.5b03932.
(42) Hopkins, W. S.; Hasan, M.; Burt, M.; Marta, R. A.; Fillion, E.; McMahon, T. B. Persistent Intramolecular C-H•••X (X = O or S) Hydrogen-Bonding in Benzyl Meldrum's Acid Derivatives. *J. Phys. Chem. A* **2014**, *118* (21), 3795–3803. https://doi.org/10.1021/jp5029245.
(43) Hopkins, W. S.; Marta, R. A.; Steinmetz, V.; McMahon, T. B. Mode-Specific Fragmentation of Amino Acid-Containing Clusters. *Phys. Chem. Chem. Phys.* **2015**, *17* (43), 28548–28555. https://doi.org/10.1039/c5cp03517a.

(44) Ieritano, C.; Carr, P. J. J.; Hasan, M.; Burt, M.; Marta, R. A.; Steinmetz, V.; Fillion, E.; McMahon, T. B.; Scott Hopkins, W. The Structures and Properties of Proton- and Alkali-Bound Cysteine Dimers. *Phys. Chem. Chem. Phys.* **2016**, *18* (6), 4704–4710. https://doi.org/10.1039/C5CP07414B.

(45) Dunbar, R. C.; Steill, J. D.; Oomens, J. Chirality-Induced Conformational Preferences in Peptide-Metal Ion Binding Revealed by IR Spectroscopy. *J. Am. Chem. Soc.* **2011**, *133* (5), 1212–1215. https://doi.org/10.1021/ja109045j.

(46) Oomens, J.; Sartakov, B. G.; Meijer, G.; Von Helden, G. Gas-Phase Infrared Multiple Photon Dissociation Spectroscopy of Mass-Selected Molecular Ions. *Int. J. Mass Spectrom.* **2006**, *254* (1–2), 1–19. https://doi.org/10.1016/j.ijms.2006.05.009.

(47) Polfer, N. C.; Oomens, J. Vibrational Spectroscopy of Bare and Solvated Ionic Complexes of Biological Relevance. *Mass Spectrom. Rev.* **2009**, *28* (3), 468–494. https://doi.org/10.1002/mas.20215.

(48) Prazeres, R.; Berset, J. M.; Glotin, F.; Jaroszynski, D.; Ortega, J. M. Optical Performance of the CLIO Infrared FEL. *Nucl. Instrum. Methods Phys. Res.* **1993**, *331* (1–3), 15–19. https://doi.org/10.1016/0168-9002(93)90006-4.

(49) Ortega, J. M.; Glotin, F.; Prazeres, R. Extension in Far-Infrared of the CLIO Free-Electron Laser. *Infrared Phys. Technol.* **2006**, *49* (1–2), 133–138. https://doi.org/10.1016/j.infrared.2006.01.01.

(50) Bera, M.; Agasti, S.; Chowdhury, R.; Mondal, R.; Pal, D.; Maiti, D. Rhodium-Catalyzed *Meta* -C−H Functionalization of Arenes. *Angew. Chem.-Int. Edit.* **2017**, *56* (19), 5272–5276. https://doi.org/10.1002/anie.201701579.

(51) Buwono, H. P.; Minami, S.; Uemura, K.; Machida, M. Surface Properties of Rh/$AlPO_4$ Catalyst Providing High Resistance to Sulfur and Phosphorus Poisoning. *Ind. Eng. Chem. Res.* **2015**, *54* (29), 7233–7240. https://doi.org/10.1021/acs.iecr.5b01720.

(52) Jat, J. L.; Paudyal, M. P.; Gao, H.; Xu, Q.-L.; Yousufuddin, M.; Devarajan, D.; Ess, D. H.; Kürti, L.; Falck, J. R. Direct Stereospecific Synthesis of Unprotected N-H and N-Me Aziridines from Olefins. *Science* **2014**, *343* (6166), 61–65. https://doi.org/10.1126/science.1245727.

(53) Jiang, H.-Y.; Zheng, X.-X. Phosphine-Functionalized Ionic Liquid-Stabilized Rhodium Nanoparticles for Selective Hydrogenation of Aromatic Compounds. *App. Cata. A: Gen.* **2015**, *499*, 118–123. https://doi.org/10.1016/j.apcata.2015.04.015.

(54) Knickelbein, M. B. Reactions of Transition Metal Clusters with Small Molecules. *Annu. Rev. Phys. Chem.* **1999**, *50* (1), 79–115. https://doi.org/10.1146/annurev.physchem.50.1.79.

(55) Machida, M.; Murakami, K.; Hinokuma, S.; Uemura, K.; Ikeue, K.; Matsuda, M.; Chai, M.; Nakahara, Y.; Sato, T. $AlPO_4$ as a Support Capable of Minimizing Threshold Loading of Rh in Automotive Catalysts. *Chem. Mat.* **2009**, *21* (9), 1796–1798. https://doi.org/10.1021/cm9005844.

(56) Meißner, A.; Alberico, E.; Drexler, H.-J.; Baumann, W.; Heller, D. Rhodium Diphosphine Complexes: A Case Study for Catalyst Activation and Deactivation. *Catal. Sci. Technol.* **2014**, *4* (10), 3409–3425. https://doi.org/10.1039/C4CY00497C.

(57) Stoll, T.; Castillo, C. E.; Kayanuma, M.; Sandroni, M.; Daniel, C.; Odobel, F.; Fortage, J.; Collomb, M.-N. Photo-Induced Redox Catalysis for Proton Reduction to Hydrogen with Homogeneous Molecular Systems Using Rhodium-Based Catalysts. *Coord. Chem. Rev.* **2015**, *304–305* (Complete), 20–37. https://doi.org/10.1016/j.ccr.2015.02.002.

(58) Noda, N.; Nambu, H.; Ubukata, K.; Fujiwara, T.; Tsuge, K.; Yakura, T. Total Synthesis of Myriocin and Mycestericin D Employing Rh(II)-Catalyzed CH Amination Followed by Stereoselective Alkylation. *Tetrahedron Lett.* **2017**, *73* (7), 868–878. https://doi.org/10.1016/j.tet.2016.12.066.

(59) Wu, X.; Neumann, H. Ruthenium and Rhodium-Catalyzed Carbonylation Reactions. *Chem. Cat. Chem.* **2012**, *4* (4), 447–458. https://doi.org/10.1002/cctc.201200069.

(60) Adlhart, C.; Uggerud, E. C–H Activation of Alkanes on Rh_n^+ (n = 1 – 30) Clusters: Size Effects on Dehydrogenation. *J. Chem. Phys.* **2005**, *123* (21), 214709. https://doi.org/10.1063/1.2131066.

(61) Gandhi, H. S.; Graham, G. W.; McCabe, R. W. Automotive Exhaust Catalysis. *J. Catal.* **2003**, *216* (1–2), 433–442. https://doi.org/10.1016/S0021-9517(02)00067-2.

(62) Heck, R. M.; Farrauto, R. J. Automobile Exhaust Catalysts. *App. Catal. A: Gen.* **2001**, *221* (1–2), 443–457. https://doi.org/10.1016/S0926-860X(01)00818-3.

(63) Lin, Y.; Meng, T.; Ma, Z. Catalytic Decomposition of N_2O over RhO_x Supported on Metal Phosphates. *J. Ind. Eng. Chem.* **2015**, *28*, 138–146. https://doi.org/10.1016/j.jiec.2015.02.009.

(64) Luo, L.; Li, H.; Peng, Y.; Feng, C.; Zeng, J. Rh-Based Nanocatalysts for Heterogeneous Reactions. *Chem. Nano Mat.* **2018**, *4* (5), 451–466. https://doi.org/10.1002/cnma.201800033.

(65) *Inventory of US Greenhouse Gas Emissions and Sinks: 1990-2013*; U.S. Environmental Protection Agency, 2015.

(66) Somorjai, G. A. *Chemistry in Two Dimensions : Surfaces*; Cornell University Press: Ithaca, 1981.

(67) Anderson, M. L.; Ford, M. S.; Derrick, P. J.; Drewello, T.; Woodruff, D. P.; Mackenzie, S. R. Nitric Oxide Decomposition on Small Rhodium Clusters, $Rh_n^{+/-}$. *J. Phys. Chem. A* **2006**, *110* (38), 10992–11000. https://doi.org/10.1021/jp062178z.

(68) Burch, R.; Daniells, S. T.; Breen, J. P.; Hu, P. A Combined Transient and Computational Study of the Dissociation of N_2O on Platinum Catalysts. *J. Cata.* **2004**, *224* (2), 252–260. https://doi.org/10.1016/j.jcat.2004.03.027.

(69) Chaves, A. S.; Piotrowski, M. J.; Da Silva, J. L. F. Evolution of the Structural, Energetic, and Electronic Properties of the 3d, 4d, and 5d Transition-Metal Clusters (30 TM_n Systems for n = 2–15): A Density Functional Theory Investigation. *Phys. Chem. Chem. Phys.* **2017**, *19* (23), 15484–15502. https://doi.org/10.1039/C7CP02240A.

(70) Chen, H.; Yue, J.; Li, Y.; Yi, C.; Yang, B.; Qi, S. Catalytic Activity Prediction of Different Metal Surfaces for N_2O Catalytic Decomposition by Density Functional Theory. *Comp. Theo. Chem.* **2015**, *1057*, 1–6. https://doi.org/10.1016/j.comptc.2015.01.009.

(71) Da Silva, J. L. F.; Piotrowski, M. J.; Aguilera-Granja, F. Hybrid Density Functional Study of Small Rh_n (n = 2 − 15) Clusters. *Phys. Rev. B* **2012**, *86* (12). https://doi.org/10.1103/PhysRevB.86.125430.

(72) Deushi, F.; Ishikawa, A.; Nakai, H. Density Functional Theory Analysis of Elementary Reactions in NO_x Reduction on Rh Surfaces and Rh Clusters. *J. Phys. Chem. C* **2017**, *121* (28), 15272–15281. https://doi.org/10.1021/acs.jpcc.7b04526.

(73) Dutta, A.; Mondal, P. Structural, Electronic and Catalytic Properties of Single Magnesium Atom Doped Small Neutral Rh_n (n = 2–8) Clusters: Density Functional Study. *Comp. Theo. Chem.* **2017**, *1115*, 284–298. https://doi.org/10.1016/j.comptc.2017.07.003.

(74) Harding, D.; Mackenzie, S. R.; Walsh, T. R. Structural Isomers and Reactivity for Rh_6 and Rh_6^+. *J. Phys. Chem. B* **2006**, *110* (37), 18272–18277. https://doi.org/10.1021/jp062603o.
(75) Harding, D. J.; Davies, R. D. L.; Mackenzie, S. R.; Walsh, T. R. Oxides of Small Rhodium Clusters: Theoretical Investigation of Experimental Reactivities. *J. Phys. Chem.* **2008**, *129* (12), 124304. https://doi.org/10.1063/1.2981810.
(76) Lecours, M. J.; Chow, W. C. T.; Hopkins, W. S. Density Functional Theory Study of $Rh_nS^{0,\pm}$ and $Rh_{n+1}{}^{0,\pm}$ (n = 1 – 9). *J. Phys. Chem. A* **2014**, *118* (24), 4278–4287. https://doi.org/10.1021/jp412457m.
(77) Rodríguez-Kessler, P. L.; Rodríguez-Domínguez, A. R. N_2O Dissociation on Small Rh Clusters: A Density Functional Study. *Comp. Mat. Sci.* **2015**, *97*, 32–35. https://doi.org/10.1016/j.commatsci.2014.09.044.
(78) Beck, D. D.; Sommers, J. W.; DiMaggio, C. L. Axial Characterization of Oxygen Storage Capacity in Close-Coupled Lightoff and Underfloor Catalytic Converters and Impact of Sulfur. *App. Cata. B: Enviro.* **1997**, *11* (3–4), 273–290. https://doi.org/10.1016/S0926-3373(96)00051-3.
(79) Chen, Y.; Xie, C.; Li, Y.; Song, C.; Bolin, T. B. Sulfur Poisoning Mechanism of Steam Reforming Catalysts: An X-Ray Absorption near Edge Structure (XANES) Spectroscopic Studyw. *Phys. Chem. Chem. Phys.* **2010**, 7.
(80) Cimino, S.; Lisi, L. Impact of Sulfur Poisoning on the Catalytic Partial Oxidation of Methane on Rhodium-Based Catalysts. *Ind. Eng. Chem. Res.* **2012**, *51* (22), 7459–7466. https://doi.org/10.1021/ie201648e.
(81) Ocsachoque, M. A.; Eugenio Russman, J. I.; Irigoyen, B.; Gazzoli, D.; González, M. G. Experimental and Theoretical Study about Sulfur Deactivation of Ni/CeO_2 and Rh/CeO_2 Catalysts. *Mat. Chem. Phys.* **2016**, *172*, 69–76. https://doi.org/10.1016/j.matchemphys.2015.12.062.
(82) Vita, A.; Italiano, C.; Pino, L.; Laganà, M.; Recupero, V. Hydrogen-Rich Gas Production by Steam Reforming of n-Dodecane. Part II: Stability, Regenerability and Sulfur Poisoning of Low Loading Rh-Based Catalyst. *App. Cata. B: Enviro.* **2017**, *218*, 317–326. https://doi.org/10.1016/j.apcatb.2017.06.059.
(83) Zheng, Q.; Janke, C.; Farrauto, R. Steam Reforming of Sulfur-Containing Dodecane on a Rh–Pt Catalyst: Influence of Process Parameters on Catalyst Stability and Coke Structure. *App. Cata. B: Enviro.* **2014**, *160–161*, 525–533. https://doi.org/10.1016/j.apcatb.2014.05.044.
(84) Cimino, S.; Lisi, L.; Russo, G. Effect of Sulphur during the Catalytic Partial Oxidation of Ethane over Rh and Pt Honeycomb Catalysts. *Int. J. Hydrog. Energy* **2012**, *37* (14), 10680–10689. https://doi.org/10.1016/j.ijhydene.2012.04.069.
(85) Beyer, H.; Emmerich, J.; Chatziapostolou, K.; Köhler, K. Decomposition of Nitrous Oxide by Rhodium Catalysts: Effect of Rhodium Particle Size and Metal Oxide Support. *App. Cata. A: Gen.* **2011**, *391* (1–2), 411–416. https://doi.org/10.1016/j.apcata.2010.03.060.
(86) Dutta, A.; Mondal, P. A Density Functional Study on the Electronic Structure, Nature of Bonding and Reactivity of NO Adsorbing $Rh_n^{0/\pm}$ (n = 2–8) Clusters. *New J. Chem.* **2018**, *42* (2), 1121–1132. https://doi.org/10.1039/C7NJ04166G.
(87) Francisco, H.; Bertin, V.; Soto, J. R.; Castro, M. Charge and Geometrical Effects on the Catalytic N_2O Reduction by Rh_6^- and Rh_6^+ Clusters. *J. Phys. Chem. C* **2016**, *120* (41), 23648–23659. https://doi.org/10.1021/acs.jpcc.6b08172.

(88) Harding, D. J.; Mackenzie, S. R.; Walsh, T. R. Density Functional Theory Calculations of Vibrational Spectra of Rhodium Oxide Clusters. *Chem. Phys. Lett.* **2009**, *469* (1–3), 31–34. https://doi.org/10.1016/j.cplett.2008.12.053.

(89) Harding, D.; Ford, M. S.; Walsh, T. R.; Mackenzie, S. R. Dramatic Size Effects and Evidence of Structural Isomers in the Reactions of Rhodium Clusters, $Rh_n^{\pm}$, with Nitrous Oxide. *Phys. Chem. Chem. Phys.* **2007**, *9* (17), 2130–2136. https://doi.org/10.1039/B618299B.

(90) Parry, I. S.; Kartouzian, A.; Hamilton, S. M.; Balaj, O. P.; Beyer, M. K.; Mackenzie, S. R. Chemical Reactivity on Gas-Phase Metal Clusters Driven by Blackbody Infrared Radiation. *Angew. Chem.-Int. Edit.* **2015**, *54* (4), 1357–1360. https://doi.org/10.1002/anie.201409483.

(91) Parry, I. S.; Kartouzian, A.; Hamilton, S. M.; Balaj, O. P.; Beyer, M. K.; Mackenzie, S. R. Collisional Activation of N_2O Decomposition and CO Oxidation Reactions on Isolated Rhodium Clusters. *J. Phys. Chem. A* **2013**, *117* (36), 8855–8863. https://doi.org/10.1021/jp405267p.

(92) Dunbar, R. C. BIRD (Blackbody Infrared Radiative Dissociation): Evolution, Principles, and Applications. *Mass Spectrom. Rev.* **2004**, *23* (2), 127–158. https://doi.org/10.1002/mas.10074.

(93) Ma, L.; Moro, R.; Bowlan, J.; Kirilyuk, A.; de Heer, W. A. Multiferroic Rhodium Clusters. *Phys. Rev. Lett.* **2014**, *113* (15). https://doi.org/10.1103/PhysRevLett.113.157203.

(94) Harding, D. J.; Walsh, T. R.; Hamilton, S. M.; Hopkins, W. S.; Mackenzie, S. R.; Gruene, P.; Haertelt, M.; Meijer, G.; Fielicke, A. Communications: The Structure of Rh_8^+ in the Gas Phase. *J. Chem. Phys.* **2010**, *132* (1), 011101. https://doi.org/10.1063/1.3285266.

(95) Atkins, P.; de Paula, J. *Atkins' Physical Chemistry*; OUP Oxford, 2010.

(96) Cornell, W. D.; Cieplak, P.; Bayly, C. I.; Gould, I. R.; Merz, K. M.; Ferguson, D. M.; Spellmeyer, D. C.; Fox, T.; Caldwell, J. W.; Kollman, P. A. A Second Generation Force Field for the Simulation of Proteins, Nucleic Acids, and Organic Molecules. *J. Am. Chem. Soc.* **1995**, *117* (19), 5179–5197. https://doi.org/10.1021/ja00124a002.

(97) Rappe, A. K.; Casewit, C. J.; Colwell, K. S.; Goddard, W. A.; Skiff, W. M. UFF, a Full Periodic Table Force Field for Molecular Mechanics and Molecular Dynamics Simulations. *J. Am. Chem. Soc.* **1992**, *114* (25), 10024–10035. https://doi.org/10.1021/ja00051a040.

(98) Perdew, J. P.; Ernzerhof, M.; Burke, K. Rationale for Mixing Exact Exchange with Density Functional Approximations. *J. Chem. Phys.* **1996**, *105* (22), 9982–9985. https://doi.org/10.1063/1.472933.

(99) Staroverov, V. N.; Scuseria, G. E.; Tao, J.; Perdew, J. P. Comparative Assessment of a New Nonempirical Density Functional: Molecules and Hydrogen-Bonded Complexes. *J. Chem. Phys.* **2003**, *119* (23), 12129–12137. https://doi.org/10.1063/1.1626543.

(100) Weigend, F.; Ahlrichs, R. Balanced Basis Sets of Split Valence, Triple Zeta Valence and Quadruple Zeta Valence Quality for H to Rn: Design and Assessment of Accuracy. *Phys. Chem. Chem. Phys.* **2005**, No. 7, 3297–3305. http://dx.doi.org/10.1039/B508541A.

(101) Weigend, F.; Häser, M.; Patzelt, H.; Ahlrichs, R. RI-MP2: Optimized Auxiliary Basis Sets and Demonstration of Efficiency. *Chem. Phys. Lett.* **1998**, *294* (1–3), 143–152. https://doi.org/10.1016/S0009-2614(98)00862-8.

(102) Jensen, K. P. Metal−Ligand Bonds of Second- and Third-Row d-Block Metals Characterized by Density Functional Theory. *J. Phys. Chem. A* **2009**, *113* (37), 10133–10141. https://doi.org/10.1021/jp9061225.
(103) Swart, I.; de Groot, F. M. F.; Weckhuysen, B. M.; Rayner, D. M.; Meijer, G.; Fielicke, A. The Effect of Charge on CO Binding in Rhodium Carbonyls: From Bridging to Terminal CO. *J. Am. Chem. Soc.* **2008**, *130* (7), 2126–2127. https://doi.org/10.1021/ja0772795.
(104) Fielicke, A.; Gruene, P.; Haertelt, M.; Harding, D. J.; Meijer, G. Infrared Spectroscopy and Binding Geometries of Oxygen Atoms Bound to Cationic Tantalum Clusters. *J. Phys. Chem. A* **2010**, *114* (36), 9755–9761. https://doi.org/10.1021/jp102084n.
(105) Banerjee, A.; Adams, N.; Simons, J.; Shepard, R. Search for Stationary Points on Surfaces. *J. Phys. Chem.* **1985**, *89* (1), 52–57. https://doi.org/10.1021/j100247a015.
(106) Helgaker, T. Transition-State Optimizations by Trust-Region Image Minimization. *Chem. Phys. Lett.* **1991**, *182* (5), 503–510. https://doi.org/10.1016/0009-2614(91)90115-P.
(107) Peng, C.; Bernhard Schlegel, H. Combining Synchronous Transit and Quasi-Newton Methods to Find Transition States. *Isreal J. Chem.* **1993**, *33* (4), 449–454. https://doi.org/10.1002/ijch.199300051.
(108) Ford, M. S.; Anderson, M. L.; Barrow, M. P.; Woodruff, D. P.; Drewello, T.; Derrick, P. J.; Mackenzie, S. R. Reactions of Nitric Oxide on Rh_6^+ Clusters: Abundant Chemistry and Evidence of Structural Isomers. *Phys. Chem. Chem. Phys.* **2005**, *7* (5), 975. https://doi.org/10.1039/b415414b.
(109) Francisco, H.; Bertin, V.; Agacino, E.; Poulain, E.; Castro, M. Dissociation of N_2O Promoted by Rh_6 Clusters. A ZORA/DFT/PBE Study. *J. Mol. Catal. A* **2015**, *406*, 238–250. https://doi.org/10.1016/j.molcata.2015.06.005.
(110) Klein, M. P.; Ehrhard, A. A.; Mohrbach, J.; Dillinger, S.; Niedner-Schatteburg, G. Infrared Spectroscopic Investigation of Structures and N_2 Adsorption Induced Relaxations of Isolated Rhodium Clusters. *Topics in Catal.* **2018**, *61* (1–2), 106–118. https://doi.org/10.1007/s11244-017-0865-2.
(111) Lide, D. *CRC Handbook of Chemistry and Physics*, Internet Version 2005.; CRC Press: Boca Raton, FL.
(112) Avery, N. R. An EELS Study of N_2O Adsorption on Pt(III). *Surf. Sci.* **1983**, No. 131, 10.
(113) Cornish, J. C. L.; Avery, N. R. Adsorption of N_2, O_2, N_2O and NO on Ir(111) by EELS and TPD. *Surf. Sci.* **1990**, *235* (2–3), 209–216. https://doi.org/10.1016/0039-6028(90)90795-A.
(114) Haq, S.; Hodgson, A. N_2O Adsorption and Reaction at Pd(110). *Surf. Sci.* **2000**, *463* (1), 1–10. https://doi.org/10.1016/S0039-6028(00)00606-3.
(115) Madey, T. E.; Avery, N. R.; Anton, A. B.; Toby, B. H.; Weinberg, W. H. Summary Abstract: The Adsorption and Decomposition of N_2O on Ru(001). *J. Vac. Sci. Technol.* **1983**, *1* (2), 1220–1221. https://doi.org/10.1116/1.572284.
(116) Cunningham, E. M.; Gentleman, A. S.; Beardsmore, P. W.; Iskra, A.; Mackenzie, S. R. Infrared Signature of Structural Isomers of Gas–Phase $M^+(N_2O)_n$ (M = Cu, Ag, Au) Ion–Molecule Complexes. *J. Phys. Chem. A* **2017**, *121* (40), 7565–7571. https://doi.org/10.1021/acs.jpca.7b07628.
(117) Armor, J. N.; Taube, H. Formation and Reactions of $[(NH_3)_5RuN_2O_2^+]$. *J. Am. Chem. Soc.* **1969**, *91* (24), 6874–6876. https://doi.org/10.1021/ja01052a069.
(118) Armor, J. N.; Taube, H. Evidence of a Binuclear Nitrous Oxide Complex of Ruthenium. *J. Chem. Soc. D* **1971**, No. 7, 287–288. https://doi.org/10.1039/C29710000287.

(119) Pamplin, C. B.; Ma, E. S. F.; Safari, N.; Rettig, S. J.; James, B. R. The Nitrous Oxide Complex, $RuCl_2(\eta^1\text{-}N_2O)(P{-}N)(PPh_3)$ (P−N = [o-(N,N-Dimethylamino)Phenyl]Diphenylphosphine); Low Temperature Conversion of N_2O to N_2 and O_2. *J. Am. Chem. Soc.* **2001**, *123* (35), 8596–8597. https://doi.org/10.1021/ja0106319.
(120) Liu, C.-G.; Guan, W.; Yan, L.-K.; Su, Z.-M. Bonding Interactions between Nitrous Oxide (N_2O) and Mono-Ruthenium Substituted Keggin-Type Polyoxometalates: Electronic Structures of Ruthenium/N_2O Adducts. *Eur. J. Inorg. Chem.* **2011**, *2011* (4), 489–494. https://doi.org/10.1002/ejic.201000907.
(121) Teffo, J.-L.; Chédin, A. Internuclear Potential and Equilibrium Structure of the Nitrous Oxide Molecule from Rovibrational Data. *J. Mol. Spec.* **1989**, *135* (2), 389–409. https://doi.org/10.1016/0022-2852(89)90164-1.
(122) Paul, J.-F.; Pérez-Ramírez, J.; Ample, F.; Ricart, J. M. Theoretical Studies of N_2O Adsorption and Reactivity to N_2 and NO on Rh(111). *J. Phys. Chem. B* **2004**, *108* (46), 17921–17927. https://doi.org/10.1021/jp048138h.
(123) Hernández, E.; Bertin, V.; Soto, J.; Miralrio, A.; Castro, M. Catalytic Reduction of Nitrous Oxide by the Low-Symmetry Pt_8 Cluster. *J. Phys. Chem. A* **2018**, *122* (8), 2209–2220. https://doi.org/10.1021/acs.jpca.7b11055.
(124) Butcher, R. J.; Jones, W. J. Study of the Rotational Raman Spectra of $^{14}N^{15}N$ and $^{15}N_2$, Using a Fabry–Perot Etalon. *J. Chem. Soc., Faraday Trans. 2* **1974**, *70* (0), 560–563. https://doi.org/10.1039/F29747000560.
(125) Li, Q.; Qiu, Y.-X.; Chen, X.-Y.; Schwarz, W. H. E.; Wang, S.-G. Investigation of Spin-Flip Reactions of Nb + CH3CN by Relativistic Density Functional Theory. *Phys. Chem. Chem. Phys.* **2012**, *14* (19), 6833–6841. https://doi.org/10.1039/C2CP23225A.
(126) Zhang, G.; Musgrave, C. B. Comparison of DFT Methods for Molecular Orbital Eigenvalue Calculations. *J. Phys. Chem. A* **2007**, *111* (8), 1554–1561. https://doi.org/10.1021/jp061633o.
(127) Shimanouchi, T. Tables of Molecular Vibrational Frequencies. Consolidated Volume II. *Journal of Physical and Chemical Reference Data* **1977**, *6* (3), 993–1102. https://doi.org/10.1063/1.555560.
(128) Wang, X.; Andrews, L. Rhodium Dinitrogen Complexes $Rh(NN)_x$ (x = 1−3) and Anions: Matrix Infrared Spectra and DFT Calculations. *J. Phys. Chem. A* **2002**, *106* (11), 2457–2464. https://doi.org/10.1021/jp013527m.
(129) Blyholder, G. Molecular Orbital View of Chemisorbed Carbon Monoxide. *J. Phys. Chem.* **1964**, *68* (10), 2772–2777. https://doi.org/10.1021/j100792a006.
(130) Carpenter, B. K. Nonstatistical Dynamics in Thermal Reactions of Polyatomic Molecules. In *Annu. Rev. Phys. Chem.*; Annual Reviews: Palo Alto, 2005; Vol. 56, pp 57–89.
(131) Carpenter, B. K. Electronically Nonadiabatic Thermal Reactions of Organic Molecules. *Chem. Soc. Rev.* **2006**, *35* (8), 736–747. https://doi.org/10.1039/b509487a.
(132) Ebata, T. Study on the Structure and Vibrational Dynamics of Functional Molecules and Molecular Clusters by Double Resonance Vibrational Spectroscopy. *Bull. Chem. Soc. Jpn.* **2009**, *82* (2), 127–151. https://doi.org/10.1246/bcsj.82.127.
(133) Gruebele, M.; Bigwood, R. Molecular Vibrational Energy Flow: Beyond the Golden Rule. *Int. Rev. Phys. Chem.* **1998**, *17* (2), 91–145. https://doi.org/10.1080/014423598230117.
(134) Shaffer, C. J.; Révész, Á.; Schröder, D.; Severa, L.; Teplý, F.; Zins, E.-L.; Jašíková, L.; Roithová, J. Can Hindered Intramolecular Vibrational Energy Redistribution Lead to Non-

Ergodic Behavior of Medium-Sized Ion Pairs? *Angew. Chem.-Int. Edit.* **2012**, *51* (40), 10050–10053. https://doi.org/10.1002/anie.201203441.
(135) Yamada, Y.; Katsumoto, Y.; Ebata, T. Picosecond IR-UV Pump-Probe Spectroscopic Study on the Vibrational Energy Flow in Isolated Molecules and Clusters. *Phys. Chem. Chem. Phys.* **2007**, *9* (10), 1170–1185. https://doi.org/10.1039/b614895f.
(136) Yoo, H. S.; McWhorter, D. A.; Pate, B. H. Vibrational Dynamics of Terminal Acetylenes: III. Comparison of the Acetylenic C-H Stretch Intramolecular Vibrational-Energy Redistribution Rates in Ultracold Molecular Beams, Room-Temperature Gases, and Room-Temperature Dilute Solutions. *J. Phys. Chem. A* **2004**, *108* (8), 1380–1387. https://doi.org/10.1021/jp0275443.
(137) Steinfeld, J. L. *An Introduction to Modern Molecular Spectroscopy, 2nd Ed.*; MIT Press: Cambridge, MA, 1986.
(138) Bagratashvili, V. N.; Letokhov, V. S.; Makarov, A. A.; Ryabov, E. A. *Multiple Photon Infrared Photophysics and Photochemistry*; Gordon and Breach: New York, 1985.
(139) Feil, F.; Naumov, S.; Michaelis, J.; Valiullin, R.; Enke, D.; Karger, J.; Brauchle, C. Single-Particle and Ensemble DiffusivitiesuTest of Ergodicity. *Angew. Chem.-Int. Edit.* **2012**, *51* (5), 1152–1155. https://doi.org/10.1002/anie.201105388.
(140) Citir, M.; Metz, R. B. Mode Selective Photodissociation Dynamics in V^+(OCO). *J. Chem. Phys.* **2008**, *128* (2), 024307. https://doi.org/10.1063/1.2818564.
(141) Diau, E. W. G.; Herek, J. L.; Kim, Z. H.; Zewail, A. H. Femtosecond Activation of Reactions and the Concept of Nonergodic Molecules. *Science* **1998**, *279* (5352), 847–851. https://doi.org/10.1126/science.279.5352.847.
(142) Holiday, R. J.; Kwon, C. H.; Annesley, C. J.; Crim, F. F. Mode- and Bond-Selective Reaction of Cl($^2P_{3/2}$) with CH_3D: C-H Stretch Overtone Excitation near 6000 Cm^{-1}. *J. Chem. Phys.* **2006**, *125* (13), 8. https://doi.org/10.1063/1.2352742.
(143) Thoemke, J. D.; Pfeiffer, J. M.; Metz, R. B.; Crim, F. F. Mode-Selective and Bond-Selective Rreactions of Chlorine Atoms with Highly Vibrationally Excited H_2O and HOD. *J. Phys. Chem.* **1995**, *99* (37), 13748–13754. https://doi.org/10.1021/j100037a023.
(144) Nahler, N. H.; White, J. D.; Larue, J.; Auerbach, D. J.; Wodtke, A. M. Inverse Velocity Dependence of Vibrationally Promoted Electron Emission from a Metal Surface. *Science* **2008**, *321* (5893), 1191–1194. https://doi.org/10.1126/science.1160040.
(145) Killelea, D. R.; Campbell, V. L.; Shuman, N. S.; Utz, A. L. Bond-Selective Control of a Heterogeneously Catalyzed Reaction. *Science* **2008**, *319* (5864), 790–793. https://doi.org/10.1126/science.1152819.
(146) Beck, R. D.; Maroni, P.; Papageorgopoulos, D. C.; Dang, T. T.; Schmid, M. P.; Rizzo, T. R. Vibrational Mode-Specific Reaction of Methane on a Nickel Surface. *Science* **2003**, *302* (5642), 98–100. https://doi.org/10.1126/science.1088996.
(147) Laskin, J.; Futrell, J. H.; Chu, I. K. Is Dissociation of Peptide Radical Cations an Ergodic Process? *J. Am. Chem. Soc.* **2007**, *129* (31), 9598–9599. https://doi.org/10.1021/ja073748r.
(148) Moss, C. L.; Liang, W.; Li, X. S.; Turecek, F. The Early Life of a Peptide Cation-Radical. Ground and Excited-State Trajectories of Electron-Based Peptide Dissociations During the First 330 Femtoseconds. *J. Am. Soc. Mass Spectrom.* **2012**, *23* (3), 446–459. https://doi.org/10.1007/s13361-011-0283-9.

(149) Schroder, D. Energy Partitioning in Single-Electron Transfer Events between Gaseous Dications and Their Neutral Counterparts. *Eur. J. Mass Spectrom.* **2012**, *18* (2), 139–148. https://doi.org/10.1255/ejms.1161.
(150) Shi, L.; Liu, S. Y.; Zubarev, R. A. ECD Technology in Biological Mass Spectrometry. *Prog. Chem.* **2011**, *23* (8), 1710–1718.
(151) Turecek, F. N-C-Alpha Bond Dissociation Energies and Kinetics in Amide and Peptide Radicals. Is the Dissociation a Non-Ergodic Process? *J. Am. Chem. Soc.* **2003**, *125* (19), 5954–5963. https://doi.org/10.1021/ja021323t.
(152) Olivucci, M.; Santoro, F. Chemical Selectivity through Control of Excited-State Dynamics. *Angew. Chem.-Int. Edit.* **2008**, *47* (34), 6322–6325. https://doi.org/10.1002/anie.200800898.
(153) Zhang, J. M.; Camden, J. P.; Brunsvold, A. L.; Upadhyaya, H. P.; Minton, T. K.; Schatz, G. C. Unusual Mechanisms Can Dominate Reactions at Hyperthermal Energies: An Example from $O(^3P)$ + HCl → ClO + H. *J. Am. Chem. Soc.* **2008**, *130* (28), 8896-+. https://doi.org/10.1021/ja803080q.
(154) Liu, C.; Le Blanc, J. C. Y.; Schneider, B. B.; Shields, J.; Federico, J. J.; Zhang, H.; Stroh, J. G.; Kauffman, G. W.; Kung, D. W.; Ieritano, C.; et al. Assessing Physicochemical Properties of Drug Molecules via Microsolvation Measurements with Differential Mobility Spectrometry. *ACS Cent. Sci.* **2017**, *3* (2), 101–109. https://doi.org/10.1021/acscentsci.6b00297.
(155) Schroder, D. Ion Clustering in Electrospray Mass Spectrometry of Brine and Other Electrolyte Solutions. *Phys. Chem. Chem. Phys.* **2012**, *14* (18), 6382–6390. https://doi.org/10.1039/c2cp40586e.
(156) Schröder, D. Applications of Electrospray Ionization Mass Spectrometry in Mechanistic Studies and Catalysis Research. *Accounts of Chemical Research* **2012**, *45* (9), 1521–1532. https://doi.org/10.1021/ar3000426.
(157) Heck, R. F. Palladium-Catalyzed Reactions of Organic Halides with Oleins. *Accounts Chem. Res.* **1979**, *12* (4), 146–151. https://doi.org/10.1021/ar50136a006.
(158) Heck, R. F.; Nolley, J. P. Palladium-Catalyzed Vinylic Substitution with Highly Activated Aryl Halides. *J. Org. Chem.* **1972**, *37* (14), 2320-. https://doi.org/10.1021/jo00979a024.
(159) Milstein, D.; Stille, J. K. Palladium-Catalyzed Coupling of Tetraorganotin Compounds with Aryl and Benzyl Halides - Synthetic Utility and Mechanism. *J. Am. Chem. Soc.* **1979**, *101* (17), 4992–4998. https://doi.org/10.1021/ja00511a032.
(160) Miyaura, N.; Suzuki, A. Stereoselective Synthesis of Arylated (E)-Alkenes by the Reation of Alk-1-Enylboranes with Aryl Halides in the Presence of Palladium Catalyst. *J. Chem. Soc.-Chem. Commun.* **1979**, No. 19, 866–867. https://doi.org/10.1039/c39790000866.
(161) Miyaura, N.; Suzuki, A. Palladium-Catalyzed Cross-Coupling Reactions of Organoboron Compounds. *Chem. Rev.* **1995**, *95* (7), 2457–2483. https://doi.org/10.1021/cr00039a007.
(162) Miyaura, N.; Yamada, K.; Suzuki, A. New Stereospecific Cross-Coupling by the Palladium-Catalyzed Reaction of 1-Alkenylboranes with 1-Alkenyl of 1-Alkynyl Halides. *Tetrahedron Lett.* **1979**, *20* (36), 3437–3440. https://doi.org/10.1016/s0040-4039(01)95429-2.
(163) Sonogashira, K.; Tohda, Y.; Hagihara, N. Convenient Synthesis of Acetylenes of Acetylenic Hydrogen with Bromoalkenes, Iodoarenes, and Bromopyridines. *Tetrahedron Lett.* **1975**, No. 50, 4467–4470.

(164) Stille, J. K. The Palladium-Catalyzed Cross-Coupling Reactions of Organotin Reagents with Organic Electrophiles. *Angew. Chem.-Int. Edit. Engl.* **1986**, *25* (6), 508–523. https://doi.org/10.1002/anie.198605081.
(165) Takahashi, S.; Kuroyama, Y.; Sonogashira, K.; Hagihara, N. A Convenient Synthesis of Ethynylarenes and Diethynylarenes. *Synthesis* **1980**, No. 8, 627–630.
(166) Ziegler, C. B.; Heck, R. F. Palladium-Catalyzed Vinylic Substitution with Highly Activated Aryl Halides. *J. Org. Chem.* **1978**, *43* (15), 2941–2946. https://doi.org/10.1021/jo00409a001.
(167) Goodson, F. E.; Wallow, T. I.; Novak, B. M. Mechanistic Studies on the Aryl−Aryl Interchange Reaction of $ArPdL_2I$ (L = Triarylphosphine) Complexes. *J. Am. Chem. Soc.* **1997**, *119* (51), 12441–12453. https://doi.org/10.1021/ja972554g.
(168) Schluter, A. D.; Wegner, G. Palladium and Nickel Catalyzed Polycondensation - The Key to Structurally Defined Polyarylenes and Other Aromatic Polymers. *Acta Polym.* **1993**, *44* (2), 59–69. https://doi.org/10.1002/actp.1993.010440201.
(169) Yamamoto, T. Electrically Conducting and Thermally Stable π-Conjugated Poly(Arylene)s Prepared by Organometallic Processes. *Prog. Polym. Sci.* **1992**, *17* (6), 1153–1205. https://doi.org/10.1016/0079-6700(92)90009-n.
(170) Brown, J. M.; Cooley, N. A. Mapping the Reaction Pathway in Palladium-Catalyzed Cross-Coupling Reactions. *Organometallics* **1990**, *9* (2), 353–359. https://doi.org/10.1021/om00116a010.
(171) Farina, V.; Krishnan, B. Large Rate Accelerations in the Stille Reaction with Tri-2-Furylphosphine and Triphenylarsine as Palladium Ligands - Mechanistic and Synthetic Implecations. *J. Am. Chem. Soc.* **1991**, *113* (25), 9585–9595. https://doi.org/10.1021/ja00025a025.
(172) Negishi, E.; Takahashi, T.; Baba, S.; Vanhorn, D. E.; Okukado, N. Nickel-Catalyzed Cross Coupling. 31. Palladium-Catalyzed or Nickle-Catalyzed Reactions of Alkenylmetals with Unsaturated Organic Halides as a Selective Route to Arylated Alkenes and Conjugated Dienes - Scope, Limitations, and Mechanism. *J. Am. Chem. Soc.* **1987**, *109* (8), 2393–2401. https://doi.org/10.1021/ja00242a024.
(173) Fiebig, L.; Schlörer, N.; Schmalz, H.-G.; Schäfer, M. Aryl-Phenyl Scrambling in Intermediate Organopalladium Complexes: A Gas-Phase Study of the Mizoroki-Heck Reaction. *Chem. Eur. J.* **2014**, *20* (17), 4906–4910. https://doi.org/10.1002/chem.201400115.
(174) Aullon, G.; Alvarez, S. Axial Bonding Capabilities of Square Planar d^8-ML_4 Complexes. Theoretical Study and Structural Correlations. *Inorg. Chem.* **1996**, *35* (11), 3137–3144. https://doi.org/10.1021/ic951643w.
(175) Fillion, E.; Trépanier, V. É.; Heikkinen, J. J.; Remorova, A. A.; Carson, R. J.; Goll, J. M.; Seed, A. Palladium-Catalyzed Intramolecular Reactions of (*E*)-2,2-Disubstituted 1-Alkenyldimethylalanes with Aryl Triflates. *Organomet.* **2009**, *28* (12), 3518–3531. https://doi.org/10.1021/om900286x.
(176) MacAleese, L.; Maitre, P. Infrared Spectroscopy of Organometallic Ions in the Gas Phase: From Model to Real World Complexes. *Mass Spectrom. Rev.* **2007**, *26* (4), 583–605. https://doi.org/10.1002/mas.20138.
(177) Roithova, J. Characterization of Reaction Intermediates by Ion Spectroscopy. *Chem. Soc. Rev.* **2012**, *41* (2), 547–559. https://doi.org/10.1039/c1cs15133a.

(178) Hopkins, W. S.; Marta, R. A.; McMahon, T. B. Proton-Bound 3-Cyanophenylalanine Trimethylamine Clusters: Isomer-Specific Fragmentation Pathways and Evidence of Gas-Phase Zwitterions. *J. Phys. Chem. A* **2013**, *117* (41), 10714–10718. https://doi.org/10.1021/jp407766j.

(179) MacAleese, L.; Simon, A.; McMahon, T. B.; Ortega, J. M.; Scuderi, D.; Lemaire, J.; Maitre, P. Mid-IR Spectroscopy of Protonated Leucine Methyl Ester Performed with an FTICR or a Paul Type Ion-Trap. *Int. J. Mass Spectrom.* **2006**, *249*, 14–20. https://doi.org/10.1016/j.ijms.2006.01.008.

(180) Lee, S.-S.; Park, S.; Hong, Y.; Lee, J.; Kim, J.-H.; Yoon, D.; Kong, X.; Lee, S.; Oh, H. B. Chiral Differentiation of D- and l-Alanine by Permethylated β-Cyclodextrin: IRMPD Spectroscopy and DFT Methods. *Phys. Chem. Chem. Phys.* **2017**, *19* (22), 14729–14737. https://doi.org/10.1039/C7CP01085K.

(181) Agrawal, D.; Zins, E.-L.; Schröder, D. Intramolecular Scrambling of Aryl Groups in Organopalladium Complexes $[ArPd(PPh_3)_2]^+$: From Solution to the Gas Phase, Back Again, and In-Between. *Chem.-Asian J.* **2010**, *5* (7), 1667–1676. https://doi.org/10.1002/asia.201000086.

(182) Black, J. G.; Yablonovitch, E.; Bloembergen, N.; Mukamel, S. COLLISIONLESS MULTIPHOTON DISSOCIATION OF SF_6 - STATISTICAL THERMODYNAMIC PROCESS. *Phys. Rev. Lett.* **1977**, *38* (20), 1131–1134. https://doi.org/10.1103/PhysRevLett.38.1131.

(183) Grant, E. R.; Schulz, P. A.; Sudbo, A. S.; Shen, Y. R.; Lee, Y. T. Is Multiphoton Dissociation of Molecules a Statistical Thermal Process. *Phys. Rev. Lett.* **1978**, *40* (2), 115–118. https://doi.org/10.1103/PhysRevLett.40.115.

(184) Lehmann, K. K.; Scoles, G.; Pate, B. H. Intramolecular Dynamics from Eigenstate-Resolved Infrared-Spectra. *Annu. Rev. Phys. Chem.* **1994**, *45*, 241–274. https://doi.org/10.1146/annurev.physchem.45.1.241.

(185) Felker, P. M.; Lambert, W. R.; Zewail, A. H. Dynamics of Intramolecular Vibrational Energy Redistribution (IVR). 4. Excess Energy-Dependence, Tert-Stilbene. *J. Chem. Phys.* **1985**, *82* (7), 3003–3010. https://doi.org/10.1063/1.448249.

(186) Felker, P. M.; Zewail, A. H. Dynamics of Intramolecular Vibrational Energy Redistribution (IVR). 1. Coherence Effects. *J. Chem. Phys.* **1985**, *82* (7), 2961–2974. https://doi.org/10.1063/1.448246.

(187) Felker, P. M.; Zewail, A. H. Dynamics of Intramolecular Vibrational Energy Redistribution (IVR). 2. Excess Energy-Dependence. *J. Chem. Phys.* **1985**, *82* (7), 2975–2993. https://doi.org/10.1063/1.448247.

(188) Felker, P. M.; Zewail, A. H. Dynamics of Intramolecular Vibrational Energy Redistribution (IVR). 3. Role of Molecular Rotations. *J. Chem. Phys.* **1985**, *82* (7), 2994–3002. https://doi.org/10.1063/1.448248.

(189) Callegari, A.; Merker, U.; Engels, P.; Srivastava, H. K.; Lehmann, K. K.; Scoles, G. Intramolecular Vibrational Redistribution in Aromatic Molecules. I. Eigenstate Resolved CH Stretch First Overtone Spectra of Benzene. *J. Chem. Phys.* **2000**, *113* (23), 10583–10596. https://doi.org/10.1063/1.1319875.

(190) Litzen, L.; Lundberg, H.; Tchange-Brillet, W.-U. L.; Launay, F.; Engleman Jr., R. Analysis of the Pd(II) Spectrum in the Ultraviolet and Infrared Regions. *Phys. Scr.* **2001**, *64*, 63–73.

(191) Huq, M. M.; Rahman, R.; Naher, M.; Khan, M. M. R.; Masud, M. K.; Hossain, G. M. G.; Zhu, N.; Lo, Y.; Younus, M.; Wong, W. Synthesis, Characterization and Catalytic Activities of Palladium (II) Nitroaryl Complexes. *J. Inorg. Organomet. Polym.* **2016**, *26*, 1243–1252.

(192) Singh, N.; Singh, B.; Thapliyal, K.; Drew, M. Synthesis, X-Ray Crystal Structures and Properties of Complex Salts and Sterically Crowded Heteroleptic Complexes of Group 10 Metal Ions with Aromatic Sulfonyl Dithiocarbimates and Triphenylphosphine Ligand. *Inorg. Chim. Acta* **2010**, No. 363, 3589–3596.

(193) Huang, W.; Sergeeva, A. P.; Zhai, H. J.; Averkiev, B. B.; Wang, L. S.; Boldyrev, A. I. A Concentric Planar Doubly Pi-Aromatic B_{19}^- Cluster. *Nat. Chem.* **2010**, *2* (3), 202–206. https://doi.org/10.1038/nchem.534.

(194) Kiran, B.; Bulusu, S.; Zhai, H. J.; Yoo, S.; Zeng, X. C.; Wang, L. S. Planar-to-Tubular Structural Transition in Boron Clusters: B_{20} as the Embryo of Single-Walled Boron Nanotubes. *Proc. Natl. Acad. Sci. U. S. A.* **2005**, *102* (4), 961–964. https://doi.org/10.1073/pnas.0408132102.

(195) Oger, E.; Crawford, N. R. M.; Kelting, R.; Weis, P.; Kappes, M. M.; Ahlrichs, R. Boron Cluster Cations: Transition from Planar to Cylindrical Structures. *Angew. Chem.-Int. Edit.* **2007**, *46* (44), 8503–8506. https://doi.org/10.1002/anie.200701915.

(196) Piazza, Z. A.; Hu, H. S.; Li, W. L.; Zhao, Y. F.; Li, J.; Wang, L. S. Planar Hexagonal B_{36} as a Potential Basis for Extended Single-Atom Layer Boron Sheets. *Nat. Commun.* **2014**, *5*, 6. https://doi.org/10.1038/ncomms4113.

(197) Popov, I. A.; Li, W. L.; Piazza, Z. A.; Boldyrev, A. I.; Wang, L. S. Complexes between Planar Boron Clusters and Transition Metals: A Photoelectron Spectroscopy and Ab Initio Study of CoB_{12}^- and RhB_{12}. *J. Phys. Chem. A* **2014**, *118* (37), 8098–8105. https://doi.org/10.1021/jp411867q.

(198) Romanescu, C.; Harding, D. J.; Fielicke, A.; Wang, L. S. Probing the Structures of Neutral Boron Clusters Using Infrared/Vacuum Ultraviolet Two Color Ionization: B_{11}, B_{16}, and B_{17}. *J. Chem. Phys.* **2012**, *137* (1), 6. https://doi.org/10.1063/1.4732308.

(199) Sergeeva, A. P.; Popov, I. A.; Piazza, Z. A.; Li, W. L.; Romanescu, C.; Wang, L. S.; Boldyrev, A. I. Understanding Boron through Size-Selected Clusters: Structure, Chemical Bonding, and Fluxionality. *Accounts Chem. Res.* **2014**, *47* (4), 1349–1358. https://doi.org/10.1021/ar400310g.

(200) Zhai, H. J.; Alexandrova, A. N.; Birch, K. A.; Boldyrev, A. I.; Wang, L. S. Hepta- and Octacoordinate Boron in Molecular Wheels of Eight- and Nine-Atom Boron Clusters: Observation and Confirmation. *Angew. Chem.-Int. Edit.* **2003**, *42* (48), 6004–6008. https://doi.org/10.1002/anie.200351874.

(201) Moreno, D.; Pan, S.; Liu-Zeonjok, L.; Islas, R.; Osorio, E.; Martinez-Guajardo, G.; Chattaraj, P. K.; Heine, T.; Merino, G. B_{18}^{2-}: A Quasi-Planar Bowl Member of the Wankel Motor Family. *Chem. Commun.* **2014**, *50* (60), 8140–8143. https://doi.org/10.1039/c4cc02225d.

(202) Pham, H. T.; Duong, L. V.; Pham, B. Q.; Nguyen, M. T. The 2D-to-3D Geometry Hopping in Small Boron Clusters: The Charge Effect. *Chem. Phys. Lett.* **2013**, *577*, 32–37. https://doi.org/10.1016/j.cplett.2013.05.041.

(203) Kroto, H. W.; Heath, J. R.; Obrien, S. C.; Curl, R. F.; Smalley, R. E. C_{60} - Buckminsterfullerene. *Nature* **1985**, *318* (6042), 162–163. https://doi.org/10.1038/318162a0.

(204) Quandt, A.; Boustani, I. Boron Nanotubes. *Chemphyschem* **2005**, *6* (10), 2001–2008. https://doi.org/10.1002/cphc.200500205.
(205) Szwacki, N. G.; Sadrzadeh, A.; Yakobson, B. I. B_{80} Fullerene: An Ab Initio Prediction of Geometry, Stability, and Electronic Structure. *Phys. Rev. Lett.* **2007**, *98* (16), 4. https://doi.org/10.1103/PhysRevLett.98.166804.
(206) Zhai, H.-J.; Zhao, Y.-F.; Li, W.-L.; Chen, Q.; Bai, H.; Hu, H.-S.; Piazza, Z. A.; Tian, W.-J.; Lu, H.-G.; Wu, Y.-B.; et al. Observation of an All-Boron Fullerene. *Nat. Chem.* **2014**, *6* (8), 727–731. https://doi.org/10.1038/nchem.1999.
(207) Alexandrova, A. N.; Boldyrev, A. I.; Zhai, H. J.; Wang, L. S. All-Boron Aromatic Clusters as Potential New Inorganic Ligands and Building Blocks in Chemistry. *Coord. Chem. Rev.* **2006**, *250* (21–22), 2811–2866. https://doi.org/10.1016/j.ccr.2006.03.032.
(208) Kirk, R. W.; Timms, P. L.; Smith, D. L.; Airey, W. Perhalogenated Polyboron and Silicon-Boron Analogs of Borane. *Dalton Trans.* **1972**, No. 13, 1392–1396. https://doi.org/10.1039/dt9720001392.
(209) Maier, A.; Hofmann, M.; Pritzkow, H.; Siebert, W. A Planar, Aromatic Bicyclo-Tetraborane$_4$. *Angew. Chem.-Int. Edit.* **2002**, *41* (9), 1529–1532. https://doi.org/10.1002/1521-3773(20020503)41:9<1529::aid-anie1529>3.0.co;2-g.
(210) Morrison, J. A. Chemistry of the Polyhedral Boron Halides and the Diboron Tetrahalides. *Chem. Rev.* **1991**, *91* (1), 35–48. https://doi.org/10.1021/cr00001a003.
(211) Pardoe, J. A. J.; Norman, N. C.; Timms, P. L.; Parsons, S.; Mackie, I.; Pulham, C. R.; Rankin, D. W. H. The Surprising Structures of B_8F_{12} and $B_{10}F_{12}$. *Angew. Chem.-Int. Edit.* **2003**, *42* (5), 571–573. https://doi.org/10.1002/anie.200390164.
(212) Szwacki, N. G.; Tymczak, C. J. $B_{12}H_n$ and $B_{12}F_n$: Planar vs Icosahedral Structures. *Nanoscale Res. Lett.* **2012**, *7*, 1–6. https://doi.org/10.1186/1556-276x-7-236.
(213) Timms, P. L.; Norman, N. C.; Pardoe, J. A. J.; Mackie, I. D.; Hinchley, S. L.; Parsons, S.; Rankin, D. W. H. The Structures of Higher Boron Halides B_8X_{12} (X = F, Cl, Br and I) by Gas-Phase Electron Diffraction and Ab Initio Calculations. *Dalton Trans.* **2005**, No. 3, 607–616. https://doi.org/10.1039/b416077k.
(214) Trefonas, L.; Lipscomb, W. N. Crystal and Molecular Structure of Diboron Tetrafluoride, B_2F_4. *J. Chem. Phys.* **1958**, *28* (1), 54–55. https://doi.org/10.1063/1.1744079.
(215) Pitochelli, A. R.; Hawthorne, M. F. The Isolation of the Icosahedral $B_{12}H_{12}^{-2}$ Ion. *J. Am. Chem. Soc.* **1960**, *82* (12), 3228–3229. https://doi.org/10.1021/ja01497a069.
(216) Bukovsky, E. V.; Lui, K. W.; Peryshkov, D. V.; Strauss, S. H. Monovalent Metal Salts of the Superweak Anion $B_{12}F_{12}^{2-}$: Crystal Structure Transformations during Reversible Binding of Solvent Molecules. *Abstr. Pap. Am. Chem. Soc.* **2011**, *242*, 1.
(217) Li, W.-L.; Chen, X.; Jian, T.; Chen, T.-T.; Li, J.; Wang, L.-S. From Planar Boron Clusters to Borophenes and Metalloborophenes. *Nat. Rev. Chem.* **2017**, *1*, 0071. https://doi.org/10.1038/s41570-017-0071.
(218) Boere, R. T.; Derendorf, J.; Jenne, C.; Kacprzak, S.; Kessler, M.; Riebau, R.; Riedel, S.; Roemmele, T. L.; Ruhle, M.; Scherer, H.; et al. On the Oxidation of the Three-Dimensional Aromatics $B_{12}X_{12}^{2-}$ (X=F, Cl, Br, I). *Chem.-Eur. J.* **2014**, *20* (15), 4447–4459. https://doi.org/10.1002/chem.201304405.
(219) Warneke, J.; Jenne, C.; Bernarding, J.; Azov, V. A.; Plaumann, M. Evidence for an Intrinsic Binding Force between Dodecaborate Dianions and Receptors with Hydrophobic Binding Pockets. *Chem. Commun.* **2016**, *52* (37), 6300–6303. https://doi.org/10.1039/C6CC01233G.

(220) Rohdenburg, M.; Mayer, M.; Grellmann, M.; Jenne, C.; Borrmann, T.; Kleemiss, F.; Azov, V. A.; Asmis, K. R.; Grabowsky, S.; Warneke, J. Superelectrophilic Behavior of an Anion Demonstrated by the Spontaneous Binding of Noble Gases to $B_{12}Cl_{11}^-$. *Angew. Chem.-Int. Edit.* **2017**, *56* (27), 7980–7985. https://doi.org/10.1002/anie.201702237.

(221) Warneke, J.; Dülcks, T.; Knapp, C.; Gabel, D. Collision-Induced Gas-Phase Reactions of Perhalogenated Closo-Dodecaborate Clusters – a Comparative Study. *Phys. Chem. Chem. Phys.* **2011**, *13* (13), 5712. https://doi.org/10.1039/c0cp02386h.

(222) Warneke, J.; Hou, G.-L.; Aprà, E.; Jenne, C.; Yang, Z.; Qin, Z.; Kowalski, K.; Wang, X.-B.; Xantheas, S. S. Electronic Structure and Stability of $[B_{12}X_{12}]^{2-}$ (X = F–At): A Combined Photoelectron Spectroscopic and Theoretical Study. *J. Am. Chem. Soc.* **2017**, *139* (41), 14749–14756. https://doi.org/10.1021/jacs.7b08598.

(223) Udovic, T. J.; Matsuo, M.; Unemoto, A.; Verdal, N.; Stavila, V.; Skripov, A. V.; Rush, J. J.; Takamura, H.; Orimo, S. Sodium Superionic Conduction in $Na_2B_{12}H_{12}$. *Chem. Commun.* **2014**, *50* (28), 3750–3752. https://doi.org/10.1039/c3cc49805k.

(224) Peryshkov, D. V. Direct Fluorination of $K_2B_{12}H_{12}$ and Synthesis and Characterization of Metal Salts of $B_{12}F_{12}^{2-}$. PhD Thesis, Colorado State University: Fort Collins, Colorado, 2011.

(225) Ivanov, S. V.; Peryshkov, D. V.; Miller, S. M.; Anderson, O. P.; Rappe, A. K.; Strauss, S. H. Synthesis, Structure, and Reactivity of $AlMe_2$(1-Me-$CB_{11}F_{11}$): An $AlMe_2^+$ Cation-like Species Bonded to a Superweak Anion. *J. Fluor. Chem.* **2012**, *143*, 99–102. https://doi.org/10.1016/j.jfluchem.2012.02.001.

(226) Naganawa, H.; Suzuki, H.; Noro, J.; Kimura, T. Selective Separation of Am(III) from Lanthanides(III) by Solvent Extraction with Hydrophobic Field of "Superweak''' Anion." *Chem. Commun.* **2005**, No. 23, 2963–2965. https://doi.org/10.1039/b502763m.

(227) Peryshkov, D. V.; Bukovsky, E. V.; Folsom, T. C.; Strauss, S. H. Solid-State Solvation and Anion Packing Patterns in X-Ray Structures of Crystalline $K_2(Solv)_nB_{12}F_{12}$ (Solv = H_2O_2(Aq), CH_3OH, CH_3NO_2, and CH_3CN). *Polyhedron* **2013**, *58*, 197–205. https://doi.org/10.1016/j.poly.2012.11.004.

(228) Plesek, J. Potential Applications of the Boron Cluster Compounds. *Chem. Rev.* **1992**, *92* (2), 269–278. https://doi.org/10.1021/cr00010a005.

(229) Roll, M. F. Ionic Borohydride Clusters for the Next Generation of Boron Thin-Films: Nano-Building Blocks for Electrochemical and Refractory Materials. *J. Mater. Res.* **2016**, *31* (18), 2736–2748. https://doi.org/10.1557/jmr.2016.261.

(230) Soloway, A. H.; Tjarks, W.; Barnum, B. A.; Rong, F. G.; Barth, R. F.; Codogni, I. M.; Wilson, J. G. The Chemistry of Neutron Capture Therapy. *Chem. Rev.* **1998**, *98* (4), 1515–1562. https://doi.org/10.1021/cr941195u.

(231) Jenne, C.; Mathias, K.; Warneke, J. Protic Anions $[H(B_{12}X_{12})]^-$ (X=F, Cl, Br, I) That Act as Brønsted Acids in the Gas Phase. *Chem. Eur. J.* **2015**, *21*, 5887–5891.

(232) Baba, T.; Imamura, Y.; Okamoto, M.; Nakai, H. Analysis on Excitation of Molecules with I-h Symmetry: Frozen Orbital Analysis and General Rules. *Chem. Lett.* **2008**, *37* (3), 322–323. https://doi.org/10.1246/cl.2008.322.

(233) Alexandrova, A. N.; Zhai, H. J.; Wang, L. S.; Boldyrev, A. I. Molecular Wheel B_8^{2-} as a New Inorganic Ligand. Photoelectron Spectroscopy and Ab Initio Characterization of LiB_8. *Inorg. Chem.* **2004**, *43* (12), 3552–3554. https://doi.org/10.1021/ic049706a.

(234) Galeev, T. R.; Romanescu, C.; Li, W. L.; Wang, L. S.; Boldyrev, A. I. Valence Isoelectronic Substitution in the B_8^- and B_9^- Molecular Wheels by an Al Dopant Atom:

Umbrella-like Structures of AlB_7^- and AlB_8^-. *J. Chem. Phys.* **2011**, *135* (10), 8. https://doi.org/10.1063/1.3625959.
(235) Li, W. L.; Romanescu, C.; Galeev, T. R.; Piazza, Z. A.; Boldyrev, A. I.; Wang, L. S. Transition-Metal-Centered Nine-Membered Boron Rings: M©B_9 and M©B_9^- (M = Rh, Ir). *J. Am. Chem. Soc.* **2012**, *134* (1), 165–168. https://doi.org/10.1021/ja209808k.
(236) Li, W. L.; Romanescu, C.; Piazza, Z. A.; Wang, L. S. Geometrical Requirements for Transition-Metal-Centered Aromatic Boron Wheels: The Case of VB_{10}. *Phys. Chem. Chem. Phys.* **2012**, *14* (39), 13663–13669. https://doi.org/10.1039/c2cp42218b.
(237) Wiesenfeldt, M. P.; Nairoukh, Z.; Li, W.; Glorius, F. Hydrogenation of Fluoroarenes: Direct Access to All-*Cis*-(Multi)Fluorinated Cycloalkanes. *Science* **2017**, *357* (6354), 908–912. https://doi.org/10.1126/science.aao0270.
(238) Cabaleiro-Lago, E. M.; Rodríguez-Otero, J. σ-σ, σ-π, and π-π Stacking Interactions between Six-Membered Cyclic Systems. Dispersion Dominates and Electrostatics Commands. *ChemistrySelect* **2017**, *2* (18), 5157–5166. https://doi.org/10.1002/slct.201700671.
(239) Crabtree, R. H.; Siegbahn, P. E. M.; Eisenstein, O.; Rheingold, A. L.; Koetzle, T. F. A New Intermolecular Interaction: UnconventionalHydrogen Bonds with Element−Hydride Bonds as ProtonAcceptor. *Acc. Chem. Res.* **1996**, *29* (7), 348–354. https://doi.org/10.1021/ar950150s.
(240) Geis, V.; Guttsche, K.; Knapp, C.; Scherer, H.; Uzun, R. Synthesis and Characterization of Synthetically Useful Salts of the Weakly-Coordinating Dianion $B_{12}Cl_{12}^{2-}$. *Dalton Trans.* **2009**, No. 15, 2687–2694. https://doi.org/10.1039/b821030f.
(241) Wang, X.-B.; Wang, L.-S. Development of a Low-Temperature Photoelectron Spectroscopy Instrument Using an Electrospray Ion Source and a Cryogenically Controlled Ion Trap. *Rev. Sci. Inst.* **2008**, *79* (7), 073108. https://doi.org/10.1063/1.2957610.
(242) Becke, A. D. Density-Functional Exchange-Energy Approximation with Correct Asyptotic Behavior. *Phys. Rev. A* **1988**, *38* (6), 3098–3100. https://doi.org/10.1103/PhysRevA.38.3098.
(243) Becke, A. D. Density-Functional Thermochemistry: The Role of Exact Exchange. *J. Chem. Phys.* **1993**, *98* (7), 5648–5652. https://doi.org/10.1063/1.464913.
(244) Andrae, D.; Haussermann, U.; Dolg, M.; Stoll, H.; Preuss, H. Energy-Adjusted Ab Initio Pseudopotentials for the 2nd and 3rd Row Transition Elements. *Theor. Chim. Acta* **1990**, *77* (2), 123–141. https://doi.org/10.1007/bf01114537.
(245) Rappoport, D.; Furche, F. Property-Optimized Gaussian Basis Sets for Molecular Response Calculations. *J. Chem. Phys.* **2010**, *133* (13), 11. https://doi.org/10.1063/1.3484283.
(246) Andersson, M. P.; Uvdal, P. New Scale Factors for Harmonic Vibrational Frequencies Using the B3LYP Density Functional Method with the Triple-Xi Basis Set 6-311+G(d,p). *J. Phys. Chem. A* **2005**, *109* (12), 2937–2941. https://doi.org/10.1021/jp045733a.
(247) Kramida, A.; Ralchenko, Y.; Reader, J. NIST Atomic Spectra Database (version 5.2).
(248) Basire, M.; Parneix, P.; Calvo, F. Finite-Temperature IR Spectroscopy of Polyatomic Molecules: A Theoretical Assessment of Scaling Factors. *J. Phys. Chem. A* **2010**, *114* (9), 3139–3146. https://doi.org/10.1021/jp9088639.

(249) Pankewitz, T.; Lagutschenkov, A.; Niedner-Schatteburg, G.; Xantheas, S. S.; Lee, Y. T. Infrared Spectrum of $NH_4^+(H_2O)$: Evidence for Mode Specific Fragmentation. *J. Chem. Phys.* **2007**, *126* (7), 14. https://doi.org/10.1063/1.2435352.

(250) Fagiani, M. R.; Liu Zeonjuk, L.; Esser, T. K.; Gabel, D.; Heine, T.; Asmis, K. R.; Warneke, J. Opening of an Icosahedral Boron Framework: A Combined Infrared Spectroscopic and Computational Study. *Chem. Phys. Lett.* **2015**, *625*, 48–52. https://doi.org/10.1016/j.cplett.2015.02.030.

(251) Stoyanov, E. S.; Stoyanova, I. V.; Reed, C. A. The Basicity of Unsaturated Hydrocarbons as Probed by Hydrogen-Bond-Acceptor Ability: Bifurcated $N\text{-}H^+\cdots\pi$ Hydrogen Bonding. *Chem. Eur. J.* **2008**, *14* (26), 7880–7891. https://doi.org/doi:10.1002/chem.200800337.

(252) Fedorova, I. V.; Safonova, L. P. Ab Initio Investigation of the Interionic Interactions in Triethylammonium-Based Protic Ionic Liquids: The Role of Anions in the Formation of Ion Pair and Hydrogen Bonded Structure. *J. Phys. Chem. A* **2019**, *123* (1), 293–300. https://doi.org/10.1021/acs.jpca.8b10906.

(253) Rowland, R. S.; Taylor, R. Intermolecular Nonbonded Contact Distances in Organic Crystal Structures: Comparison with Distances Expected from van Der Waals Radii. *J. Phys. Chem.* **1996**, *100* (18), 7384–7391. https://doi.org/10.1021/jp953141+.

(254) Bondi, A. Van Der Waals Volumes and Radii. *J. Phys. Chem.* **1964**, *68* (3), 441–451. https://doi.org/10.1021/j100785a001.

(255) Warneke, J.; Konieczka, S. Z.; Hou, G.-L.; Aprà, E.; Kerpen, C.; Keppner, F.; Schäfer, T. C.; Deckert, M.; Yang, Z.; Bylaska, E. J.; et al. Properties of Perhalogenated *Closo*-B_{10} and *Closo*-B_{11} Multiply Charged Anions and a Critical Comparison with *Closo*-B_{12} in the Gas and the Condensed Phase. *Phys. Chem. Chem. Phys.* **2019**, *21* (11), 5903–5915. https://doi.org/10.1039/C8CP05313H.

(256) Thoelmann, D.; Tonner, D. S.; McMahon, T. B. Spontaneous Unimolecular Dissociation of Small Cluster Ions, $(H_3O^+)L_n$ and $Cl^-(H_2O)_n$ (n = 2 - 4), under Fourier Transform Ion Cyclotron Resonance Conditions. *J. Phys. Chem.* **1994**, *98* (8), 2002–2004. https://doi.org/10.1021/j100059a002.

(257) Linstrom, P. J.; Millard, W. G. NIST Chemistry WebBook.

(258) Paul, G. J. C.; Kebarle, P. Stabilities in the Gas Phase of the Hydrogen Bonded Complexes, $YC_6H_4OH\text{-}X^-$, of Substituted Phenols, YC_6E_4OH, with the Halide Anions X^- (Cl^-, Br^-, I^-). *Can. J. Chem.* **1990**, *68* (11), 2070–2077. https://doi.org/10.1139/v90-316.

(259) McQuarrie, D.; Simon, J. *Physical Chemistry: A Molecular Approach*; University Science Books, 1997.

(260) Sosa, G. L.; Peruchena, N. M.; Contreras, R. H.; Castro, E. A. Topological and NBO Analysis of Hydrogen Bonding Interactions Involving C–H···O Bonds. *Journal of Molecular Structure: THEOCHEM* **2002**, *577* (2–3), 219–228. https://doi.org/10.1016/S0166-1280(01)00670-4.